Conical intersections within linear-response time-dependent density functional theory

A thesis submitted in partial fulfillment for the degree of Doctor of Philosophy in Chemistry.

April 2025

Department of Chemistry
Durham University

Jack Thomas Taylor
St Cuthbert's Society, Durham University

Author's declaration

The material contained within this thesis has not previously been submitted for a degree at Durham University or any other university. The research reported within this thesis has been conducted by the author unless indicated otherwise.

Statement of copyright

SIGNED: **Jack Thomas Taylor** DATE: **09 April 2025**

Abstract

Regions of nuclear-configuration space away from the Franck-Condon geometry can prove problematic for many popular electronic-structure methods, given the propensity of such regions to possess conical intersections (CXs), i.e., (highly-connected) points of degeneracy between potential energy surfaces (PESs). CXs constitute the mechanistic bedrock of our theoretical framework to understand the ultrafast, non-radiative decay processes in photochemistry and photophysics. With the likelihood (perhaps even inevitability) for nonadiabatic dynamics simulations to explore molecular geometries in close proximity to CXs, it is vital that the performance of electronic-structure methods is routinely examined in this context. As such, this thesis scrutinises the ability of linear-response time-dependent density functional theory within the adiabatic approximation (AA LR-TDDFT) to correctly describe (i) ground-to-excited state and (ii) excited-to-excited state minimum-energy CXs (MECXs), the latter experiencing much less attention in the literature than the former. Initially, we compare the performance of AA LR-TDDFT in terms of the location, topology and topography of the MECXs it affords in two prototypical molecules, protonated formaldimine (S_2/S_1 and S_1/S_0) and pyrazine (S_2/S_1), to those afforded by two popular wavefunction-based methods. Such a comparison highlights a connection between two observations made previously in the literature regarding defective ground-to-excited state intersections within AA LR-TDDFT; both are shown in this thesis to emanate from the same defective PES feature. The thesis then examines the accumulated topological phase of the corresponding adiabatic electronic wavefunction in both aforementioned S_2/S_1 and S_1/S_0 MECX cases, and goes on to provide a detailed investigation of trajectory-surface hopping dynamics in protonated formaldimine, focused on the influence of the defective AA LR-TDDFT S_1/S_0 intersection.

Acknowledgments

First and foremost, I would like to thank my supervisors, David Tozer (Durham University) and Basile Curchod (Bristol University), for their constant advice, support and patience throughout the past three and a half years. I am truly grateful for their academic mentorship, enthusiasm for always doing good science, and most importantly, their friendships. I am indebted to their generosity.

I would, of course, also like to thank my fellow PhD and Postdoc members of the In Silico Photochemistry Group (ISPG): Lea, Antonio, Lewis, Ema, Yorick (Yorg), Daniel, Dasha, Harry, Jiří (Jirka), Vera, Federico (Fede), Juliette, Javi, Will, and Freddie (and honorary member, Veronika). Together, they have served as the dearest of academic families, and I am very excited to see where we all end up! Special thanks, however, must first go to Antonio for his kind supervision and immediate friendship at the very beginning of my time in the ISPG as a summer undergraduate intern in 2019, as well as his continued assistance (from a far) throughout my PhD. Special academic thanks go to Jirka and Daniel for their numerous discussions regarding the trajectory-surface hopping dynamics carried out in Chapter 5 of this thesis, and their implementation of the Baeck-An (Jirka) and SHωIT (Daniel) hopping schemes in ABIN for me to test and use. Lastly, special thanks go to Yorick and Vera. Thank you for being unapologetically yourselves, and for allowing me to be the same. I will cherish our friendships always.

I have been in the very fortunate position during my PhD of having two supervisors at two separate universities. Therefore, a wider thanks must go to two groups of people, apart from those already mentioned, who I have been lucky enough to spend most of my PhD working day with. These include my fellow occupants of CG200(X) in the Department of Chemistry at Durham [Eoin, Ajeeth, Rachel, David, Robbie, Yesh (honorary member), Jing, Fred, James, Elliot, Yufeng and George], as well as my fellow members of the Centre for Computational Chemistry (CCC) in the School of Chemistry at Bristol [Alex, Oli, Helen, Josh, Joe, Cam (honorary member), Liv (honorary member), Abbie, Dan, Marv, Papu, Juno, Jack, Harry, Lorenzo and Matt]. I would also like to extend my thanks to Prof. Jan Verlet, Prof. Mark Wilson and Dr Mark Miller (Durham), and Prof. Andrew Orr-Ewing, Dr Tom Oliver and Prof. Mike Ashfold (Bristol) for their encouragement and academic interactions throughout my PhD.

During my time in Durham, both during undergrad and postgrad, I am thankful to have

been a part of another group of people, my family from home: Izzy, Ben, Lydia, Ryan, Haijing, Lauren, Arabella and Ronnie. Thank you for all the fond memories we have made together over the years. Further thanks go to my Durham Parkrun family (Izzy, Ryan, Catherine, Gillian, Dave, Melanie, Sabrina, Simon and Geetanjali) for (re-)introducing me to the joy of running, but more importantly the joy of catching up on everyone's weeks over coffee afterwards.

I acknowledge the EPSRC for an EPSRC Doctoral Studentship (Grant No. EP/T518001/1), as well as thank Dr Eckart Wrede (internal) and Dr Rachel Crespo-Otero (external) for agreeing to be my PhD thesis examiners.

The proverbial saying goes "it takes a village to raise a child". No truer statement can be made about one's academic journey, especially for those of us who also happen to be first-generation university students. Therefore, I would now like to thank several family and friends, none of whom are part of this curious bubble that is academia, but who have nonetheless been by my side throughout my journey within it so far. Firstly, to Phil and Deb Worthing, The Lindesays (Will, Ben and Dan), The Proberts (Adam, Hannah, Thea and Ludo), my grandfather (Tommy Taylor, Snr) and Matt Norton, I am immensely grateful for the endless love and support you have given me each year during my time at Durham and Bristol. I am indebted to each and every one of you. Secondly, to The Rones (Paul, Julie, Georgia, Charlie and William) and The Pridays (Dave, Bev, Brad, Yas and Harley), although our paths cross less frequently now (as is life), I am tremendously thankful for all the loving encouragement you have given me throughout my studies, whether that be at university, or before at school. I am equally indebted to each and everyone of you.

Lastly, but by no means least, here's to Tommy and Heather Taylor, my beautiful parents, for their unwavering love, sacrifice and guidance throughout my studies, and more importantly, life in general. Whatever I may or may not have amounted to as a person so far is purely down to you. No words can describe the extent of love I have for the two of you. Thank you.

To my grandmothers, Jennifer Manning and Joyce Phillips,
and my great-grandmother, Phyllis Pratt.

Table of Contents

List of Figures

List of Tables

List of acronyms

AA	Adiabatic approximation
AC	Avoided crossing
ADC(*n*)	*nth*-order algebraic diagrammatic construction
AE	Adiabatically exact
AIMS	Ab-initio multiple spawning
BH	Born-Huang
BO	Born-Oppenheimer
CAS	Complete active-space
CASSCF	Complete active-space self-consistent field
CI	Configuration interaction
CIS	Configuration interaction singles
CX	Conical intersection
DBOC	Diagonal Born-Oppenheimer correction
DFA	Density functional approximation
DFT	Density functional theory
EDC	Energy-based decoherence correction
EOM-CCSD	Equation-of-motion coupled cluster theory singles and doubles
FC	Franck-Condon
FCI	Full configuration interaction
FSSH	Fewest-switches surface hopping
GGA	Generalised gradient approximation
GP	Gradient-projection
GPU	Graphics processing unit

HF	Hartree-Fock
HK	Hohenberg-Kohn
HOMO	Highest occupied molecular orbital
Hxc	Hartree-exchange-correlation
KS	Kohn-Sham
KS-DFT	Kohn-Sham density functional theory
LDA	Local density approximation
LIIC	Linear interpolation in internal coordinates
LN	Lagrange-Newton
LR	Linear-response
LR-TDDFT	Linear-response time-dependent density functional theory
LUMO	Lowest unoccupied molecular orbital
LZ	Landau-Zener
LZSH	Landau-Zener surface hopping
MCSCF	Multiconfigurational self-consistent field
MCTDH	Multiconfigurational time-dependent Hartree
MECP	Minimum-energy crossing point
MECX	Minimum-energy conical intersection
MFE	Mean-field Ehrenfest
MP*n*	*nth*-order Møller-Plesset perturbation theory
MQC	Mixed quantum/classical
MRCI	Multireference configuration interaction
MRCISD	Multireference configuration interaction singles and doubles
MS-CASPT2	Multi-state complete active-space second-order perturbation theory
PES	Potential energy surface
PF	Penalty-function
QR	Quadratic-response
QR-TDDFT	Quadratic-response time-dependent density functional theory
RG	Runge-Gross
RPA	Random-phase approximation
SA-CASSCF	State-averaged complete active-space self-consistent field

SCF	Self-consistent field
SF-TDDFT	Spin-flip time-dependent density functional theory
SHωIT	Surface hopping with induced transition
SPA	Single-pole approximation
SS-SR	Single-state, single-reference
TBF	Trajectory basis function
TDA	Tamm-Dancoff approximation
TDC	Time-derivative (nonadiabatic) coupling
TDDFT	Time-dependent density functional theory
TDM	Transition dipole moment
TDSE	Time-dependent Schrödinger equation
TISE	Time-independent Schrödinger equation
TSH	Trajectory surface hopping
vMCG	Variational multiconfigurational Gaussian
xc	Exchange-correlation
XMS-CASPT2	Extended multi-state complete active-space second-order perturbation theory

Chapter 1

Introduction and motivation

Electronic-structure theory has been at the epicentre of quantum chemistry since its inception in the early 1930s. Describing precisely the intimate choreography between electrons remains a formidable task, as evidenced by the unremitting activity of the electronic-structure community to date. The mathematical object responsible for encoding such an electron dance is the electronic wavefunction, afforded upon solving the (electronic time-independent) Schrödinger equation. Given the high dimensionality of the electronic wavefunction, exact solution of the Schrödinger equation is precluded, except for the simplest chemical systems. Numerous approximate methods have been developed to predict the electronic structure of molecules, each with a different philosophy in addressing the problem.

By far the most popular approach nowadays is to bypass the calculation of the electronic wavefunction altogether, the fundamental principle underpinning density functional theory (DFT) [1]. Taking instead the electron density as its central quantity, DFT offers an excellent compromise between computational affordability and chemical accuracy. Although exact in principle, DFT in its conventional form–that attributed to Kohn and Sham (KS) [2]–is limited in practice by the need to approximate the so-called exchange-correlation (xc) functional, for which a "zoo" of approximations exist [3]. Despite this, KS-DFT is still considered the electronic-structure workhorse for tackling the ground-state properties of medium- to large-sized systems. With a diverse range of applications, spanning molecular (bio)chemistry, materials science and condensed matter physics, the widespread success of KS-DFT was recognised by the (joint) award of the 1998 Nobel Prize in Chemistry to Walter Kohn "for his development of density-functional theory" [4].

More recent years have seen a similar level of popularity garnered by time-dependent density functional theory (TDDFT) [5]. Unlike its time-independent counterpart, TDDFT offers a route to describing dynamical processes, such as the response of a molecule to a

time-dependent external field. As such, TDDFT considers the time-evolving electron density and, provided the external field is weak, enables access to the excited electronic states of a molecule, as well as its absorption spectrum. This is achieved through a linear-response (LR) formalism [6–8], in which excitation energies and oscillator strengths are given as the poles and residues of the dynamic polarisability, respectively. Like KS-DFT, LR-TDDFT is rooted in an exact formalism, however, its accuracy in practical applications is restricted by two approximations: the so-called adiabatic approximation (AA), as well as the same xc functional approximation as in KS-DFT. Both lead to a number of well-documented problems, in contrast to the "black-box" status LR-TDDFT often naively receives.

Historically, electronic-structure methods have been predominantly used either in purely ground-state applications (e.g., in calculation of binding energies, reaction barrier heights, vibrational frequencies, etc.), or in probing processes from the ground to excited electronic states within the Franck-Condon (FC) region (i.e., absorption spectroscopy). In such applications, it is sufficient to consider the nuclei as evolving on a single electronic state [or potential energy surface (PES)], a direct consequence of the Born-Oppenheimer (BO) approximation [9]. This evolution can relate to the explicit movement of nuclei within ab initio molecular dynamics, the Car-Parrinello method [10] being a notable example that famously exploits KS-DFT, or relate to the sampling of molecular geometries for absorption spectrum generation. Absorption of light, however, can also result in a plethora of photochemical and photophysical processes, in which the subsequently excited molecules are able to explore PES pathways that would otherwise be inaccessible (i.e., thermally). Such pathways allow molecules to venture to regions of nuclear-configuration space potentially far from the FC region, thus, the application of electronic-structure methods beyond the FC point [11] is of vital consideration. Photoactivated processes also inevitably lead to molecules exploring multiple PESs, synonymous with the breakdown of the BO approximation and the subject of nonadiabatic dynamics.

One unique feature of PESs that molecules can encounter during nonadiabatic dynamics away from the FC region is a conical intersection (CX), a point of degeneracy between two (or more) adiabatic electronic states, which is lifted linearly along two specific nuclear coordinates, the so-called branching space vectors. Despite previous scepticism, CXs are now understood to play a pivotal role in the non-radiative relaxation of a molecule from its excited electronic states to its ground electronic state. In practice, the correct description of a CX is important from two perspectives: (i) the electronic-structure theorists' perspective [i.e., a want to obtain as accurate electronic energy values (or PESs, more generally) as possible] and (ii) the nonadiabatic dynamicists' perspective (i.e., a want to gain reliable insight into how the photodynamics of a molecule transitions between electronic states). CXs provide an interesting challenge for the first community, given their dependence not only on the electronic states involved, but also the mutual coupling between such states, something that

is not naturally accessible with certain electronic-structure methods.

Progress in emerging frontiers of quantum chemistry–such as machine learning [12–18] and quantum computing [19–26]–has likewise been impeded by complications arising from CXs, hindering their immediate adoption within the nonadiabatic dynamics community. AA LR-TDDFT, on the other hand, has experienced a semi-routine use within the community since the late 2000s. In particular, CXs in AA LR-TDDFT were first investigated as early as 2006 [27], with AA LR-TDDFT initially showing a far from satisfactory description of CXs between the ground and first-excited electronic states. Discussion in the literature, however, of the possibility for AA LR-TDDFT to afford "approximate" ground-to-excited state CXs was introduced soon after [28]. With a supposedly appealing balance between accuracy and efficiency, AA LR-TDDFT and its imperfect description of CXs involving the ground electronic state has caught the attention of a number of research groups over the last 15 years.

Several observations can be made about the general approach taken in previous studies within the literature on this topic. (i) Only a handful of studies fully address the question of "why" AA LR-TDDFT struggles to describe ground-to-excited state CXs; the vast majority address the question of "how". (ii) Most studies discuss the ground-to-excited CX problem by comparing AA LR-TDDFT to a newly proposed approach, the performance of the latter often being the focal point. (iii) The majority of newly proposed methods take a pragmatic approach and leapfrog the ground-to-excited CX problem, rather than addressing it fundamentally within LR-TDDFT. (iv) The original studies either plotted KS-DFT and AA LR-TDDFT PESs on top of geometries optimised at another level of theory, or plotted them along natural molecular distortions (i.e., bond lengths, bond angles, dihedral angles, etc.) instead of the formal branching space vectors. (v) There remain differing opinions as to what predominantly causes the ground-to-excited state CX problem in AA LR-TDDFT. We would therefore argue that there is enough ambiguity or nuance in the "soup" of previous literature to warrant revisiting the specifics of the ground-to-excited state CX problem in AA LR-TDDFT. Equally, very few studies have explicitly investigated AA LR-TDDFT nonadiabatic dynamics all the way to the ground electronic state; potential problems with dynamics simulations caused by AA LR-TDDFT incorrectly describing CXs involving the ground electronic state have typically only been inferred from static, electronic-structure comparisons.

The situation with excited-to-excited state CXs in AA LR-TDDFT is different: they are assumed to be described correctly. This assumption, along with the computational affordability of AA LR-TDDFT, are the primary reasons for the widespread use of AA LR-TDDFT in excited-state dynamics. However, it is important to remember all the elements that contribute to the description of a CX, namely, the molecular geometry (or geometries) at which the degeneracy occurs, the branching space vectors along which the degeneracy is lifted and then finally the PESs, themselves. In TDDFT, both excited-to-excited state branching space vectors can only be obtained together formally exactly if one goes beyond linear-response. Since

very little has been reported on the performance of AA LR-TDDFT in specifically describing excited-to-excited state CXs, it brings into question whether such an assumption is in fact valid.

Taking the above discussion into account, the aims of this thesis include:

(1) To provide an explicit investigation of the description of excited-to-excited state CXs in AA LR-TDDFT from a static, electronic-structure perspective.

(2) To revisit the description of ground-to-excited state CXs in AA LR-TDDFT without consideration of any other (newly proposed) density-based approaches.

(3) To accomplish aims (1) and (2) using an internally consistent protocol for plotting the CX of a given molecule, with electronic energies, branching space vectors and nuclear geometries obtained at the same level of theory.

(4) To determine the practical impact of potentially defective ground-to-excited state CXs in AA LR-TDDFT on nonadiabatic dynamics in their close proximity.

The structure of this thesis is as follows. Chapter 2 starts by introducing the theoretical "lens" through which most chemists view photochemistry, namely the Born-Huang representation of the molecular wavefunction, in preparation for then outlining the foundations, characterisation and practical implications of CXs. An overview of (AA LR-)TDDFT is subsequently given, starting with ground-state (KS-)DFT, before focussing on known limitations of practical AA LR-TDDFT that are pertinent to this thesis. Chapter 3 constitutes the first of three research chapters. It addresses aims (1) and (2) in relation to the location, topology and topography of CXs in two exemplar molecules, protonated formaldimine and pyrazine, comparing the performance of AA LR-TDDFT with two wavefunction-based approaches that are also routinely used in nonadiabatic dynamics studies. Different approximations for the xc functional are tested for the excited-to-excited state CX in pyrazine and all CXs are plotted with aim (3) in mind. In Chapter 4, the topological phase of the electronic wavefunction–a definitive signature of CXs–is calculated to verify the quality of the excited-to-excited state and ground-to-excited state CXs afforded by AA LR-TDDFT in Chapter 3 for the same prototypical molecules. Chapter 5 provides a detailed investigation of nonadiabatic dynamics close to the ground-to-excited state intersection in protonated formaldimine with AA LR-TDDFT, comparing the aptitude of four variants of the popular trajectory-surface hopping approach to deal with this potentially problematic region. The practical "size" of CXs, as well as the use of natural molecular distortions to analyse dynamics in their vicinity are considered. Chapter 6 presents conclusions, bringing them into wider context, and highlighting open questions for future work.

Chapter 2

Theoretical background

Part of this chapter is based on the following publications:
J. T. Taylor, D. J. Tozer and B. F. E. Curchod, "On the description of conical intersections between excited electronic states with LR-TDDFT and ADC(2)", *The Journal of Chemical Physics*, 2023, **159**, 214115. (Ref. [29])
A. Prlj, J. T. Taylor[†], J. Janoš, P. Slavíček, F. Agostini and B. F. E. Curchod, "Best practices for nonadiabatic molecular dynamics simulations [Article v1.0]", 2025, 10.48550/arXiv.2508.05263. [†]Contribution: provided the main-text section and FAQs on conical intersections and the geometric (or topological) phase; contributed to reviewing and editing the final draft of the manuscript. (Ref. [30])

2.1 Basic concepts of theoretical photochemistry

Any quantum-mechanical treatment of a (pure-state) molecular system necessitates consideration of its wavefunction, $\Psi(\mathbf{r}, \mathbf{R}, t)$, an object that depends on all $3N_\mathrm{e}$ electronic ($\mathbf{r} = \mathbf{r}_1, \mathbf{r}_2, \ldots, \mathbf{r}_{N_\mathrm{e}}$) and $3N_\mathrm{n}$ nuclear coordinates ($\mathbf{R} = \mathbf{R}_1, \mathbf{R}_2, \ldots, \mathbf{R}_{N_\mathrm{n}}$), and on time, t (ignoring electron and nuclear spin for simplicity). The molecular wavefunction possesses the entire information on all properties of the system and, as such, fully characterises the state of the molecule. The time-evolution of the molecular wavefunction is dictated by the molecular time-dependent Schrödinger equation (TDSE) [31],

$$i\frac{\partial}{\partial t}\Psi(\mathbf{r}, \mathbf{R}, t) = \hat{H}_\mathrm{mol}(\mathbf{r}, \mathbf{R})\Psi(\mathbf{r}, \mathbf{R}, t)\,, \tag{2.1}$$

where the molecular Hamiltonian, $\hat{H}_\mathrm{mol}(\mathbf{r}, \mathbf{R})$, neglecting relativistic effects and any applied external fields, takes the form

$$\begin{aligned}\hat{H}_{\mathrm{mol}}(\mathbf{r},\mathbf{R}) =& \hat{T}_{\mathrm{N}}(\mathbf{R}) + \hat{T}_{\mathrm{e}}(\mathbf{r}) + \hat{V}_{\mathrm{eN}}(\mathbf{r},\mathbf{R}) + \hat{V}_{\mathrm{ee}}(\mathbf{r}) + \hat{V}_{\mathrm{NN}}(\mathbf{R}) \\ =& -\frac{1}{2}\sum_{\alpha}^{N_{\mathrm{n}}}\frac{1}{M_\alpha}\nabla^2_{\mathbf{R}_\alpha} - \frac{1}{2}\sum_{i}^{N_{\mathrm{e}}}\nabla^2_{\mathbf{r}_i} - \sum_{i}^{N_{\mathrm{e}}}\sum_{\alpha}^{N_{\mathrm{n}}}\frac{Z_\alpha}{|\mathbf{R}_\alpha - \mathbf{r}_i|} + \sum_{i}^{N_{\mathrm{e}}}\sum_{j>i}^{N_{\mathrm{e}}}\frac{1}{|\mathbf{r}_i - \mathbf{r}_j|} \\ &+ \sum_{\alpha}^{N_{\mathrm{n}}}\sum_{\beta>\alpha}^{N_{\mathrm{n}}}\frac{1}{|\mathbf{R}_\alpha - \mathbf{R}_\beta|} \\ =& \hat{T}_{\mathrm{N}}(\mathbf{R}) + \hat{H}_{\mathrm{el}}(\mathbf{r},\mathbf{R})\,.\end{aligned} \tag{2.2}$$

Here, $\hat{T}_{\mathrm{N}}(\mathbf{R})$ and $\hat{T}_{\mathrm{e}}(\mathbf{r})$ are the nuclear and electronic kinetic energy operators, respectively; and $\hat{V}_{\mathrm{eN}}(\mathbf{r},\mathbf{R})$, $\hat{V}_{\mathrm{ee}}(\mathbf{r})$ and $\hat{V}_{\mathrm{NN}}(\mathbf{R})$ are the Coulombic potential operators (electron-nuclear, electron-electron and nuclear-nuclear, respectively). The latter four terms collectively constitute the electronic Hamiltonian, $\hat{H}_{\mathrm{el}}(\mathbf{r},\mathbf{R})$. The indices i and j label the electrons, whereas α and β label the nuclei. Equally, Z_α (M_α) denotes the charge (mass) of atom α, and $\nabla_{\mathbf{r}_i}$ and $\nabla_{\mathbf{R}_\alpha}$ are the gradients over the electronic and nuclear coordinates, respectively. Note, atomic units ($M_{\mathrm{e}} = e = \hbar = 4\pi\epsilon_0 = 1$) are used throughout this thesis.

2.1.1 The Born-Huang expansion: representing the molecular wavefunction

It is customary to choose a representation for the molecular wavefunction in order to disentangle its complexity and simplify its interpretation. For a fixed nuclear configuration $\mathbf{R}$ [i.e., the limit of neglecting $\hat{T}_{\mathrm{N}}(\mathbf{R})$ in Eq. (2.2)], the electronic time-independent Schrödinger equation (TISE),

$$\hat{H}_{\mathrm{el}}(\mathbf{r},\mathbf{R})\psi_J(\mathbf{r};\mathbf{R}) = E^{\mathrm{el}}_J(\mathbf{R})\psi_J(\mathbf{r};\mathbf{R})\,, \tag{2.3}$$

can be solved to determine the eigenvalues and eigenfunctions of $\hat{H}_{\mathrm{el}}(\mathbf{r},\mathbf{R})$. This equates to respectively affording the (adiabatic) electronic energies, $E^{\mathrm{el}}_J(\mathbf{R})$, of all electronic states and their associated (adiabatic) electronic wavefunctions, $\psi_J(\mathbf{r};\mathbf{R})$, at this specific nuclear configuration (signified by the notation "; $\mathbf{R}$"). The index J labels the electronic state. The electronic energies for all nuclear configurations, that is, defined as a function of $\mathbf{R}$, gives rise to the notion of potential energy surfaces (PESs), a concept fundamental to chemistry and central to this thesis. Equally, the (adiabatic) electronic wavefunctions for all nuclear configurations comprise a complete orthonormal basis,

$$\int \psi^*_I(\mathbf{r};\mathbf{R})\psi_J(\mathbf{r};\mathbf{R})d\mathbf{r} = \delta_{IJ}\,, \tag{2.4}$$

and, as such, may be employed to expand the molecular wavefunction within the Born-Huang representation (BH) [32],

$$\Psi(\mathbf{r},\mathbf{R},t) = \sum_{J}^{\infty}\chi_J(\mathbf{R},t)\psi_J(\mathbf{r};\mathbf{R})\,. \tag{2.5}$$

Provided the expansion is not truncated (i.e., runs over all electronic states), the BH expansion is a formally exact approach to separating the electronic and nuclear components of the molecular wavefunction, whereby the nuclear wavefunctions, $\chi_J(\mathbf{R},t)$, act as time-dependent expansion coefficients, capturing the complete time dependence of the molecular wavefunction. The time evolution of the nuclear wavefunction can be realised by inserting the BH expansion [Eq. (2.5)] into the molecular TDSE [Eq. (2.1)], left multiplying by $\psi_I^*(\mathbf{r};\mathbf{R})$ and integrating over all electronic coordinates $\mathbf{r}$,

$$i\frac{\partial}{\partial t}\chi_I(\mathbf{R},t) = \left[\hat{T}_{\mathrm{N}}(\mathbf{R}) + E_I^{\mathrm{el}}(\mathbf{R})\right]\chi_I(\mathbf{R},t) + \sum_J^{\infty} C_{IJ}(\mathbf{R})\chi_J(\mathbf{R},t)\,. \tag{2.6}$$

The first and second terms on the right-hand side of Eq. (2.6) represent the adiabatic evolution of the nuclear wavefunction solely on the PES of the I-th electronic state. The last term, however, introduces the so-called nonadiabatic couplings, $C_{IJ}(\mathbf{R})$, which act to facilitate coupling between different (adiabatic) electronic states via the influence of nuclear motion; they take the form

$$C_{IJ}(\mathbf{R}) = -\frac{1}{2}\sum_{\alpha}^{N_{\mathrm{n}}}\frac{1}{M_\alpha}\left[D_{IJ}(\mathbf{R}) + 2\mathbf{d}_{IJ}(\mathbf{R})\cdot\nabla_{\mathbf{R}_\alpha}\right]\,. \tag{2.7}$$

As a result, solving the coupled set of nuclear equations of motion [Eqs (2.6) and (2.7)] rigorously equates to finding solutions to the molecular TDSE [Eq. (2.1)], but arguably through a simplified, more interpretable way centred on the inclusion of the nonadiabatic couplings. The dominant contribution to $C_{IJ}(\mathbf{R})$ is from the first-order nonadiabatic coupling vectors,

$$\mathbf{d}_{IJ}(\mathbf{R}) = \langle\psi_I(\mathbf{R})|\nabla_{\mathbf{R}}|\psi_J(\mathbf{R})\rangle_{\mathbf{r}}\,, \tag{2.8}$$

which, for real-valued wavefunctions, are non-zero for $I \neq J$ only. The notation $\langle\ldots\rangle_{\mathbf{r}}$ denotes integration over all electronic coordinates $\mathbf{r}$. The $\mathbf{d}_{IJ}(\mathbf{R})$ vectors describe the extent to which varying the nuclear coordinate changes the (adiabatic) electronic wavefunction and, as will be shown later in Section 2.2.3, depend explicitly on the energy difference between the two electronic states I and J. The other term in Eq. (2.7) are the second-order (scalar) nonadiabatic couplings,

$$D_{IJ}(\mathbf{R}) = \left\langle\psi_I(\mathbf{R})|\nabla^2_{\mathbf{R}}|\psi_J(\mathbf{R})\right\rangle_{\mathbf{r}}\,, \tag{2.9}$$

which have a non-zero contribution both for $I \neq J$ and $I = J$.

As already stated, the BH expansion offers an exact reformulation of the molecular wavefunction, however, it becomes approximate (although not necessarily too inaccurate) when it is truncated. In the limit of considering only a single product of electronic and nuclear

wavefunctions, one arrives at the well-known Born-Oppenheimer (BO) approximation [9] of the molecular wavefunction,

$$\Psi(\mathbf{r},\mathbf{R},t) \approx \Psi_{\mathrm{BO}}(\mathbf{r},\mathbf{R},t) = \chi_J(\mathbf{R},t)\psi_J(\mathbf{r};\mathbf{R})\,. \tag{2.10}$$

The BO approximation, $\Psi_{\mathrm{BO}}(\mathbf{r},\mathbf{R},t)$, assumes that the nuclear and electronic motion can be decoupled completely, rationalised by the much higher relative mass (and, therefore, significantly slower motion) of nuclei compared to electrons. Conceptually, the BO approximation equates to assuming a near-instantaneous spatial rearrangement of the electrons in response to a change in the nuclear configuration.[1] This is made clear by replacing the BH expansion [Eq. (2.5)] with the BO approximation [Eq. (2.10)] in Eq. (2.6),

$$i\frac{\partial}{\partial t}\chi_I(\mathbf{R},t) = \left[\hat{T}_{\mathrm{N}}(\mathbf{R}) + E_I^{\mathrm{el}}(\mathbf{R}) - \frac{1}{2}\sum_{\alpha}^{N_{\mathrm{n}}}\frac{1}{M_\alpha}D_{II}(\mathbf{R})\right]\chi_I(\mathbf{R},t)\,, \tag{2.11}$$

meaning Eq. (2.6) reduces to an uncoupled set of nuclear equations of motion, where propagation of a given nuclear wavefunction is restricted to a single (adiabatic) electronic state I. Thus, no electronic transitions from state I to any other state J can be induced by nuclear motion. Such propagation is referred to as adiabatic dynamics. The last term in the square brackets in Eq. (2.11), which includes the diagonal contributions of the nonadiabatic couplings, $D_{II}(\mathbf{R})$, is called the diagonal Born-Oppenheimer correction (DBOC) and acts simply as an isotope-dependent shift in the (adiabatic) electronic PESs [i.e., $E_I^{\mathrm{el}}(\mathbf{R}) + C_{II}(\mathbf{R})$] upon which the nuclear wavefunctions evolve [35, 36]. Since such a term is generally small, it is often neglected. This gives rise to the more common adiabatic BO approximation where Eq. (2.6) now reduces to

$$i\frac{\partial}{\partial t}\chi_I(\mathbf{R},t) = \left[\hat{T}_{\mathrm{N}}(\mathbf{R}) + E_I^{\mathrm{el}}(\mathbf{R})\right]\chi_I(\mathbf{R},t)\,. \tag{2.12}$$

As will be shown later in Section 2.2.3, the (adiabatic) BO approximation (i.e., the neglect of the off-diagonal components of the nonadiabatic couplings) is only valid when electronic states are far apart in energy, where the coupling between them is small. This is generally the case in regions of nuclear-configuration space near the Franck-Condon (FC) region. However, during photochemical or photophysical processes, it is highly likely that regions of nuclear-configuration space will be visited where two (or more) electronic states become energetically close and, thus, where the coupling between them is large. In these instances, nonadiabatic effects cannot be ignored, so Eq. (2.6) [not Eqs (2.11) or (2.12)] should be considered. Practical

[1] In other words, the nuclei move so slowly, from the viewpoint of the electrons, that the electrons have ample time to smoothly adjust to the new nuclear configuration (i.e., without changing their eigenstate) [33]. We note that despite what is often perpetuated in the chemistry community, the BO approximation does not equate to enforcing the nuclei of a molecule to be (i) frozen or (ii) treated as classical particles, as explicitly emphasised by Agostini and Curchod in their recent pedagogical book chapter [34].

methods for solving Eq. (2.6) are discussed later in Chapter 5; for the rest of this chapter, we will focus on the electronic component of the molecular wavefunction.

2.1.2 Adiabatic vs diabatic basis: representing the electronic wavefunction

Similar to the molecular wavefunction, it is also necessary to choose a representation to express the electronic basis [37, 38]. Following Eq. (2.5), one typically uses the adiabatic representation, where the electronic wavefunctions are the eigenfunctions of the electronic Hamiltonian, resulting in the matrix representation of the latter, denoted $\mathbf{H}_{\text{el}}^{(\text{adia})}(\mathbf{R})$, being diagonal. This is easily illustrated by considering the matrix of the molecular Hamiltonian for a simple two-state systems within the adiabatic electronic basis,

$$\begin{aligned}\mathbf{H}_{\text{mol}}^{(\text{adia})}(\mathbf{R}) =& \begin{pmatrix} \hat{T}_{\text{N}}(\mathbf{R}) + C_{11}(\mathbf{R}) & C_{12}(\mathbf{R}) \\ C_{21}(\mathbf{R}) & \hat{T}_{\text{N}}(\mathbf{R}) + C_{22}(\mathbf{R}) \end{pmatrix} + \begin{pmatrix} E_1^{\text{el}}(\mathbf{R}) & 0 \\ 0 & E_2^{\text{el}}(\mathbf{R}) \end{pmatrix} \\ =& \mathbf{T}_{\text{N}}^{(\text{adia})}(\mathbf{R}) + \mathbf{H}_{\text{el}}^{(\text{adia})}(\mathbf{R}) \,. \end{aligned} \tag{2.13}$$

As discussed in the preceding section, coupling between different adiabatic electronic states occurs through the off-diagonal elements of the nuclear kinetic energy operator matrix, $\mathbf{T}_{\text{N}}^{(\text{adia})}(\mathbf{R})$, that is, through the off-diagonal nonadiabatic couplings, $C_{12}(\mathbf{R})$. Within the adiabatic representation, the electronic wavefunctions depend parametrically on the nuclear positions (again, indicated by the notation "; $\mathbf{R}$") and the electronic energies, despite being able to become degenerate, cannot cross. As a result, adiabatic electronic states are labelled according to their energy ordering (i.e., S_0, S_1, S_2 etc.).

An alternative choice of electronic basis is to use the diabatic representation. Diabatic electronic wavefunctions, $\psi_J^{(\text{dia})}(\mathbf{r}; \mathbf{R}')$, are not eigenfunctions of the electronic Hamiltonian, but are alternatively chosen to diagonalise the matrix of the nuclear kinetic energy operator, $\mathbf{T}_{\text{N}}^{(\text{dia})}(\mathbf{R})$, causing the nonadiabatic couplings to vanish. (The "$\mathbf{R}'$" signifies that diabatic electronic states are defined only at one chosen nuclear geometry.[2]) This is evident again by inspecting the two-state molecular Hamiltonian matrix, but this time, expressed in the diabatic electronic basis,

$$\begin{aligned}\mathbf{H}_{\text{mol}}^{(\text{dia})}(\mathbf{R}) =& \begin{pmatrix} \hat{T}_{\text{N}}(\mathbf{R}) & 0 \\ 0 & \hat{T}_{\text{N}}(\mathbf{R}) \end{pmatrix} + \begin{pmatrix} V_{11}(\mathbf{R}) & V_{12}(\mathbf{R}) \\ V_{21}(\mathbf{R}) & V_{22}(\mathbf{R}) \end{pmatrix} \\ =& \mathbf{T}_{\text{N}}^{(\text{dia})}(\mathbf{R}) + \mathbf{H}_{\text{el}}^{(\text{dia})}(\mathbf{R}) \,. \end{aligned} \tag{2.14}$$

Within the diabatic representation, the (scalar) coupling between electronic states occurs instead through preserved off-diagonal elements, $V_{12}(\mathbf{R})$, of the electronic Hamiltonian

[2] Strictly speaking, here we are denoting a "crude adiabatic" basis [39], where $\psi_J^{(\text{dia})}(\mathbf{r}; \mathbf{R}')$ are eigenfunctions of the electronic Hamiltonian only at a particular nuclear geometry $\mathbf{R}'$, and not at any other [40]. Such an electronic basis acts practically as a locally well-defined (quasi-)diabatic basis [41, 42].

matrix, $\mathbf{H}_{\text{el}}^{(\text{dia})}(\mathbf{R})$. Diabatic electronic energies can cross and therefore labelling relates instead to the electronic character of each state (i.e., nπ^*, $\pi\pi^*$, $\sigma\pi^*$ etc.), which is retained upon varying the nuclear positions.[3] It should be noted that for polyatomic molecules (i.e., those with more than one internal nuclear degree of freedom) [43], or for systems with more than two electronic states [44], exact diabatic states [i.e., for which $C_{IJ}(\mathbf{R}) = 0$] cannot be defined. However, quasi-diabatic states [i.e., for which $C_{IJ}(\mathbf{R})$ is minimised, but non-zero] may be obtained in practice [40].

2.1.3 Photochemical and photophysical processes

Within chemistry, photoprocesses can be divided into either photophysics, which results in the same molecule the process started with (i.e, in optical spectroscopy, or in photostability); or photochemistry, where the process ends with a different molecule (i.e., photoproducts). Such phenomena typically start with a molecule in its ground electronic state, which can absorb a photon of light with energy ($\Delta E = h\nu$) equal to the energy gap ($\Delta E_{IJ}^{\text{el}} = E_J^{\text{el}} - E_I^{\text{el}}$) between the ground and a given excited electronic state. Absorption (< 1 fs) then leads to an electronic transition with the molecule being promoted to the excited electronic state. Several pathways exist that can allow the molecule to relax back down to the ground electronic state, reforming the FC molecular structure (i.e., as in photophysics), or leading to new molecular structures (i.e., as in photochemistry). They can be categorised as either radiative or non-radiative decay processes [Fig. 2.1(a)]. (Note, typical timescales for each process are provided in parentheses after they are first introduced [45–47].) Radiative decay involves relaxation to a lower energy electronic state via the emission of light and can occur either through fluorescence ($\sim$ 1-100 ns) or phosphorescence ($\sim$ 100 μs to 100 ms). The former occurs between electronic states of the same spin-multiplicity, whereas the latter involves electronic states of different spin-multiplicity. In contrast, non-radiative decay involves transition to a lower energy electronic state in regions of nuclear-configuration space where the electronic states become close in energy and couple due to nuclear motion (i.e., nonadiabatic coupling). If the transition occurs between electronic states of the same spin-multiplicity, then the non-radiative decay process is internal conversion ($\sim$ 10 fs to 10 ps); if it occurs between electronic states of different spin-multiplicity, the process is intersystem crossing ($\sim$ 10 ps to 1 μs). Relativistic effects, such as spin-orbit coupling, should be considered for a correct description of intersystem crossing (and phosphorescence). Vibrational relaxation ($\sim$ 10 fs to 1 ps) is also a possibility, where a molecule transitions to lower vibrational states within a given electronic state by transferring quanta of vibrational energy to its surroundings as heat. All these processes can be schematically depicted in a Jabłoński diagram [Fig. 2.1(b)] [48].

[3] This behaviour contrasts that of adiabatic states, whose electronic character necessarily changes with nuclear position. As such, it is important to specify at which geometry one is referring when quoting the electronic character of an adiabatic state [e.g., S_1 possesses a $\pi\pi^*$ character at the S_0 minimum (or FC) geometry].

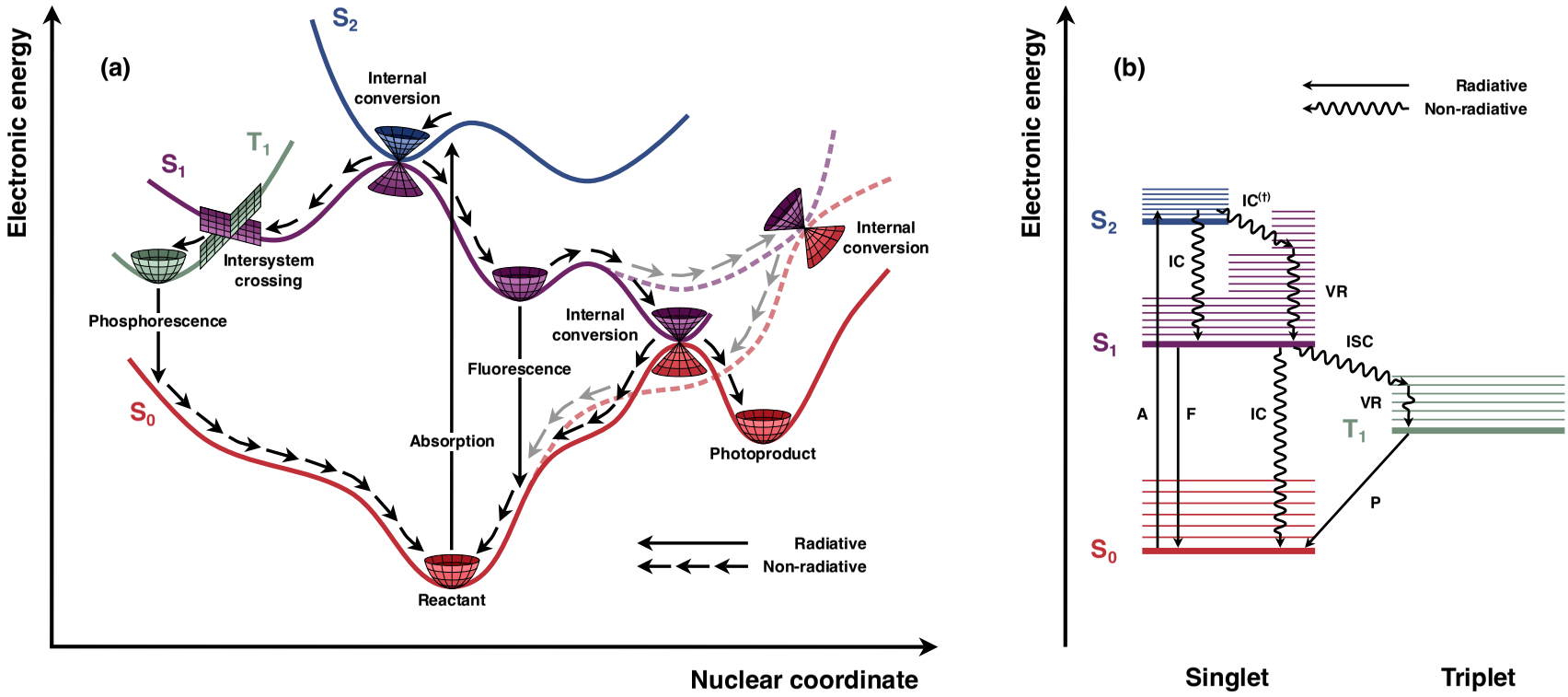

Figure 2.1: (a) Schematic representation of photochemical and photophysical processes possible in a photoexcited molecule. Upon excitation to S_2, the molecule (in a hypothetical case) may undergo internal conversion to S_1 via an excited-to-excited state CX, after which its dynamics might proceed along two different pathways. Following the right-hand pathway, the molecule might either decay radiatively to S_0 via fluorescence after reaching a local minimum on S_1, or encounter a ground-to-excited state CX and instead undergo internal conversion to S_0. If the CX is strongly peaked (solid lines, black arrows), it is likely that bifurcation will occur upon reaching S_0, leading to nuclear population either continuing to the photoproducts at a local S_0 minimum, or reforming the reactants at the global S_0 minimum. If the CX is strongly sloped (dashed lines, grey arrows), reforming the reactants predominates (i.e., the typical mechanism behind photostability). Following the left-hand pathway, the molecule might undergo intersystem crossing from S_1 to T_1, where upon the molecule can decay to S_0 radiatively via phosphorescence, again leading back to the reactants. Adapted from Ref. [49]. **(b)** Jabłoński diagram of a photoexcited molecule: absorption (A), fluorescence (F), phosphorescence (P), internal conversion (IC), vibrational relaxation (VR) and intersystem crossing (ISC).

Internal conversion[4] can occur via conical intersections (CXs), where two (or more) adiabatic PESs become energetically degenerate at a given molecular geometry, or via avoided crossings (ACs), where two adiabatic PESs approach each other in energy, but refrain from touching. As will be elaborated in Section 2.2 below, CXs, in particular, can provide a common route for non-radiative decay of photoexcited molecules, enabling rapid population transfer from the excited electronic states of a molecule to its ground electronic state. Approximating the description of CXs with an affordable (and in principle exact) electronic structure method is at the heart of this thesis. Defining, characterising and practically locating such features between electronic PESs is the subject of the next section.

2.2 Conical intersections

The earliest mathematical discussion of CXs was introduced by von Neumann and Wigner in their 1929 paper [55], outlining the conditions for the existence of electronic degeneracies between two adiabatic states of the same spatial symmetry. Later, in 1937 Teller argued [56] that CXs have the potential to facilitate efficient internal conversion on ultrafast timescales (i.e., within a single vibrational period), an idea echoed by Zimmerman's 1996 revision [57] of the famous Woodward-Hoffman rules [58, 59], which highlighted the significance of CXs in pericyclic reactions along the photochemical pathway between excited-state reactants and ground-state products [60].

Nonetheless, the history of CXs within the 20th century, for the most part, was one of scepticism. Contrary to Zimmerman's work, the most common understanding of photochemical reactions at the time was primarily based on the Van der Lugt-Oosteroff model [61]: for certain pericyclic reactions, the stereochemical outcome (i.e., whether disrotatory or conrotatory photoproducts are predominantly formed) was determined based on the concept of a small energy gap at an AC minimum along a linear path between reactants and products [62]. On the other hand, CXs were considered by many as rare, mathematical curiosities, unlikely to occur at chemically relevant energies, unless their existence was required by symmetry [63]. Even then, since most molecules do not exhibit point group symmetry, not to mention high enough symmetry to impose electronic degeneracies, the prevalence of CXs was thought to be severely limited [64]. In his 1974 review [65], Michl wrote of the consensual feeling of doubt towards the importance of CXs in a photochemical context:

[4]We note, internal conversion need not occur near a CX (or at an AC), where nonadiabatic coupling is large. Alternative internal conversion pathways also exist in regions of low, but non-zero nonadiabatic coupling (i.e., typical of the Franck-Condon region) [50, 51]. Such internal conversion pathways result from strong overlap of vibrational wavefunctions [52], generally between a low-lying vibrational wavefunction in the upper electronic state and a high-lying vibrational wavefunction in the lower electronic state [53]. Due to the weak nonadiabatic coupling in these instances, this type of internal conversion can be modelled using Fermi's golden rule [54], and are usually represented in a Jabłoński diagram [e.g., see "(†)" in Fig. 2.1(b)].

> *"While in principle the various hypersurfaces can cross as the nuclear configuration coordinate is varied along various paths, this is a relatively uncommon occurrence and along most paths such crossings, even if "intended", are more or less avoided."*

It was not until the early 1990s (some 60 years after their initial conception) that CXs began to receive the recognition they do today [66]. Thanks to increased computer power, implementation of gradients in multiconfigurational electronic-structure methods and improved algorithms for geometry optimisation, CXs could be located without the aid of symmetry constraints [67]. The respective efforts of the Ruedenberg [68, 69] and Yarkony [70] groups (for small molecules), as well as the international collaboration of Bernardi, Olivucci and Rob [71, 72] (for larger molecules) showed not only do "non-symmetry-required" CXs exist (which was known before), but are in fact omnipresent in numerous organic molecules [73]. More recently, Truhlar and Mead [74] further demonstrated that, in contrast to previous opinions, CXs are indeed much more likely to exist than ACs. They proved that if a local minimum in the energy gap (i.e., a supposed AC) between two electronic PESs is encountered upon traversing a path through nuclear configuration space, rather than being a true AC, it is much more likely to instead be associated with the neighbourhood (or shoulder) of a CX.

Advances in ultrafast, femtosecond pump-probe spectroscopy have also made it possible to experimentally observe excited-state lifetimes in the sub-picosecond regime [73, 75–77]. Such lifetimes are much too short to be rationalised by consideration of ACs, but instead indicate the inarguable participation of CXs. The combined experimental and computational study of Polli *et al.* in 2010 of rhodopsin [78] gave the first convincing experimental evidence for the direct significance of CXs in vision photochemistry [79].

It is now widely agreed that, far from being arcane theoretical concepts [80], CXs constitute the bedrock of our mechanistic understanding of a wide array of photochemical and photophysical processes [81]. Charge-transfer in photosynthesis [60, 73], cis/trans isomerisation of retinal in vision [82], proton/hydrogen transfer-driven photostability in DNA nucleases and amino acids [83, 84], and non-radiative recombination in semiconducting nanomaterials [85] are just a few notable examples.

2.2.1 Foundations: the non-crossing rule, the branching space and the seam space

In order to determine the conditions for the existence of a CX, it is instructive to consider again the matrix of the two-state diabatic electronic Hamiltonian previously introduced in Eq. (2.14) [86],

$$\mathbf{H}_{\mathrm{el}}^{(\mathrm{dia})}(\mathbf{R}) = \begin{pmatrix} V_{11}(\mathbf{R}) & V_{12}(\mathbf{R}) \\ V_{12}(\mathbf{R}) & V_{22}(\mathbf{R}) \end{pmatrix}, \tag{2.15}$$

where $V_{IJ}(\mathbf{R}) = \langle \psi_I^{(\mathrm{dia})}(\mathbf{R}')|\hat{H}_{\mathrm{el}}(\mathbf{R})|\psi_J^{(\mathrm{dia})}(\mathbf{R}')\rangle_{\mathbf{r}}$ and $V_{21}(\mathbf{R}) = {V_{12}}^*(\mathbf{R}) = V_{12}(\mathbf{R})$ as $\mathbf{H}_{\mathrm{el}}^{(\mathrm{dia})}(\mathbf{R})$ is a Hermitian matrix defined with real matrix elements (i.e., a symmetric matrix). Diagonalisation of $\mathbf{H}_{\mathrm{el}}^{(\mathrm{dia})}(\mathbf{R})$ can be achieved via the unitary transformation matrix,

$$\mathbf{U}(\mathbf{R}) = \begin{pmatrix} \cos[\theta(\mathbf{R})] & \sin[\theta(\mathbf{R})] \\ -\sin[\theta(\mathbf{R})] & \cos[\theta(\mathbf{R})] \end{pmatrix} . \tag{2.16}$$

The eigenfunctions of $\mathbf{H}_{\mathrm{el}}^{(\mathrm{dia})}(\mathbf{R})$ are thus given as the adiabatic electronic states expanded in terms of the two diabatic electronic states,

$$\begin{aligned} \psi_1(\mathbf{r};\mathbf{R}) &= \cos[\theta(\mathbf{R})]\psi_1^{(\mathrm{dia})}(\mathbf{r};\mathbf{R}') + \sin[\theta(\mathbf{R})]\psi_2^{(\mathrm{dia})}(\mathbf{r};\mathbf{R}') \\ \psi_2(\mathbf{r};\mathbf{R}) &= -\sin[\theta(\mathbf{R})]\psi_1^{(\mathrm{dia})}(\mathbf{r};\mathbf{R}') + \cos[\theta(\mathbf{R})]\psi_2^{(\mathrm{dia})}(\mathbf{r};\mathbf{R}') , \end{aligned} \tag{2.17}$$

with the rotation angle, $\theta(\mathbf{R})$, defining the diabatic-to-adiabatic transformation,

$$\theta(\mathbf{R}) = \frac{1}{2}\arctan\left(\frac{2V_{12}(\mathbf{R})}{V_{11}(\mathbf{R}) - V_{22}(\mathbf{R})}\right) . \tag{2.18}$$

Equivalently, one yields the adiabatic electronic energies (written in terms of the diabatic electronic energies) as the eigenvalues of $\mathbf{H}_{\mathrm{el}}^{(\mathrm{dia})}(\mathbf{R})$ [68, 87],

$$E_{1,2}^{\mathrm{el}}(\mathbf{R}) = \overline{V}(\mathbf{R}) \pm \sqrt{[\Delta V(\mathbf{R})]^2 + [V_{12}(\mathbf{R})]^2} \tag{2.19}$$

where

$$\overline{V}(\mathbf{R}) = \frac{V_{11}(\mathbf{R}) + V_{22}(\mathbf{R})}{2} \quad \text{and} \quad \Delta V(\mathbf{R}) = \frac{V_{11}(\mathbf{R}) - V_{22}(\mathbf{R})}{2} . \tag{2.20}$$

Inspecting Eqs (2.19) and (2.20), it is clear that for the eigenvalues of $\mathbf{H}_{\mathrm{el}}^{(\mathrm{dia})}(\mathbf{R})$ (i.e., two adiabatic electronic states) to be degenerate, the following two conditions must be satisfied,

$$\begin{aligned} V_{11}(\mathbf{R}_{\mathrm{CX}}) &= V_{22}(\mathbf{R}_{\mathrm{CX}}) \\ V_{12}(\mathbf{R}_{\mathrm{CX}}) &= 0 , \end{aligned} \tag{2.21}$$

where $\mathbf{R}_{\mathrm{CX}}$ is the geometry at the CX. For a nonlinear molecule with $F = 3N_{\mathrm{n}} - 6$ internal nuclear degrees of freedom, these two conditions are fulfilled in an $(F-2)$-dimensional subspace (i.e., one independent nuclear degree of freedom must be lost to satisfy each of the two conditions) [40]. Therefore, the full F-dimensional space associated with a given molecule can be divided into two subspaces: (i) this $(F-2)$-dimensional seam (or intersection) space [68] [Fig. 2.2, top right], where the adiabatic electronic states are degenerate and (ii) a two-dimensional branching [68] (or g-h) [88] space [Fig. 2.2, top left] orthogonal to it, where the degeneracy is lifted. Therefore, rather than occurring at an isolated geometry (as may appear to be the case in the branching space), CXs exist as an infinite number of points

(with necessarily different electronic energies, associated with different nuclear geometries) connected [89–92] along the so-called intersection seam [Fig. 2.2, bottom middle]. The idea of an "intersection *seam*" compared to a "seam (or intersection) *space*" is exactly equivalent and thus the two are interchangeable; the former simply refers to an $(F-2)$-dimensional hyperline, which may be more appropriate to consider given the context. Von Neumann and Wigner first presented these conditions for electronic degeneracy in the context of diatomic molecules. Since only one internal nuclear degree of freedom exists in an isolated diatomic (i.e., the bond distance between the two nuclei), two adiabatic electronic states with the same spatial symmetry can never become degenerate[5]–this is the origin of their "non-crossing rule" [55]. Polyatomic molecules, on the other hand, possess many internal nuclear degrees of freedom (or at the very least, the required two), so fulfilment of both conditions in Eq. (2.21) is indeed highly possible, but not necessarily guaranteed [93].

Complete characterisation of a given CX requires the determination (and subsequent visualisation) of its branching space. To do so for a two-state CX, it is useful to first redefine the matrix of the diabatic electronic Hamiltonian [Eq. (2.15)] in terms of the quantities given in Eq. (2.20) [87, 94],

$$\mathbf{H}_{\mathrm{el}}^{(\mathrm{dia})}(\mathbf{R}) = \overline{V}(\mathbf{R})\mathbb{I}_2 + \begin{pmatrix} \Delta V(\mathbf{R}) & V_{12}(\mathbf{R}) \\ V_{12}(\mathbf{R}) & -\Delta V(\mathbf{R}) \end{pmatrix}, \tag{2.22}$$

where $\mathbb{I}_2$ is a (2×2) identity matrix. Consider two electronic states that are energetically degenerate at nuclear geometry $\mathbf{R}_{\mathrm{CX}}$. At a neighbouring geometry, $\mathbf{R} = \mathbf{R}_{\mathrm{CX}} + \delta\mathbf{R}$, it is possible to expand $\mathbf{H}_{\mathrm{el}}^{(\mathrm{dia})}(\mathbf{R})$ in a Taylor expansion around the intersection point $\mathbf{R}_{\mathrm{CX}}$. This is given as [95]

$$\begin{aligned}
\mathbf{H}_{\mathrm{el}}^{(\mathrm{dia})}(\mathbf{R}) =& \mathbf{H}_{\mathrm{el}}^{(\mathrm{dia})}(\mathbf{R}_{\mathrm{CX}}) + \nabla_{\mathbf{R}}\mathbf{H}_{\mathrm{el}}^{(\mathrm{dia})}(\mathbf{R}_{\mathrm{CX}})\cdot\delta\mathbf{R} + \ldots \\
=& V(\mathbf{R}_{\mathrm{CX}})\mathbb{I}_2 + \left[\nabla_{\mathbf{R}}\overline{V}(\mathbf{R}_{\mathrm{CX}})\mathbb{I}_2 + \begin{pmatrix} \nabla_{\mathbf{R}}\Delta V(\mathbf{R}_{\mathrm{CX}}) & \nabla_{\mathbf{R}}V_{12}(\mathbf{R}_{\mathrm{CX}}) \\ \nabla_{\mathbf{R}}V_{12}(\mathbf{R}_{\mathrm{CX}}) & -\nabla_{\mathbf{R}}\Delta V(\mathbf{R}_{\mathrm{CX}}) \end{pmatrix}\right]\cdot\delta\mathbf{R} + \ldots \\
=& \left(V(\mathbf{R}_{\mathrm{CX}}) + \nabla_{\mathbf{R}}\overline{V}(\mathbf{R}_{\mathrm{CX}})\cdot\delta\mathbf{R}\right)\mathbb{I}_2 + \begin{pmatrix} \nabla_{\mathbf{R}}\Delta V(\mathbf{R}_{\mathrm{CX}}) & \nabla_{\mathbf{R}}V_{12}(\mathbf{R}_{\mathrm{CX}}) \\ \nabla_{\mathbf{R}}V_{12}(\mathbf{R}_{\mathrm{CX}}) & -\nabla_{\mathbf{R}}\Delta V(\mathbf{R}_{\mathrm{CX}}) \end{pmatrix}\cdot\delta\mathbf{R} + \ldots,
\end{aligned} \tag{2.23}$$

where $V_{11}(\mathbf{R}) = V_{22}(\mathbf{R}) = V(\mathbf{R})$ at $\mathbf{R} = \mathbf{R}_{\mathrm{CX}}$. Given the first term in the last line of Eq. (2.23) corresponds to a diagonal matrix (and thus has no effect on the coupling between the two

[5]The same does not apply for electronic states of different spatial symmetry. In this case, the second condition in Eq. (2.21) is trivially satisfied (i.e., $V_{12}(\mathbf{R}_{\mathrm{CX}})$ is identically zero), so only one nuclear degree of freedom must be lost to fulfil the remaining condition, something generally possible in diatomic molecules. It was this observation that caused many to erroneously assume that CXs could only form between electronic PESs because of point group symmetry and that intersections between electronic PESs of the same spatial symmetry were primarily avoided [87].

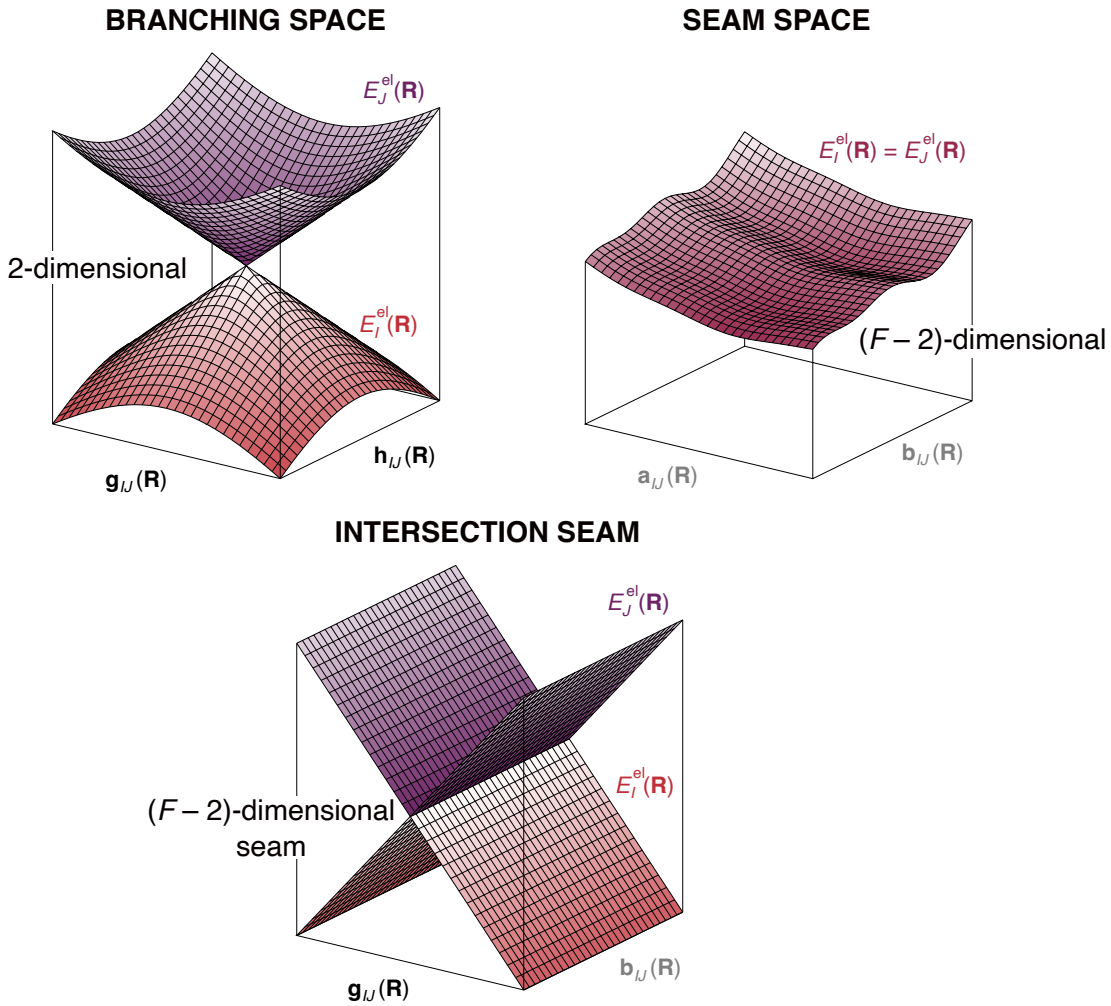

Figure 2.2: Schematic representation of the adiabatic PESs in the branching space **(top left)** and seam space **(top right)** of a two-state CX, where $\mathbf{g}_{IJ}(\mathbf{R})$ and $\mathbf{h}_{IJ}(\mathbf{R})$ are the branching space vectors (expressed in terms of adiabatic electronic states) and $\mathbf{a}_{IJ}(\mathbf{R})$ and $\mathbf{b}_{IJ}(\mathbf{R})$ are two arbitrarily chosen seam space coordinates. Plotting the PESs along one branching space vector [here $\mathbf{g}_{IJ}(\mathbf{R})$] and one seam space coordinate reveals the intersection seam **(bottom middle)**–see text for discussion.

electronic states), it is apparent that, to first order in $\mathbf{R}$, the conditions for the degeneracy to remain upon moving from $\mathbf{R}_{\mathrm{CX}}$ to $\mathbf{R}$ become

$$\begin{aligned} \nabla_{\mathbf{R}} \Delta V(\mathbf{R}_{\mathrm{CX}}) \cdot \delta\mathbf{R} &= 0 \\ \nabla_{\mathbf{R}} V_{12}(\mathbf{R}_{\mathrm{CX}}) \cdot \delta\mathbf{R} &= 0\,. \end{aligned} \tag{2.24}$$

To retain the degeneracy, the nuclear displacement vector, $\delta\mathbf{R}$, is restricted to the subspace orthogonal to that spanned by the vectors $\nabla_{\mathbf{R}} \Delta V(\mathbf{R}_{\mathrm{CX}})$ and $\nabla_{\mathbf{R}} V_{12}(\mathbf{R}_{\mathrm{CX}})$. The conditions in Eq. (2.21) have therefore been extended and the branching space vectors, $\nabla_{\mathbf{R}} \Delta V(\mathbf{R}_{\mathrm{CX}})$ and $\nabla_{\mathbf{R}} V_{12}(\mathbf{R}_{\mathrm{CX}})$, defined. The branching space vectors (or any linear combination between them)

[81] constitute the two possible[6] nuclear coordinates along which the molecule can distort in order to exit the strong nonadiabatic region at the CX; the degeneracy is lifted linearly to first order upon an infinitesimal displacement in either direction. Movement along any of the remaining $F-2$ nuclear coordinates retains the degeneracy and simply translates the molecule along the intersection seam (or within the seam space), which can be characterised in terms of minima and transition states [96].

Since the definition of diabatic electronic states is arbitrary [94, 97, 98], it is customary to express the branching space vectors in terms of adiabatic electronic states instead. As such, using Yarkony's notation [88], the two branching space vectors can now be defined as

$$\mathbf{g}_{IJ}(\mathbf{R}) = \frac{1}{2}\nabla_{\mathbf{R}}\left[E_I^{\mathrm{el}}(\mathbf{R}) - E_J^{\mathrm{el}}(\mathbf{R})\right] , \tag{2.25}$$

which is referred to as the gradient difference vector, and

$$\mathbf{h}_{IJ}(\mathbf{R}) = \left\langle \psi_I(\mathbf{R}) | \nabla_{\mathbf{R}} \hat{H}_{\mathrm{el}} | \psi_J(\mathbf{R}) \right\rangle_{\mathbf{r}} , \tag{2.26}$$

which is referred to as the derivative coupling vector.[7] Another useful quantity to define for the characterisation of the branching space is the seam coordinate [100],

$$\mathbf{s}_{IJ}(\mathbf{R}) = \frac{1}{2}\nabla_{\mathbf{R}}\left[E_I^{\mathrm{el}}(\mathbf{R}) + E_J^{\mathrm{el}}(\mathbf{R})\right] , \tag{2.27}$$

where the projections of $\mathbf{s}_{IJ}(\mathbf{R})$ onto the branching plane are subsequently given by

$$s_x = \mathbf{s}_{IJ}(\mathbf{R}) \cdot \bar{\mathbf{x}}_{IJ}(\mathbf{R}) \quad \text{and} \quad s_y = \mathbf{s}_{IJ}(\mathbf{R}) \cdot \bar{\mathbf{y}}_{IJ}(\mathbf{R}) , \tag{2.28}$$

with

$$\bar{\mathbf{x}}_{IJ}(\mathbf{R}) = \frac{\bar{\mathbf{g}}_{IJ}(\mathbf{R})}{\bar{g}} \quad \text{and} \quad \bar{\mathbf{y}}_{IJ}(\mathbf{R}) = \frac{\bar{\mathbf{h}}_{IJ}(\mathbf{R})}{\bar{h}} \tag{2.29}$$

being the orthonormalised versions of the $\mathbf{g}_{IJ}(\mathbf{R})$ and $\mathbf{h}_{IJ}(\mathbf{R})$ vectors introduced in Eqs (2.25) and (2.26), respectively; they are the so-called intersection-adapted coordinates. Here, $\bar{g} = ||\bar{\mathbf{g}}_{IJ}(\mathbf{R})||$ and $\bar{h} = ||\bar{\mathbf{h}}_{IJ}(\mathbf{R})||$ are the norms of the respective orthogonalised branching space vectors. A rigorous way to orthogonalise the (raw) branching space vectors is outlined later in Section 3.5.1.3. The electronic Hamiltonian matrix of Eq. (2.15) can now be recast within the branching space (to first-order) as [76]

$$\mathbf{H}_{\mathrm{el,\,bs}}(x,y) = \left(E^{\times} + s_x x + s_y y\right)\mathbb{I}_2 + \begin{pmatrix} \bar{g}x & \bar{h}y \\ \bar{h}y & -\bar{g}x \end{pmatrix} , \tag{2.30}$$

[6] Strictly speaking the branching space vectors collectively constitute the branching plane, which spans an infinite number of linearly-dependent nuclear coordinates that can lift the degeneracy. Further discussion on this point is provided later in Section 3.5.1.3.

[7] For accidental symmetry-allowed CXs (see Section 2.2.2.1), the $\mathbf{g}_{IJ}(\mathbf{R})$ and $\mathbf{h}_{IJ}(\mathbf{R})$ vectors are referred to as the tuning and coupling coordinates, respectively [99].

where x and y are displacements along the $\bar{\mathbf{g}}_{IJ}(\mathbf{R})$ and $\bar{\mathbf{h}}_{IJ}(\mathbf{R})$ directions. The eigenvalues of Eq. (2.30) are thus given by

$$E_{1,2}^{\text{el, bs}}(x,y) = \left(E^{\times} + s_x x + s_y y\right) \pm \sqrt{(\bar{g}x)^2 + \left(\bar{h}y\right)^2}, \tag{2.31}$$

where $V(\mathbf{R}_{\text{CX}}) = E^{\times}$ is the energy at the point of degeneracy [95, 101]. This results in the two adiabatic electronic energies, $E_{1,2}^{\text{el, bs}}(x,y)$, plotted around the CX along the two branching space directions exhibiting the characteristic double-cone (or diabolical) [93, 102] shape.[8]

Having laid out over the last few pages (i) the origin of the "non-crossing rule", (ii) the definitions of the complementary branching and seam spaces, as well as (iii) the double-cone shape given by adiabatic electronic energies within the branching space, it is now necessary to characterise CXs further. There are a number of ways this can be achieved, namely by symmetry, by topography and by topology. Each will be discussed in turn below.

2.2.2 The characterisation of conical intersections

2.2.2.1 Characterising conical intersections by symmetry

One way to classify two-state CXs is by the part played by point group symmetry in satisfying the degeneracy conditions given in Eq. (2.21). There are three main groups: symmetry-required, accidental symmetry-allowed and accidental same-symmetry CXs (see Fig. 2.3).

Symmetry-required CXs arise when the molecule exhibits a particular point group symmetry where the intersecting electronic states belong to the same doubly-degenerate irreducible representation of a non-Abelian point group. For nuclear geometries for which this holds, both conditions in Eq. (2.21) are trivially satisfied, guaranteeing the degeneracy by symmetry [64]. In order for the degeneracy to be lifted, and thus for the double-cone shape to be revealed in the branching space, two symmetry-breaking nuclear coordinates must be traversed. The Jahn-Teller effect [103] is a symmetry-lowering process intrinsically related to this class of CX [97]. (This should not be confused with the Renner-Teller intersections [104] often observed in linear molecules [105]. These are formally not CXs [80], given the degeneracy is lifted only at second order in $\mathbf{R}$. The electronic energies depend quadratically, not linearly, on $\mathbf{R}$ near the degeneracy point [87], hence they touch tangentially [106], giving the characteristic "double-bowl" shape, instead of a double-cone.)

Accidental symmetry-allowed CXs occur when one of the intersecting electronic states possesses a distinct spatial symmetry to the other (i.e., they belong to different irreducible representations). As a result, the second condition in Eq. (2.21) is automatically fulfilled for

[8] If we take a random one-dimensional slice through the adiabatic PESs in the branching space of a CX, it is unlikely that it will pass directly through the point of intersection, $\mathbf{R}_{\text{CX}}$. We are much more likely to observe a supposed AC, as was argued and proven by Truhlar and Mead (mentioned above) [74]. ACs are formally different to CXs, in that the energy gap is lifted at second (or higher) order in all directions around the former, whereas the degeneracy is lifted at first order only in two directions around the latter [63].

(a)

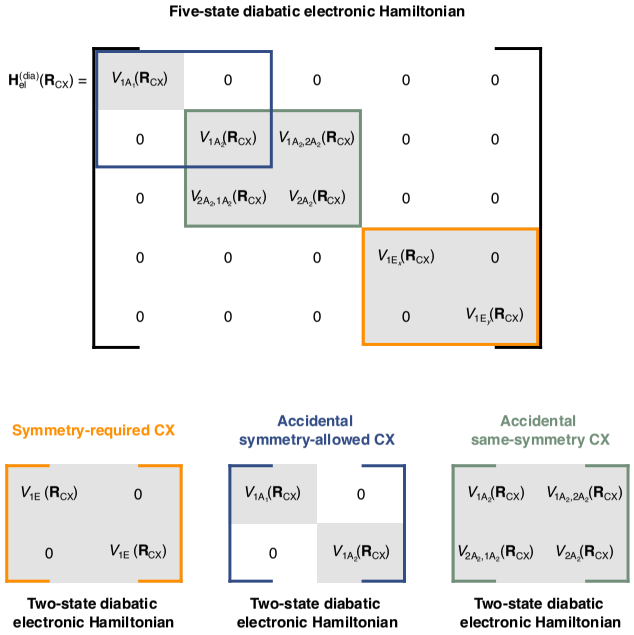

(b)

$$V_{\Gamma_I,\Gamma_J}(\mathbf{R}) = \langle\, \Psi_{\Gamma_I}^{(\mathrm{dia})}(\mathbf{R}) \mid \hat{H}_{\mathrm{el}}(\mathbf{R}) \mid \Psi_{\Gamma_J}^{(\mathrm{dia})}(\mathbf{R}) \,\rangle_{\mathbf{r}}$$

$$\begin{cases} \neq 0, & \text{if } \Gamma_I \otimes \Gamma_{\hat{H}_{\mathrm{el}}} \otimes \Gamma_J \supset \Gamma_{\text{tot. sym.}} \\ = 0, & \text{otherwise} \end{cases}$$

(c)

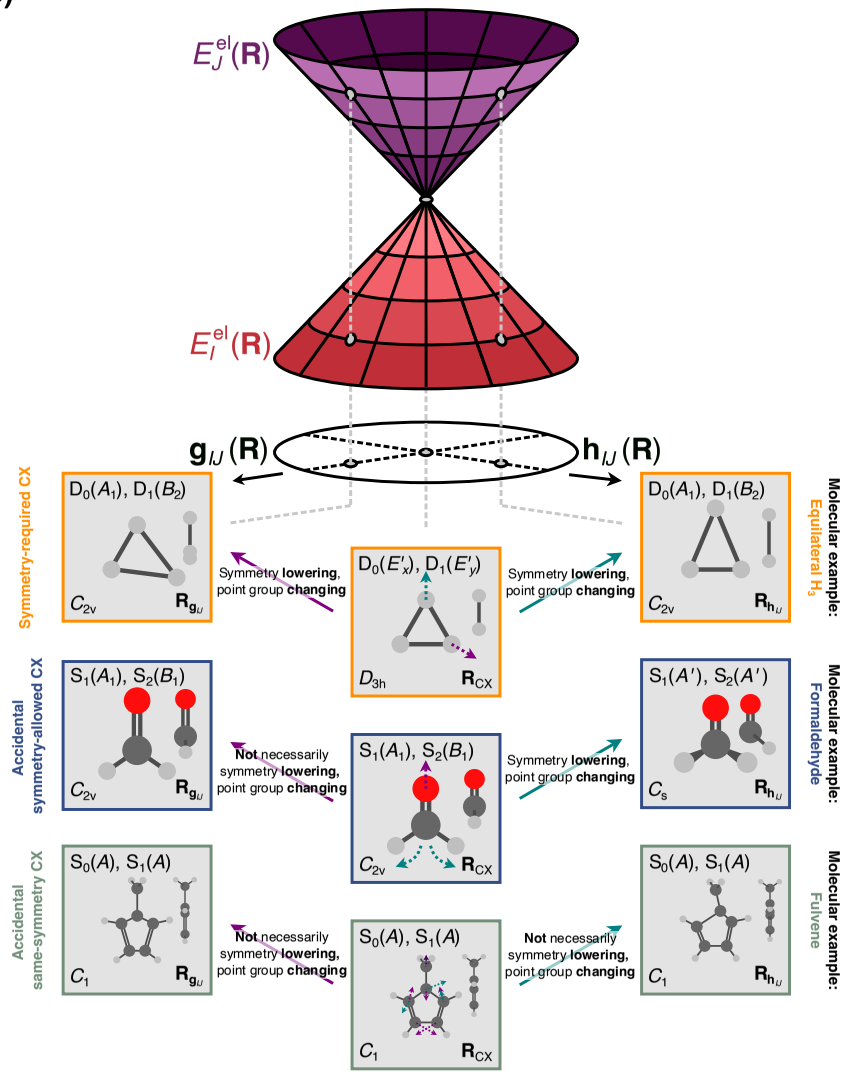

Figure 2.3: (Previous page.) **(a)** Schematic representation of a five-state diabatic electronic Hamiltonian matrix, considering a hypothetical molecule with C_{3v} point group symmetry. The Hamiltonian is block diagonal with each block transforming as a different irreducible representation (irrep) in C_{3v} symmetry, represented by the grey shading. Three different types of two-state CXs are considered, each described by a separate two-state diabatic electronic Hamiltonian matrix: symmetry-required (orange), accidental symmetry-allowed (blue) and accidental same-symmetry (green). Both conditions for degeneracy [Eq. (2.21)] are trivially satisfied in the symmetry-required CX [where $V_{1E_x}(\mathbf{R}) = V_{1E_y}(\mathbf{R}) = V_{1E}(\mathbf{R})$] because the two states transform as the respective components (i.e., x and y) of the same doubly-degenerate E irrep in C_{3v} symmetry. (Typically, components of a degenerate irrep are taken to be orthogonal, thus fulfilling the off-diagonal condition automatically. [45]) In the accidental symmetry-allowed CX, only the off-diagonal condition is satisfied by symmetry, due to the two states transforming as different irreps (i.e., A_1 and A_2) in C_{3v} symmetry, remembering that the Hamiltonian is block diagonal. Neither condition is fulfilled by group theoretical arguments in the accidental same-symmetry CX, with both states transforming as A_2. **(b)** Group theoretical arguments for why the diabatic electronic Hamiltonian matrix elements in Fig. 2.3(a) are (non-)zero at a given nuclear geometry, where Γ_α is the irrep of species α and $\Gamma_{\text{tot. sym.}}$ is the totally symmetric irrep of the point group under consideration. [Note, in Fig. 2.3(a), $V_{\Gamma_I,\Gamma_I}(\mathbf{R}) = V_{\Gamma_I}(\mathbf{R})$ for brevity.] **(c)** Schematic representation of the nuclear distortions (purple/turquoise) defining the branching space vectors for three molecular examples: D_1/D_0 CX in equilateral H_3 (symmetry-required, orange) [107], S_2/S_1 CX in formaldehyde (accidental symmetry-allowed, blue) [108] and S_1/S_0 CX in fulvene (accidental same-symmetry, green) [109]. In H_3, the branching space vectors both act to break the equilateral MECX symmetry (i.e., D_{3h}), lowering it to that of two respective isosceles configurations (i.e., C_{2v}), with scalene configurations (i.e., C_s) obtained by distorting along both vectors simultaneously. (Note, distorting H_3 along the opposite direction of either branching space vector past the equilateral geometry reverses the symmetry labels of D_0 and D_1 [110].) In formaldehyde, the branching space vectors constitute a C=O stretching mode and a CH_2 pyramidalisation mode, respectively; the latter lowers the symmetry from planar C_{2v} to non-planar C_s. Fulvene possesses a twisted/slightly pyramidalised CH_2 MECX, the branching space vectors for which do not change the C_1 point group symmetry of the molecule.

all nuclear geometries where this is the case; [80] the off-diagonal matrix elements of the totally-symmetric $\mathbf{H}_{\text{el}}^{(\text{dia})}(\mathbf{R})$ are zero by symmetry [111]. It may be possible to satisfy the first condition in Eq. (2.21) as well, by distorting the molecule along an appropriate nuclear coordinate, but as the term "accidental" suggests, this is not guaranteed.[9] (Such a change in geometry must be restricted to those which retain the point group symmetry, so as to keep the second condition satisfied [93].)

Accidental same-symmetry CXs involve electronic states which exhibit the same spatial symmetry (i.e., belong to the same (non-degenerate) irreducible representation). Unlike the two cases already discussed, neither condition in Eq. (2.21) is therefore fulfilled by group

[9] Put explicitly, accidental CXs (symmetry-allowed or same-symmetry) are CXs whose existence cannot be anticipated *a priori* by group theoretical arguments [112].

theoretical arguments [111]. Degeneracy can only occur "accidentally" by distorting the molecule along two independent nuclear coordinates, symmetry-breaking or otherwise.[9] Given most molecules do not possess sufficiently high symmetry to form the above two classes of CXs, accidental same-symmetry CXs are the by far the most common in photochemistry [86]. As such, they are the sole focus of this thesis. The lack of this "guiding" symmetry, however, means that accidental same-symmetry CXs are more difficult to locate [67]. Methods for optimising accidental same-symmetry CXs are the topic of Section 2.2.5.

2.2.2.2 Characterising conical intersections by topography

So far in Section 2.2, the discussion of CXs has centred around what we now refer to as their topology, that is, the dimensionality of the CX branching and seam spaces. However, an equally important aspect to consider is the topography of a given CX [86, 113], which relates instead to the shape of the PESs in the vicinity of the intersection point within the branching space (of typically a two-state CX). A number of ways exist to characterise the local topography of a CX, each of which make use of the four parameters $(\overline{g}, \overline{h}, s_x, s_y)$ given in Eq. (2.28) and (2.29).

Firstly, the parameters $\overline{g}$ and $\overline{h}$ characterise the slope of a CX in the directions of the two branching space vectors, respectively [114]. The average of these is related to the pitch,

$$\delta_{\mathrm{gh}} = \sqrt{\frac{1}{2}\left(\overline{g}^2 + \overline{h}^2\right)}\,, \tag{2.32}$$

which defines the overall steepness of the PESs within the branching space, whereas their relative difference relates to the asymmetry,

$$\Delta_{\mathrm{gh}} = \frac{\overline{g}^2 - \overline{h}^2}{\overline{g}^2 + \overline{h}^2}\,, \tag{2.33}$$

which defines the extent to which the shape of the CX differs from a reference double cone of perfect radial symmetry [115]. A CX is classified as symmetric (asymmetric) if it gives a zero (non-zero) value of Δ_{gh}. Visually, symmetric CXs possess PESs with the same slope in both the $\overline{\mathbf{g}}_{IJ}(\mathbf{R})$ and $\overline{\mathbf{h}}_{IJ}(\mathbf{R})$ vector directions (i.e., $\overline{g} = \overline{h}$), whereas the slopes differ in asymmetric CXs (i.e., $\overline{g} \neq \overline{h}$). It is seen in certain cases, like in trivial unavoided crossings [116, 117], that if the CX is strongly asymmetric, it may appear as (but is not) a one-dimensional, or linear, intersection in the branching space, with a $(F-1)$-dimensional seam space [81]. Such intersections are common in systems involving long-range charge or energy transfer. (The implications of this unique topography for nonadiabatic dynamics simulations is briefly touched on later in relation to our results in Chapter 5.)

Secondly, the parameters s_x and s_y characterise the tilt of a CX and lead to further classifications of CX topography, that of peaked and sloped[10] (Fig. 2.4) [68]. For a CX to be defined as peaked, s_x and s_y must be (close or equal to) zero; for a sloped CX, either one or both of s_x and s_y must be non-zero. Depending on which is larger, the CX will be tilted either more in the $\overline{\mathbf{g}}_{IJ}(\mathbf{R})$ or $\overline{\mathbf{h}}_{IJ}(\mathbf{R})$ vector directions, respectively. Visually, a CX is peaked if the intersection point in the branching space is the lowest (highest) energy point on the upper (lower) PES. Although, in this case, the point of degeneracy relates to a minimum on the upper PES, this should not be confused with a stationary point, as the nuclear gradient at such a geometry is not zero, but in fact discontinuous [81]. A sloped CX, in contrast, can be recognised visually when the principle axis of the CX is tilted to such an extent that now, in some directions along the branching plane, the energy of the upper (lower) PES becomes lower (higher) in energy than the intersection point [118].

Rewriting Eq. 2.31 explicitly in terms of the pitch, asymmetry and tilt parameters [Eqs 2.32, 2.33 and 2.28, respectively] yields

$$E_{1,2}^{\text{el, bs}}(x,y) = E^{\times} + \delta_{\text{gh}}\left(s_x x + s_y y \pm \sqrt{(x^2+y^2) + \Delta_{\text{gh}}\left(x^2-y^2\right)}\right), \tag{2.34}$$

which provides a direct means in plotting the branching space of CXs exhibiting different topographies (Fig. 2.4).[11] It may be argued, however, that in their current form the aforementioned CX branching space topography parameters do not bear an immediate connection to the possible reactive outcomes of nonadiabatic dynamics near a CX [119]. Fdez. Galván *et al.* [101, 115] recognised this by defining the following composite parameters,

$$\mathcal{P} = \frac{\sigma^2}{{\delta_{\text{gh}}}^2\left(1-{\Delta_{\text{gh}}}^2\right)}\left(1-\Delta_{\text{gh}}\cos(2\theta_{\text{s}})\right) \tag{2.35}$$

and

$$\mathcal{B} = \sqrt[3]{\frac{\sigma^2}{4\left(\delta_{\text{gh}}\Delta_{\text{gh}}\right)^2}}\left(\sqrt[3]{\left(1+\Delta_{\text{gh}}\right)\cos^2\left(\theta_{\text{s}}\right)} + \sqrt[3]{\left(1-\Delta_{\text{gh}}\right)\sin^2\left(\theta_{\text{s}}\right)}\right), \tag{2.36}$$

where

$$\sigma = \sqrt{{s_x}^2 + {s_y}^2} \tag{2.37}$$

[10] Atchity *et. al.* [68] classified a third CX topography of "intermediate", where on one side of the degeneracy point, the upper PES has a zero slope, and on the other side, the lower PES has a zero slope [81]. However, we do not consider this intermediate CX topography further in this thesis.

[11] Let us make a brief comment on some differences in notation used in this thesis. For simplicity, we use the notation x and y in Eqs 2.30, 2.31 and 2.34 within this introductory chapter, instead of $\overline{x}_{IJ}$ and $\overline{y}_{IJ}$ (or $\overline{x}'_{IJ}$ and $\overline{y}'_{IJ}$), which are used later in Chapter 3. The difference between the latter two relates to the use of different electronic-structure methods (see Section 3.5.1.3). Equally, in Figs 2.2-2.4 we use the (raw) $\mathbf{g}_{IJ}(\mathbf{R})$ and $\mathbf{h}_{IJ}(\mathbf{R})$ vector notation for schematic simplicity, rather than the more formally correct $\overline{x}_{IJ}$ and $\overline{y}_{IJ}$ (orthornormalised) scalar quantities (again, see Section 3.5.1.3).

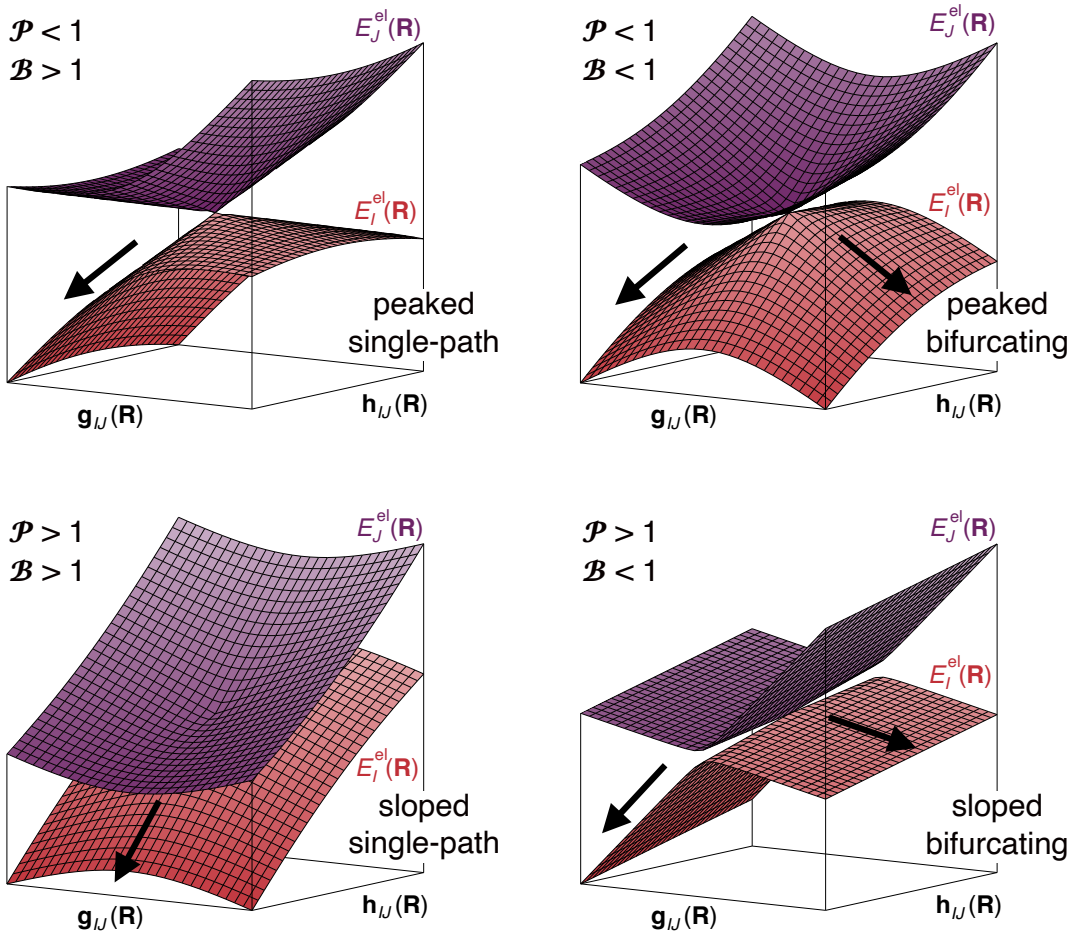

Figure 2.4: Schematic representation of the adiabatic PESs in the branching space of four two-state CXs characterised by different local topographies: **(top left)** peaked and single-path ($\delta_{\text{gh}} = 0.0949$, $\Delta_{\text{gh}} = 0.5320$, $s_x = 0.9550$, $s_y = 0.0000$); **(top right)** peaked and bifurcating ($\delta_{\text{gh}} = 0.1249$, $\Delta_{\text{gh}} = 0.3402$, $s_x = 0.0000$, $s_y = 0.7133$); **(bottom left)** sloped and single-path ($\delta_{\text{gh}} = 0.1326$, $\Delta_{\text{gh}} = 0.2680$, $s_x = 0.0000$, $s_y = 2.1588$); and **(bottom right)** sloped and bifurcating ($\delta_{\text{gh}} = 0.1399$, $\Delta_{\text{gh}} = 0.8753$, $s_x = 0.0000$, $s_y = 0.4553$). The numerical CX branching space topography parameters used to generate the plots in this figure were taken from Ref. [101].

is a collective tilt parameter and

$$\theta_{\text{s}} = \arctan\left(\frac{s_y}{s_x}\right) \tag{2.38}$$

is the tilt heading, i.e., the polar angle within the xy-plane (defined with respect to the x-axis) for which the average energy of the two PESs is maximum. Depending on the numerical value of these composite parameters, a CX can be characterised as [120]

$$\mathcal{P} = \begin{cases} < 1 & \text{peaked} \\ > 1 & \text{sloped} \end{cases} \quad \text{and} \quad \mathcal{B} = \begin{cases} < 1 & \text{bifurcating} \\ > 1 & \text{single-path} \end{cases} . \tag{2.39}$$

Here, the terms peaked and sloped are the exact same as those already discussed above [68]. However, additionally a CX can be classified as bifurcating if there are two minima on the lower PES, affording two preferred relaxation paths from the CX; single-path refers to when there is just one (Fig. 2.4). Similar ideas were initially discussed by Atchity *et. al.* [68]. By defining these composite parameters, it is possible to get a rough, but immediate feeling for the possible effect a given CX may have on nonadiabatic dynamics within its vicinity, simply based on its topography.

Early considerations of how local CX topography can influence nonadiabatic dynamics were first discussed by the Ruedenberg [68] and Yarkony [114] groups in the context of reduced-dimensionality models, however, these analyses were corroborated not long after by the groups of Robb [121, 122] and Martínez [123, 124] for real (full-dimensional) molecules. It is widely understood that peaked CXs are highly effective at steering the nuclear wavepacket towards the degeneracy point on the upper PES (and equally, away from it on the lower PES) [114]. Given they represent local minima (maxima) on the upper (lower) PES, peaked CXs are able to direct the nuclear wavepacket downhill towards (away from) the degeneracy point from (along) every direction). Thus, peaked CXs act, in essence, as photochemical "funnels", encouraging highly efficient nonadiabatic transitions from the upper to lower PES [125], usually with (near-)complete population transfer after only a single pass of the degeneracy point, accompanied by little to no reduction in nuclear velocity. Such nonadiabatic transfer occurs under far-from-equilibrium conditions, often retaining significant memory of the initial conditions imposed by the photoexcitation process in the FC region [81].

Sloped CXs, on the other hand, are generally associated with uphill approaches to the degeneracy point from the FC region on the upper PES, meaning (parts of) the nuclear wavepacket can in fact be directed away from a sloped CX on the upper PES (cf. peaked CXs). If (part of) the nuclear wavepacket does reach a sloped CX, it will likely cross to the lower PES, but then shortly after recross back to the upper PES, doing so back and forth several times [114]. This behaviour arises because parts of the lower PES are higher in energy than parts of the upper PES, and is helped in part by the relatively low velocity of the nuclear wavepacket upon its uphill approach to a sloped CX on the upper PES. Sloped CXs are thus inefficient at promoting population transfer from the upper to lower PES [125], but instead provide a viable means of nonadiabatic transitions in the opposite direction (i.e., from lower to upper), a process referred to as "up-funnelling". As alluded to already, (near-)complete nonadiabatic transfer seldom occurs within the first passage of a sloped CX. Instead appreciable wavepacket fragmentation is expected, further reducing the nuclear velocity and leading to population transfer occurring under near-to-equilibrium conditions (again, cf. peaked CXs) [81].

Local CX topography may also have an impact on photochemical branching ratios. Given they afford minimal wavepacket fragmentation, it may be argued that peaked CXs primarily result in a single photochemical pathway on the lower PES (and thus a single photoproduct, if

the latter is the ground electronic state). Similarly, significant wavepacket fragmentation could imply sloped CXs lead to multiple (i.e., a statistical distribution of) photoproducts [123], owed to each of the different "up-funnelled" parts of the nuclear wavepacket experiencing different forces and momenta upon return to the upper PES. However, peaked CXs are well known to be much more photochemically active than their sloped counterparts [81], giving the possibility of multiple lower PES reaction pathways [i.e., giving two photoproducts, or one photoproduct and regeneration of the reactants–see Fig. 2.1(a)]. Conversely, it is well documented that sloped CXs play a key role in photostability, due to the strong directionality of the PESs near the degeneracy point, leading solely to the recovery of the reactants [Fig. 2.1(a)]. It is therefore evident how both peaked and sloped CXs, depending on the context, can also be described as either single-path or bifurcating (see Eq. 2.39).

In reality, whether dynamics through a (ground-to-excited state) CX leads to a single or multiple photoproducts is not just determined by local CX topography (i.e., peaked vs sloped) [126, 127], but rather also strongly influenced by non-local PES topography (i.e., between the FC region and CX of interest), as well as purely dynamical factors (i.e., properties of the nuclear wavepacket, such as width, velocity and direction of approach) [81, 101]; such considerations were initially highlighted by Malhado and coworkers [125, 128].

2.2.2.3 Characterising conical intersections by topology

Finally, the most fundamental characteristic of a CX, i.e., its topology, can also be used to classify it, with different CXs (or, more generally, different intersections) possessing different topologies. The most common type of CX encountered in photochemical investigations, as discussed already, are those between two electronic states of the same spin-multiplicity (considered within a non-relativistic framework). Such CXs afford the archetypal $(F-2)$-dimensional seam space and orthogonal two-dimensional branching space, in which the electronic PESs form the distinctive double cone. For completeness, we now consider two alternative cases: (i) CXs between three (or more) electronic states and (ii) CXs between two electronic states considered within a relativistic framework.

To start, we address case (i). Let us consider the three-state analogue of Eq. (2.15) [76],

$$\mathbf{H}_{\mathrm{el}}^{(\mathrm{dia})}(\mathbf{R}) = \begin{pmatrix} V_{11}(\mathbf{R}) & V_{12}(\mathbf{R}) & V_{13}(\mathbf{R}) \\ V_{21}(\mathbf{R}) & V_{22}(\mathbf{R}) & V_{23}(\mathbf{R}) \\ V_{31}(\mathbf{R}) & V_{32}(\mathbf{R}) & V_{33}(\mathbf{R}) \end{pmatrix} . \tag{2.40}$$

Using the same procedure as for the two-state case, the eigenvalues of $\mathbf{H}_{\mathrm{el}}^{(\mathrm{dia})}(\mathbf{R})$ (i.e., the three adiabatic electronic energies) can only become degenerate if the following five conditions are met,

$$\begin{aligned} V_{11}(\mathbf{R}_{\mathrm{CX}}) &= V_{22}(\mathbf{R}_{\mathrm{CX}}) = V_{33}(\mathbf{R}_{\mathrm{CX}}) \\ V_{12}(\mathbf{R}_{\mathrm{CX}}) &= V_{13}(\mathbf{R}_{\mathrm{CX}}) = V_{23}(\mathbf{R}_{\mathrm{CX}}) = 0\,. \end{aligned} \tag{2.41}$$

In other words, degeneracy requires (a) all diagonal matrix elements to be equal and (b) all off-diagonal matrix elements to be zero. Three-state CXs, therefore, have a five-dimensional branching space and an $(F-5)$-dimensional seam space. These arguments can be generalised to consider the branching space dimensionality, denoted η, of a CX involving an arbitrary number of M electronic states of the same spin-multiplicity. In order for M-fold degeneracy, $M-1$ diagonal conditions and $M(M-1)/2$ off-diagonal conditions must be fulfilled [considering an $(M \times M)$ matrix] [67]. Thus, the total number of conditions that need to be obeyed, that is, the branching space dimensionality of the M-state CX is

$$\eta = \frac{(M-1)\,(M+2)}{2}\,, \tag{2.42}$$

where the dimensionality of the corresponding seam space can then also be given as $F-\eta$.

For a discussion relating to case (ii), it is prudent to distinguish between two sub-cases, that of intersections between electronic states of different spin-multiplicity (i.e., $\mathrm{S}_n/\mathrm{T}_n$) and that of intersections exhibited by systems of an odd number of electrons [33, 129]. In both cases, relativistic effects should not be neglected and, as such, the Hamiltonian that needs to be considered is $\hat{H}_{\mathrm{el}}^{\mathrm{full}}(\mathbf{r},\mathbf{R}) = \hat{H}_{\mathrm{el}}(\mathbf{r},\mathbf{R}) + \hat{H}_{\mathrm{SO}}(\mathbf{r},\mathbf{R})$, where $\hat{H}_{\mathrm{el}}(\mathbf{r},\mathbf{R})$ is the non-relativistic electronic Hamiltonian in Eq. (2.2) and $\hat{H}_{\mathrm{SO}}(\mathbf{r},\mathbf{R})$ is the operator accounting for spin-orbit coupling. It is well understood that intersections between electronic states of different spin-multiplicity, when viewed in a non-relativistic framework, exhibit linear $(F-1)$-dimensional intersections, where both states cross one another [130, 131]. In other words, CXs do *not* occur between states of different spin-multiplicity within a spin-diabatic representation of the electronic wavefunction [i.e., the eigenstates of $\hat{H}_{\mathrm{el}}(\mathbf{r},\mathbf{R})$]. The inclusion of spin-orbit coupling, however, allows electronic states of differing spin-multiplicity to couple and mix, affording a new set of electronic states (now labelled by total angular momentum instead of spin-multiplicity, as the latter is no longer a "good" quantum number [132]), where, for example, the components of a triplet state are no longer degenerate, and in which no states cross. It may be possible, in such a case, for a previously designated singlet state to form a conical $(F-2)$-dimensional intersection with one of the previously designated components of a triplet state. This situation involves a spin-adiabatic representation of the electronic wavefunction [i.e., the eigenstates of $\hat{H}_{\mathrm{el}}^{\mathrm{full}}(\mathbf{r},\mathbf{R})$].

As stated several times before, in a non-relativistic framework, the electronic Hamiltonian is real-valued and, as such, the branching space of a CX between two electronic states of the same spin-multiplicity is two-dimensional. The same holds true within a relativistic framework so long as the molecule has an even number of electrons. For a two-state CX

in a system of an odd number of electrons, inclusion of the spin-orbit interaction leads to five conditions needing to be satisfied in order to allow degeneracy [133–136]. Three conditions arise solely from the electronic Hamiltonian now being complex-valued as a result of including $\hat{H}_{\mathrm{SO}}(\mathbf{r},\mathbf{R})$, which can be complex [137]. Two further conditions arise due to combination of $\hat{H}_{\mathrm{el}}^{\mathrm{full}}(\mathbf{r},\mathbf{R})$ being complex-valued and as a consequence of time-reversal symmetry, which dictates that all eigenvalues of $\hat{H}_{\mathrm{el}}^{\mathrm{full}}(\mathbf{r},\mathbf{R})$ be doubly-degenerate irrespective of the nuclear geometry, a subtlety known as Kramer's degeneracy [138]. This means that such CXs, in the general case of no spatial symmetry, have a five-dimensional branching space. If, however, the molecule exhibits C_s or higher spatial symmetry, the two extra conditions related to Kramer's degeneracy are trivially satisfied. As such, the dimensionality of the branching space reduces to three (i.e., the value corresponding to an otherwise non-degenerate complex-valued Hermitian matrix) [133].

2.2.3 The topological phase effect (and other signatures of conical intersections)

Apart from possessing a vanishing electronic energy difference, points of CX exhibit two other intrinsically related properties, or signatures, that can be used to identify their presence. The first can be highlighted by expressing the nonadiabatic coupling vector, $\mathbf{d}_{IJ}(\mathbf{R})$ [Eq. (2.8)], in terms of the derivative coupling vector, $\mathbf{h}_{IJ}(\mathbf{R})$ [Eq. (2.8)], given as [67]

$$\mathbf{d}_{IJ}(\mathbf{R}) = \frac{\mathbf{h}_{IJ}(\mathbf{R})}{E_J^{\mathrm{el}}(\mathbf{R}) - E_I^{\mathrm{el}}(\mathbf{R})}\,, \tag{2.43}$$

where $\mathbf{d}_{IJ}(\mathbf{R})$ is shown to be inversely proportional to the electronic energy difference between the adiabatic electronic states, I and J. When the electronic states are energetically well separated, the $\mathbf{d}_{IJ}(\mathbf{R})$ vector is small, so can, for the majority of such cases, be considered irrelevant and thus can be ignored. The BO approximation [Eq. (2.10)] then appears a valid framework to operate in. However, when the adiabatic electronic states become close in [Fig. 2.5(left)], especially in the vicinity of a CX (or directly at an AC), the $\mathbf{d}_{IJ}(\mathbf{R})$ vector becomes large(r), leading to a tendency for strong nonadiabaticity (i.e., a change in electronic state induced by movement of the nuclei) [76]. In the extreme case, that is directly at a CX, the two adiabatic electronic states are degenerate and the energy difference zero, so the $\mathbf{d}_{IJ}(\mathbf{R})$ vector becomes maximum (i.e, infinite or singular). Therefore, the BO approximation not only begins to break down in the region surrounding CXs, where $\mathbf{d}_{IJ}(\mathbf{R})$ is no longer negligible, but in fact it becomes completely meaningless at the point of a CX, where the $\mathbf{d}_{IJ}(\mathbf{R})$ blows up to infinity. Note, this is different to the (scalar) diabatic couplings [in Eq. (2.14)], which always remain finite and are smooth functions of nuclear coordinate. The divergence of the $\mathbf{d}_{IJ}(\mathbf{R})$ vector is a major indication of the existence of a CX at a given nuclear geometry.

Arguably, a more definitive signature of a CX is related to the effect that such a pole in the $\mathbf{d}_{IJ}(\mathbf{R})$ vector field has on the adiabatic electronic wavefunction. In general, it is

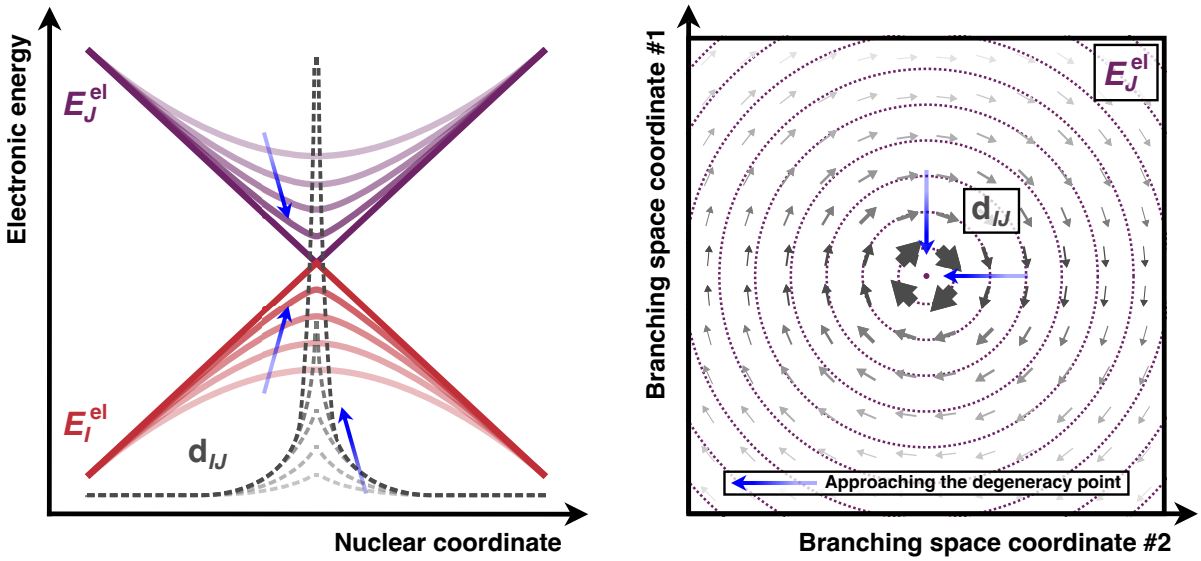

Figure 2.5: (Left) Schematic representation of different 1D cuts of the adiabatic PESs and nonadiabatic coupling vector, $\mathbf{d}_{IJ}(\mathbf{R})$, upon approaching the degeneracy point of a conical intersection in its branching space (as indicated by the colouring and blue arrows). Adapted from Ref. [132]. **(Right)** Schematic representation of the nonadiabatic coupling vector field in the vicinity of a conical intersection viewed from above the double cone. Arrow size is proportional to the magnitude of the nonadiabatic coupling vector, decreasing radially away from the degeneracy point; colouring loosely matches the corresponding 1D cuts of $\mathbf{d}_{IJ}(\mathbf{R})$ in Fig. 2.5(left). Adapted from Ref. [40].

understood that the (real-valued) adiabatic wavefunction of a given electronic state picks up a purely geometric phase factor, $\exp(i\gamma_n)$, when parallel-transported along a path in nuclear-configuration space, in addition to the familiar dynamical phase factor, which appears naturally from solution of the electronic TDSE [139]. The associated phase, γ_n, is a geometric quantity given that its value depends on (the geometry of) the path and is not quantised [140, 141]. If, however, the path along which the adiabatic electronic wavefunction traverses is a closed one, then the phase becomes topological [140]. The phase is now quantised and depends simply on the winding number around the path, not its geometry [141]. It is well known that if the closed path encircles a CX, then the topological phase takes a value of π; if it does not enclose a CX, then it takes a value of zero [142]. In the former case, this results in the adiabatic electronic wavefunction gaining a phase factor of -1 (i.e., its sign flips) when traversing one full loop around the CX [i.e., $\psi_I(\alpha) = -\psi_I(\alpha + 2\pi)$, where α is the angle traced around the CX]. This process is termed the topological phase effect and was first recognised by Longuet-Higgins and coworkers [143–145] in 1958 for a two-state Jahn-Teller system. The subsequent seminal works of Mead and Truhlar [146] for the single electronic state case and Berry [147], who generalised the concept of the topological (or geometric, or Berry) phase to any arbitrary adiabatically evolving system, followed soon after. It goes without saying that an additional phase factor of +1 affords no such sign flip; as is the case when the path does

not enclose a CX.[12] One important consequence of the topological phase effect is that it causes the adiabatic electronic wavefunction to be double-valued [i.e., the signs of ψ_I are opposite at $\mathbf{R}(\alpha)$ and $\mathbf{R}(\alpha + 2\pi)$, but for a closed path $\mathbf{R}(\alpha) = \mathbf{R}(\alpha + 2\pi)$]. In order to guarantee the total molecular wavefunction remains single-valued, either (i) the (real-valued) nuclear wavefunction must also gain a topological phase of π upon full rotation around a CX [148], or (ii) as suggested by Mead and Truhlar [146], the adiabatic electronic Hamiltonian can be transformed to introduce the resolution of identity, $1 = \exp[i\theta(\mathbf{R})] \exp[-i\theta(\mathbf{R})]$, giving now single-valued (but complex) electronic and nuclear wavefunctions [148, 149].

As will be revealed in Chapter 4, the topological phase may be calculated using information of the $\mathbf{d}_{IJ}(\mathbf{R})$ vector along the closed path considered above. However, the discussion in the preceding paragraph is concerned with isolated two-state CXs. Interesting subtleties can occur when one also considers the possibility of proximal CXs, that is, other two- (or multi-)state CXs that exist nearby to the two-state CX of interest [80]. Two cases can arise: either the proximal CXs involve an electronic state (or states) that are different to those involved in the CX of interest, or the proximal CXs share the exact same electronic states as the CX of interest. Three-state CXs constitute an example of the former. Their five-dimensional branching space in fact contains a pair of three-dimensional subspaces, termed the degeneracy subspaces [150], one where the upper two electronic states (J, K) remain degenerate and one where the lower two electronic states (I, J) remain degenerate [151–154]. As such, three-state CXs (I, J, K) can be viewed as the intersection between two linked two-state CXs (I, J and J, K) [90, 155]. Complications arise in calculating a value for the topological phase in this case because the associated $\mathbf{d}_{IJ}(\mathbf{R})$ vectors can become double-valued around the loop encircling three-state CXs, or, more accurately, around two two-state CXs involving different pairs of electronic states. This phenomenon has been termed the induced topological phase effect [156]. One can get around the double-valuedness of the corresponding $\mathbf{d}_{IJ}(\mathbf{R})$ vectors by introducing appropriate branch cuts, however, the $\mathbf{d}_{IJ}(\mathbf{R})$ vectors then become single-valued at the expense of rendering the calculated value of the topological phase dependent on the point at which you start traversing the closed path; this leads to problems of non-uniqueness making such calculations practically difficult [80, 157]. Note, the need to include branch cuts does not arise when considering the $\mathbf{d}_{IJ}(\mathbf{R})$ vectors along a closed path encircling multiple two-state CXs that share the same two electronic states (I, J). This latter situation is relevant to the work in Chapter 4 and, as such, further discussion will be left until then.

Lastly, it is important to remind oneself that the topological phase, as well as CXs themselves, are mere artefacts of using adiabatic electronic states within the BH representation [158]. If one was to instead use (i) a diabatic representation for the electronic wavefunction, or (ii) the exact factorisation [159–161] of the molecular wavefunction, CXs would no longer appear, so neither would the topological phase effect, nor the divergence in the $\mathbf{d}_{IJ}(\mathbf{R})$ vector,

[12] ACs also do not exhibit the topological phase [63]. The two adiabatic electronic states remain non-degenerate and as a result avoided crossings are characterised by large, but finite-valued $\mathbf{d}_{IJ}(\mathbf{R})$ vectors.

manifest [162–164]. As such, given its dependence on representation, the topological phase does not constitute a physical observable of the system, despite contrary comments in the literature.

2.2.4 Electronic-structure methods for describing conical intersections

As always, the insolubility of the exact electronic Schrödinger equation [Eq. (2.3)] for chemically relevant systems necessitates the use of approximate electronic-structure methods. Three requirements are often highlighted as being critical for an accurate description of any two-state CX. The chosen electronic-structure method should be able to (a) compute analytic nuclear gradients [$\nabla_{\mathbf{R}} E_I^{\mathrm{el}}(\mathbf{R})$] and derivative coupling vectors [$\mathbf{h}_{IJ}(\mathbf{R})$]; (b) include both dynamic and static electron correlation, given the rapid change in character of the electronic states in the vicinity of (and passing through) a CX; and (c) provide a balanced treatment of the ground and excited electronic states, so as to allow explicit interstate coupling between them [165]. Whether or not a given electronic-structure method can satisfy these three criteria can have a dramatic affect on its ability to describe the following CX properties, namely (i) its location (i.e., the molecular geometry and electronic energy at which it occurs); (ii) its topology (i.e., conical $F-2$ vs linear $F-1$); and (iii) its topography (i.e., peaked vs sloped) [166].

In simplistic terms, one may view the problem as follows. Inclusion (or exclusion) of dynamic electron correlation [one half of criterion (b)] may lead to different CX topographies [property (iii)], as well as a shifted location [property (i)]. Inclusion of static electronic correlation [the other half of criterion (b)] and satisfying criterion (c) [for ground-to-excited CXs] leads to a CX exhibiting the correct topology [property (ii)]. Satisfying criterion (a), on the other hand, is important not only for constructing the CX branching space, but also in nonadiabatic dynamics simulations (see Chapter 5). Of course, it is clear that in reality the problem cannot be so readily divided, with many contributing factors playing an equal role in the (photo)chemistry under investigation. Nonetheless, it can still be helpful, in some cases, to consider it in this way.

Owing to the many subtleties involved in describing the CX branching space accurately, the obvious electronic-structure methods of choice have been multiconfigurational and multireference approaches[13] [86, 167]. These techniques go beyond the simple Hartree-Fock

[13]A brief note on nomenclature: (a) "Single-reference" refers to a wavefunction built upon a single (usually closed-shell HF) Slater determinant. Other (excited) Slater determinants (i.e., those generated from the HF determinant) also contribute, albeit typically minimally. It is these extra excited Slater determinants, however, that account for dynamic correlation, something no possible in HF. (b) "Multiconfigurational" refers to a wavefunction constructed from several Slater determinants, specifically those with comparable contributions (i.e., where the HF and few excited Slater determinants possess similar weights). This chosen form enables static correlation to be captured, something not possible in single-reference methods. Note, although approaches like CISD involve several Slater determinants (i.e., HF, singly- and doubly-excited), the singly- and doubly-excited Slater determinants do not contribute on par with the HF determinant; as such, CISD is typically not referred to as a multiconfigurational method. (c) "Multireference" refers to a wavefunction built upon an underlying multiconfigurational reference,

(HF) description [168–170] of the electronic wavefunction as an antisymmetrised product of single-electron wavefunctions, i.e., a single Slater determinant of HF orbitals. The key idea underlying most multiconfigurational methods is that of configuration interaction (CI). In the CI approach [171], the wavefunction is represented as a linear combination of Slater determinants and their expansion coefficients are optimised by the Rayleigh-Ritz variation principle. When all possible excited determinants are included (that is, when all possible electronic configurations are accounted for) the method is called full CI (FCI). This amounts to the best approximation to the exact electronic wavefunction within a given basis set [172]. The term basis set refers to the set of spatial functions in which the HF orbitals are expanded and typical examples used in photochemistry are those attributed to Pople [173] and to Dunning [174], as well as the Karlsruhe basis sets [175]. In contrast, if one truncates the CI expansion to include the HF reference and only all possible single-excitations, this leads to the well-known CI singles (CIS) approach.

If the HF orbitals, which make up the Slater determinants, are also re-optimised variationally during the energy minimisation procedure this leads to the multiconfigurational self-consistent field (MCSCF) method [176]. The resulting orbitals no longer constitute those of HF (i.e., those optimised to minimise the energy of a single Slater determinant, the single-reference problem), but instead new orbitals (i.e., the MCSCF orbitals) that are optimal for the multireference problem. A number of variants of the MCSCF method exist, yet arguably the most common is complete active-space self-consistent field (CASSCF), which involves dividing the orbitals up into those that are inactive (i.e., always doubly occupied), active (i.e., can be doubly-, singly- or un-occupied) and virtual (i.e., always unoccupied). In practice, one must choose how many active electrons (n) are occupying how many active orbitals (m) and then an FCI calculation is performed within this restricted orbital subspace; the method is denoted CASSCF(n/m). The optimised CASSCF wavefunction, and therefore the CASSCF electronic energy, is invariant under orbital rotations within each subspace (i.e., active-to-active etc.), but not between subspaces (i.e., active-to-virtual etc.) [177]. If the active space is extended such that all possible electron configurations are captured, one again reaches the FCI limit (within a given basis). In state-specific CASSCF, only a single electronic state is variationally optimised, however, it can often arise that a more balanced description of multiple electronic states is desirable. This can be achieved by instead optimising the CI expansion coefficients and HF orbitals to minimise the average energy of all electronic states of interest (k), a method called state-averaged CASSCF [SA(k)-CASSCF]. Provided an appropriate active space is selected, SA-CASSCF represents a reliable method to correctly describe the topology of a CX [86, 166], since it recovers static correlation. State-averaging also helps to avoid variational collapse onto the ground state [178] and ensures state orthogonality, the latter being unachievable via a state-specific formulation [179]. However, SA-CASSCF can still be susceptible to root-flipping,

with each new excited Slater determinant generated from the space of multiple determinants making up the reference. In this way, multireference methods are able to describe both dynamic and static correlation.

leading to incorrect ordering of the excited electronic states [60].

One way to partially alleviate this issue is to explicitly include dynamic correlation, something which (SA-)CASSCF fails to account for. Dynamic correlation relates to the tendency of electrons to avoid each other at short distances [180], as indicated by the presence of the Coulombic electron-electron cusp in the exact electronic wavefunction as two electrons approach, a direct consequence of the $1/|\mathbf{r}_i - \mathbf{r}_j|$ term in $\hat{H}_{\text{el}}(\mathbf{r}, \mathbf{R})$ [181]. Dynamic correlation can be accounted for by including a large number of excited electronic configurations, each providing only a small contribution; an accurate description of the cusp is slow to converge with respect to orbital expansions [177]. Static correlation, on the other hand, arises due to the inclusion of a few important, (near-)degenerate electronic configurations with similar weights to the HF reference [182]. It is possible to add dynamic correlation on top of the static correlation already provided by CASSCF either via configuration interaction, which leads to multireference CI (MRCI) [183] or by applying Rayleigh-Schödinger perturbation theory, which yields complete active-space second-order perturbation theory (CASPT2) [184, 185]. One can also improve upon SA-CASSCF by employing multi-state CASPT2 (MS-CASPT2) [186], with the more recent variant, extended MS-CASPT2 (XMS-CASPT2) [187], now acting as one of the go-to reference methods, against which cheaper electronic-structure methods are usually benchmarked [188, 189]. By incorporating dynamic correlation [166, 190, 191], XMS-CASPT2 is able to provide, for the most part, improved CX topographies over SA-CASSCF [192, 193]. With a refined treatment of interstate coupling, XMS-CASPT2 also appears to be much less prone to electronic energy divergence/stability problems [194–196] that can sometimes arise near the CX intersection point in state-specific CASPT2 and even MS-CASPT2. However, XMS-CASPT2 is not without its problems. Like any variant of CASPT2 [161, 197], it can suffer from intruder states [198], which arise from singularities in the PT2 expansion. The effects of intruder states can be remedied by applying a small real or imaginary shift to the zeroth-order Hamiltonian [199, 200]; acceptable values of such (empirical) shifts are typically between 0.0 and 0.5 Hartree [201, 202].

Despite their overall success, CAS-based methods are unavoidably computationally demanding, given that the number of electronic configurations scales factorially [203] with an increase in active-space size [204]. This, along with the practical difficulty of choosing a set of stable active-space orbitals, hinders the use of CAS-based approaches as "black-box" methods, which can be applied to medium- to large-sized systems using standard computational setups. Therefore, cheaper alternatives to add to the photochemist's electronic-structure toolkit are still in demand. A notable example, which has seen a recent surge in popularity in the excited-state dynamics simulations community, comes from the algebraic diagrammatic construction (ADC) family of wavefunction-based methods [205–208]. The ground-state wavefunction and electronic energy in such approaches are obtained by Møller-Plesset (MP) perturbation theory [209], providing the inclusion of dynamic correlation. Excitation energies arise as the poles of

the so-called polarisation propagator [210], with respective excited states given by summing these to the MP ground-state energy. Depending on the order of perturbation theory one extends to in the ground state (i.e., MP2 or MP3), this leads to either ADC(2) or ADC(3); the former arguably being the sole variant applied in photochemical simulations [211]. However, as will be shown explicitly in Chapter 3, ADC(2) struggles to correctly describe CXs between the ground and first-excited electronic states of molecules [96]. In certain cases, that is, for carbonyl-containing molecules along C=O elongation, such ground-to-excited state crossings can even artificially appear in place of a truly avoided crossing exhibited by multireference methods [212].

A further affordable electronic-structure method, which also accounts for dynamic correlation and upon which this thesis is based, is linear-response time-dependent density functional theory. A detailed discussion of this approach, starting with a recap of ground-state density functional theory, will be presented in Section 2.3.

2.2.5 Locating conical intersections

As was emphasised in Section 2.2.1, CXs do not exist as isolated points, but instead span (in the case of two-state CXs) an entire $(F-2)$-dimensional seam. Therefore, it is convenient (and perhaps intuitive) to search for nuclear geometries along this seam, which may be of some chemical importance [213]. It is commonly presumed that local minima within the seam space–termed minimum-energy conical intersections (MECXs)–dominate population transfer between electronic states. It should be noted, however, that it is often the case that nonadiabatic transitions are indeed facilitated by CXs that lie higher in energy than the closest MECX.[63] This is not to say that MECXs do not constitute a practical set of geometries from which we can attempt to elucidate the photochemical reaction mechanism.

In order to locate a two-state MECX, one must carry out a constrained geometry optimisation: minimise the energy of either electronic state (or the average of the two), whilst ensuring that the energy difference between the two electronic states goes to zero [86]. A number of algorithms have been proposed to carry out this task, which can be divided into those that require knowledge of the derivative coupling vectors [$\mathbf{h}_{IJ}(\mathbf{R})$] and those that do not. Examples used in this thesis of the former include the gradient-projection (GP) method and the Lagrange-Newton (LN) method, whilst that of the latter includes the penalty-function (PF) approach. Since their inception, the GP and LN methods have been considered efficient algorithms for use alongside multiconfigurational and multireference methods in CX geometry optimisation calculations because such electronic structure methods give access to the required $\mathbf{h}_{IJ}(\mathbf{R})$ vectors. However, there still exist cases where an expression for the $\mathbf{h}_{IJ}(\mathbf{R})$ vector has yet to be derived, as is the case for the ADC family of electronic structure methods [211], or where simply the electronic wavefunction is not uniquely defined, such as for CXs in the condensed phase, where free energy (rather than potential energy) surfaces should

be considered [213]. Even for electronic-structure methods that do provide $\mathbf{h}_{IJ}(\mathbf{R})$ vectors, evaluation can become too computationally costly, or implementation too involved at present [214]. In such cases, the PF method provides a simple way to locate MECXs.

2.2.5.1 Gradient-projection method

In the GP method proposed by Bearpark *et al.* [215], an MECX is located by minimising the energy difference, $\Delta E_{IJ}^{\mathrm{el}}(\mathbf{R})$, between the upper and lower electronic states within the branching space, whilst also minimising the energy of the upper electronic state, $E_J^{\mathrm{el}}(\mathbf{R})$, within its orthogonal complement, the seam space. The gradient that minimises the energy difference is

$$\mathbf{f}_1^{\mathrm{GP}}(\mathbf{R}) = 2\Delta E_{IJ}^{\mathrm{el}} \cdot \bar{\mathbf{x}}_{IJ}(\mathbf{R})\,. \tag{2.44}$$

In order for the upper state energy to be minimised within the seam space, its gradient must be projected onto the $F-2$ nuclear coordinates perpendicular to the branching plane. Therefore, the upper state gradient projection is

$$\mathbf{f}_2^{\mathrm{GP}}(\mathbf{R}) = \mathbf{P}(\mathbf{R}) \cdot \frac{\partial E_J^{\mathrm{el}}(\mathbf{R})}{\partial \mathbf{R}}\,, \tag{2.45}$$

where $\mathbf{P} = \mathbb{I} - \mathbf{x}_{IJ}\mathbf{x}_{IJ}^{\mathrm{T}} - \mathbf{y}_{IJ}\mathbf{y}_{IJ}^{\mathrm{T}}$ is the facilitating projection matrix [216]. It is through the projection matrix that the GP method acquires its dependence on the $\mathbf{h}_{IJ}(\mathbf{R})$ vector (or more specifically, its orthonormalised form). The gradient used in the overall minimisation procedure is then the linear combination

$$\mathbf{F}^{\mathrm{GP}}(\mathbf{R};\alpha_0,\alpha_1) = \alpha_0 \left[\alpha_1 \mathbf{f}_1^{\mathrm{GP}}(\mathbf{R}) + (1-\alpha_1)\,\mathbf{f}_2^{\mathrm{GP}}(\mathbf{R})\right]\,, \tag{2.46}$$

where $\alpha_0 > 0$ and $0 < \alpha_1 \leq 1$. The parameter α_0 scales the gradient in Eq. (2.46) as a whole, whereas α_1 dictates the relative importance of its two components [Eqs (2.44) and (2.45)] [217]. As such, the MECX optimisation can be viewed as proceeding in two steps [218]. First, the two electronic states are far apart, so the minimisation is dominated by $\mathbf{f}_1^{\mathrm{GP}}(\mathbf{R})$, which forces the states to come closer together. After the intersection seam is reached, the optimisation will be directed towards the MECX as $\mathbf{f}_2^{\mathrm{GP}}(\mathbf{R})$ then takes over.

2.2.5.2 Lagrange-Newton method

The LN method, proposed by Manaa and Yarkony [219], enforces the conditions for degeneracy [Eq. (2.21)] by associating each with a Lagrange multiplier (λ_1, λ_2) and minimising the corresponding Lagrangian function,

$$L^{\mathrm{LN}}(\mathbf{R};\lambda_1,\lambda_2,\xi) = E_I^{\mathrm{el}}(\mathbf{R}) + \lambda_1 \Delta E_{IJ}^{\mathrm{el}}(\mathbf{R}) + \lambda_2 V_{IJ}(\mathbf{R}) + \sum_{k=1}^{M} \xi_k C_k\,. \tag{2.47}$$

The first term minimises the energy of the lower electronic state, $E_I^{\mathrm{el}}(\mathbf{R})$; the second and third terms impose the first and second constraints in Eq. (2.21), respectively; and the optional fourth term relates to M additional constraints for freezing certain natural geometric distortions of the molecule (e.g., bond lengths or angles, dihedral angles etc.) [217]. As the name suggests, a Newton-Raphson procedure is generally the method of choice to locate stationary points of the Lagrangian. The gradients of the second and third terms give the respective branching space vectors, so it is through the third term that the LN method depends on the $\mathbf{h}_{IJ}(\mathbf{R})$ vector.

2.2.5.3 Penalty function method

In the PF approach, the requirement for $\Delta E_{IJ}^{\mathrm{el}}(\mathbf{R}) = 0$ at the CX is accomplished through the inclusion of a term in an objective function that monotonically increases with the value of $\Delta E_{IJ}^{\mathrm{el}}(\mathbf{R})$:

$$F^{\mathrm{PF}}(\mathbf{R};\alpha_2,\alpha_i) = \overline{E}_{IJ}(\mathbf{R}) + \alpha_2 G(\mathbf{R};\alpha_i) \;\text{ for }\; i = 3,4\,. \tag{2.48}$$

The first term minimises the average energy of the upper and lower electronic states, $\overline{E}_{IJ}(\mathbf{R})$, and the second term (i.e., the penalty function) minimises their difference in energy. Two different forms of the penalty function used in this thesis are that of Ciminelli *et al.* [220],

$$G^{\mathrm{CGP}}(\mathbf{R};\alpha_3) = {\alpha_3}^2 \ln\left[1 + \left(\frac{\Delta E_{IJ}(\mathbf{R})}{\alpha_3}\right)^2\right], \tag{2.49}$$

and that of Levine *et al.* [213],

$$G^{\mathrm{CIOpt}}(\mathbf{R};\alpha_4) = \left[\frac{\Delta E_{IJ}(\mathbf{R})^2}{\Delta E_{IJ}(\mathbf{R}) + \alpha_4}\right], \tag{2.50}$$

which together with Eq. (2.48) is referred to as the CIOpt method. The parameters α_2, α_3 and α_4 in Eqs (2.48) to (2.50) are all user defined constants and no information of $\mathbf{h}_{IJ}(\mathbf{R})$ is needed. In CIOpt, α_2 acts to guide the geometry optimisation towards the seam space minimum and α_4 is responsible for smoothing the penalty function, partially ensuring it is differentiable at the CX. The parameters α_2 and α_3 in the PF method of Ciminelli *et al.* [220] play similar roles.

Keal *et al.* [217] compared the three MECX optimisation approaches (GP, LN, PF) outlined above for a set of 12 small molecules. Unsurprisingly, they found the GP and LN approaches to be overall more efficient than the PF method. For butadiene, the former required only 15-16 iterations to converge to the MECX geometry, whereas the latter took 86 iterations. Whilst each iteration is much cheaper in the PF method due to the lack of need for computing $\mathbf{h}_{IJ}(\mathbf{R})$, this benefit is outweighed by the need for larger numbers of individual optimisation steps to obtain overall convergence [86]. Keal *et al.* therefore recommended that the PF method only be used when $\mathbf{h}_{IJ}(\mathbf{R})$ vectors are not available, a view that was subsequently reinforced by

studies of Zhang and Herbert [221], and Winslow *et al.* [188]. It should be noted, however, that recent years have seen the introduction of MECX optimisation techniques in the chemical literature that are based on the GP or LN methods, but which do not require knowledge of, or at least explicit evaluation of, (wavefunction-based) $\mathbf{h}_{IJ}(\mathbf{R})$ vectors [214, 222–225]. Implementation of such approaches in widely used program packages is expected in the near future.

2.3 Density functional theory and its time-dependent extension

2.3.1 Density functional theory

Since the 1980s, density functional theory (DFT) with its competitively high accuracy, yet generally low computational cost, has proven to be a popular alternative to correlated wavefunction methods in tackling the many-electron problem in chemistry [226]. For an N_e-electron system, the many-electron wavefunction is a function of $3N_e$ spatial + N_e spin variables [227]. Because of the wavefunction's dependency on N_e, solving the electronic TISE becomes an exponentially difficult task as the system size (and thus the value of N_e) increases [228]. DFT significantly eases the problem of obtaining solutions to the electronic TISE for medium to large systems, by bypassing the many-electron wavefunction and instead, using the electron density,

$$\rho(\mathbf{r}) = \int \int \cdots \int |\psi_I(\mathbf{r}, \sigma, \boldsymbol{x_2}, \ldots, \boldsymbol{x_N})|^2 d\sigma d\boldsymbol{x_2} \ldots d\boldsymbol{x_N}, \tag{2.51}$$

as its fundamental variable (where $\boldsymbol{x_i} = \mathbf{r}_i + \sigma_i$ is the space-spin coordinate of i^{th} electron) [229]. The complexity of the problem is, in theory, greatly diminished because the electron density, $\rho(\mathbf{r})$, only depends on three Cartesian coordinates [229]. As the switch between wavefunction and electron density is accompanied by no loss of information about the system,[14] DFT is exact in principle.

2.3.1.1 Hohenberg-Kohn theorems

The rigorous mathematical foundation of DFT originates in the Hohenberg-Kohn (HK) existence theorem [1], which proves by a disarmingly simple *reductio ad absurdum* argument that the electron density $\rho(\mathbf{r})$ of a system of interacting electrons determines the external potential, $v_{\text{ext}}(\mathbf{r})$ (usually taken as the electron-nuclear Coulomb attraction), up to an arbitrary additive constant [227]:

$$v_{\text{ext}}[\rho](\mathbf{r}) \xleftrightarrow{\text{Hohenberg-Kohn 1-1 mapping for interacting system}} \rho(\mathbf{r}). \tag{2.52}$$

[14] Considering that the electronic Hamiltonian in Eq. (2.2) is constructed only from one- and two-body operators, it is clear that in fact the wavefunction contains much more information [230] than is needed to compute the electronic energy or any other property of the molecular system.

As the electron number, N_e, is also obtained through quadrature, the electron density uniquely determines the Hamiltonian and thus by extension all the ground-state properties of the system. This allows the ground-state electronic energy to be expressed as a *functional* of the ground-state electron density,

$$E^{\mathrm{el}}[\rho] = \int \rho(\mathbf{r}) v_{\mathrm{ext}}(\mathbf{r}) d\mathbf{r} + F_{\mathrm{HK}}[\rho], \tag{2.53}$$

where $F_{\mathrm{HK}}[\rho]$ is the universal density functional,

$$F_{\mathrm{HK}}[\rho] = T_{\mathrm{e}}[\rho] + V_{\mathrm{ee}}[\rho] = \min_{\psi \to \rho} \langle \psi | \hat{T}_{\mathrm{e}} + \hat{V}_{\mathrm{ee}} | \psi \rangle_{\mathbf{r}}, \tag{2.54}$$

which is independent of $v_{\mathrm{ext}}(\mathbf{r})$ and so is universally valid for describing the electronic kinetic and electron-electron potential interaction energy in *any* system [229].

The second HK theorem [1] introduces a variational principle of the electron density, analogous to that applied in wavefunction methods,[15] which minimises Eq. (2.53) with respect to varying the density, subject to the constraint that the number of electrons, $N_{\mathrm{e}} = \int \rho(\mathbf{r}) d\mathbf{r}$, remains constant. The electronic energy evaluated using a trial density will always be higher than the true energy of the ground-state evaluated with the exact, ground-state density [231],

$$E_0^{\mathrm{el}} \leq E^{\mathrm{el}}[\tilde{\rho}] = F_{\mathrm{HK}}[\tilde{\rho}] + \int \tilde{\rho}(\mathbf{r}) v_{\mathrm{ext}}(\mathbf{r}) d\mathbf{r}. \tag{2.55}$$

Applying the second HK theorem to Eq. (2.53) gives the Euler-Lagrange equation,

$$v_{\mathrm{ext}}(\mathbf{r}) + \frac{\delta F_{\mathrm{HK}}[\rho]}{\delta \rho(\mathbf{r})} - \mu = 0, \tag{2.56}$$

where μ is the chemical potential of the system. Eq. (2.56) is the fundamental equation one tries to solve in DFT and if the exact form of $F_{\mathrm{HK}}[\rho]$ was known then the solution of Eq. (2.56) would yield the exact ground-state density.

2.3.1.2 Kohn-Sham formalism

Approximating $F_{\mathrm{HK}}[\rho]$ (or more specifically $T_{\mathrm{e}}[\rho]$) as an explicit density functional to a sufficiently high accuracy is quite a formidable task. In practice, the framework of DFT used in calculations is that proposed by Kohn and Sham [2], which allows incorporation of orbitals into the DFT formalism [232]. In this formulation, the real system of interacting electrons is mapped onto a fictitious system of non-interacting electrons moving in an effective potential, $v_{\mathrm{s}}(\mathbf{r})$:

$$v_{\mathrm{ext}}[\rho](\mathbf{r}) \xleftarrow[\text{for interacting system}]{\text{Hohenberg-Kohn 1-1 mapping}} \rho(\mathbf{r}) \xleftarrow[\text{for non-interacting system}]{\text{Hohenberg-Kohn 1-1 mapping}} v_{\mathrm{s}}[\rho](\mathbf{r}). \tag{2.57}$$

[15] The Rayleigh-Ritz variational principle, $E_0^{\mathrm{el}} \leq E^{\mathrm{el}}[\tilde{\psi}] = \langle \tilde{\psi} | \hat{H}_{\mathrm{el}} | \tilde{\psi} \rangle_{\mathbf{r}}$, states that the electronic energy calculated with a trial wavefunction can never be lower than the ground-state electronic energy calculated with the exact, ground-state wavefunction.

These non-interacting electrons satisfy the Kohn-Sham (KS) equations,

$$\left[-\frac{1}{2}\nabla_{\mathbf{r}}^2 + v_{\mathrm{s}}(\mathbf{r})\right]\phi_i(\mathbf{r}) = \epsilon_i\phi_i(\mathbf{r}), \tag{2.58}$$

where $\phi_i(\mathbf{r})$ and ϵ_i are the KS orbitals and orbital energies, respectively and

$$\rho(\mathbf{r}) = \sum_i^{N_{\mathrm{e}}} |\phi_i(\mathbf{r})|^2. \tag{2.59}$$

This choice of $v_{\mathrm{s}}(\mathbf{r})$ ensures that the ground-state density of the fictitious, non-interacting system,

$$\begin{aligned} v_{\mathrm{s}}(\mathbf{r}) &= v_{\mathrm{ext}}(\mathbf{r}) + v_{\mathrm{H}}(\mathbf{r}) + v_{\mathrm{xc}}(\mathbf{r}) \\ &= v_{\mathrm{ext}}(\mathbf{r}) + \int \frac{\rho(\mathbf{r}')}{|\mathbf{r}-\mathbf{r}'|}d\mathbf{r}' + \frac{\delta E_{\mathrm{xc}}[\rho]}{\delta\rho(\mathbf{r})}, \end{aligned} \tag{2.60}$$

is exactly the same as the ground-state density of the real, interacting system. We have therefore replaced the complicated many-electron TISE in Eq. (2.3) by a much simpler set of single-particle equations, in which each electron is treated individually, moving in an average field of all other electrons [227, 231, 233]. In KS-DFT Eq. (2.53) can be rewritten as,

$$E^{\mathrm{el}}[\rho] = \int \rho(\mathbf{r})v_{\mathrm{ext}}(\mathbf{r})d\mathbf{r} + T_{\mathrm{s}}[\rho] + J[\rho] + E_{\mathrm{xc}}[\rho], \tag{2.61}$$

where $T_{\mathrm{s}}[\rho]$ is the non-interacting kinetic energy,

$$T_{\mathrm{s}}[\rho] = \sum_i^{N_{\mathrm{e}}} \langle\phi_i| -\frac{1}{2}\nabla_{\mathbf{r}}^2|\phi_i\rangle_{\mathbf{r}}, \tag{2.62}$$

which is an explicit (implicit) functional of the KS orbitals (electron density).[227] $E_{\mathrm{H}}[\rho]$ is the classical Coulomb repulsion (Hartree) energy,

$$E_{\mathrm{H}}[\rho] = \iint \frac{\rho(\mathbf{r})\rho(\mathbf{r}')}{|\mathbf{r}-\mathbf{r}'|}d\mathbf{r}d\mathbf{r}', \tag{2.63}$$

and $E_{\mathrm{xc}}[\rho]$ is the exchange-correlation (xc) energy,

$$E_{\mathrm{xc}}[\rho] = T[\rho] - T_{\mathrm{s}}[\rho] + V_{\mathrm{ee}}[\rho] - E_{\mathrm{H}}[\rho], \tag{2.64}$$

which accounts for the non-classical, purely quantum mechanical nature of electrons not considered in the non-interacting kinetic energy or Hartree energy [227, 232, 234].

2.3.1.3 Jacob's ladder of functionals

All terms in Eq. (2.61) are known exactly, except for $E_{\mathrm{xc}}[\rho]$, which must be approximated. Therefore, DFT is only ever approximate in practice, despite its exact formulation. Numerous

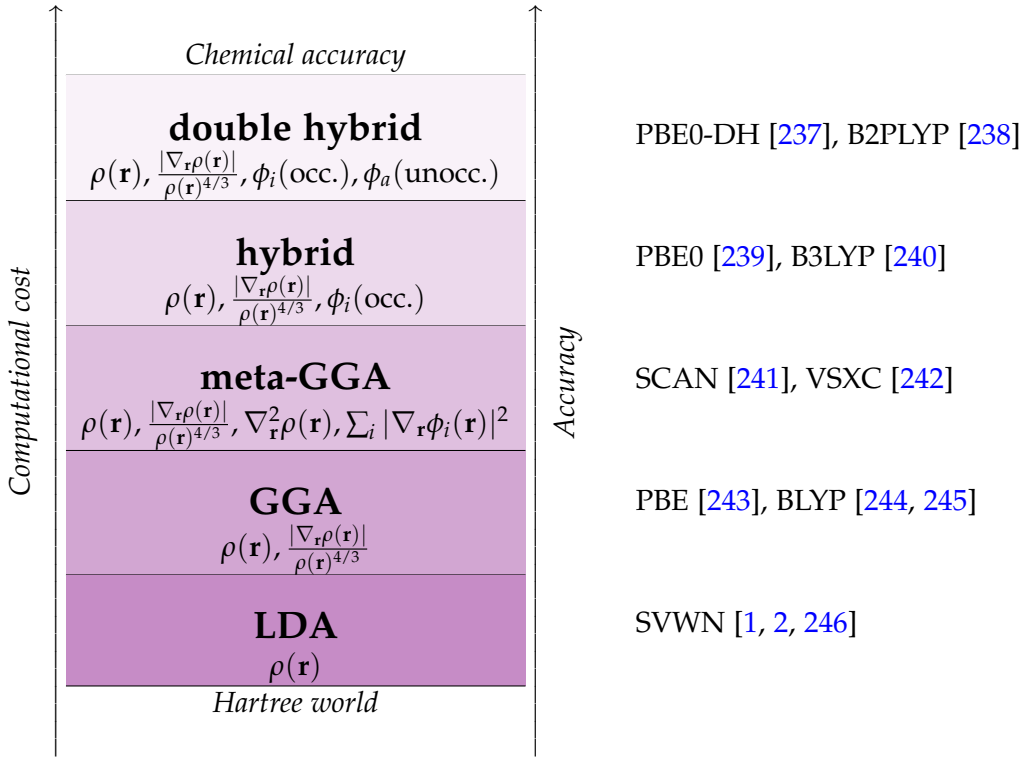

Figure 2.6: Jacob's ladder of DFAs: local density approximation (LDA), generalised gradient approximation (GGA), meta-GGA, (global or range-separated) hybrid GGA, double hybrid GGA [185]. Examples of common DFAs for each rung of the ladder are given on the right; where applicable, the ordering follows non-empirical example first, semi-empirical example second.

density functional approximations (DFAs) [235] to $E_{\text{xc}}[\rho]$ exist, which Perdew has hierarchically organised into the so-called Jacob's ladder (Fig. 2.6) according to the number and complexity of ingredients they depend on [236]. The first two rungs depend explicitly on the density, whereas higher rungs also depend on (KS and/or HF) orbitals [232].

Two philosophies exist to develop DFAs in DFT based either on (a) satisfying as many physical conditions of the exact functional as possible (popular among physicists) or (b) selecting a physically-motivated functional form and optimising its parameters semi-empirically, by minimising the error in a training set relative to experimental thermochemical data (popular among chemists) [247, 248]. Inclusion of more ingredients allows for more exact constraints to be satisfied and greater flexibility, which leads in general to, but does not necessitate in all cases, the DFA possessing a greater overall accuracy [236].

2.3.2 Time-dependent density functional theory

Given the reliance of the HK theorems on a variational principle, KS-DFT is only suitable for studying ground-state properties (or at the very most, properties of the lowest electronic

state of a given space-spin symmetry) [249]. In order to describe excited electronic states, one must employ instead time-dependent density functional theory (TDDFT). In analogy with the static, ground-state case, we circumvent solving the electronic TDSE [31, 232],

$$i\frac{\partial}{\partial t}\psi_I(\mathbf{r},t) = \hat{H}_{\text{el}}(\mathbf{r},t)\psi_I(\mathbf{r},t), \tag{2.65}$$

by swapping the time-dependent many-electron wavefunction $\psi_I(\mathbf{r},t)$ for the time-dependent density $\rho(\mathbf{r},t)$ as the central quantity.

2.3.2.1 Runge-Gross theorems

The formal basis of TDDFT is the Runge-Gross (RG) existence theorem [5], which can be regarded as the time-dependent analogue of the first HK theorem in ground-state DFT. It proves that for a given initial state the time-dependent electron density, $\rho(\mathbf{r},t)$ of a system of interacting electrons determines the time-dependent external potential, $v_{\text{ext}}(\mathbf{r},t)$, up to a spatially constant, time-dependent function,

$$v_{\text{ext}}[\rho;\psi_0](\mathbf{r},t) \xleftrightarrow[\text{for interacting system}]{\text{Runge-Gross 1-1 mapping}} \rho(\mathbf{r},t), \tag{2.66}$$

and thus the time-dependent wavefunction up to a time-dependent phase factor [250, 251]. The proof of the RG existence theorem proceeds in two steps [227]. In the first step, one shows that physically different time-dependent external potentials[16] lead to different time-dependent current densities, $j(\mathbf{r},t)$, infinitesimally later than the initial time, t_0 [249]. This assumes that the external potential is Taylor expandable (time-analytic) about the initial time [232] and makes use of the Heisenberg equations of motion for the time-derivatives of $j(\mathbf{r},t)$ [252]. One uses the continuity equation in the second step to prove that physically different time-dependent electron densities must follow from different time-dependent current densities [227]. This unique 1-1 mapping allows the time-dependent external potential to be expressed as a *functional* of the time-dependent electron density.

Runge and Gross also proposed a time-dependent equivalent of the second (variational) HK theorem [5] by finding the stationary conditions of the Dirac-Frenkel action functional,

$$\mathcal{A}[\rho] = \int_{t_0}^{t_1} \langle\psi(t)|i\frac{\partial}{\partial t} - \hat{H}_{el}(t)|\psi(t)\rangle_{\mathbf{r}}\ dt, \tag{2.67}$$

rather than minimising the electronic energy, which in a time-dependent system is not a conserved quantity [232]. This leads to the following time-dependent Euler-Lagrange equation,

$$\frac{\delta\mathcal{A}[\rho]}{\delta\rho(\mathbf{r},t)} = 0, \tag{2.68}$$

[16] Potentials must differ by more than a time-dependent constant to be physically different. In other words, $v_{\text{ext}}(\mathbf{r},t)$ and $v_{\text{ext}}(\mathbf{r},t)+c(t)$ are not physically different as they lead to wavefunctions that differ only by a time-dependent phase factor, $\exp(-i\alpha(t))$ (where $d\alpha(t)/dt = c(t)$), which cancel out when expectation values of Hermitian operators are taken in calculating observables [227, 252]

which can be solved to obtain the exact time-dependent density. However, this formulation violates the causality principle and in order to remedy this, one must instead use either a Keldysh action [253, 254] or more simply the action of Dirac, Frenkel and Vignale [255].

2.3.2.2 Time-dependent Kohn-Sham formalism

In order to use a scheme analogous to the KS system in ground-state DFT, one needs to generalise the RG theorems. This was achieved in 1998 by the van Leeuwen theorem [256], which states that a time-dependent density $\rho(\mathbf{r},t)$ associated with a many-body system with a given particle-particle interaction $w(\mathbf{r}-\mathbf{r}')$, external potential $v_{\text{ext}}(\mathbf{r})$ and initial state $\psi_0(\mathbf{r})$ can be reproduced by a unique external potential $v'_{\text{ext}}(\mathbf{r})$[17] of a different many-body system with a particle-particle interaction $w'(\mathbf{r}-\mathbf{r}')$ and initial state $\psi'_0(\mathbf{r})$ [227]. This assumes that the external potential (like in the first RG theorem) as well as the densities are Taylor expandable (time-analytic) about the initial time [249].

Two important cases arise from the van Leeuwen theorem: (a) when $w(\mathbf{r}-\mathbf{r}')=w'(\mathbf{r}-\mathbf{r}')$ the two systems are identical and the van Leeuwen theorem reduces to the first RG theorem; (b) when $w'(\mathbf{r}-\mathbf{r}')=0$ the second system is non-interacting [227]. Therefore, the van Leeuwen theorem states that $\rho(\mathbf{r},t)$ of an interacting system with external potential $v_{\text{ext}}(\mathbf{r},t)$ and initial state $\psi_0(\mathbf{r})$ can be exactly reproduced by considering instead a non-interacting system with potential $v_{\text{s}}(\mathbf{r},t)$ and initial state $\Phi_0(\mathbf{r})$:

$$v_{\text{ext}}[\rho;\psi_0](\mathbf{r},t) \xleftrightarrow{\text{Runge-Gross 1-1 mapping for interacting system}} \rho(\mathbf{r},t) \xleftrightarrow{\text{van Leeuwen 1-1 mapping for non-interacting system}} v_{\text{s}}[\rho;\Phi_0](\mathbf{r},t). \tag{2.69}$$

This second case provides a formal justification of the time-dependent KS formalism [257], where the exact time-dependent density is obtained from a non-interacting system of N occupied single-particle orbitals [252],

$$\rho(\mathbf{r},t)=\sum_i^N |\phi_i(\mathbf{r},t)|^2. \tag{2.70}$$

The time-dependent KS orbitals, $\phi_i(\mathbf{r},t)$, obey the time-dependent KS equations,

$$i\frac{\partial}{\partial t}\phi_i(\mathbf{r},t)=\left[-\frac{1}{2}\nabla^2_{\mathbf{r}}+v_{\text{s}}(\mathbf{r},t)\right]\phi_i(\mathbf{r},t), \tag{2.71}$$

where $v_{\text{s}}(\mathbf{r},t)$ is uniquely chosen to reproduce the exact density of the interacting system [250–252]. Here $v_{\text{s}}(\mathbf{r},t)$ is given as,

$$v_{\text{s}}(\mathbf{r},t)=v_{\text{ext}}(\mathbf{r},t)+v_{\text{H}}(\mathbf{r},t)+v_{\text{xc}}(\mathbf{r},t) \tag{2.72}$$

where $v_{\text{H}}(\mathbf{r},t)=\int \frac{\rho(\mathbf{r}',t)}{|\mathbf{r}-\mathbf{r}'|}d\mathbf{r}'$ and $v_{\text{xc}}(\mathbf{r},t)$ are the time-dependent Hartree and xc potentials, respectively.

[17] The potentials $v'_{\text{ext}}(\mathbf{r},t)$ and $v_{\text{ext}}(\mathbf{r},t)$ are physically different, such that $v'_{\text{ext}}(\mathbf{r},t)\neq v_{\text{ext}}(\mathbf{r},t)+c(t)$.

2.3.2.3 Adiabatic approximation of the $v_{\mathbf{xc}}(\mathbf{r},t)$

The exact xc potential formally has a functional dependence on the time-dependent density, the initial many-body state of the interacting system and the initial state of the non-interacting KS system, $v_{\mathrm{xc}}[\rho,\psi_0,\Phi_0](\mathbf{r},t)$ [252, 258, 259]. However, if both the true and KS states are initially in the ground state (which is usually the case) then, by virtue of the HK existence theorem, they are themselves functionals of the initial (ground-state) density and so the xc potential can be written simply as a functional of the density, $v_{\mathrm{xc}}[\rho](\mathbf{r},t)$ [227]. The density dependence of xc potential is nonlocal, in that the xc potential at point in space r at time t, depends on the density at all other points in space r' at all previous times $t' \leq t$ [227]. The functional dependence of the exact xc potential on the whole history of past densities and the initial states ψ_0 and Φ_0 is called memory-dependence [252, 260].

As is the case in ground-state DFT, the exact $v_{\mathrm{ext}}(\mathbf{r},t)$ is unknown in practice and approximations must be employed, the most common of which is the adiabatic approximation (AA) [261]. This involves inserting the instantaneous time-dependent density into a static, ground-state approximation for the xc potential [257],

$$\begin{aligned} v_{\mathrm{xc}}^{\mathrm{AA}}(\mathbf{r},t) =& v_{\mathrm{xc}}^{\mathrm{gs}}[\rho_0](\mathbf{r})\big|_{\rho_0(\mathbf{r})\to\rho(\mathbf{r},t)} \\ =& \left.\frac{\delta E_{\mathrm{xc}}^{\mathrm{gs}}[\rho_0]}{\delta\rho_0(\mathbf{r})}\right|_{\rho_0(\mathbf{r})\to\rho(\mathbf{r},t)} . \end{aligned} \tag{2.73}$$

Therefore, the AA provides a practical way to perform TDDFT, by making use of known DFAs in ground-state DFT to approximate the unknown $v_{\mathrm{xc}}(\mathbf{r},t)$ in TDDFT. As $v_{\mathrm{xc}}^{\mathrm{AA}}(\mathbf{r},t)$ at any time t only depends on the density at that time and not its entire history [251], all memory-dependencies are neglected [252]. Therefore, the AA is a local approximation in time, being exact only for a system that varies infinitely slowly in time and always in its ground-state [251]. This is analogous to the LDA in ground-state DFT, which is a local approximation in space and exact for the uniform electron gas [232].

2.3.3 Linear-response time-dependent density functional theory

2.3.3.1 Linear-response theory

How to access the electronic excited-state energies of a given molecular system still remains to be addressed. One approach, the so-called real-time TDDFT [262, 263], directly solves the time-dependent KS equations and propagates the KS orbitals in time after an initial $\delta-$kick at time t_0, with the result then being Fourier transformed into the frequency domain. Within the chemistry community however, linear-response time-dependent density functional theory (LR-TDDFT) is unquestionably the more popular choice.

Consider a molecular system initially in its ground state with electron density $\rho_0(\mathbf{r})$ and external potential $v_{\mathrm{ext},0}(\mathbf{r})$ [252]. Applying a weak external perturbation $\delta v_{\mathrm{app}}(\mathbf{r},t)$ in-

finitesimally later in time (such that now $v_{\text{ext}}(\mathbf{r},t) = v_{\text{ext},\,0}(\mathbf{r}) + \delta v_{\text{app}}(\mathbf{r},t)$) affords a time dependence in the electron density. Such a time-dependent density can be expanded about the ground-state external potential,

$$\begin{aligned}\rho(\mathbf{r},t)[v_{\text{ext},0}+\delta v_{\text{app}}] &= \rho_0(\mathbf{r}) + \delta\rho(\mathbf{r},t) + \dots \\ &= \rho_0(\mathbf{r})[v_{\text{ext},0}] + \iint \left.\frac{\delta\rho(\mathbf{r},t)[v_{\text{ext}}]}{\delta v_{\text{ext}}(\mathbf{r}',t')}\right|_{v_{\text{ext},0}(\mathbf{r})} \cdot \delta v_{\text{app}}(\mathbf{r}',t')d\mathbf{r}'dt' + \dots .\end{aligned} \tag{2.74}$$

The second term on the right-hand side of Eq. (2.74) is the linear response of the electronic density,

$$\delta\rho(\mathbf{r},t) = \iint \chi(\mathbf{r},t,\mathbf{r}',t')\delta v_{\text{app}}(\mathbf{r}',t')d\mathbf{r}'dt', \tag{2.75}$$

where $\chi(\mathbf{r},t,\mathbf{r}',t')$ is the density-density response function,

$$\chi(\mathbf{r},t,\mathbf{r}',t') = \left.\frac{\delta\rho(\mathbf{r},t)[v_{\text{ext}}]}{\delta v_{\text{ext}}(\mathbf{r}',t')}\right|_{v_{\text{ext},0}(\mathbf{r})}, \tag{2.76}$$

which measures the change in the density to the applied external perturbation [264]. However, in order to retrieve excited electronic energies, one makes use of the Fourier transform of Eq. (2.75) into the frequency domain,

$$\delta\rho(\mathbf{r},\omega) = \int \chi(\mathbf{r},\mathbf{r}',\omega)\delta v_{\text{app}}(\mathbf{r}',\omega)d\mathbf{r}'. \tag{2.77}$$

Then, the density-density response function for finite systems can be written in a Lehmann (spectral) representation [227],

$$\chi(\mathbf{r},\mathbf{r}',\omega) = \lim_{\eta\to 0^+}\sum_{J=1}^{\infty}\left\{\frac{\langle\psi_0|\hat{\rho}(\mathbf{r})|\psi_J\rangle_{\mathbf{r}}\langle\psi_J|\hat{\rho}(\mathbf{r}')|\psi_0\rangle_{\mathbf{r}}}{\omega-(E_J^{\text{el}}-E_0^{\text{el}})+i\eta} + c.c.(-\omega)\right\}, \tag{2.78}$$

where $\hat{\rho}(\mathbf{r}) = \sum_i^{N_e}\delta(\mathbf{r}-\mathbf{r}_i)$ is the density operator, the sum is over all interacting states ψ_J with electronic energy E_J^{el} and the notation $c.c.(-\omega)$ denotes the complex conjugate of the first term evaluated at $-\omega$ [252]. It is clear from Eq. (2.78) that the poles of $\chi(\mathbf{r},t,\mathbf{r}',t')$ occur at the exact excitation energies (i.e $\Omega_J = E_J^{\text{el}} - E_0^{\text{el}}$) of the interacting system [265], whereas its residues give the corresponding oscillator strengths [261].

Within the KS framework, the linear density response in Eq. (2.77) of the real, interacting system can also be reproduced exactly by considering a fictitious, non-interacting system [227],

$$\delta\rho(\mathbf{r},\omega) = \int \chi_{\text{s}}(\mathbf{r},\mathbf{r}',\omega)\delta v_{\text{s}}(\mathbf{r}',\omega)d\mathbf{r}', \tag{2.79}$$

where $\chi_{\text{s}}(\mathbf{r},\mathbf{r}',\omega)$ is the KS density-density response function and $\delta v_{\text{s}}(\mathbf{r}',\omega)$ is the effective KS perturbation [252],

$$\delta v_{\text{s}}(\mathbf{r}',\omega) = \delta v_{\text{ext}}(\mathbf{r}',\omega) + \delta v_{\text{H}}(\mathbf{r}',\omega) + \delta v_{\text{xc}}(\mathbf{r}',\omega). \tag{2.80}$$

The KS density-density response function equally has a Lehmann representation in the frequency domain for finite systems [261],

$$\chi_{\mathrm{s}}(\mathbf{r},\mathbf{r}',\omega) = \lim_{\eta\to 0^+} \sum_{k,j=1}^{\infty} (f_j - f_k)\, \frac{\phi_j^*(\mathbf{r})\phi_k(\mathbf{r})\phi_k^*(\mathbf{r})\phi_j(\mathbf{r})}{\omega - (\epsilon_k - \epsilon_j) + i\eta}, \tag{2.81}$$

where the sum is over ground-state KS orbitals $\phi_j(\mathbf{r})$ with energies ϵ_j and occupations f_j. The KS density-density response function has poles at the KS excitation energies, the differences between occupied and unoccupied ground-state KS orbitals (i.e. $\omega_{jk} = \epsilon_k - \epsilon_j$) [257]. The density-density response function of the interacting system, $\chi(\mathbf{r},\mathbf{r}',\omega)$, can be related to that of the KS non-interacting system, $\chi_{\mathrm{s}}(\mathbf{r},\mathbf{r}',\omega)$ by a Dyson-like equation [251],

$$\chi(\mathbf{r},\mathbf{r}',\omega) = \chi_{\mathrm{s}}(\mathbf{r},\mathbf{r}',\omega) + \iint \chi_{\mathrm{s}}(\mathbf{r},\mathbf{r}'',\omega) f_{\mathrm{Hxc}}(\mathbf{r}'',\mathbf{r}''',\omega)\chi(\mathbf{r}''',\mathbf{r}',\omega) d\mathbf{r}'' d\mathbf{r}''', \tag{2.82}$$

where the inverse of these two quantities can also be related by [252],

$$\chi^{-1}(\mathbf{r},\mathbf{r}',\omega) = \chi_{\mathrm{s}}^{-1}(\mathbf{r},\mathbf{r}',\omega) - f_{\mathrm{Hxc}}(\mathbf{r},\mathbf{r}',\omega). \tag{2.83}$$

Here $f_{\mathrm{Hxc}}(\mathbf{r},\mathbf{r}',\omega)$ is the Hartree-exchange-correlation (Hxc) kernel,

$$\begin{aligned} f_{\mathrm{Hxc}}(\mathbf{r},\mathbf{r}',\omega) =& f_{\mathrm{H}}(\mathbf{r},\mathbf{r}') + f_{\mathrm{xc}}(\mathbf{r},\mathbf{r}',\omega) \\ =& \frac{1}{|\mathbf{r}-\mathbf{r}'|} + \left.\frac{\delta v_{\mathrm{xc}}[\rho](\mathbf{r},t)}{\delta\rho(\mathbf{r}',t')}\right|_{\rho_0(\mathbf{r})}. \end{aligned} \tag{2.84}$$

Solving Eq. (2.82) and obtaining the exact, interacting $\chi(\mathbf{r},\mathbf{r}',\omega)$ from the non-interacting $\chi_{\mathrm{s}}(\mathbf{r},\mathbf{r}',\omega)$ is the central task in LR-TDDFT.

2.3.3.2 Casida formalism

Despite, the fundamental importance of Eq. (2.82), it is only ever solved directly for extended systems, such as solids [252]. For atoms and molecules [261], a matrix formulation expanded in a basis of KS single-electron transitions is used, which involves solving a set of non-Hermitian pseudo-eigenvalue equations, known as the Casida equation [6, 266],

$$\begin{bmatrix} \mathbb{A}(\omega) & \mathbb{B}(\omega) \\ \mathbb{B}^*(\omega) & \mathbb{A}^*(\omega) \end{bmatrix} \begin{bmatrix} \boldsymbol{X}(\omega) \\ \boldsymbol{Y}(\omega) \end{bmatrix} = \omega \begin{bmatrix} \mathbb{1} & 0 \\ 0 & -\mathbb{1} \end{bmatrix} \begin{bmatrix} \boldsymbol{X}(\omega) \\ \boldsymbol{Y}(\omega) \end{bmatrix}, \tag{2.85}$$

where the eigenvalues ω $(-\omega)$ are the excitation (de-excitation) energies [266] and the eigenvectors $\boldsymbol{X}(\omega)$ $(\boldsymbol{Y}(\omega))$ are the transition amplitudes for excitations (de-excitations) corresponding to the related oscillator strengths.[18] The matrix elements of $\mathbb{A}(\omega)$ and $\mathbb{B}(\omega)$ are

[18] Note, solving the Casida equation (Eq. (2.85)) for its eigenvalues and eigenvectors is just a reformulation of generating the poles and residues of the density-density response function (Eq. (2.78)); both cases give the excitation energies and oscillator strengths, respectively.

given as,

$$A_{ia,jb} = \delta_{ij}\delta_{ab}(\epsilon_a - \epsilon_i) + (ia|jb) + (ia|f_{xc}(\omega)|jb), \tag{2.86}$$

$$B_{ia,jb} = (ia|bj) + (ia|f_{xc}(\omega)|bj), \tag{2.87}$$

where the two-electron integrals are represented in Mulliken notation,

$$(pq|rs) = \iint \phi_p^*(\mathbf{r})\phi_q(\mathbf{r})\frac{1}{|\mathbf{r}-\mathbf{r}'|}\phi_r^*(\mathbf{r}')\phi_s(\mathbf{r}')d\mathbf{r}d\mathbf{r}', \tag{2.88}$$

$$(pq|f_{xc}(\omega)|rs) = \iint \phi_p^*(\mathbf{r})\phi_q(\mathbf{r})f_{xc}(\mathbf{r},\mathbf{r}',\omega)\phi_r^*(\mathbf{r}')\phi_s(\mathbf{r}')d\mathbf{r}d\mathbf{r}'. \tag{2.89}$$

The labels i, j and a, b denote occupied and virtual KS orbitals, respectively, whereas p, q denote any arbitrary KS orbitals. Physically, matrix elements $A_{ia,jb}$ couple a one-electron excitation ($i \rightarrow a$) to another one-electron excitation ($j \rightarrow b$), whereas matrix elements $B_{ia,jb}$ couple a one-electron excitation ($i \rightarrow a$) to a one-electron de-excitation ($j \leftarrow b$) [8, 267].

2.3.3.3 Adiabatic approximation of the $f_{\mathbf{xc}}(\mathbf{r},\mathbf{r}',\omega)$

The exact xc kernel is non-local both in space and in time, $f_{\text{xc}}(\mathbf{r},t,\mathbf{r}',t')$ [251]. The non-locality in time (i.e. memory dependence) manifests as a frequency dependence in the frequency domain, $f_{\text{xc}}(\mathbf{r},\mathbf{r}',\omega)$ [251]. However, as discussed in Section 3.2.3, for most practical applications of LR-TDDFT the AA is invoked. A consequence of using the AA for $v_{\text{xc}}(\mathbf{r},t)$ is that the $f_{\text{xc}}(\mathbf{r},t,\mathbf{r}',t')$ becomes proportional to $\delta(t-t')$ [252], i.e.

$$f_{\text{xc}}^{\text{AA}}(\mathbf{r},t,\mathbf{r}',t') = \delta(t-t')\frac{\delta^2 E_{\text{xc}}^{\text{gs}}[\rho_0]}{\delta\rho_0(\mathbf{r})\delta\rho_0(\mathbf{r}')}\bigg|_{\rho_0(\mathbf{r})\rightarrow\rho(\mathbf{r},t)}, \tag{2.90}$$

which when Fourier transformed to the frequency domain means that the xc kernel loses its frequency dependence, $f_{\text{xc}}^{\text{AA}}(\mathbf{r},\mathbf{r}',\omega) = f_{\text{xc}}(\mathbf{r},\mathbf{r}')$ [261]. Compare this to the Hartree kernal, which is non-local in space, yet local in time and so has no frequency dependence, $f_{\text{H}}(\mathbf{r},\mathbf{r}')$; the Hartree kernel is described exactly in the AA [227]. The implications of the frequency dependence of the exact $f_{\text{xc}}(\mathbf{r},\mathbf{r}',\omega)$ and the loss of its frequency dependence in the AA (within the context of the Casida equations) [8] is of key importance to the subject of this thesis and will make up a large portion of Section 2.4.

2.3.3.4 Tamm-Dancoff approximation

In 1999, Hirata and Head-Gordon introduced the Tamm-Dancoff approximation (TDA) to LR-TDDFT [268], which involves setting $\mathbb{B}$ in Eq. (2.85) to zero, after applying the AA. This leads to the following Hermitian eigenvalue equation [227],

$$\mathbb{A}\boldsymbol{X} = \omega\boldsymbol{X}, \tag{2.91}$$

which is computationally somewhat simpler to solve than Casida's full LR-TDDFT equation [266]. Physically, the TDA neglects the coupling between excitations and de-excitations. In doing so, it decouples the calculation of the LR-TDDFT excitation energies from any ground-state stability problems that can arise due to the use of approximate $v_{\text{xc}}(\mathbf{r})$ functionals [269]. Therefore, the advantage of the TDA is that it can be used to rectify (or at least diminish) problems in LR-TDDFT with triplet and near-singlet instabilities, where in both cases excitation energies can erroneously appear imaginary [232, 266]. This is particularly important in obtaining accurate excited state PESs in LR-TDDFT [270]. However, the downside of the TDA is that it does not satisfy the Thomas-Reine-Kuhn f-sum rule for oscillator strengths, which leads to possible issues with the accurate prediction of absorption spectra [271, 272].

2.4 Limitations of practical LR-TDDFT

In the exact limit, an LR-TDDFT calculation involves the following two steps:

(1) A ground-state DFT calculation using the exact $v_{\text{xc}}(\mathbf{r})$ is performed to compute the energy differences between occupied and virtual KS orbitals. The KS orbital energy differences act as zeroth-order approximations to optical excitations [251].

(2) A LR-TDDFT calculation on the ground-state KS orbitals is then performed, which involves solving the exact (frequency-dependent) form of Eq. (2.85) [251]. This corrects the bare KS orbital energy differences towards the true excitation energies [264], by the exact (frequency-dependent) $f_{\text{Hxc}}(\mathbf{r}, \mathbf{r}', \omega)$ shifting the individual KS single excitations and the mixing of different excitations upon diagonalisation of the Casida matrix [273].

However, when LR-TDDFT is carried out in practice a source of error arises in both of these steps. In (1) a ground-state approximation to $v_{\text{xc}}(\mathbf{r})$ must be used [252] and in (2) one must employ the AA, which neglects the memory dependence in the xc kernel, making it frequency independent [252]. Therefore, as Casida succinctly put it in his 2012 review [232, 274],

> *"conventional LR-TDDFT only works best for (a) low energy, (b) one-electron excitations involving (c) little or no charge-transfer and (d) that are not too delocalised."*

This translates to AA LR-TDDFT experiencing problems with describing Rydberg and charge-transfer excitations, excited states dominated by double (or multiple) excitations, as well as excitations that lead to ionisation. The case of double (and multiple) excitations will now be addressed given its pertinence to the problem of ground-to-excited state CXs in AA LR-TDDFT, a discussion of which follows in Section 2.4.2.

2.4.1 Double (and multiple) excitations

An accurate description of double (and multiple) excitations is crucial not only in the context of single-point excitation energies, but also when describing ground-to-excited CXs. In this subsection, we focus on the former case and leave the latter to be discussed fully in Section 2.4.2. Notably, double excitations are required to describe the low-lying excitation energies of (long-chain) polyenes [264], i.e., the first singlet excited state of butadiene possesses predominant double excitation character [266, 275, 276]. Furthermore, multiple excitations are essential for accurately describing excitations of molecules with unpaired electrons in their ground state [266]. Not including double (or multiple) excitations in either case can result in spurious states making state assignments problematic [267].

But what is meant by double excitation? In a non-interacting system (i.e. a KS system), a double excitations refers to the promotion of two electrons from occupied orbitals in the ground-state to two virtual orbitals generating a "doubly-excited" Slater determinant [264, 276]. Thus, in the non-interacting picture, "double excitation" is shorthand for a state of *pure* double excitation character. In an interacting system, the true electronic states, ψ_I, can be expanded as a linear combination of Slater determinants with single, double, triple and any other multiple excitation character [276],

$$|\psi_I\rangle = C_0^I|\Phi_0\rangle + \sum_S C_S^I|\Phi_S\rangle + \sum_D C_D^I|\Phi_D\rangle + \sum_T C_T^I|\Phi_T\rangle + \dots \tag{2.92}$$

where $S = (i \to a)$ represents all single excitations out of the KS ground-state determinant, Φ_0, $D = (i \to a, j \to b)$ represents all double excitations and $T = (i \to a, j \to b, k \to c)$ represents all triple excitations, etc. [261] Therefore, in the interacting picture, "double excitation" is shorthand for a state of *significant* double excitation character, i.e. one where the third term in Eq. (2.92) dominates the expansion [264].

Recalling Subsection 3.3.1, the poles of $\chi_s(\mathbf{r}, \mathbf{r}', \omega)$ occur at the KS single excitations [250], whereas $\chi(\mathbf{r}, \mathbf{r}', \omega)$ possesses poles at the exact excitation energies, so included not only single excitations, but double and multiple excitations as well. Therefore, it is easy to see that $\chi_s(\mathbf{r}, \mathbf{r}', \omega)$ has fewer poles than $\chi(\mathbf{r}, \mathbf{r}', \omega)$ [261]. To understand why, consider $\chi_s(\mathbf{r}, \mathbf{r}', \omega)$ in the form of Eq. (2.78), where the numerator instead contains KS Slater determinants, i.e. $\langle\Phi_0|\hat{\rho}(\mathbf{r})|\Phi_J\rangle_\mathbf{r}$ [252]. Due to its one-body nature [264], matrix elements of the density operator, $\hat{\rho}(\mathbf{r})$, disappear if the excited determinant, Φ_J, differs from the ground-state determinant, Φ_0, by more than one orbital [250]. As a result, doubly-excited KS states make a null contribution to $\chi_s(\mathbf{r}, \mathbf{r}', \omega)$ [252]. This relates physically to needing two photons to excite two electrons in a non-interacting system, a process that is beyond linear response [252]. On the other hand, $\chi(\mathbf{r}, \mathbf{r}', \omega)$ is able to retain poles at the exact excitation energies because its numerator $\langle\psi_0|\hat{\rho}(\mathbf{r})|\psi_J\rangle_\mathbf{r}$ remains finite from contributions between components of the two many-body wavefunctions, ψ_0 and ψ_J, that differ by only one orbital [252].

Given LR-TDDFT is formally exact, it should be expected that all of the excitations of the exact, interacting system (i.e. single and multiple) should be described when the Casida equation is solved, however this is not the case when the AA is invoked. Double and higher-electron-number excitations are missing in the AA and so states with significant double-excitation character are either poorly described, or are missing completely [277]. As discussed in Subsection 3.3.4, within the AA the xc kernel loses its frequency dependence, rendering the $\mathbb{A}$ and $\mathbb{B}$ matrices in Eq. (2.85) also frequency-independent [266]. Therefore, the Casida equation becomes a linear pseudo-eigenvalue problem, restricting the number of its solutions to the dimensionality of the Casida matrix [232], i.e., the number of single (de)excitations, albeit "dressed" to include some correlation effects that can implicitly treat multiple excitations [278, 279]. In other words, a frequency-independent xc kernel can not change the number of poles, it can only shift them [257].

The exact xc kernel is frequency-dependent, which gives rise to a frequency dependence in the $\mathbb{A}$ and $\mathbb{B}$ matrices of the exact Casida equation. As a result, the Casida equation is formally a non-linear pseudo-eigenvalue equation [227], where the number of its solutions exceeds the dimensionality of the matrix problem [232]. In this way, the frequency-dependent $f_{\text{xc}}(\mathbf{r}, \mathbf{r}', \omega)$ generates new, additional solutions to the Casida equation, i.e. the double and multiple excitations missed in the AA [261, 266]. But how exactly does the frequency dependence of $f_{\text{xc}}(\mathbf{r}, \mathbf{r}', \omega)$ generate extra solutions to the Casida equation (or equally extra poles in the density-density response function)? Let us consider a $(c \times c)$ linear eigenvalue problem [280],

$$\boldsymbol{A}\boldsymbol{X} = \omega \boldsymbol{X}, \tag{2.93}$$

where $\boldsymbol{A}$ is a $(c \times c)$ matrix associated with all the (single and multiple) excitations of a given molecular system [280]. We can recast this matrix equation into two smaller coupled matrix equations [281],

$$\begin{bmatrix} \boldsymbol{A}_{S,S} & \boldsymbol{A}_{S,M} \\ \boldsymbol{A}_{S,M} & \boldsymbol{A}_{M,M} \end{bmatrix} \begin{bmatrix} \boldsymbol{X}_S \\ \boldsymbol{X}_M \end{bmatrix} = \omega \begin{bmatrix} \boldsymbol{X}_S \\ \boldsymbol{X}_M \end{bmatrix}, \tag{2.94}$$

where $\boldsymbol{A}_{S,S}$ is an $(a \times a)$ matrix associated with single excitations and $\boldsymbol{A}_{M,M}$ is a $(b \times b)$ matrix associated with multiple excitations (where $a + b = c$); $\boldsymbol{A}_{S,M}$ and $\boldsymbol{A}_{M,S}$ are the couplings between the single and multiple excitations [249, 277, 280]. Applying the standard Löwdin partitioning technique to Eq. (2.94) yields [249],

$$\tilde{\boldsymbol{A}}_S(\omega)\boldsymbol{X}_S = \omega \boldsymbol{X}_S, \tag{2.95}$$

where,

$$\tilde{\boldsymbol{A}}_S(\omega) = \underbrace{\boldsymbol{A}_{S,S}}_{\text{single excitations}} + \underbrace{\boldsymbol{A}_{S,M}\left[\omega \mathbb{I}_{M,M} - \boldsymbol{A}_{M,M}\right]^{-1} \boldsymbol{A}_{M,S}}_{\text{multiple excitations}}. \tag{2.96}$$

The resulting expression in Eq. (2.95) is now effectively an $(a \times a)$ non-linear eigenvalue equation, which possesses by construction exactly the same number of solutions as the $(c \times c)$

linear eigenvalue problem in Eq. (2.93), but at a lower dimension [280]. This is achieved by converting spatial degrees of freedom into a frequency dependence in $\tilde{A}_S(\omega)$ given in Eq. (2.96) [277]. As such, $\tilde{A}_S(\omega)$, which is built in a basis of single-excitations, has "folded" in it all the information from the multiple excitations [280]. Considering again LR-TDDFT within the AA, it is clear that losing the frequency dependence in the $\mathbb{A}$ (and $\mathbb{B}$) matrices in the Casida equation (i.e. analgous to neglecting the second term in Eq. (2.96)) prevents double or higher-electron-number excitations from appearing [280].

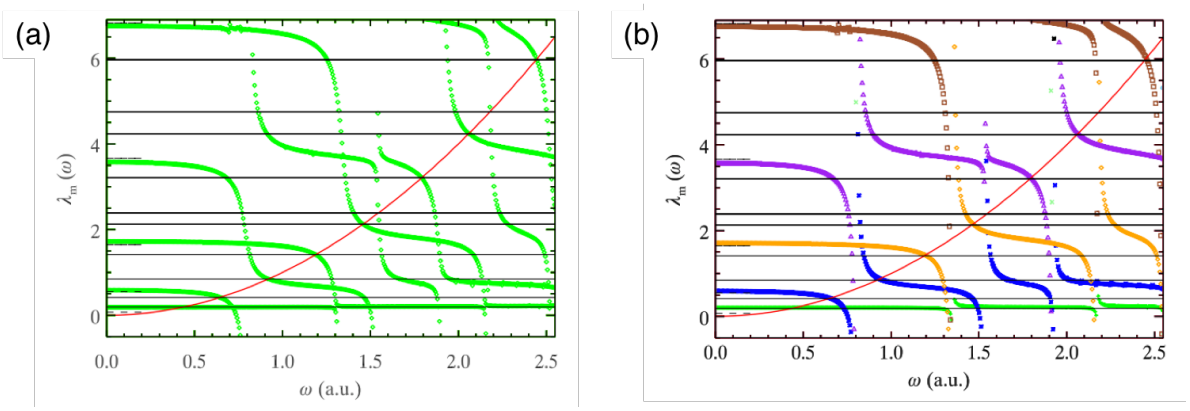

Figure 2.7: Graphical representation of how the frequency dependence of the exact exchange-correlation kernel gives rise to the exact excitation energies of the interacting system from fewer orbital energy differences of the non-interacting system. **(a)** Lowest 10 excitation energies, $\lambda_m(\omega)$ [green], for the A6-Hooke atom obtained using the numerically exact, frequency dependent $f_{\mathrm{Hxc}}(\omega)$, plotted as a function of frequency, ω. **(b)** Same as left plot, except showing the SPA solutions instead: $\lambda_1(\omega)$ [green] follows from λ_1^{AE}; $\lambda_2(\omega)$ and $\lambda_3(\omega)$ [blue] follow from the divergence of λ_2^{AE}; $\lambda_4(\omega)$ and $\lambda_5(\omega)$ [orange] follow from the divergence of λ_3^{AE}; $\lambda_7(\omega)$ and $\lambda_8(\omega)$ [purple] follow from the divergence of λ_4^{AE}; $\lambda_{10}(\omega)$ [brown] follows from λ_5^{AE}; $\lambda_6(\omega)$ and $\lambda_9(\omega)$ follow from two coincident diverging λ_m^{AE} solutions. For further details see main text. Adapted from Ref. [151]. Copyright 2014 American Physical Society.

In 2014, Thiele and Kümmel showed graphically how the frequency dependence of $f_{\mathrm{xc}}(\mathbf{r},\mathbf{r}',\omega)$ (for an exactly solvable case) can generate all the poles in $\chi(\mathbf{r},\mathbf{r}',\omega)$ from the limited number of poles of $\chi_{\mathrm{s}}(\mathbf{r},\mathbf{r}',\omega)$. They reconstructed $\chi(\mathbf{r},\mathbf{r}',\omega)$ and $\chi_{\mathrm{s}}(\mathbf{r},\mathbf{r}',\omega)$ for the A6-Hooke[19] atom and used their inverse to derive a numerically exact form of $f_{\mathrm{xc}}(\mathbf{r},\mathbf{r}',\omega)$ [282]. Fig. 2.7 plots, as a function of the frequency ω, the lowest 10 excitation energies, $\lambda_m(\omega)$, that are obtained as solutions of the Casida equation using the numerically reconstructed $f_{\mathrm{xc}}(\mathbf{r},\mathbf{r}',\omega)$ and an adiabatically exact (AE)[20] ground-state $v_{\mathrm{xc}}(\mathbf{r})$ [282]. Fig. 2.7(a) shows the eigenvalues of the full Casida equation (green diamond), whereas Fig. 2.7(b) shows

[19] A6-Hooke is shorthand for the two-electron, one-dimensional anharmonic Hooke's atom.

[20] The adiabatically exact limit equates to using the exact ground-state $v_{\mathrm{xc}}(\mathbf{r})$ within AA LR-TDDFT. AE excitation energies are denoted λ_m^{AE} [250].

the eigenvalues obtained using the single-pole approximation (SPA)[21] (coloured markers) [282]. The system's lowest 10 excitation energies are found as the intersections between the $\lambda_m(\omega)$ curves and the solid red ω^2 parabola [282]. Included for comparison are analytically exact (solid horizontal lines) and bare KS (short dashed horizontal lines) excitation energies. Two observations can be made from Fig. 2.7: in (a) the intersections of $\lambda_m(\omega)$ and the ω^2 parabola coincide with the analytically exact excitation energies [282] and in (b) each of the 10 exact solutions can be traced back to the five bare KS excitations, using the coloured curves, (See Fig. 2.7 caption for details) [282]. By constructing Fig. 2.7, Thiele and Kümmel visually revealed the mechanism of exact TDDFT [282]:

> "(i) *In the AE limit the Casida matrix shifts and mixes the KS transitions,* (ii) *the frequency dependent main diagonal (which is used in the SPA) generates the necessary poles, and* (iii) *the off-diagonal elements bend and fuse the divergences to remove spurious solutions and correct the remaining ones.*"

Several methods [277, 281, 283–288] have been proposed to go beyond the AA within LR-TDDFT in order to directly incorporate contributions from double excitations. All come under the umbrella of Dressed TDDFT and show varying degrees of practical success [232] and general applicability [257].

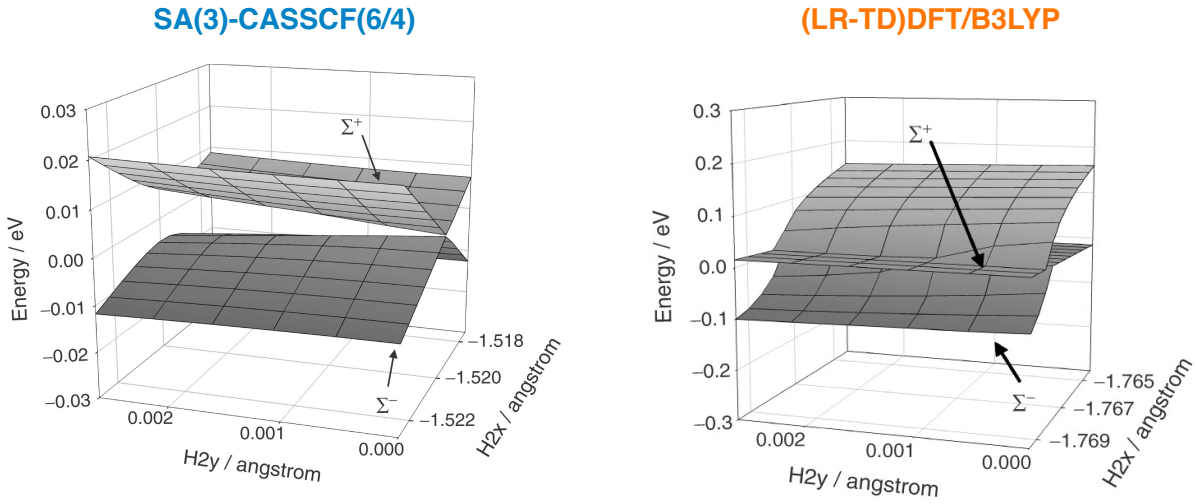

Figure 2.8: Branching space of the S_1/S_0 MECX (or MECP) in linear H_2O. Comparison of the S_0 and S_1 PESs obtained with SA(3)-CASSCF(6/4)/6-31G **(left)** and (LR-TD)DFT/B3LYP/6-31G **(right)**. Adapted from Ref. [10]. Copyright 2006 Taylor & Francis.

2.4.2 Description of ground-to-excited state CXs

The inaccurate description of PESs in the vicinity of CXs involving the ground electronic state is, by now, a well-reported deficiency of LR-TDDFT within the AA. The first investigation to highlight this problem was that of Levine *et al.* [27], where for linear H_2O (Fig. 2.8) the dimensionality of the intersection was shown to be $F-1$ rather than $F-2$ (i.e., incorrect topology), whilst for H_3 (Fig. 2.9) the shape of the first excited-state PES was shown to vary too rapidly near the intersection point (i.e., incorrect topography), despite the CX possessing the correct dimensionality. Tapavicza *et al.* [28] subsequently showed that applying the TDA not only helps to reduce excited-state instability problems, but also gives an approximate S_1/S_0 CX for oxirane (Fig. 2.10) with a slightly interpenetrating double cone. Further studies have provided additional examples of the issues of AA LR-TDDFT in describing CXs between the ground and first excited electronic states, e.g., see Refs. [94, 166, 289–291]. We note, however, that AA LR-TDDFT has been shown to predict reasonably accurate S_1/S_0 CX geometries and branching planes, despite issues with the PESs [27, 292].

A common starting point for analysing the deficiencies of AA LR-TDDFT is to consider the description of CXs involving the ground electronic state within the alternative (wavefunction) approach of configuration interaction singles (CIS). Like AA LR-TDDFT, CIS (i) uses a single Slater determinant as its reference and (ii) comprises a set of linear equations restricted to a single-excitation subspace. Hamiltonian matrix elements between the Hartree-Fock (HF) ground state and singly-excited Slater determinants are zero by virtue of Brillouin's theorem [172], meaning there is no coupling between ground and excited states in CIS. It follows that one of the two conditions for electronic degeneracy [100, 293] at a CX is satisfied trivially and the derivative coupling vector, $\mathbf{h}_{01}(\mathbf{R})$, is zero (either within just the seam space, or for any nuclear configuration, depending on how the derivative coupling vector is defined [100].) As a result, CIS exhibits a linear $(F-1)$-dimensional intersection (as opposed to a conical $(F-2)$-dimensional intersection), where the degeneracy is only lifted along one (not both) branching space vector direction(s) [27, 28]. Given the CIS excited state and HF reference state do not 'see each other' due to the lack of coupling [28], their corresponding PESs cross each other within the branching space, leading to regions where the CIS excited state becomes lower in energy than the HF reference state (i.e., one observes negative excitation energies). The HF reference state struggles to reproduce the necessary rapid change in electronic character near the CX [27].

Despite the similarity between the approaches, these CIS arguments cannot be used to explain why AA LR-TDDFT fails to correctly describe CXs between the ground and excited electronic states. This is because Brillouin's theorem does *not* hold within (LR-TD)DFT [28, 257, 294] because the method does not provide formal access to wavefunctions

[21] The SPA involves expanding the Casida equation around each individual KS transition frequency, or equivalently neglecting the off-diagonal terms in the Casida matrix [283].

(only electron densities). The Kohn-Sham (KS) determinant is the wavefunction of the non-interacting system, not the interacting system. Similarly, while excited-state wavefunctions can be reconstructed using excited Kohn-Sham determinants (for electronic state assignment purposes–see Ref. [6]), they do not correspond to excited-state wavefunctions of the interacting system. The situation is reminiscent of the calculation of $\langle S^2 \rangle$ / spin contamination in DFT, whereby the usual single determinant expression is not appropriate for the interacting system [295, 296]. In spite of the absence of Brillouin's theorem, it is still argued [86, 249, 297–299] that there is no coupling between the ground and excited states in AA LR-TDDFT and so the method is expected to exhibit *similar* CX problems to CIS. This lack of coupling in LR-TDDFT is a consequence of using the adiabatic approximation, as well as the ground-state exchange-correlation functional approximation. Within AA LR-TDDFT, the ground (reference) state is variationally obtained within an initial DFT calculation, separate to the singly-excited (response) states, which are obtained when the Casida equation is solved (i.e., $E_J(\boldsymbol{R}) = E_0(\boldsymbol{R}) + \omega_J(\boldsymbol{R})$, where $\omega_J(\boldsymbol{R})$ is the J^{th} vertical excitation energy) [299], The ground and excited states are therefore not treated on an equal footing, and so the coupling between them is absent. We note, this is the same reason why ADC(2) struggles to accurately predict CXs involving the ground state–the ground state is obtained at the MP2 level of theory, whereas the excited states are obtained with ADC(2) [96].

Many attempts have been made to fix (or, at least, circumvent) the incorrect description of CXs involving the ground electronic state within AA LR-TDDFT; these approaches can be broadly divided into two categories: (i) those that artificially expand the dimension of the LR-TDDFT(/TDA) problem to introduce coupling between the ground and excited states

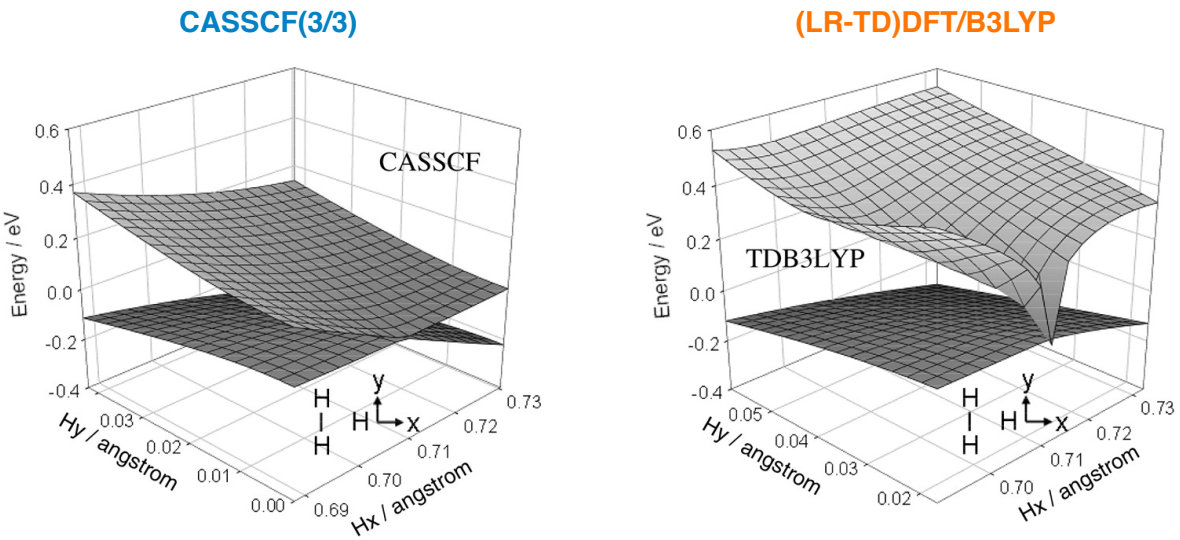

Figure 2.9: Branching space of the D_1/D_0 MECX (or MECP) in equilateral H_3. Comparison of the D_0 and D_1 obtained with CASSCF(3/3)/6-31G **(left)** and (LR-TD)DFT/B3LYP/6-31G **(right)**. Adapted from Ref. [10]. Copyright 2006 Taylor & Francis.

and (ii) those rooted solely within the formal linear response framework of TDDFT. For the first category, methods either incorporate explicit double excitations [249, 300, 301] (since these introduce coupling between the ground and excited states within a configuration interaction picture, improving upon CIS), or include direct coupling between the reference KS determinant and (at least one) singly-excited determinant(s) [298, 302–305]. Some fulfil this goal by using DFT quantities in a larger CI-type matrix, interpreting Slater determinants constructed from KS orbitals as approximations to the real, interacting wavefunctions [300–303], whilst others add selected excited contributions to the AA LR-TDDFT/TDA matrix equations from those derived within many-body perturbation theory [249]. The second category of methods instead comprise different variants of standard LR-TDDFT; they generate, via a modified linear response formalism, the ground and excited states of interest *together* as response states from a sacrificial reference state [100, 270, 299, 306] while still preserving the AA. These methods include (mixed-reference) [307–309] spin-flip TDDFT [310–312], particle-particle RPA(/TDA)[22] [297, 313–315] and hole-hole TDA [316, 317] and, in all cases, the resulting ground and excited states are treated on the same footing.

The aforementioned approaches are pragmatic. However, the ultimate goal within conventional LR-TDDFT is to rigorously go beyond the AA by using a frequency-dependent exchange-correlation kernel. In the exact case, the LR-TDDFT matrix problem represents a set of non-linear equations[23] that, despite being built in a basis of single excitations, have

[22] RPA denotes random-phase approximation.

[23] We note, this is in contrast to the situation in CIS, where the equations are always linear and only ever approximate (i.e., the exact case would be full CI). Even within the AA, where now the LR-TDDFT equations are indeed linear, the response matrix elements in AA LR-TDDFT(/TDA) differ from that in CIS (Ref. [231]), where the former depends on the response of the multiplicative exchange-correlation potential, whereas the latter

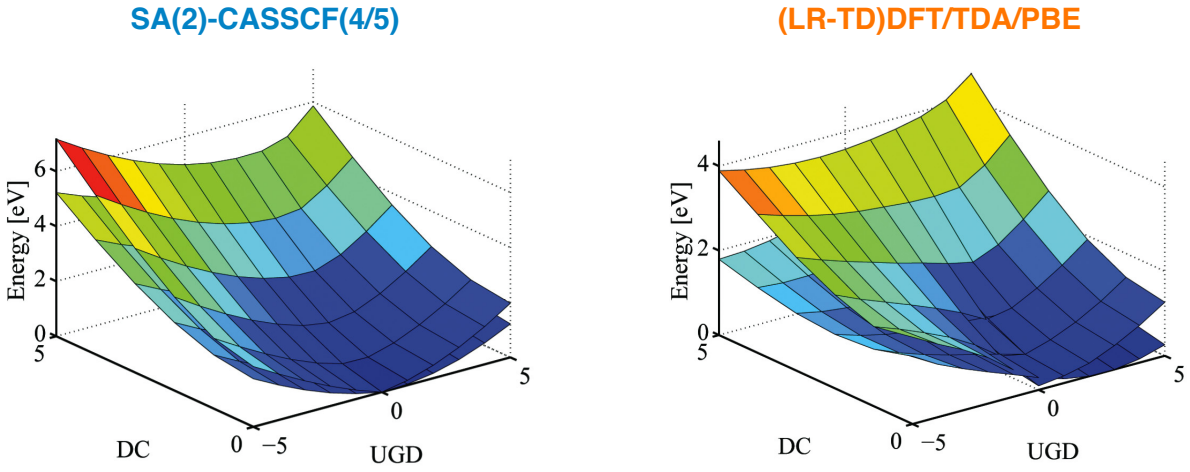

Figure 2.10: Branching space of the S_1/S_0 MECX (or MECP) in oxirane. Comparison of the S_0 and S_1 PESs obtained with SA-2-CASSCF(4/5)/6-311G** **(left)** and (LR-TD)DFT/TDA/PBE/aug-cc-pVTZ **(right)**. Adapted from Ref. [11]. Copyright the Owner Societies 2010.

folded in all the information from double and higher (de-)excitations thanks to the frequency dependence of the exact exchange-correlation kernel [249, 277, 280]. It could be argued (i.e., along similar lines to comments made by Huix-Rottlant and Casida in Ref. [249]) that a combination of these single, double and higher (de-)excitations from the DFT reference state (i.e., a single KS determinant) could lead to the true correlated ground state being reproduced in the linear-response excitation manifold along with the (similarly correlated) excited states [318, 319]. The ground and excited electronic states would then, therefore, be treated on an equal footing, establishing the required coupling between them.

depends on the response of the non-multiplicative HF exchange potential.

CHAPTER 3

On the location, topology and topography of conical intersections with AA LR-TDDFT

This chapter is primarily based on the publication:
J. T. Taylor, D. J. Tozer and B. F. E. Curchod, "On the description of conical intersections between excited electronic states with LR-TDDFT and ADC(2)", *The Journal of Chemical Physics*, 2023, **159**, 214115. (Ref. [29])

3.1 Introduction

As discussed in the previous chapter, the ability of AA LR-TDDFT(/TDA) to describe CXs involving the ground electronic state has been well-documented. Much less attention [27, 320, 321], however, has been paid to the precise quality of AA LR-TDDFT(/TDA) in describing CXs between excited electronic states. This lack of attention arguably stems from the fact that excited states are obtained together when one solves the Casida equation and thus, provided they are dominated by single-excitation character, excited states are treated on an equal footing in AA LR-TDDFT(/TDA) and coupling between them is indeed present, in contrast to the case of ground-to-excited state CXs. As a result, the aptitude of AA LR-TDDFT(/TDA) to correctly predict the topology and topography of CXs between excited electronic states is often taken for granted, even if little (in the way of explicit plotting of excited-to-excited state CX branching spaces) is known about the performance of the method in this context.[1] We note that the same also applies to excited electronic states obtained with

[1]It should be noted that Levine *et al.* [27] did provide a very brief discussion about the description of CXs between excited states with AA LR-TDDFT for molecules, such as malonaldehyde and benzene, within their seminal work. However, no explicit branching space plots were presented. Further discussion has also been reported in the context of density functional tight-binding [321] and LR-TDDFT(/TDA) within continuum solvation models [320].

ADC(2).

One aspect, in particular, that requires close attention when discussing CXs between excited electronic states with AA LR-TDDFT(/TDA) is the description of the branching space vectors. In LR-TDDFT(/TDA) nuclear gradients are readily available, allowing easy access to the gradient difference vector, $\mathbf{g}_{IJ}(\mathbf{R})$. Computing the derivative coupling vector, $\mathbf{h}_{IJ}(\mathbf{R})$, and the related (first-order) nonadiabatic coupling vector, $\mathbf{d}_{IJ}(\mathbf{R})$, is also possible in TDDFT(/TDA), in contrast to ADC(2), where no formal expression for either quantity has yet been derived. The $\mathbf{h}_{IJ}(\mathbf{R})$ vectors between ground and excited electronic states are well defined in linear-response TDDFT(/TDA) and can be derived from the excited electronic density [322–328]. These $\mathbf{h}_{01}(\mathbf{R})$ vectors are formally exact in the limit that LR-TDDFT, itself, becomes exact (i.e., beyond the AA and when using the exact ground-state exchange-correlation functional), and they only become approximate when the aforementioned approximations are invoked. This contrasts with $\mathbf{h}_{01}(\mathbf{R})$ vectors in CIS, which, as already mentioned in Section 2.4.2, are formally zero by definition.

On the other hand, the $\mathbf{h}_{IJ}(\mathbf{R})$ vectors between excited electronic states can be defined in CIS, but their quality depends on the accuracy of the underlying CIS level of theory used to describe the coupled electronic states. The situation is different for LR-TDDFT, as even in the exact case, the $\mathbf{h}_{IJ}(\mathbf{R})$ vectors can formally only ever be approximate within a linear-response formalism–quadratic response is required to derive an exact expression [329–333]. Nonetheless, using quadratic-response TDDFT within the AA can afford unphysical divergences in such $\mathbf{h}_{IJ}(\mathbf{R})$ vectors (as well as any other excited-to-excited state property) whenever the energy difference between the two states matches the excitation energy to any other excited state from the ground state [272, 331, 334–337]. Therefore, the current solution remains to employ LR-TDDFT(/TDA) $\mathbf{h}_{IJ}(\mathbf{R})$ vectors. While numerical tests indicate that $\mathbf{h}_{IJ}(\mathbf{R})$ vectors between excited electronic states might be fairly well approximated within a linear-response formalism [329, 338], in particular within the TDA, a proper description of the branching space for CXs between excited electronic states is far from granted within AA LR-TDDFT, despite its routine use in excited-state dynamics simulations involving multiple excited electronic states.

Therefore, although considering electronic energies alone may suggest an adequate representation of CXs within AA LR-TDDFT/TDA [and ADC(2)] in this context, is this what one observes in practice? How well do the topology and topography of CXs between excited electronic states given by these single-determinant methods reproduce those predicted by multiconfigurational and multireference techniques?

The present chapter attempts to address these questions from a pragmatic perspective by investigating the ability of AA LR-TDDFT/TDA and ADC(2) to describe CXs between the lowest two excited singlet electronic states, S_1 and S_2, for two exemplar molecules, protonated formaldimine and pyrazine. We also revisit the problem faced by AA LR-TDDFT/TDA in

describing CXs between the ground electronic state, S_0, and S_1 for the case of protonated formaldimine, focusing on the behavior of the PESs within the branching space at varied distances away from the MECX geometry. Despite providing a static, electronic structure perspective in this work, we bear nonadiabatic dynamics in mind, choosing to compare our AA LR-TDDFT/TDA and ADC(2) results to reference XMS-CASPT2 results. Our work is organized as follows: We start by (i) presenting the computational details of our calculations, paying particular attention to our internally consistent approach in generating CX branching spaces. We then (ii) explore the S_2/S_1 and S_1/S_0 MECX branching spaces of protonated formaldimine as predicted by the three electronic structure methods, followed by (iii) the S_2/S_1 MECX of pyrazine, where further considerations of the exchange–correlation functional used in AA LR-TDDFT/TDA are provided.

3.2 Computational details

3.2.1 Electronic structure

All XMS-CASPT2 energies, energy gradients [339] and nonadiabatic coupling vectors [340] were determined with the BAGEL 1.2.0 program package [341]. The single-state, single-reference (SS-SR) contraction scheme [339, 342] was employed for all XMS-CASTP2 calculations with a real vertical shift of 0.3 a.u. to avoid intruder state issues. Density fitting and frozen core approximations were also applied. For protonated formaldimine, a three-state averaging and a (6/4) active space, comprising two C-H,N-H σ orbitals and the C-N $\pi\pi^*$ orbital pair [Fig. 3.1(a)], were used (following Ref. [343]).[2] For pyrazine, a three-state averaging and a (10/8) active space, including the six π orbitals and two nitrogen lone pairs [Fig. 3.1(b)], were employed (based on Ref. [198]). All DFT [1, 2, 230] and AA LR-TDDFT energies, energy gradients and nonadiabatic coupling vectors were determined within the TDA using a development version of the graphics processing unit (GPU)-accelerated TeraChem 1.9 program package [346–352]. The PBE0 (global hybrid) exchange-correlation functional [239, 243, 353] was used throughout (unless otherwise stated). All MP2 [209] and ADC(2) energies and energy gradients [208, 354] were determined with the Turbomole 7.4.1 program package [355, 356], employing frozen core and resolution of identity [357] approximations. The Dunning cc-pVTZ basis set was used in all XMS-CASPT2, MP2 and ADC(2) calculations, whereas the Dunning cc-pVDZ basis set was used in all DFT and AA LR-TDDFT/TDA calculations [174]. The density fitting procedure, utilised in all XMS-CASPT2 calculations, made use of the cc-pVTZ-jkfit auxiliary basis set from the BAGEL library.

For brevity, we will hereafter drop the "AA" when discussing our LR-TDDFT/TDA results.

[2] In Ref. [29] and [344], we referred to the two σ orbitals as a C-N $\sigma\sigma^*$ pair, however, here we correct this misclassification and simply denote them as two different C-H,N-H σ orbitals [see Fig. 3.1(a)], in line with Ref. [343] (and a more recent work by the same authors [345]).

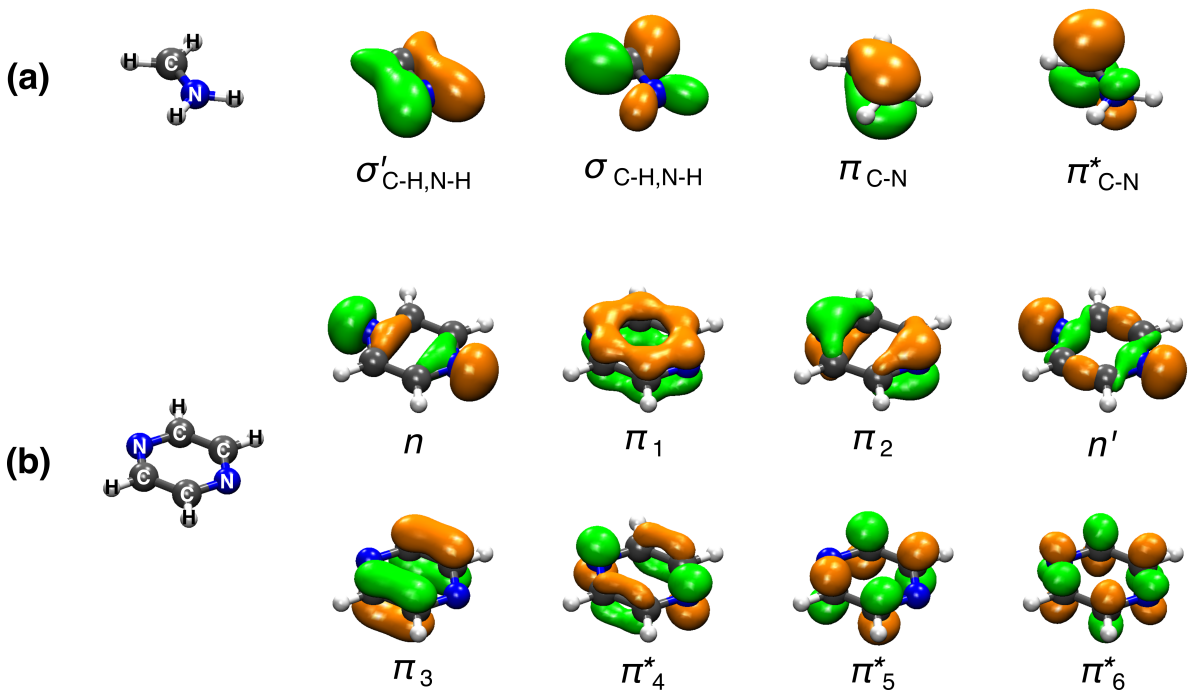

Figure 3.1: Underlying SA-CASSCF natural orbitals employed in **(a)** the XMS(3)-CASPT2(6/4)/cc-pVTZ calculations for protonated formaldimine and **(b)** the XMS(3)-CASPT2(10/8)/cc-pVTZ calculations for pyrazine. The active space orbitals are presented here for the S_0 minimum geometry of the two respective molecules plotted using an isovalue of 0.075, with the labelled geometries provided on the left.

For quantities involving excited states only, we use the notation LR-TDDFT/TDA/PBE0 and ADC(2). For quantities involving ground and excited states, we use the notation (LR-TD)DFT/TDA/PBE0 and MP2/ADC(2). Note, the same prescription for nomenclature is subsequently employed in the results sections of Chapters 4 and 5.

3.2.2 Critical geometries and linear interpolation in internal coordinates

3.2.2.1 Protonated formaldimine

The S_0 minimum (commonly denoted FC), S_2/S_1 MECX and S_1/S_0 MECX geometries were first optimised with XMS-CASPT2. MECX geometry optimisation utilised the GP algorithm of Bearpark *et al.* [215]. Linear interpolation in internal coordinates (LIIC) pathways were generated to connect these three critical geometries of protonated formaldimine. An LIIC pathway serves as the most direct way of connecting two key points in configurational space by interpolating new points based on internal (rather than Cartesian) coordinates [358]; as such, they do not constitute minimum-energy pathways. A single-point XMS-CASPT2 energy calculation was performed for each geometry to obtain the three lowest electronic states, S_0, S_1, and S_2, along the LIIC. Electronic energies are given relative to the S_0 energy at the S_0

minimum.

The same procedure was repeated to acquire the electronic energies along corresponding LIIC pathways for (LR-TD)DFT/TDA/PBE0 and for MP2/ADC(2), respectively. As noted in Section 2.4.2, neither (LR-TD)DFT/TDA, nor MP2/ADC(2) are expected to adequately describe the branching space of S_1/S_0 CXs. Therefore, we use the term minimum-energy *crossing points* (MECPs) [211] instead of minimum-energy *conical intersections* (MECXs) when referring to the S_1/S_0 intersection geometries located upon applying MECX optimisation algorithms with these two electronic-structure methods. To locate the MECXs (or MECPs) with (LR-TD)DFT/TDA or MP2/ADC(2), we used a combination of different geometry optimisation algorithms to ensure that the lowest possible electronic energy was found for these critical points. For (LR-TD)DFT/TDA, the GP method of Bearpark *et al.* [215], the LN method of Manaa and Yarkony [219], the PF of Ciminelli *et al.* [220] and the CIOpt method of Levine *et al.* [213] were used; CIOpt was used for MP2/ADC(2) with subsequent refinement of the MECX (or MECP) geometries carried out within their respective branching spaces. The details of these procedures can be found in Section 3.5.1.2 of the Appendix of this chapter. We note that use of a hybrid exchange-correlation functionals (i.e., PBE0) was required to converge the S_1/S_0 MECP geometry optimisation; attempts at using non-hybrid (GGA) exchange-correlation functionals (i.e., PBE) in preliminary test calculations resulted in KS SCF instability problems, prohibiting S_1/S_0 MECP geometry convergence.

It is important to stress here that in each case, the same electronic-structure method was used to calculate the electronic energies and to optimise the three critical geometries.

3.2.2.2 Pyrazine

The same procedure was used to optimise the critical geometries and generate the LIICs for pyrazine. However, only the S_0 minimum and S_2/S_1 MECX geometries were considered using the three electronic-structure methods.

3.2.3 Plotting the CX branching space

The branching space vectors, $\mathbf{g}_{IJ}(\mathbf{R})$ and $\mathbf{h}_{IJ}(\mathbf{R})$, were first computed using XMS-CASPT2 at the optimised XMS-CASPT2 S_J/S_I MECX geometry. The raw branching space vectors were then orthogonalised by the Yarkony procedure [88, 359] and appropriately normalised, before being used to generate a 2D grid of 29×29 geometries along the branching plane, centred on the optimised XMS-CASPT2 S_J/S_I MECX geometry. To facilitate this, nuclear distortions along the orthonormalised $\bar{\mathbf{x}}_{IJ}(\mathbf{R})$ and $\bar{\mathbf{y}}_{IJ}(\mathbf{R})$ vector directions (see Section 3.5.1.3 of the Appendix of this chapter for branching space vector definitions) were multiplied by an appropriate scale factor and added in fourteen increments in the positive and negative directions, respectively, spanning ± 0.001 Å in both branching space vector directions, as was done similarly in Ref. [360]. At each grid-point geometry, a single-point XMS-CASPT2

energy calculation was performed, giving the S_I and S_J PESs in the region surrounding the optimised XMS-CASPT2 S_J/S_I MECX geometry. Electronic energies are given relative to the S_I energy at the MECX geometry, which is located at the grid origin. Note, in certain cases, it is more illustrative to plot the $S_J - S_I$ energy difference at each grid-point geometry instead of absolute energies.

The same procedure was repeated to obtain the corresponding S_J/S_I MECX (or MECP) branching spaces of (LR-TD)DFT/TDA/PBE0 and MP2/ADC(2), respectively. For direct comparison of the branching space plots in Figs 3.3-3.8 (and Fig. 3.13) obtained by the different electronic-structure methods, we followed the approach taken in Ref. [165]: the orthonormalised branching space vectors were rotated within their respective branching planes to ensure maximal overlap with the reference orthonormalised vectors of XMS-CASPT2. These new rotated (orthonormalised) branching space vectors are denoted $\overline{\mathbf{x}}'_{IJ}(\mathbf{R})$ and $\overline{\mathbf{y}}'_{IJ}(\mathbf{R})$. Details of the rotation procedure (for the (LR-TD)DFT/TDA/PBE0 and MP2/ADC(2) branching space vectors) and the process used to orthonormalise the raw branching space vectors (for all three electronic structure methods) are outlined in Section 3.5.1.3 of the Appendix of this chapter.

We stress again that in each case, the same electronic-structure method was used to compute the electronic energies, branching space vectors and to optimise the MECX (or MECP) geometries, except for MP2/ADC(2), where the $\mathbf{h}_{IJ}(\mathbf{R})$ vector from XMS-CASPT2 was used instead. Therefore, the branching spaces constructed are fully-consistent within each electronic-structure method, except for the $\mathbf{h}_{IJ}(\mathbf{R})$ vectors in MP2/ADC(2).

3.2.4 CX branching space topography parameters

To provide a numerical comparison of the topography of the MECXs obtained by different electronic-structure methods, we calculated the CX branching space topography parameters, $\mathcal{P}$ and $\mathcal{B}$, as defined in Eqs (2.35) and (2.36) in Section 2.2.2.2, respectively. As already stated, using the topography characterisation system of Fdez. Galván *et al.* [68, 101], MECXs can be defined as peaked ($\mathcal{P} < 1$) or sloped ($\mathcal{P} > 1$), and bifurcating ($\mathcal{B} < 1$) or single-path ($\mathcal{B} > 1$). To be consistent with Ref. [101], we chose the value of n in the definition of β in Eq. (3.2) in Section 3.5.1.3 of the Appendix of this chapter, such that the value of the asymmetry parameter, Δ_{gh}, given in Eq. (2.33) of Section 2.2.2.2 was greater or equal to 0. Therefore, in all cases n took a value of 0 or 1.

3.3 Results and discussion

3.3.1 Protonated formaldinine

The photophysics of protonated formaldimine, $CH_2NH_2^+$, has been extensively studied (e.g., Refs. [361–365]), due to the molecule acting as the simplest model system for the chromo-

phore in rhodopsin, the protonated Schiff base of retinal. Within the FC region, protonated formaldimine possesses an optically dark S_1 state and a bright S_2 state of predominantly $\sigma\pi^*$ and $\pi\pi^*$ electronic character, respectively [294, 343].[3] (We note that the $\sigma\pi^*$ transition is also characterised in the literature as $\pi'^*\pi^*$, with π'^* being orthogonal to the π^* orbital.) Given the much higher oscillator strength exhibited by S_2, photoexcitation occurs predominantly to S_2, with relaxation to the S_0 ground state involving passage through two subsequent MECXs. The first (S_2/S_1) has been shown to exhibit a peaked topography, whilst the second (S_1/S_0) has been shown to be sloped [343]. Hence, protonated formaldimine constitutes a perfect model system (i.e., possessing MECXs (i) between different types of electronic states and (ii) exhibiting different topographies) to assess the quality of the branching space provided by (LR-TD)DFT/TDA/PBE0 and MP2/ADC(2).

3.3.1.1 Linear interpolation in internal coordinates

In the following, we compare the photochemical pathway of protonated formaldimine by calculating the three lowest electronic-state energies along an LIIC pathway connecting the FC, S_2/S_1 MECX and S_1/S_0 MECX critical geometries obtained with XMS-CASPT2, MP2/ADC(2) and (LR-TD)DFT/TDA/PBE0 (see molecular representation in Fig. 3.2).

According to XMS-CASPT2 [Fig. 3.2(a)], following photoexcitation to S_2, protonated formaldimine decays to S_1 via a strongly peaked S_2/S_1 MECX,[4] which is encountered by a stretch of the C-N bond whilst retaining the planarity of the molecule exhibited at the FC geometry (S_0 min, 1.281 Å; S_2/S_1 MECX, 1.420 Å). Such a peaked topography is assumed to provide highly efficient nonadiabatic population transfer from S_2 to S_1 [343]. [The effect of CX topography (and topology) on the efficacy of dynamics will be discussed in greater detail later within the context of the results of Chapter 5.] Subsequent relaxation to the ground electronic state occurs through a weakly sloped S_1/S_0 MECX,[4] which for XMS-CASPT2 is reached via a 90° twist about the C-N bond and an additional 31.3° pyramidalisation of the CH_2 moiety. Less efficient S_1-to-S_0 decay is expected for the predicted sloped topography of the S_1/S_0 MECX [343]. Previous investigations with MRCISD have reported purely twisted S_1/S_0 MECX geometries with no CH_2 pyramidalisation [98, 213], whereas others employing MS-CASPT2 have instead predicted the C-N torsion accompanied by pyramidalisation of the NH_2 group [213]. The differences in S_1/S_0 MECX geometry obtained by different multiconfigurational and multireference methods have been ascribed to an apparent flatness of the intersection seam with respect to pyramidalisation (at either end of the C-N bond) [213].

[3] The σ orbital involved in the electronic transition that characterises the S_1 state of protonated formaldimine within the FC region is the C-H,N-H σ orbital reported in Fig. 3.1(a).

[4] The peaked and sloped topographies of the S_2/S_1 and S_1/S_0 MECXs in XMS-CASPT2, respectively, are confirmed later in Figs 3.3(a) and 3.4(b). However, some indication of their MECX topographies can still be loosely inferred from the shape of the corresponding potential energy curves near each degeneracy point in Fig. 3.2(a).

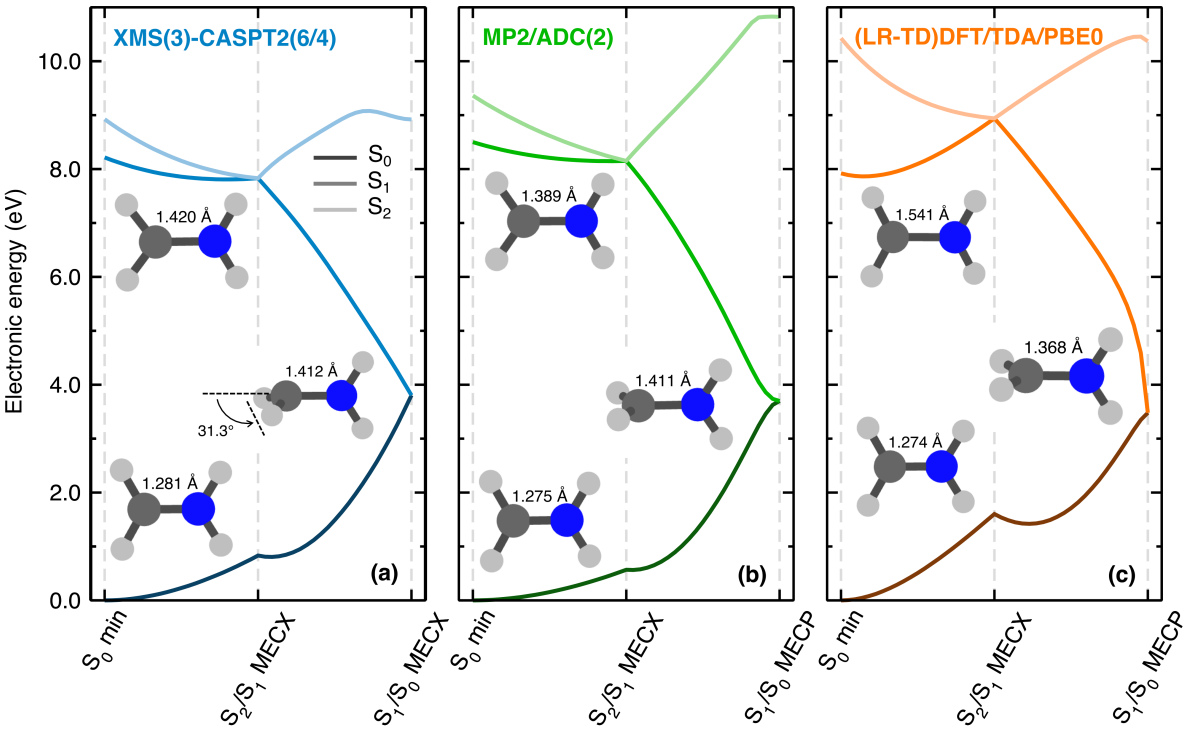

Figure 3.2: LIIC pathways connecting the S_0 minimum, S_2/S_1 MECX and S_1/S_0 MECX (or MECP) in protonated formaldimine. Comparison of the S_0 (dark colour), S_1 (mid colour) and S_2 (light colour) electronic energies obtained with **(a)** XMS(3)-CASPT2(6/4)/cc-pVTZ (blue), **(b)** MP2/ADC(2)/cc-pVTZ (green) and **(c)** (LR-TD)DFT/TDA/PBE0/cc-pVDZ (orange). In each panel, the critical geometries were optimised at the same level of theory used to compute the electronic energies. The insets show the molecular structures of the three critical points [S_0 min, bottom left; S_2/S_1 MECX, top left; S_1/S_0 MECX (or MECP), middle right] along with the calculated C-N bond lengths (and the CH_2 pyramidalisation angle for the XMS(3)-CASPT2(6/4) S_1/S_0 MECX geometry).

We now compare the XMS-CASPT2 LIIC pathway to those obtained with MP2/ADC(2) [Fig. 3.2(b)] and (LR-TD)DFT/TDA/PBE0 [Fig. 3.2(c)]. Considering the overall electronic energy profiles of the different methods along the LIIC, an obvious observation is the striking agreement between MP2/ADC(2) and XMS-CASPT2; the only notable difference is the behaviour of S_2 in the segment connecting the two MECXs (explained by the involvement of other electronic states not included in XMS-CASPT2). On the other hand, LR-TDDFT/TDA/PBE0 predicts an $S_2 - S_1$ energy difference at the S_0 minimum over twice that given by either ADC(2) or XMS-CASPT2. This is in spite of the electronic character of S_1 and S_2 at the respective S_2/S_1 MECX geometries in LR-TDDFT/TDA/PBE0 and ADC(2) being in agreement (see Fig. 3.12 in Section 3.5.2 of the Appendix of this chapter). We note here that a detailed discussion of the performance of LR-TDDFT/TDA in describing the character of the electronic states of protonated formaldimine goes beyond the scope of this work. The approach to the respective MECX (or MECP) points are also markedly different in (LR-TD)DFT/TDA/PBE0 compared

to that in the wavefunction-based methods. Notably, the LR-TDDFT/TDA/PBE0 S_1 state approaches the S_1/S_0 MECP too steeply relative to XMS-CASPT2. This observation further corroborates that the LR-TDDFT/TDA first excited electronic state can vary too rapidly in the vicinity of a CX with the ground state, as previously shown in Ref. [27]. Interestingly, neither MP2/ADC(2) nor (LR-TD)DFT/TDA/PBE0 predict the CH_2 pyramidalisation exhibited by XMS-CASPT2 for the S_1/S_0 MECX geometry, despite all three geometries being at approximately the same relative energy. Earlier works using (LR-TD)DFT/TDA/PBE presented similar observations [294].

3.3.1.2 S_2/S_1 branching space

We now focus our attention on the first intersection seam encountered by protonated formaldimine upon photoexcitation to S_2, by calculating the electronic energies with each electronic-structure method within the branching space of their respective S_2/S_1 MECX (Fig. 3.3). All three electronic-structure methods correctly predict a conical $(F-2)$-dimensional intersection between S_1 and S_2, where the degeneracy is lifted in both branching space vector directions. We stress again (Section 3.1) that the success of LR-TDDFT/TDA to accurately describe the topology of the S_2/S_1 MECX is *not necessarily guaranteed*. Our results, however, confirm that linear-response $\mathbf{h}_{12}(\mathbf{R})$ vectors do indeed offer an adequate description of the CX branching space in protonated formaldimine.

Table 3.1: CX branching space topography parameters [101] as defined in Eqs (2.35) and (2.36) in Section 2.2.2.2.

	$\mathcal{P}$	$\mathcal{B}$	Characterisation	Fig.
protonated formaldimine S_2/S_1 MECX				
XMS(3)-CASPT2(6/4)	0.02	0.29	peaked bifurcating	3.3(a)
ADC(2)	0.08	0.45	peaked bifurcating	3.3(b)
LR-TDDFT/TDA/PBE0	0.59	0.86	peaked bifurcating	3.3(c)
protonated formaldimine S_1/S_0 MECX				
XMS(3)-CASPT2(6/4)	1.49	1.32	sloped single-path	3.4(a)
pyrazine S_2/S_1 MECX				
XMS(3)-CASPT2(10/8)	3.57	1.96	sloped single-path	3.7(a)
ADC(2)	12.78	1.14	sloped single-path	3.7(b)
LR-TDDFT/TDA/PBE0	7.16	2.64	sloped single-path	3.7(c)
LR-TDDFT/TDA/PBE	0.21	0.79	peaked bifurcating	3.8(a)
LR-TDDFT/TDA/LC-ωPBE	5.19	2.60	sloped single-path	3.8(b)

We note that the S_1 and S_2 PESs obtained with LR-TDDFT/TDA/PBE0 are in relatively poor agreement with those of the XMS-CASPT2 reference [compare Figs 3.3(c) and 3.3(a)]. Using the CX branching space topography parameters [101] defined in Eqs (2.35)

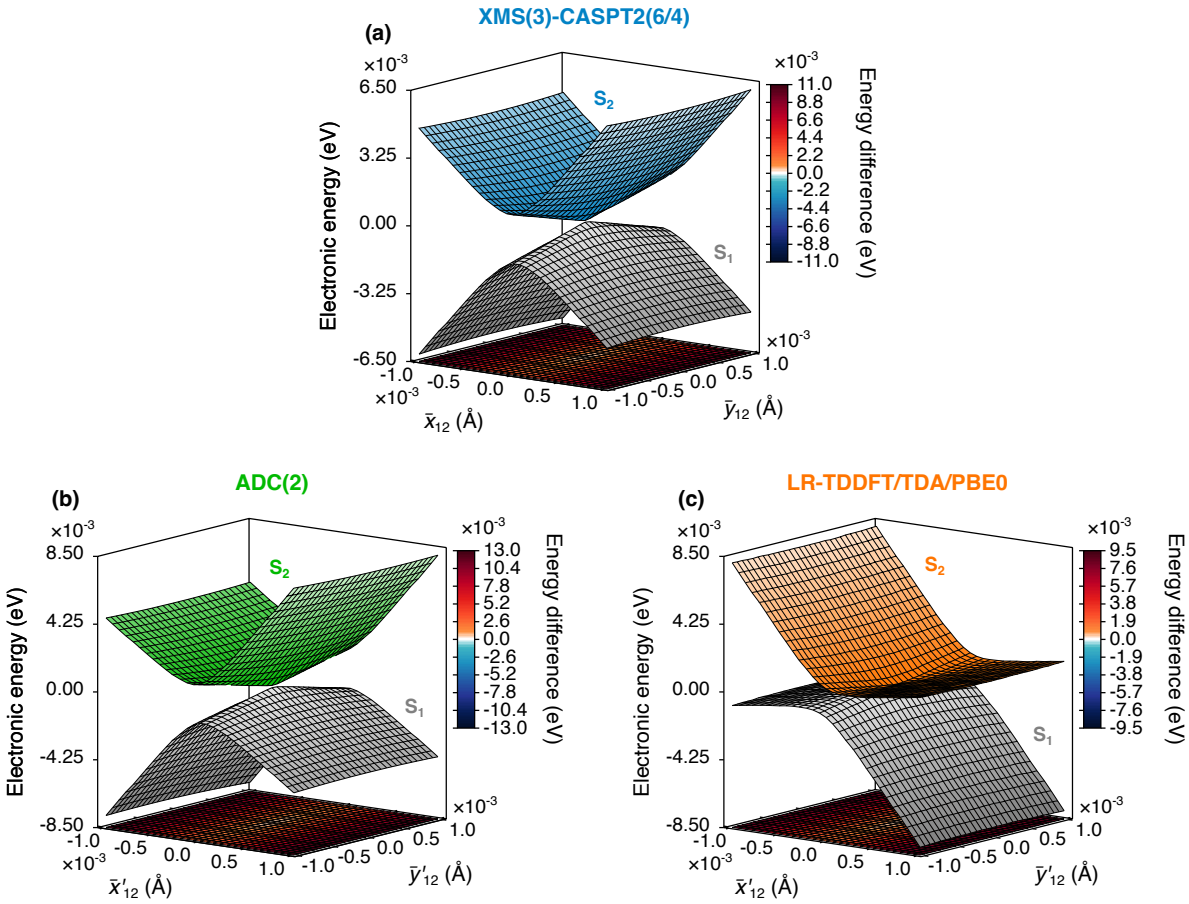

Figure 3.3: Branching space of the S_2/S_1 MECX in protonated formaldimine. Comparison of the S_1 and S_2 PESs obtained with **(a)** XMS(3)-CASPT2(6/4)/cc-pVTZ (blue/grey), **(b)** ADC(2)/cc-pVTZ (green/grey) and **(c)** LR-TDDFT/TDA/PBE0/cc-pVDZ (orange/grey). In each plot, the MECX geometries and branching space vectors were obtained at the same level of theory used to calculate the electronic energies (except for the ADC(2) plot, which used the $\mathbf{h}_{12}(\mathbf{R})$ vector of XMS(3)-CASPT2(6/4)–see Section 3.2.3 for details). The base in each plot shows a 2D colour map of the $S_2 - S_1$ energy difference (see colour bar on the right).

and (2.36) in Section 2.2.2.2, both methods yield a peaked bifurcating topography, but LR-TDDFT/TDA/PBE0 exhibits larger values of $\mathcal{P}$ and $\mathcal{B}$ (0.59 and 0.86, respectively) than XMS-CASPT2 (0.02 and 0.29). These parameters are summarised in Table 3.1. This disparity between LR-TDDFT/TDA/PBE0 and XMS-CASPT2 links to the LIIC plots in Fig. 3.2, where the approach of the LR-TDDFT/TDA/PBE0 S_2 and S_1 states (i.e., the $S_2 - S_1$ energy gap and slope of the S_2 and S_1 energies) towards the S_2/S_1 MECX is markedly different in LR-TDDFT/TDA/PBE0 to that in either XMS-CASPT2 or ADC(2). On the other hand, the S_1 and S_2 PESs obtained with ADC(2) are in close agreement with those of XMS-CASPT2; ADC(2) also yields a peaked bifurcating topography for the S_2/S_1 MECX [compare Figs 3.3(b) and 3.3(a)] with similar parameter values of $\mathcal{P} = 0.08$ and $\mathcal{B} = 0.45$. The ability of ADC(2) to ad-

equately describe the branching space of a CX between excited electronic states is reassuring, given its extended use within excited-state molecular dynamics simulations [211, 366–381]. Despite the difference in the abilities of LR-TDDFT/TDA/PBE0 and ADC(2) to closely reproduce the topography of the XMS-CASPT2 S_2/S_1 MECX branching space in Fig. 3.3, the branching space vectors of LR-TDDFT/TDA/PBE0 show a striking resemblance to those of ADC(2)(/XMS-CASPT2)–see Fig. 3.12 in Section 3.5.2 of the Appendix of this chapter. Whether this difference in topographies between LR-TDDFT/TDA/PBE0 and the other two methods is due to the approximate linear-response $\mathbf{h}_{12}(\mathbf{R})$ vector, or simply down to the approximate choice of exchange-correlation functional, is left open for future scrutiny. For now, we have explicitly shown that LR-TDDFT/TDA can adequately describe the topology of an excited-to-excited state MECX, arguably the greater feat.

3.3.1.3 S_1/S_0 branching space

Next, we take the opportunity to focus on the performance of the methods in describing the S_1/S_0 MECX branching space of protonated formaldimine. XMS-CASPT2 gives a conical $(F-2)$-dimensional intersection as expected [Fig. 3.4(a)], with a sloped single-path topography (with parameters, $\mathcal{P} = 1.49$ and $\mathcal{B} = 1.32$) similar to that reported in Ref. [343]. As expected from the discussion in Section 2.4.2, (LR-TD)DFT/TDA/PBE0 and MP2/ADC(2) incorrectly predict a linear $(F-1)$-dimensional intersection at the S_1/S_0 MECP [Figs 3.4(c) and 3.4(b)], respectively), where the degeneracy is only lifted along a single branching space vector direction [i.e., $\overline{\mathbf{y}}'_{01}(\mathbf{R})$]. In both cases, the first response (S_1) state becomes lower in energy than the reference (S_0) state, leading to negative excitation energies along certain regions of the branching plane (see colour map in [Figs 3.4(b) and 3.4(c)]). This observation corroborates earlier results obtained for (LR-TD)DFT [27] and MP2/ADC(2) [96]. When plotted using the same vertical axis energy range (see Fig. 3.13 in Section 3.5.2 of the Appendix of this chapter), it is clear that the (LR-TD)DFT/TDA/PBE0 S_1 PES varies too rapidly in the vicinity of the S_1/S_0 MECP compared to that of both XMS-CASPT2 (where a conical intersection is obtained), and MP2/ADC(2) (where a linear seam of intersection is observed). This difference in behaviour between the different electronic-structure methods is consistent with the LIIC plots in Fig. 3.2 close to the S_1/S_0 intersection region. [We note that replacing the (LR-TD)DFT branching space vectors used to generate the (LR-TD)DFT S_1/S_0 MECP (and S_2/S_1 MECX) branching space plots in Fig. 3.4 (and 3.3) with those of XMS-CASPT2 results in no observable difference to the PESs–except for a trivial reflection in the $\overline{\mathbf{y}}'_{IJ}(\mathbf{R})$ vector direction.]

Despite indeed being $(F-1)$-dimensional near the point where the two electronic states become degenerate, the (LR-TD)DFT/TDA/PBE0 intersection in Fig. 3.4(c) appears significantly more curved than the strictly linear S_1/S_0 intersection of MP2/ADC(2) in Fig. 3.4(b). This observation warrants further investigation of the (LR-TD)DFT/TDA/PBE0 intersection at larger distances along the $\overline{\mathbf{y}}'_{01}(\mathbf{R})$ vector direction. Plotting the (LR-TD)DFT/TDA/PBE0

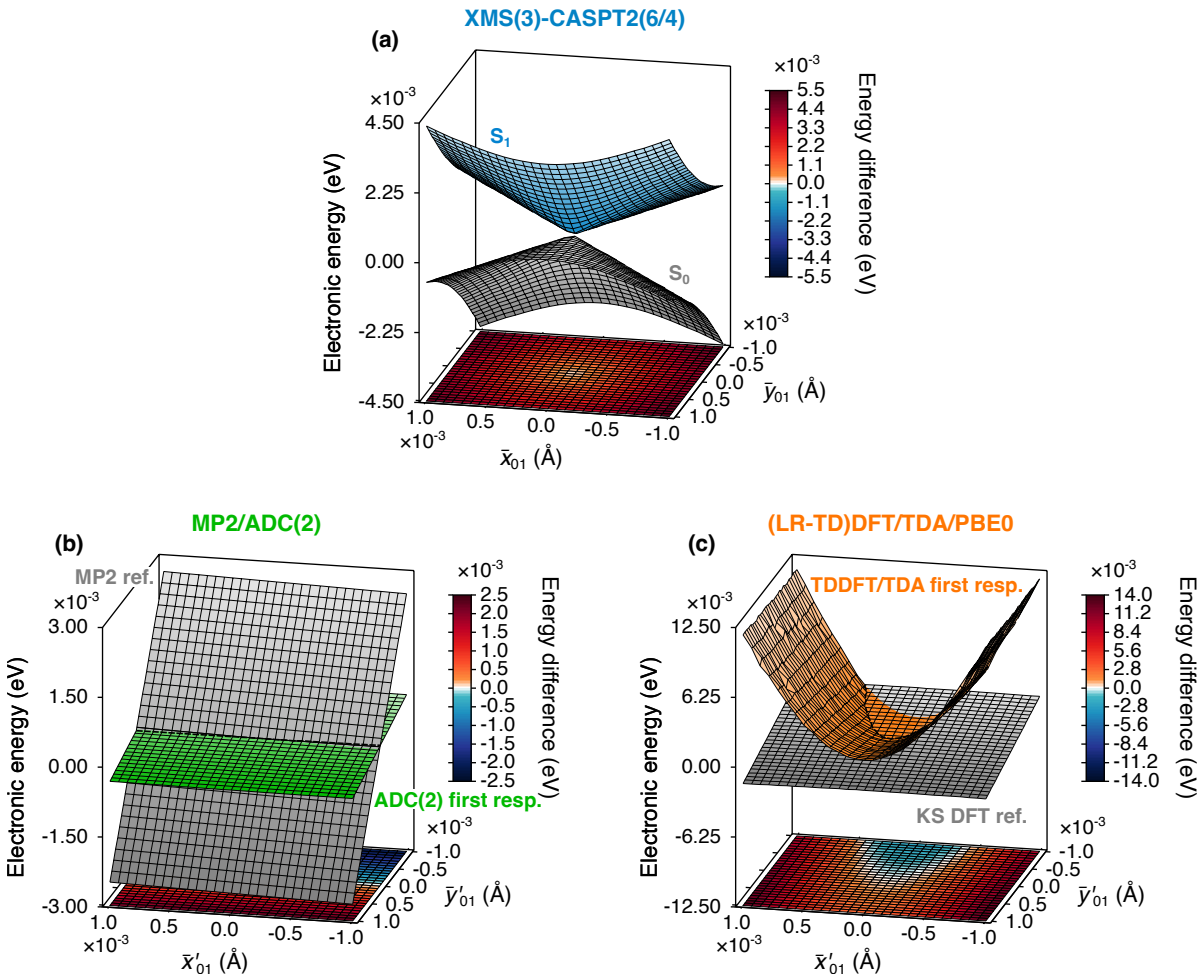

Figure 3.4: Branching space of the S_1/S_0 MECX (or MECP) in protonated formaldimine. Comparison of the S_0 and S_1 PESs obtained with **(a)** XMS(3)-CASPT2(6/4)/cc-pVTZ (blue/grey), **(b)** MP2/ADC(2)/cc-pVTZ (green/grey) and **(c)** (LR-TD)DFT/TDA/PBE0/cc-pVDZ (orange/grey). In each plot, the MECX (or MECP) geometries and branching space vectors were obtained at the same level of theory used to calculate the electronic energies (except for the MP2/ADC(2) plot, which used the $\mathbf{h}_{01}(\mathbf{R})$ vector of XMS(3)-CASPT2(6/4)–see Section 3.2.3 for details). The dashed lines in the Figs 3.4(b) and 3.4(c) indicate the seam where $E_0^{\mathrm{el}}(\mathbf{R}) = E_1^{\mathrm{el}}(\mathbf{R})$. (We note that the rendering of the colours for the PESs does not reflect precisely this intersection.) The base in each plot shows a 2D colour map of the $S_1 - S_0$ energy difference (see colour bar on the right).

S_0 and S_1 PESs along an extended branching plane [$\pm 0.003 \times \bar{\mathbf{x}}'_{01}(\mathbf{R})$ and $\pm 0.03 \times \bar{\mathbf{y}}'_{01}(\mathbf{R})$ in Fig. 3.5(b) compared to the original $\pm 0.001 \times \bar{\mathbf{x}}'_{01}(\mathbf{R})$ and $\pm 0.001 \times \bar{\mathbf{y}}'_{01}(\mathbf{R})$ in Fig. 3.4–see Section 3.5.1.3 of the Appendix of this chapter for branching space vector definitions] reveals that the curved intersection seam in Fig. 3.4(c) is in fact just one part of a larger intersection ring - something that shows a striking resemblance to two interpenetrating cones. On the other hand, the strictly linear intersection seam in MP2/ADC(2) observed along the standard

branching plane [Fig. 3.4(b)] remains even along this extended branching plane [Fig. 3.5(a)]. Overall, our results connect the different pictures proposed previously in the literature (Section 2.4.2) for the description of S_1/S_0 MECPs within (LR-TD)DFT/TDA: performing an S_1/S_0 MECP optimisation with (LR-TD)DFT/TDA will in fact locate a geometry on the intersection ring and the MECP will look different depending on the extent of the branching space explored to unravel the shape of the S_0 and S_1 PESs around this location–either a (near-to-linear) seam of intersection for minute variations along $\overline{\mathbf{x}}'_{01}(\mathbf{R})$ and $\overline{\mathbf{y}}'_{01}(\mathbf{R})$ [like in Fig. 3.4(c) and as first reported by Levine *et al.* [27]], or an *intersection ring* (reminiscent of two interpenetrating cones) when a more extended scan along $\overline{\mathbf{x}}'_{01}(\mathbf{R})$ and $\overline{\mathbf{y}}'_{01}(\mathbf{R})$ is performed [like in Fig. 3.5(b) and as alluded to by Tapavicza *et al.* [28]]. We note that it may be possible to miss the negative-energy region of the intersection ring for more extreme scans around the (LR-TD)DFT/TDA S_1/S_0 intersection point (i.e., if one "zooms out" further from the crossing point), giving a false impression that (LR-TD)DFT/TDA can describe the intersection point adequately. This observation is further discussed in relation to the dynamics results in Chapter 5.

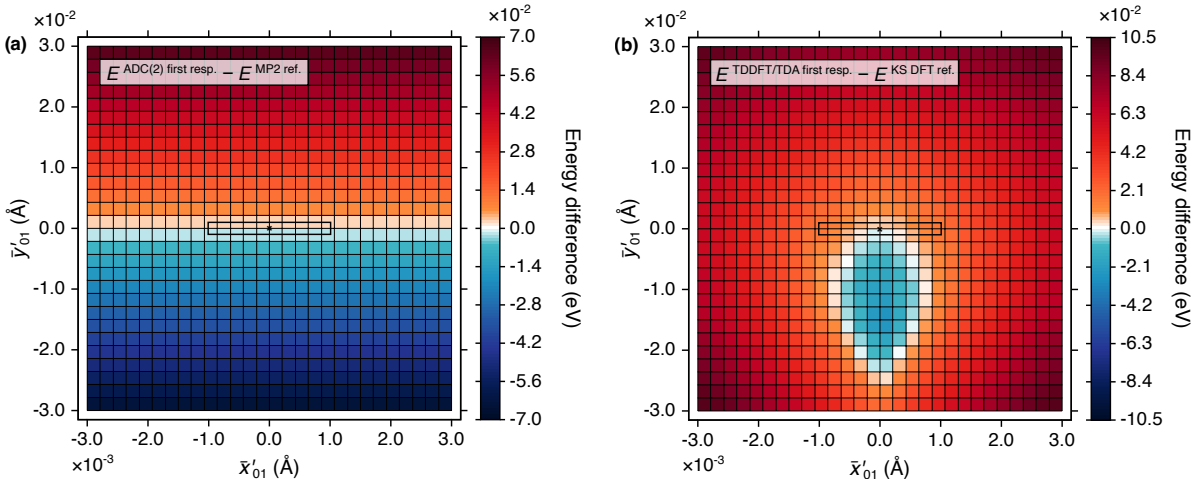

Figure 3.5: 2D colour map of the electronic energy difference between S_0 (reference state) and S_1 (first response state) obtained with **(a)** MP2/ADC(2)/cc-pVTZ and **(b)** (LR-TD)DFT/TDA/PBE0/cc-pVDZ in the vicinity of the S_1/S_0 MECP in protonated formaldimine along an extended branching plane ($\pm 0.003 \times \overline{\mathbf{x}}'_{01}(\mathbf{R})$, $\pm 0.03 \times \overline{\mathbf{y}}'_{01}(\mathbf{R})$). The black box encloses the area spanned by the branching plane used to generate the plots in Fig. 3.4; the black cross indicates the location of the S_1/S_0 MECP geometry.

We conclude this Section by noting that we also calculated the HF/CIS S_1/S_0 MECP branching space for both the standard [Fig. 3.6(a)] and extended [Fig. 3.6(b)] grid of geometries around the intersection point. As expected (Section 2.4.2) HF/CIS predicts a strictly linear $(F-1)$-dimensional intersection along the standard branching plane that likewise remains along the extended branching plane, which is analogous to the behaviour of MP2/ADC(2), but in contrast to that of (LR-TD)DFT/TDA/PBE0. This is despite the fact that HF/CIS is

able to pick up the slight pyramidalisation in the CH_2 group observed for XMS-CASPT2 (see Fig. 3.14 in Section 3.5.2 of the Appendix of this chapter). We have confirmed that our (LR-TD)DFT/TDA findings are unaffected by improving the numerical accuracy of our calculations (i.e., increased DFT grid size–see also Section 3.5.1.3 of the Appendix of this chapter for details regarding KS SCF convergence). These observations solidify our conclusions that the description of CXs involving the ground state by (LR-TD)DFT/TDA and HF/CIS are not completely analogous, contrary to comments in the literature.

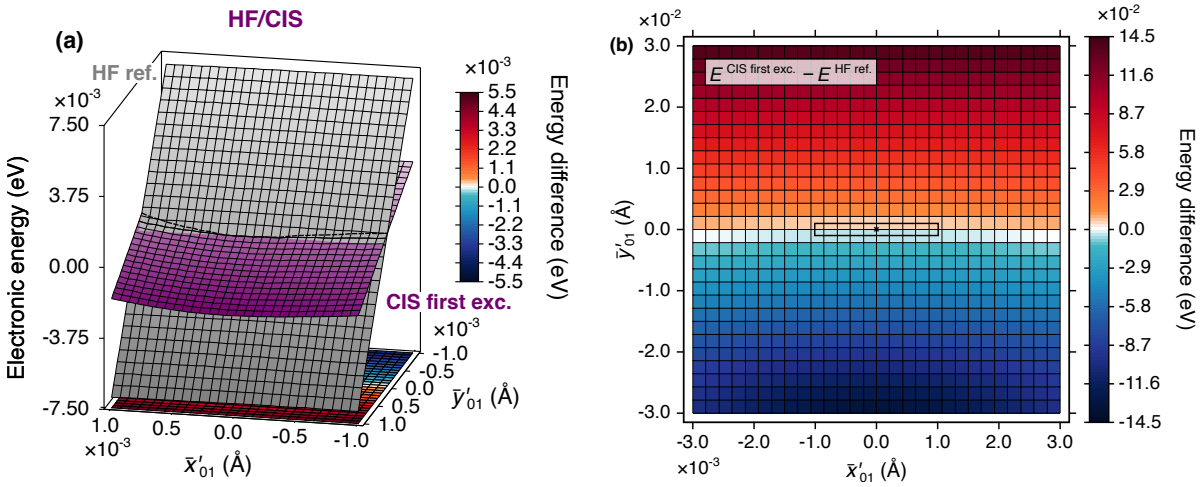

Figure 3.6: (a) Branching space of the S_1/S_0 MECP in protonated formaldimine. The S_0 and S_1 PESs obtained with HF/CIS/cc-pVDZ (purple/grey). The MECP geometry and branching space vectors were obtained at the same level of theory used to compute the PESs. The dashed line in the plot indicates the seam where $E_1^{\text{el}}(\mathbf{R}) = E_0^{\text{el}}(\mathbf{R})$. (We note that the rendering of the colours for the PESs does not reflect precisely this intersection.) The base shows a 2D colour map of the energy difference between the reference and first excited states (see colour bar on the right). **(b)** 2D map of the energy difference between the S_0 (reference state) and S_1 (first excited state) obtained with HF/CIS/cc-pVDZ in the vicinity of the S_1/S_0 MECP in protonated formaldimine along an extended branching plane ($\pm 0.003 \times \bar{\mathbf{x}}'_{ij}(\mathbf{R})$, $\pm 0.03 \times \bar{\mathbf{y}}'_{ij}(\mathbf{R})$). The black box encloses the area spanned by the branching plane used to generate the Fig. 3.6(a) ($\pm 0.001 \times \bar{\mathbf{x}}'_{ij}(\mathbf{R})$, $\pm 0.001 \times \bar{\mathbf{y}}'_{ij}(\mathbf{R})$); the black cross indicates the location of the S_1/S_0 MECP geometry.

3.3.2 Pyrazine

Next, we consider CXs between excited states for a second exemplar molecule, pyrazine. Like for protonated formaldimine, the excited electronic states of pyrazine have been well-studied, often considered the definitive case for vibronic coupling in aromatic systems; pyrazine is also a precursor to numerous biologically active molecules [198, 382–388]. Within the FC region, the S_1 state in pyrazine exhibits an $n\pi^*$ character and S_2 is of $\pi\pi^*$ character [385]. At the XMS-CASPT2 level, the S_2/S_1 MECX is reached (from the planar S_0 minimum geometry)

by simultaneous elongation of the C-N and C-C bonds, but with an overall stretching of the ring along the axis bisecting the two nitrogen atoms (see Fig. 3.15 in Section 3.5.2 of the Appendix of this chapter and the insets of Fig. 3.9). LR-TDDFT/TDA/PBE0 and ADC(2) predict S_0 minimum and S_2/S_1 MECX geometries that agree closely with those of XMS-CASPT2. The only difference is the stretching of the S_2/S_1 MECX geometry observed in LR-TDDFT/TDA/PBE0 is slightly more exaggerated than in the wavefunction-based methods, as indicated by the larger (smaller) N-C-C (C-N-C) bond angles. This distortion in the LR-TDDFT/TDA/PBE0 S_2/S_1 MECX geometries is accompanied by it being approximately 1 eV higher in energy (Fig. 3.9) than the S_2/S_1 MECX geometry in either XMS-CASPT2 or ADC(2).

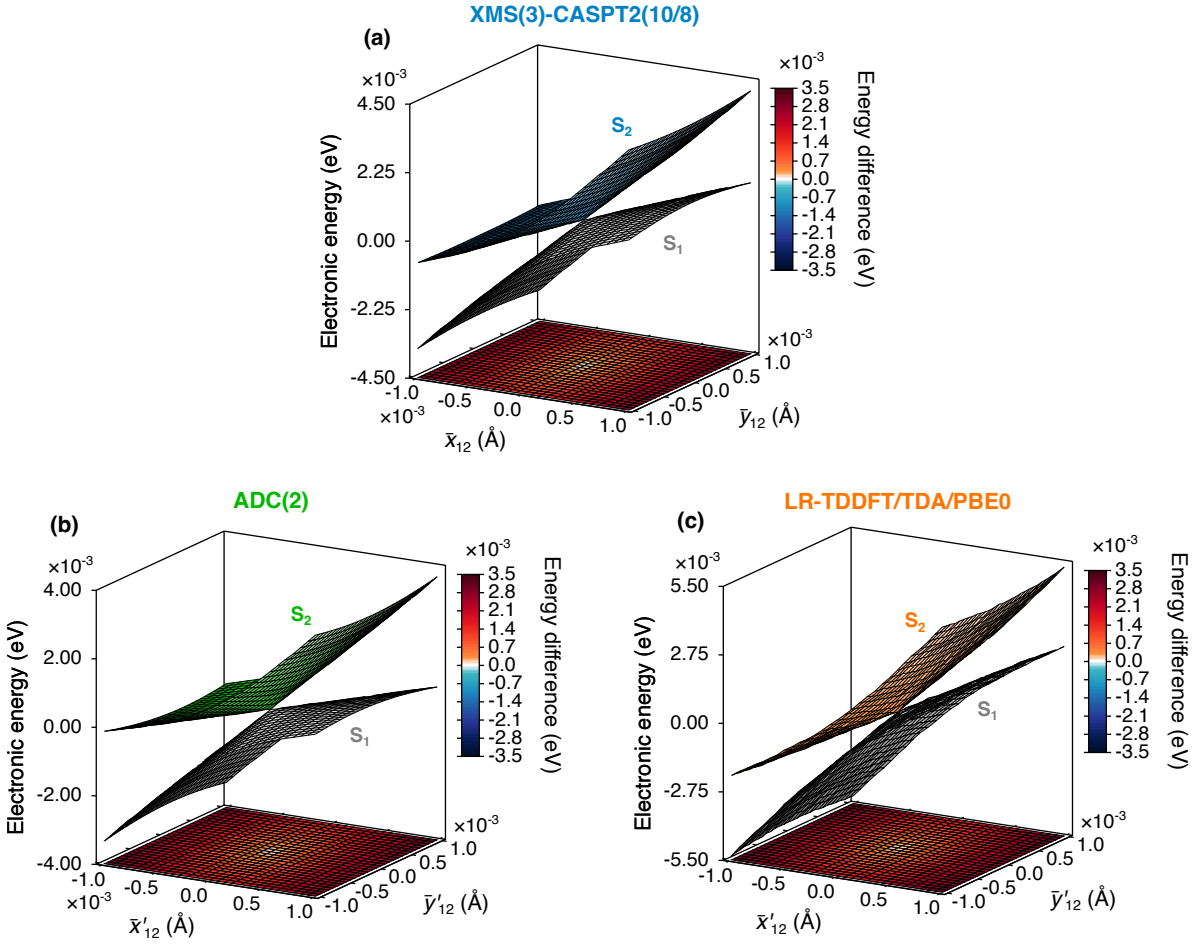

Figure 3.7: Branching space of the S_2/S_1 MECX in pyrazine. Comparison of the S_1 and S_2 PESs obtained with **(a)** XMS(3)-CASPT2(10/8)/cc-pVTZ (blue/grey), **(b)** ADC(2)/cc-pVTZ (green/grey) and **(c)** LR-TDDFT/TDA/PBE0/cc-pVDZ (orange/grey). In each plot, the MECX geometries and branching space vectors were obtained at the same level of theory used to calculate the electronic energies (except for the ADC(2) plot, which used the $\mathbf{h}_{12}(\mathbf{R})$ vector of XMS(3)-CASPT2(10/8)–see Section 3.2.3 for details). The base in each plot shows a 2D colour map of the $S_2 - S_1$ energy difference (see colour bar on the right).

3.3.2.1 S_2/S_1 branching space

We now focus on the respective branching spaces for the S_2/S_1 MECX (Fig. 3.7). As for protonated formaldimine, all three methods correctly predict a conical $(F-2)$-dimensional intersection between S_1 and S_2, where the degeneracy is lifted along both branching space vector directions. LR-TDDFT/TDA/PBE0 exhibits a sloped single-path MECX, mirroring the topography observed with both XMS-CASPT2 and ADC(2), with $\mathcal{P}$ and $\mathcal{B}$ parameters (7.16 and 2.64, respectively) that are closer to those obtained with XMS-CASPT2 (3.57 and 1.96) than ADC(2) (12.78 and 1.14). Therefore, for pyrazine, the S_1 and S_2 PESs in LR-TDDFT/TDA/PBE0 show an improved agreement to those of the other two methods than in the case of protonated formaldimine. A natural question to ask is whether this agreement in CX topography can be improved upon further (or, at least, affected) by changing the exchange-correlation functional used.

To this end, we recalculated the S_2/S_1 MECX geometry and its corresponding branching space for the GGA functional, PBE, and for the range-separated hybrid functional, LC-ωPBE (with range-separation parameter $\omega = 0.4\ a_0^{-1}$). The former constitutes moving down one rung of Jacob's ladder (Fig. 2.6) from the global hybrid, PBE0, whereas the latter corresponds to climbing up one rung. Using LC-ωPBE instead of PBE does indeed show a visual improvement in the afforded CX topography [Fig. 3.8(b)]; the $\mathcal{P}$ and $\mathcal{B}$ parameters (5.19 and 2.60) are also closer to those of XMS-CASPT2. However, when HF exchange is not included, going from PBE0 to PBE, a much more significant change is observed [Fig. 3.8(a)]. Now, the S_2/S_1 MECX is characterised differently, being peaked and bifurcating (as opposed to sloped and

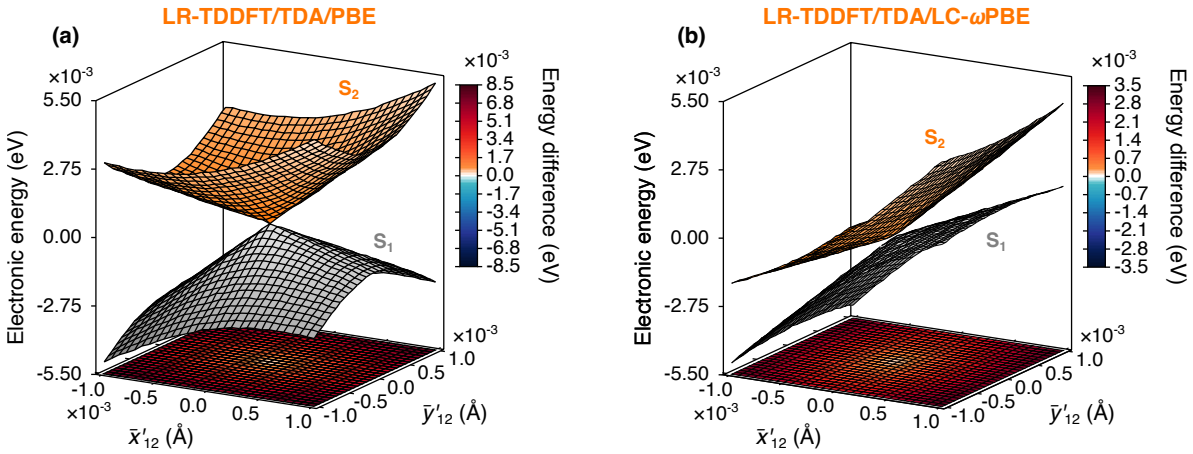

Figure 3.8: Branching space of the S_2/S_1 MECX in pyrazine. S_1 and S_2 excited states obtained with **(a)** LR-TDDFT/TDA/PBE/cc-pVDZ (orange/grey) and **(b)** LR-TDDFT/TDA/LC-ωPBE/cc-pVDZ (orange/grey). In each plot, the MECX geometries and branching space vectors were obtained at the same level of theory used to calculate the electronic energies. The base in each plot shows a 2D colour map of the $S_2 - S_1$ energy difference (see colour bar on the right).

single-path in the other two functionals and in the wavefunction-based methods). To shine partial light on why PBE is showing such a difference in behaviour, it was instructive to plot the four lowest electronic energies along an LIIC pathway between the FC and S_2/S_1 MECX geometries (Fig. 3.9). It is clear that four of the approaches (PBE0, LC-ωPBE, ADC(2) and XMS-CASPT2), locate a higher-lying sloped S_2/S_1 MECX, whereas PBE in fact locates a different much lower-lying S_2/S_1 MECX, which is peaked. Therefore, it is not a matter of PBE incorrectly describing the topography of the MECX of interest, but rather a matter of locating the wrong MECX. This is likely due to the sloped S_2/S_1 MECX in PBE lying too high in

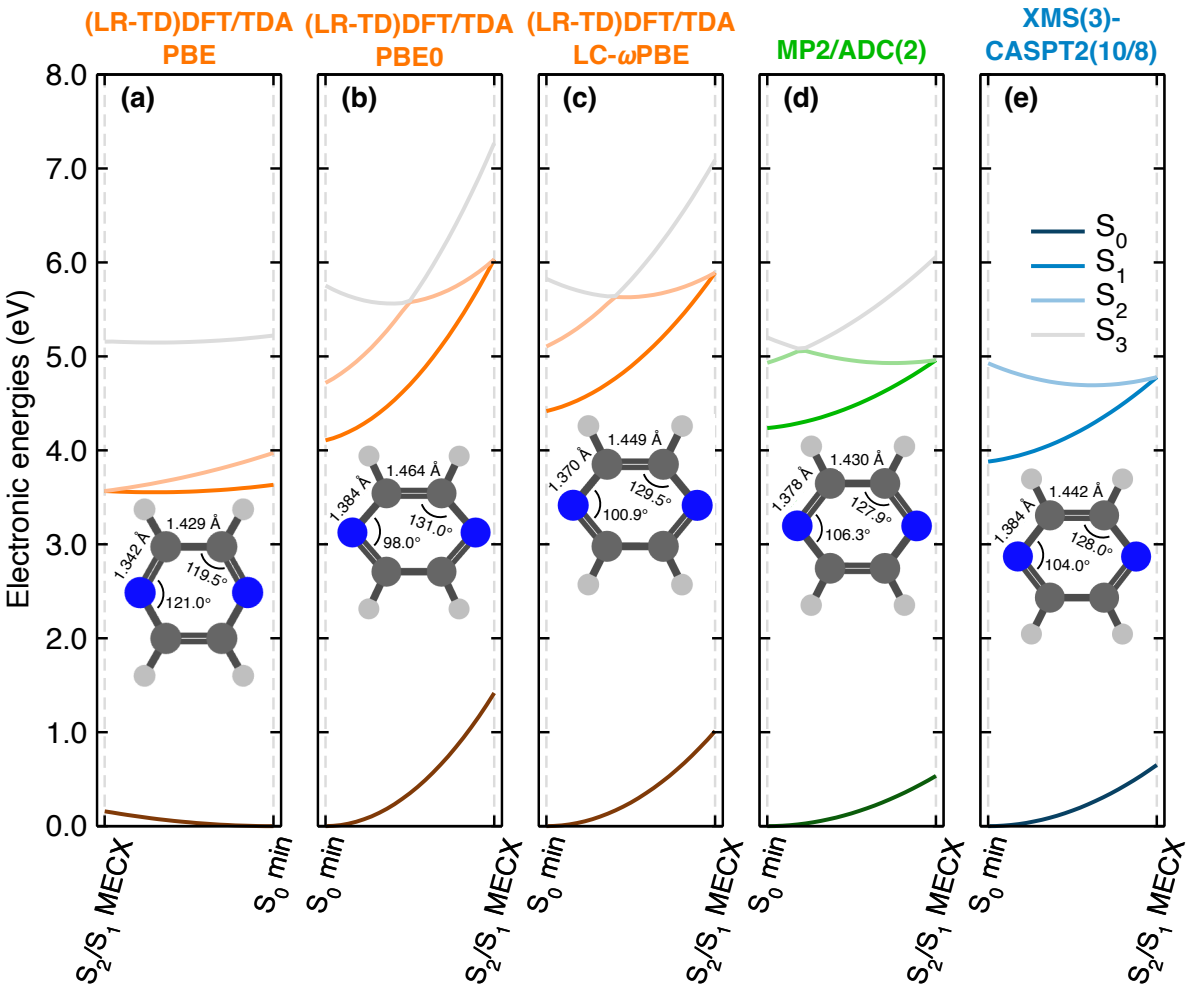

Figure 3.9: LIIC pathways connecting the S_0 minimum and S_2/S_1 MECX in pyrazine. Comparison of the S_0 (dark colour), S_1 (mid colour), S_2 (light colour) and S_2 (grey) electronic energies obtained with **(a)** (LR-TD)DFT/TDA/PBE/cc-pVDZ (orange), **(b)** (LR-TD)DFT/TDA/PBE0/cc-pVDZ (orange), **(c)** (LR-TD)DFT/TDA/LC-ωPBE/cc-pVDZ (orange), **(d)** MP2/ADC(2)/cc-pVTZ (green) and **(e)** XMS(3)-CASPT2(6/4)/cc-pVTZ (blue). In each panel, the critical geometries were optimised at the same level of theory used to compute the electronic energies. The insets show the molecular structures of the S_2/S_1 MECX along with the calculated C-N and C-C bond lengths, and C-N-C and N-C-C bond angles.

energy (i.e., extending beyond the right side of the first panel in Fig. 3.9) to be readily located using the MECX geometry optimisation procedure outlined in Section 3.5.1.2 of the Appendix of this chapter and without manually forcing the optimisation in its direction. Instead the optimisation comes across a more energetically accessible, and thus a more easily locatable, peaked S_2/S_1 MECX. Regardless of this, the performance of all three methods generalises our conclusions that LR-TDDFT/TDA can adequately reproduce the topology of a CX between two excited electronic states, whether or not it is the CX of photochemical interest.

3.4 Conclusions

This chapter has shown explicitly that LR-TDDFT/TDA/PBE0 within the AA is able to exhibit the correct topology of a CX between two *excited* electronic states for two exemplar molecules, protonated formaldimine and pyrazine. The correct CX topology was unchanged when alternative exchange-correlation functionals were investigated for pyrazine. We further showed that ADC(2) offers an accurate description of both the topology and topography of CXs between excited electronic states, and note that this is in contrast to that of (conventional) coupled cluster theory, which can be flawed in this context [111, 208, 211, 389, 390]. We stress that all CX branching spaces analysed in this chapter (and in the entire thesis) were constructed within a fully-consistent approach where all required electronic quantities were computed at the same level of theory [except for the $\mathbf{h}_{IJ}(\mathbf{R})$ vectors in ADC(2)].

Re-inspection of the problem faced by AA (LR-TD)DFT/TDA to adequately describe CXs involving the ground electronic states also proved fruitful. Our findings for protonated formaldimine show that the two, supposedly different, pictures related to the S_1/S_0 MECP branching space of AA (LR-TD)DFT/TDA/PBE0–a seam of intersection vs two interpenetrating cones–both emanate from the intersection ring, which can be reconciled by analysing the behaviour of the PESs, either in the immediate vicinity of the S_1/S_0 MECP, or at further distances from the MECP geometry. The intersection ring from AA (LR-TD)DFT/TDA/PBE0 is in stark contrast to the linear intersection observed from MP2/ADC(2) (and, as expected, HF/CIS). One arguably still needs to pinpoint precisely how nonadiabatic dynamics simulations is influenced by the intersection ring and whether the difference in behaviour of AA (LR-TD)DFT/TDA/PBE0 to that of HF/CIS gives any grounds for optimism when applying AA (LR-TD)DFT/TDA in this context. This is the focus of Chapter 5. Again, extending the use of previously proposed expressions for the (exact) frequency-dependent exchange-correlation kernel [249, 272, 277, 280, 282, 283, 287, 288, 391, 392] to the problem of CXs involving the ground electronic state still remains as pertinent as ever. Nonetheless, for the case of CXs between excited electronic states, greater confidence (at least for electronic states dominated by single excitations) should be felt when applying AA LR-TDDFT/TDA to chemically (and biologically) relevant systems, whose size still prohibits the use of multiconfigurational and

multireference methods.

3.5 Appendix

3.5.1 Supplementary computational details

3.5.1.1 Electronic structure

All electronic energies, nuclear gradients, and nonadiabatic coupling vectors that were computed with the PBE (GGA) functional, the LC-ωPBE (range-separated hybrid) functional, HF and CIS [172] were obtained using a development version of the GPU-accelerated TeraChem 1.9 program [346–352]. In LC-ωPBE, a range-separation parameter of 0.4 a_0^{-1} was used and all AA LR-TDDFT calculations for PBE and LC-ωPBE were performed within the Tamm-Dancoff approximation [268]. The Dunning cc-pVDZ basis set was used in all DFT, AA LR-TDDFT/TDA, HF and CIS calculations [174].

3.5.1.2 Critical points and linear interpolation in internal coordinates

An iterative procedure was used to locate the MECXs (or MECPs) in (LR-TD)DFT/TDA using TeraChem. Each iteration involved performing four separate MECX geometry optimisation calculations using four different algorithms: (i) the GP method of Bearpark *et al.* [215], (ii) the LN method of Manaa and Yarkony [219], (iii) the PF method of Ciminelli *et al.* [220] and (iv) the CIOpt approach (with a CIGap criterion of 0.001 a.u.) of Levine *et al.* [213]. Methods (i)-(iii) were used within TeraChem, whilst method (iv) was externally interfaced to TeraChem. The input geometry for the four MECX optimisation calculations of a given iteration of the procedure was the geometry obtained from the previous iteration that best satisfied the following criteria: the geometry (a) possesses the smallest $E_J^{\mathrm{el}}(\mathbf{R}) - E_I^{\mathrm{el}}(\mathbf{R})$ energy gap [i.e., represents a CX (or CP)], (b) possesses the lowest $E_I^{\mathrm{el}}(\mathbf{R})$ and $E_J^{\mathrm{el}}(\mathbf{R})$ energies (i.e., represents a minimum-energy CX (or CP)) and (c) is chemically sensible/relevant (i.e., corresponds to the MECX (or MECP) of interest). The XMS-CASPT2/cc-pVTZ geometries were used as the initial input geometries for the first iteration of the procedure. The process was repeated until either, all four MECX optimisation algorithms converged on the same geometry, or until the current iteration resulted in an MECX (or MECP) geometry that satisfied the above criteria less well than the geometry obtained in the previous iteration. The procedure took 3-4 iterations in all cases. The final geometry was then taken to be *the* optimised (LR-TD)DFT/TDA MECX (or MECP) geometry.

Similarly, an iterative procedure was used to optimise the MECXs (or MECPs) with MP2/ADC(2). Four consecutive MECX optimisation calculations were performed using CIOpt [213] externally interfaced to Turbomole, where the geometry obtained in the previous optimisation served as the input to the current optimisation. The CIGap criterion was set to

0.01 a.u. for the first MECX optimisation and was decreased by an order of magnitude for each subsequent optimisation, with the XMS-CASPT2/cc-pVTZ geometries again being used as the initial input geometry. After the four consecutive MECX optimisation calculations, the geometry that best satisfied the three criteria (i) to (iii) in the above paragraph was taken to be the preliminary MP2/ADC(2) MECX (or MECP) geometry. Further refinement was performed by computing the raw branching space vectors at this geometry and generating its corresponding raw branching space. The branching space geometry with the smallest $E_J^{\text{el}}(\mathbf{R}) - E_I^{\text{el}}(\mathbf{R})$ energy gap [if different to the original MECX (or MECP) geometry located at the origin] was then redefined as *the* optimised MP2/ADC(2) MECX (or MECP) geometry.

The same procedure used to locate the MECP in (LR-TD)DFT/TDA was used to optimise the MECP geometry in HF/CIS. Further refinement of the HF/CIS S_1/S_0 MECP geometry was carried out by generating the corresponding raw branching space, analogous to the procedure used in optimising the MECX (or MECP) geometries in MP2/ADC(2).

3.5.1.3 Plotting the CX branching space

Orthonormalisation (and alignment) of branching space vectors

To generate the branching space vectors used to construct the MECX (or MECP) branching space plots investigated in this chapter (as well as in Chapters 4 and 5), we followed the approach taken in Ref. [165]. We now summarise this here. The raw branching space vectors, $\mathbf{g}_{IJ}(\mathbf{R})$ and $\mathbf{h}_{IJ}(\mathbf{R})$, were first computed directly at the optimised S_J/S_I MECX (or MECP) geometry. [Note, the $\mathbf{h}_{IJ}(\mathbf{R})$ vectors were first obtained from the corresponding $\mathbf{d}_{IJ}(\mathbf{R})$ vectors by the reverse of the relationship given in Eq. (2.43) in Section 2.2.3, in which $\mathbf{h}_{IJ}(\mathbf{R}) = [E_J^{\text{el}}(\mathbf{R}) - E_I^{\text{el}}(\mathbf{R})] \times \mathbf{d}_{IJ}(\mathbf{R})$. For clarity, we will drop the explicit dependence on '$\mathbf{R}$' hereafter.] At a CX, the two adiabatic electronic states are not uniquely defined, given their degeneracy. The same is true for the raw branching space vectors defined at the CX. Any linear combination of the two adiabatic electronic states are still eigenfunctions of the electronic Hamiltonian, $\hat{H}_{\text{el}}(\mathbf{r}, \mathbf{R})$, with the same eigenvalue; it is this that leads to their non-uniqueness (and that of the branching space vectors) at the CX [86, 118]. In addition, the raw branching space vectors computed using a given electronic-structure method (at an MECX–or MECP–geometry optimised using finite numerical accuracy) are also, in general, not orthogonal to one another [94]. To overcome these two points, we used the Yarkony procedure [88, 359] to obtain the following orthogonalised versions of the branching space vectors,

$$\begin{aligned} \overline{\mathbf{g}}_{IJ} &= \cos(2\beta)\mathbf{g}_{IJ} + \sin(2\beta)\mathbf{h}_{IJ} \\ \overline{\mathbf{h}}_{IJ} &= \cos(2\beta)\mathbf{h}_{IJ} - \sin(2\beta)\mathbf{g}_{IJ} \,. \end{aligned} \tag{3.1}$$

To ensure orthogonality between $\overline{\mathbf{g}}_{IJ}$ and $\overline{\mathbf{h}}_{IJ}$, the required value of β is determined by

satisfying the following equation,

$$\tan(4\beta) = \frac{2\left(\mathbf{g}_{IJ} \cdot \mathbf{h}_{IJ}\right)}{\left(\mathbf{g}_{IJ} \cdot \mathbf{g}_{IJ}\right) - \left(\mathbf{h}_{IJ} \cdot \mathbf{h}_{IJ}\right)}, \tag{3.2}$$

where $\beta = \beta_0 + n\frac{\pi}{4}$ for $n = 0, \pm1, \pm2, ...$ and β_0 is the initial value solution of Eq. (3.2) as stated in Ref. [165]. (Note, this orthogonalisation procedure does not change the branching plane obtained by a given electronic-structure method, but simply orthogonalises the branching space vectors within the plane. This is because, in spite of the non-uniqueness of the individual branching space vectors, the branching plane is, itself, uniquely defined, invariant to which linear combination of the raw branching space vectors is chosen [94].) The $\overline{\mathbf{g}}_{IJ}$ and $\overline{\mathbf{h}}_{IJ}$ vectors were then normalised to give the corresponding unit vectors (or intersection-adapted coordinates) as given already in Eq. (2.29) in Section 2.2.1. These orthonormalised branching space vectors are now uniquely defined (up to trivial transpositions and changes of sign) [101, 165].

To facilitate direct comparison between the MECX (or MECP) branching space plots of the electronic-structure method of *interest* and that of the *reference* electronic-structure method, XMS-CASPT2, we carried out the following. We rotated the orthonormalised branching space vectors of the electronic-structure method of interest, now given as

$$\begin{aligned} \overline{\mathbf{x}}'_{IJ} &= \cos(\theta)\overline{\mathbf{x}}_{IJ} + \sin(\theta)\overline{\mathbf{y}}_{IJ} \\ \overline{\mathbf{y}}'_{IJ} &= \cos(\theta)\overline{\mathbf{y}}_{IJ} - \sin(\theta)\overline{\mathbf{x}}_{IJ} \end{aligned} \tag{3.3}$$

within their corresponding branching plane, to ensure maximal overlap between the rotated $\overline{\mathbf{x}}'_{IJ}$ vector in Eq. (3.3) and the (unrotated) reference branching space vector of XMS-CASPT2, denoted here as $\overline{\mathbf{x}}^{\text{ref}}_{IJ}$. This requires θ in Eq. (3.3) to take the value

$$\theta = \arctan\left(\frac{\overline{\mathbf{y}}_{IJ} \cdot \overline{\mathbf{x}}^{\text{ref}}_{IJ}}{\overline{\mathbf{x}}_{IJ} \cdot \overline{\mathbf{x}}^{\text{ref}}_{IJ}}\right), \tag{3.4}$$

where $\theta = \theta_0 + m\pi$ for $m = 0, \pm1, \pm2, ...$ and θ_0 is the initial value solution of Eq. (3.4) as stated in Ref. [165]. (Note again, this rotation procedure does not change the branching plane obtained by the given electronic-structure method of interest, but simply modifies the orientation of the branching space vectors within the plane by a rigid rotation [94].) The value of m was chosen to ensure that $\overline{\mathbf{x}}'_{IJ} \cdot \overline{\mathbf{x}}^{\text{ref}}_{IJ} > 0$. Therefore, in all cases m took a value of 0 or 1. Equally, the rotated $\overline{\mathbf{y}}'_{IJ}$ vector obtained in Eq. (3.3) agrees well, in general, with the unrotated $\overline{\mathbf{y}}^{ref}_{IJ}$ vector of XMS-CASPT2 (up to a trivial negative sign) [165]. The orthonormalisation and alignment via rigid rotation procedures are summarised schematically in Fig. 3.10.

As a result, a given geometry within the 29×29 grid used to construct the various branching planes studied in this work can be defined as [101]

$$\mathbf{R}(\overline{x}_{IJ}, \overline{y}_{IJ}) = \mathbf{R}_{\text{CX}} + \overline{x}_{IJ}\overline{\mathbf{x}}_{IJ} + \overline{y}_{IJ}\overline{\mathbf{y}}_{IJ} \tag{3.5}$$

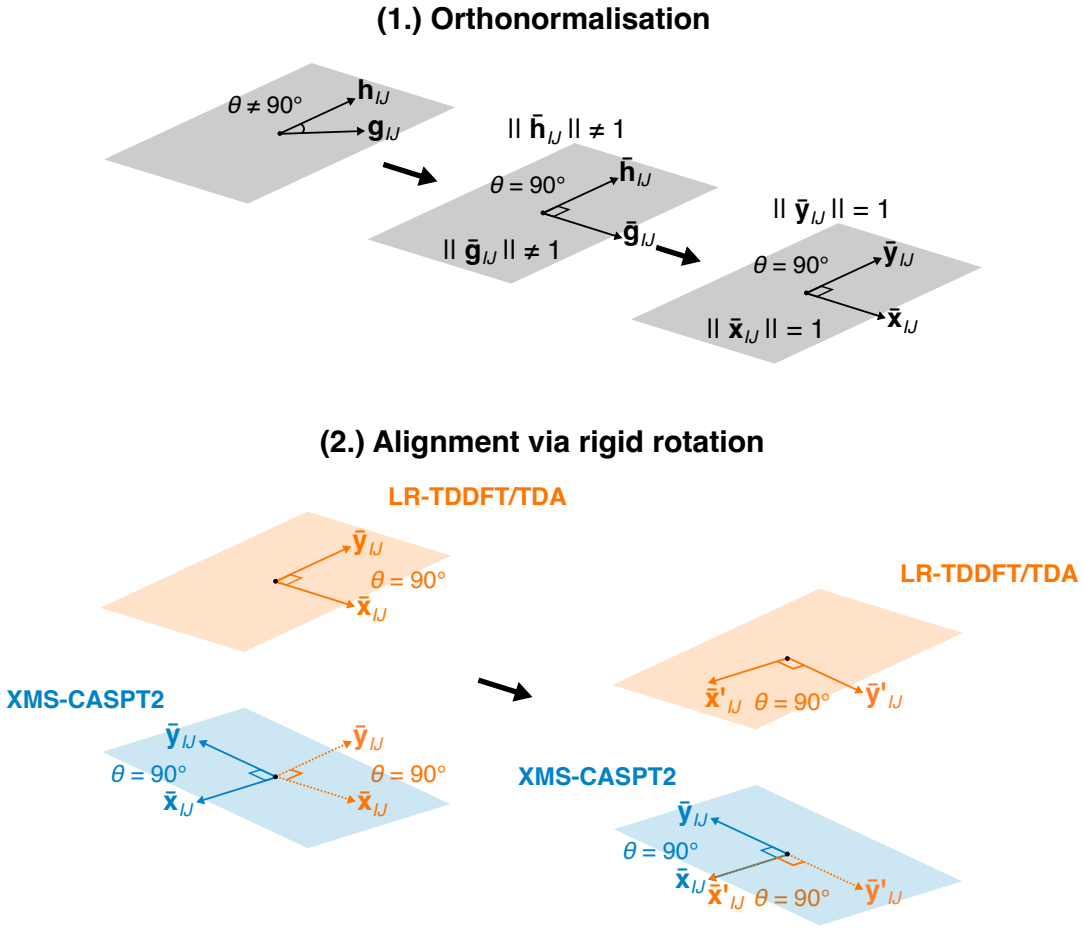

Figure 3.10: Schematic representation of the orthonormalisation and alignment via rigid rotation procedures used to transform the raw branching space vectors.

for XMS-CASPT2, and defined as

$$\mathbf{R}(\overline{x}'_{IJ}, \overline{y}'_{IJ}) = \mathbf{R}_{\mathrm{CX}} + \overline{x}'_{IJ}\overline{\mathbf{x}}'_{IJ} + \overline{y}'_{IJ}\overline{\mathbf{y}}'_{IJ} \tag{3.6}$$

for all other electronic-structure methods, where $\mathbf{R}_{\mathrm{CX}}$ is the optimised MECX (or MECP) geometry, and $\overline{x}_{IJ}/\overline{y}_{IJ}$ and $\overline{x}'_{IJ}/\overline{y}'_{IJ}$ are arbitrary lengths (in units of Å) along the corresponding orthonormalised (and linearised) [393] branching space vectors given in Eqs (2.29) and (3.3), respectively. (Note, $\overline{x}_{IJ}/\overline{y}_{IJ}$ and $\overline{x}'_{IJ}/\overline{y}'_{IJ}$ should not be confused with the magnitudes of the orthonormalised branching space vectors themselves, which are trivially unity by definition, i.e., here $\overline{x}_{IJ} \neq ||\overline{\mathbf{x}}_{IJ}||$, $\overline{y}_{IJ} \neq ||\overline{\mathbf{y}}_{IJ}||$, etc.) It is these lengths ($\overline{x}_{IJ}/\overline{y}_{IJ}$ and $\overline{x}'_{IJ}/\overline{y}'_{IJ}$) that we label the x- and y-axes with in the branching space plots studied in this work.

Practicalities of plotting the extended S_1/S_0 branching space in (LR-TD)DFT/TDA

We note that we experienced initial issues with KS SCF convergence for certain geometries along the extended S_1/S_0 branching plane. Such convergence problems have been attributed

previously by Casida and coworkers [28, 94, 232, 274, 291] to an effective violation of (pure state) non-interacting v-representability near the CX (i.e., the LUMO energy becomes lower than the HOMO energy). We followed Ref. [28] and used the converged KS orbitals from neighbouring geometries as the initial guesses for the KS SCF calculations at the problematic geometries. This leads to much improved convergence and smoother PESs along the extended S_1/S_0 branching plane. In line with Ref. [394], we present the scheme used to propagate the initial KS orbital guesses along the extended S_1/S_0 branching plane (Fig. 3.11) so to restrict the region of geometries which afford negative excitation energies. It is worth highlighting that the process of using converged KS orbitals from the previous iteration or time step as the starting guess for the next geometry has been routine practice within geometry optimisations and BO molecular dynamics simulations for some time [395–398].

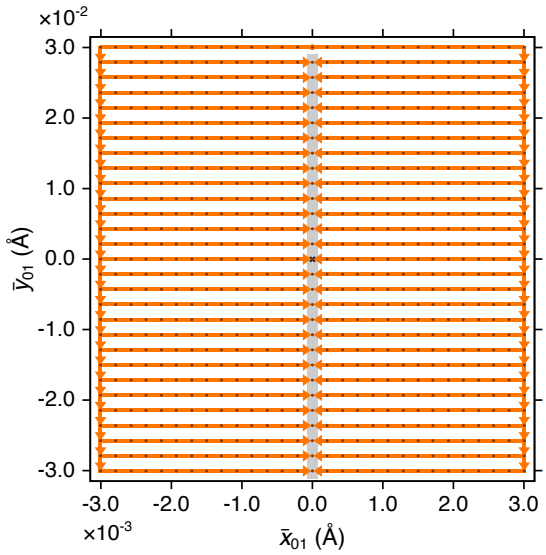

Figure 3.11: Schematic representation of the algorithm used to propagate the KS orbitals along the extended S_1/S_0 branching space. The grey shaded area represents the geometries where a choice was made to either use the converged KS orbitals of the left or right neighbour as an initial guess for the KS SCF calculation, depending on which gave the lowest S_0 energy at that geometry. The black cross indicates the location of the S_1/S_0 MECP geometry.

3.5.2 Supplementary figures

This section includes additional figures that have already been referred to at various points in the main text of this chapter. Here, we provide further commentary on Fig. 3.12. The S_1 and S_2 electronic characters reported for LR-TDDFT/TDA/PBE0 and ADC(2) at their respective S_2/S_1 MECX geometries [Fig. 3.12(a)] show reasonable agreement with one another (except for differences in the minor orbital contributions). The branching space vectors [Fig. 3.12(b)] given by both methods also agree strongly.

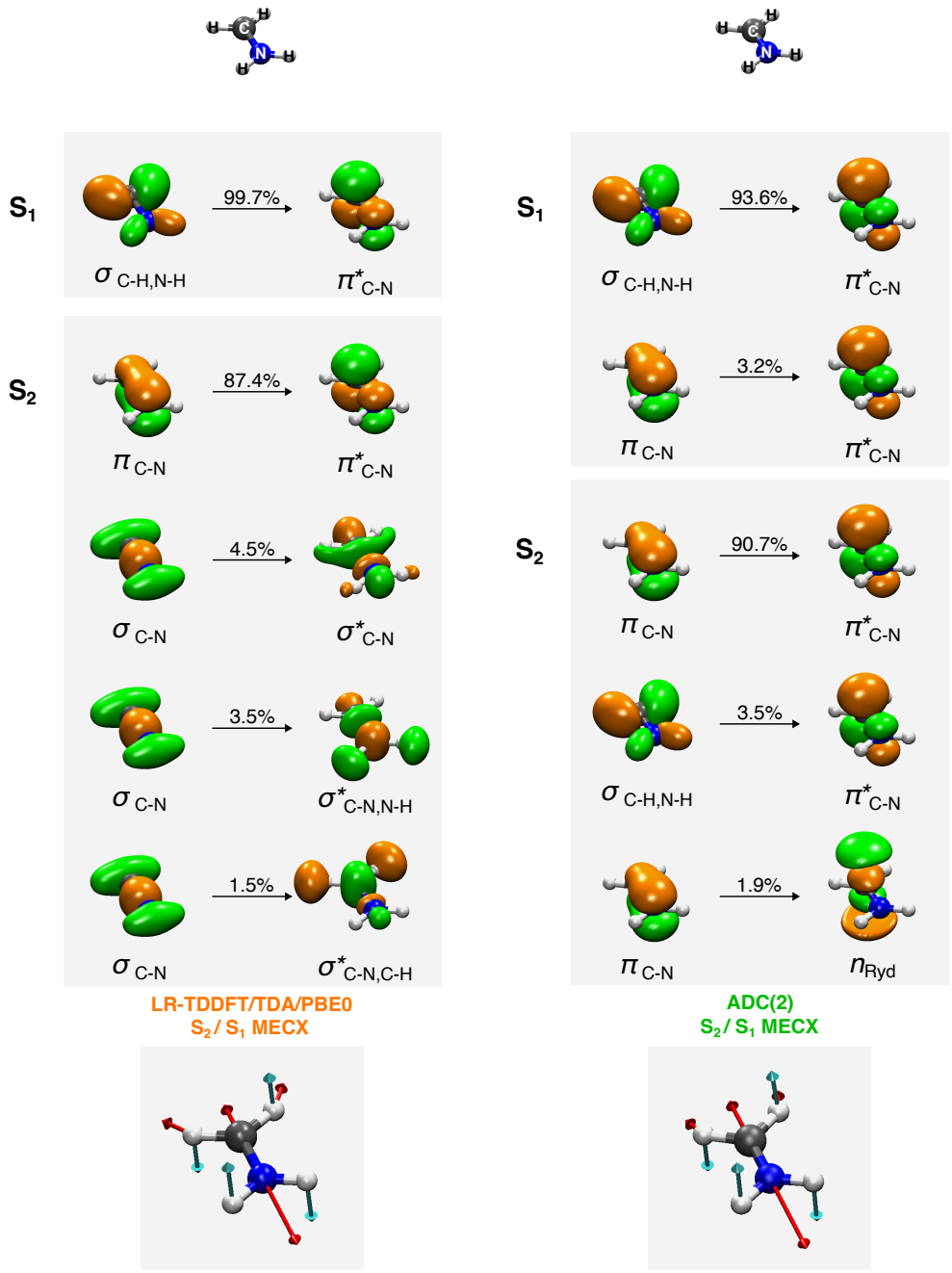

Figure 3.12: (Top) Orbital excitation contributions to the S_1 and S_2 electronic energies computed at the optimised S_2/S_1 MECX geometry in protonated formaldimine for LR-TDDFT/TDA/PBE0/cc-pVDZ and ADC(2)/cc-pVTZ, respectively. The orbitals are plotted using an isovalue of 0.075, with the labelled geometries provided above. **(Bottom)** Branching space vectors, $\bar{\mathbf{x}}'_{12}(\mathbf{R})$ (red, using a scaling factor of 5.0) and $\bar{\mathbf{y}}'_{12}(\mathbf{R})$ (cyan, using a scaling factor of 2.5), plotted on the optimised S_2/S_1 MECX geometry for LR-TDDFT/TDA/PBE0/cc-pVDZ and ADC(2)/cc-pVTZ(/XMS(3)-CASPT2(6/4)/cc-pVTZ), respectively.

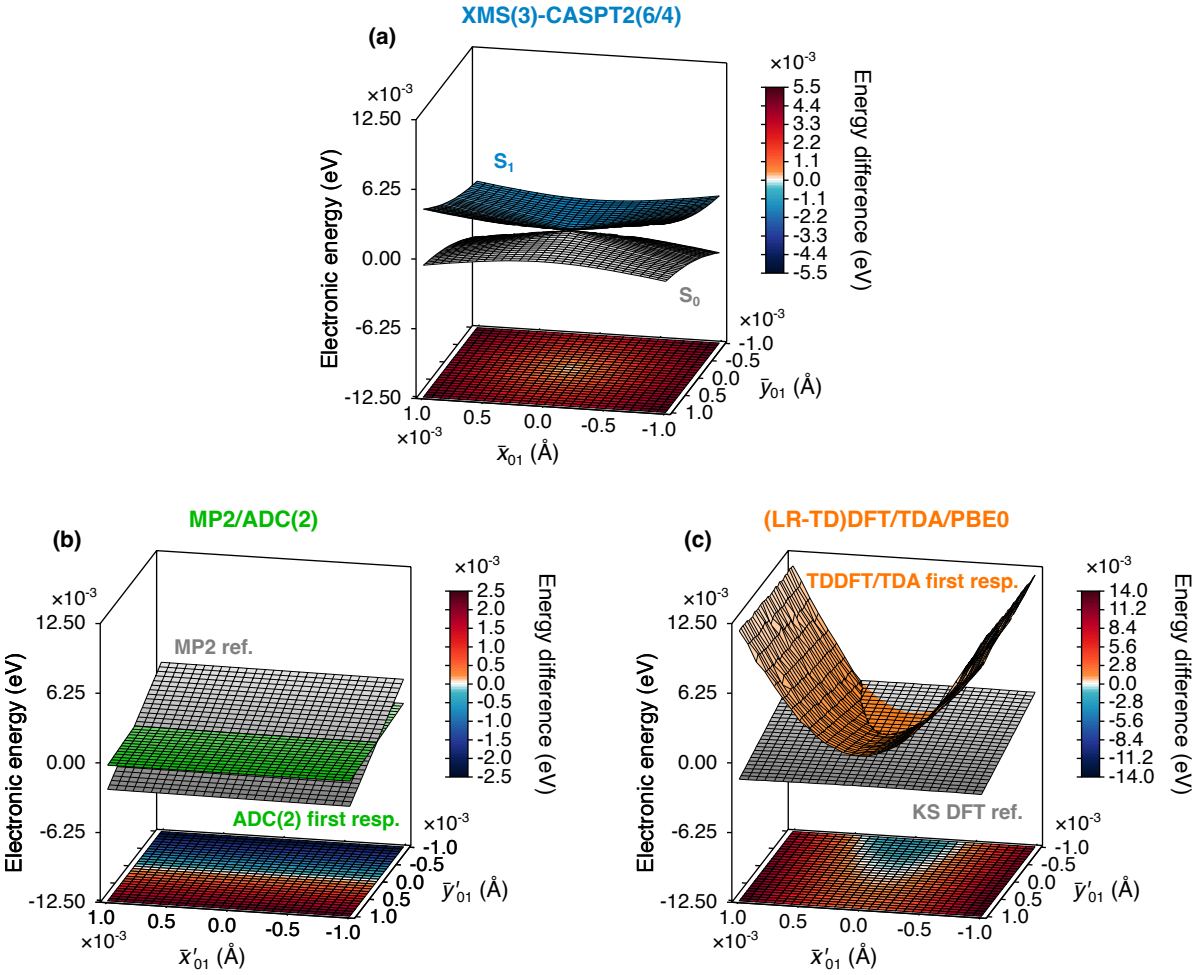

Figure 3.13: Branching space of the S_1/S_0 MECX (or MECP) in protonated formaldimine. Same as in Fig. 3.4 except all PESs are plotted at the same electronic energy range on the vertical axis.

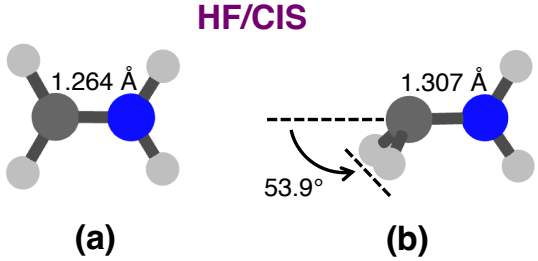

Figure 3.14: Molecular structure of **(a)** the S_0 minimum and **(b)** the S_2/S_1 MECX geometries in protonated formaldimine optimised at the HF/CIS/cc-pVDZ level of theory.

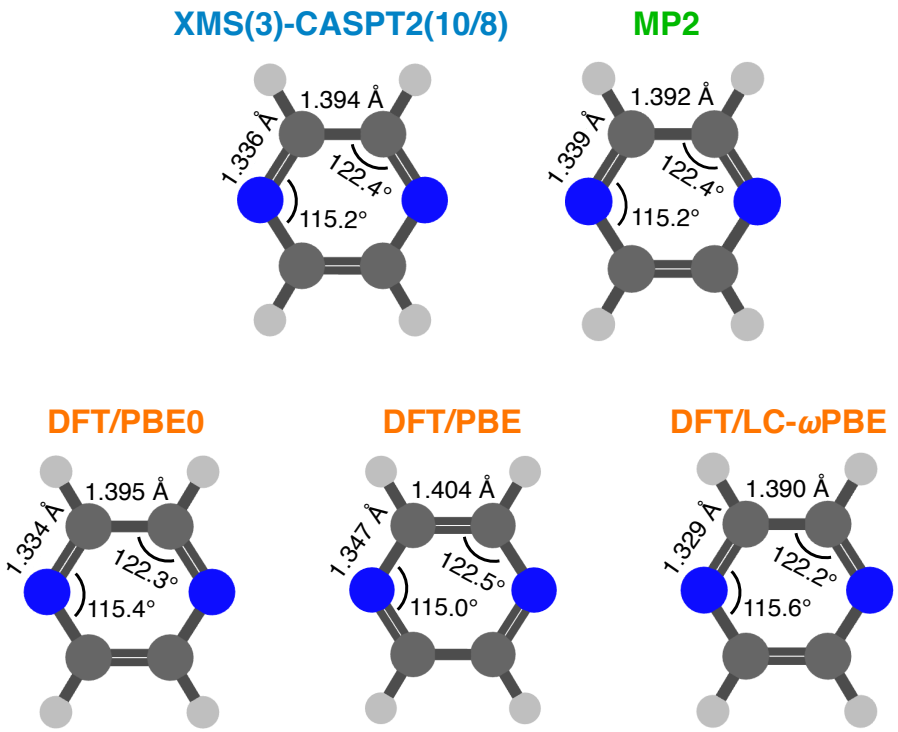

Figure 3.15: Molecular structure of the S_0 minimum in pyrazine optimised at the XMS(3)-CASPT2(10/8)/cc-pVTZ, MP2/cc-pVTZ, DFT/PBE0/cc-pVDZ, DFT/PBE/cc-pVDZ and DFT/LC-ωPBE/cc-pVDZ levels of theory.

Chapter 4

On the topological phase around conical intersections with AA LR-TDDFT

This chapter is based on the publication:
J. T. Taylor, D. J. Tozer and B. F. E. Curchod, "On the topological phase around conical intersections in Tamm-Dancoff linear-response time-dependent density functional theory", *The Journal of Physical Chemistry A*, 2024, **128**, 5314-5320. (Ref. [344])

4.1 Introduction

The analysis in Chapter 3 centred primarily on visualising the PESs in the branching space of a given MECX (or MECPs) [29] to establish its dimensionality, as well as calculating numerical parameters [68, 101] to characterise its topography (where appropriate). Electronic energies computed at 'optimised' CX geometries determined using standard electronic-structure codes are, however, never exactly degenerate due to finite numerical accuracy [88]. Therefore, it is not strictly possible to establish whether a CX (rather than a narrowly avoided crossing) has been located from inspection of the PESs in the branching space alone [80]. The existence of a CX can, however, be verified (as mentioned in Section 2.2.3) by considering the topological phase effect: [141, 142, 147, 399] a (real-valued) adiabatic electronic wavefunction accumulates an additional topological phase of π, i.e., it changes sign, as it traverses a path enclosing a CX. Thus, examining the sign of the electronic wavefunction obtained from a given electronic-structure method along a closed path within the branching plane can be used to determine whether a CX has indeed been located. In the absence of a CX, no additional topological phase/sign-change of the adiabatic electronic wavefunction is observed along the closed path.

The focus of this thesis, however, is the performance of AA LR-TDDFT/TDA, which has no formal access to the interacting electronic wavefunction. It is therefore necessary to examine

an alternative, albeit intrinsically related, signature of CXs. Specifically, the circulation of the (first-order) nonadiabatic coupling vector, $\mathbf{d}_{IJ}(\mathbf{R})$, that is its (vector) line integral along a closed path C_n,

$$\gamma_n = \oint_{C_n} \mathbf{d}_{IJ}(\mathbf{R}) \cdot d\mathbf{R} \ , \tag{4.1}$$

should, in the case of an infinitesimal path, return the accumulated topological phase – i.e., it should return a value of π if the path C_n encloses a CX, or a value of zero if the path does not enclose a CX [80, 88, 102, 400–404]. In Eq. (4.1), I and J denote electronic states, $\mathbf{R}$ denotes a collective variable for all nuclear coordinates and n labels the closed path of interest. In practical calculations, the path C_n will be small but not infinitesimal, so values close to, but not exactly equal to, π or zero will be obtained.

Given that $\mathbf{d}_{IJ}(\mathbf{R})$ vectors are well-defined [332] quantities in TDDFT, they can be used within Eq. (4.1) to provide incontrovertible evidence of the presence of a CX. However, as mentioned in Section 3.1, when evaluated between two excited electronic states, the $\mathbf{d}_{IJ}(\mathbf{R})$ vectors can only be defined exactly within a quadratic-response (QR) formalism [329–333, 336]. An interesting question therefore arises: does Eq. (4.1) return a value close to π when evaluated using AA LR-TDDFT/TDA along paths enclosing the optimised S_2/S_1 MECXs in protonated formalidimine and pyrazine in Ref. [29], despite the use of (approximate) linear-response $\mathbf{d}_{IJ}(\mathbf{R})$ vectors? We note, earlier works in connection with the pseudo-wavefunction approximation to AA LR-TDDFT(/TDA) [335, 338, 405, 406], as well as AA QR-TDDFT(/TDA) [335], have discussed the value of Eq. (4.1) in this context–all reported a value of γ_n close to π.

A second interesting question is what value will Eq. (4.1) return when evaluated using AA LR-TDDFT/TDA along a path enclosing the S_1/S_0 intersection ring observed for protonated formaldimine in Chapter 3? In this case, exact $\mathbf{d}_{IJ}(\mathbf{R})$ vectors involving the ground electronic state can be obtained from linear-response TDDFT, yet it is the incorrect behaviour of the PESs within the vicinity of the supposed degeneracy point that results in the infamous failure of LR-TDDFT in this context. As stressed most recently by Williams *et al.* [407] in relation to 'defective' excited-to-excited state MECXs in EOM-CCSD,[1] the topological phase effect is only observed (i.e., Eq. (4.1) returns π) if the path C_n encloses an odd number of CXs ; if C_n encloses an even number of CXs, then the topological phase effect is not observed (i.e., Eq. (4.1) returns zero). This is a more general statement than that presented above and is an important detail relevant to our present work–the AA LR-TDDFT/TDA S_1/S_0 intersection ring arguably comprises an *infinite* number of degeneracy points, not just a single point of degeneracy, so it is not immediately obvious as to what value Eq. (4.1) should take.

The purpose of this chapter is to address these two questions. We organise the chapter as follows: We begin by providing computational details, in particular highlighting how Eq. (4.1)

[1] EOM-CCSD denotes equation-of-motion coupled-cluster theory with singles and doubles.

was numerically evaluated in practice. We then compare values of γ_n from Eq. (4.1), determined using AA LR-TDDFT/TDA, with those from XMS-CASPT2–our reference electronic-structure method of choice–evaluated along closed paths on the respective MECX (or MECP) branching planes for protonated formaldimine (S_2/S_1 and S_1/S_0) and pyrazine (S_2/S_1).

4.2 Computational details

4.2.1 Electronic structure

All electronic structure details relating to the XMS-CASPT2, DFT and AA LR-TDDFT calculations performed in this chapter are the same as those reported in Section 3.2.1 of Chapter 3.

4.2.2 Plotting the CX branching space

All details relating to the optimisation of the S_J/S_I MECX (or MECP) geometries and the plotting of their corresponding branching spaces performed in this chapter are the same as those reported in Sections 3.2.2, 3.2.3, 3.5.1.2 and 3.5.1.3 of Chapter 3. However, within all figures in this chapter, it is the $S_J - S_I$ energy difference, rather than the electronic energies of the individual adiabatic states, that is plotted at each grid-point geometry along the branching plane.

4.2.3 Calculating the circulation of the nonadiabatic coupling vector

To evaluate γ_n in Eq. (4.1), we defined a closed rectangular [403, 404] path, C_n, utilising the precomputed grid of geometries[2] that defined the respective S_J/S_I MECX (or MECP) branching plane (see Figs 4.1 and 4.2). The total line integral in Eq. (4.1) was split into four separate line integrals, one along each of the four straight-line segments [Eq. (4.2a)]. For each straight-line segment, the nuclear coordinate vector, $\mathbf{R}_m$, was parameterised as a linear interpolation between the initial and final geometries, $\mathbf{R}_m = \mathbf{R}_m^{\text{init.}} + \alpha_m \Delta\mathbf{R}_m$, using a scalar parameter, $0 \leq \alpha_m \leq 1$. The line integral was then transformed to a standard integral over α_m, for which the integrand, $f(\alpha_m)$, is the dot product of the $\mathbf{d}_{IJ}(\mathbf{R})$ vector and the vector defining the difference between the initial and final geometries along the segment, $\Delta\mathbf{R}_m = \mathbf{R}_m^{\text{fin.}} - \mathbf{R}_m^{\text{init.}}$ [Eqs (4.2b) and (4.2c)]. This integral was evaluated numerically using the trapezoidal rule [408] with the relevant grid-point geometries [Eq. (4.2d)]. This can all be summarised as follows:

[2]As mentioned in Section 2.2.3, since we only consider closed paths, γ_n does not depend on the geometry of such paths. Therefore, we are formally free to choose whichever geometry of path we wish. For simplicity, we opt to use a rectangular path, in keeping with the precomputed grid of geometries, however, we could have equally defined a circular one, which is more typical in the literature [335, 338, 405, 406].

$$\oint_{C_n} \mathbf{d}_{IJ}(\mathbf{R}) \cdot d\mathbf{R} = \sum_{m=1}^{4} \int_{C_n^{(m)}} \mathbf{d}_{IJ}(\mathbf{R}_m) \cdot d\mathbf{R}_m \tag{4.2a}$$

$$= \sum_{m=1}^{4} \int_0^1 \mathbf{d}_{IJ}(\mathbf{R}_m(\alpha_m)) \cdot \Delta\mathbf{R}_m(\alpha_m)\, d\alpha_m \tag{4.2b}$$

$$= \sum_{m=1}^{4} \int_0^1 f(\alpha_m)\, d\alpha_m \tag{4.2c}$$

$$\approx \sum_{m=1}^{4} \frac{1}{N_{\text{grid}-1}} \left[\sum_{k=2}^{N_{\text{grid}-1}} f(\alpha_m^{(k)}) + \frac{f(\alpha_m^{(1)}) + f(\alpha_m^{(N_{\text{grid}})})}{2} \right], \tag{4.2d}$$

where m runs over the number of straight-line segments, k runs over the numerical integration grid-points and N_{grid} is the number of grid-point geometries along each straight-line segment. We note, errors arising from the use of a finite grid of geometries will contribute to the discrepancies between γ_n and π (or zero), in addition to those mentioned in Section 4.1.

To correct random sign-flipping of the $\mathbf{d}_{IJ}(\mathbf{R})$ vectors[3] along the closed rectangular paths in protonated formaldimine, we first inspected the sign of a related quantity, namely the transition dipole moment (TDM), along the same path and manually flipped the sign of the TDM at a given geometry to ensure it varied smoothly (i.e., it was continuous) as a function of the nuclear coordinates. At the same geometries, we then manually corrected the sign of the corresponding $\mathbf{d}_{IJ}(\mathbf{R})$ vector accordingly. The same procedure could not be used for pyrazine because the TDM is zero by symmetry. Instead, we manually corrected the sign of $\mathbf{d}_{IJ}(\mathbf{R})$ in order to ensure that the dot product between $\mathbf{d}_{IJ}(\mathbf{R})$ vectors computed at subsequent geometries along the closed rectangular path was positive.

4.3 Results and discussion

4.3.1 S_2/S_1 MECX branching space

We start by considering the lowest two singlet excited states, S_1 and S_2, in protonated formaldimine, plotting the $S_2 - S_1$ energy difference in the vicinity of the S_2/S_1 MECX within the branching space [Figs 4.1(a) and 4.1(b)]. The value of γ_n in Eq. (4.1) was calculated along two closed rectangular paths: (i) one centred on the optimised S_2/S_1 MECX geometry, i.e., point $\overline{x}_{12} = 0.0$ Å, $\overline{y}_{12} = 0.0$ Å (C_1 in Fig. 4.1) and (ii) the other displaced from the optimised S_2/S_1 MECX geometry, i.e., centred on grid point $\overline{x}_{12} = 0.0005$ Å, $\overline{y}_{12} = -0.0005$ Å ($C_{1'}$ in

[3]The signs of (adiabatic) electronic wavefunctions computed with standard electronic-structure codes are assigned arbitrarily [409]. This result arises because multiplying a given adiabatic electronic wavefunction (i.e., an eigenfunction of the electronic Hamiltonian) by a phase factor still returns a valid eigenfunction [12]. Therefore, it is highly possible, in practice, for an (adiabatic) electronic wavefunction, $\psi_I(\mathbf{R})$, computed at two neighbouring geometries to randomly differ in sign. The same can also apply to $\mathbf{d}_{IJ}(\mathbf{R})$ [Eq. 2.8], as the phases of two different (adiabatic) electronic states, $\psi_I(\mathbf{R})$ and $\psi_J(\mathbf{R})$, may not necessarily cancel out [12, 14, 409, 410].

Fig. 4.1). In the former case, the MECX is enclosed by the path, whereas in the latter it is not. It is therefore expected that in the first (second) case, when Eq. (4.1) is evaluated exactly along a modest-sized loop, the value of γ_n should be close to π (zero). Indeed, this is what is observed for XMS-CASPT2, as is evident from the corresponding values of γ_n reported in Table 4.1.

Table 4.1: Values of γ_n [Eq. (4.1)] along the closed paths C_n (Fig. 4.1) on the branching plane of the S_2/S_1 MECXs in protonated formaldimine and pyrazine. Values are reported in units of π.

protonated formaldimine	XMS(3)-CASPT2(6/4)	LR-TDDFT/TDA/PBE0
C_1	0.99967	1.00050
$C_{1'}$	0.00021	0.00172
pyrazine	XMS(3)-CASPT2(10/8)	LR-TDDFT/TDA/PBE0
C_1	0.99932	0.99916

As alluded to in Section 4.1, the situation for LR-TDDFT/TDA/PBE0 is arguably not as clear. Between excited electronic states, $\mathbf{d}_{IJ}(\mathbf{R})$ vectors computed within linear-response TDDFT can only ever be approximate (even in the limit that the linear-response formalism is, itself, exact), due to the formal requirement of needing to go to quadratic response. Therefore, should it be expected that the LR-TDDFT/TDA/PBE0 $\mathbf{d}_{12}(\mathbf{R})$ vectors match the correct behaviour of those of XMS-CASPT2? Inspecting Table 4.1, the answer to this question is Yes; Eq. (4.1) calculated using LR-TDDFT/TDA/PBE0 quantities appropriately returns values of γ_n close to π and zero, respectively, for paths C_1 and $C_{1'}$, respectively. For these two states, which are admittedly dominated by single excitations, LR-TDDFT/TDA unequivocally provides not only the correct topology of CXs between excited electronic states (as discussed in Chapter 3), but also shows the correct physics (i.e., the topological phase) in their vicinity. The success of LR-TDDFT/TDA/PBE0 at reproducing the topological phase upon adiabatic transport around a CX between two excited electronic states is further corroborated by considering the S_2/S_1 MECX in pyrazine [Figs 4.1(c) and 4.1(d)]. Again, both XMS-CASPT2 and LR-TDDFT/TDA/PBE0 correctly predict a value of γ_n close to π for a path enclosing the MECX–see Table 4.1.

4.3.2 S_1/S_0 MECX (or MECP) branching space

We now focus our attention on the S_1/S_0 MECX in protonated formaldimine. For direct comparison between both methods, we plotted the XMS-CASPT2 $S_1 - S_0$ energy difference along an extended branching plane ($\pm 0.003 \times \bar{\mathbf{x}}_{01}(\mathbf{R})$ and $\pm 0.03 \times \bar{\mathbf{y}}_{01}(\mathbf{R})$), the same dimensions as required to observe the S_1/S_0 intersection ring in (LR-TD)DFT/TDA/PBE0 (Fig. 4.2). Again for XMS-CASPT2, the value of γ_n for a rectangular path enclosing the S_1/S_0 MECX geometry [C_1 in Fig. 4.2(a)] is correctly close to π (Table 4.2). This is unsurprising given that

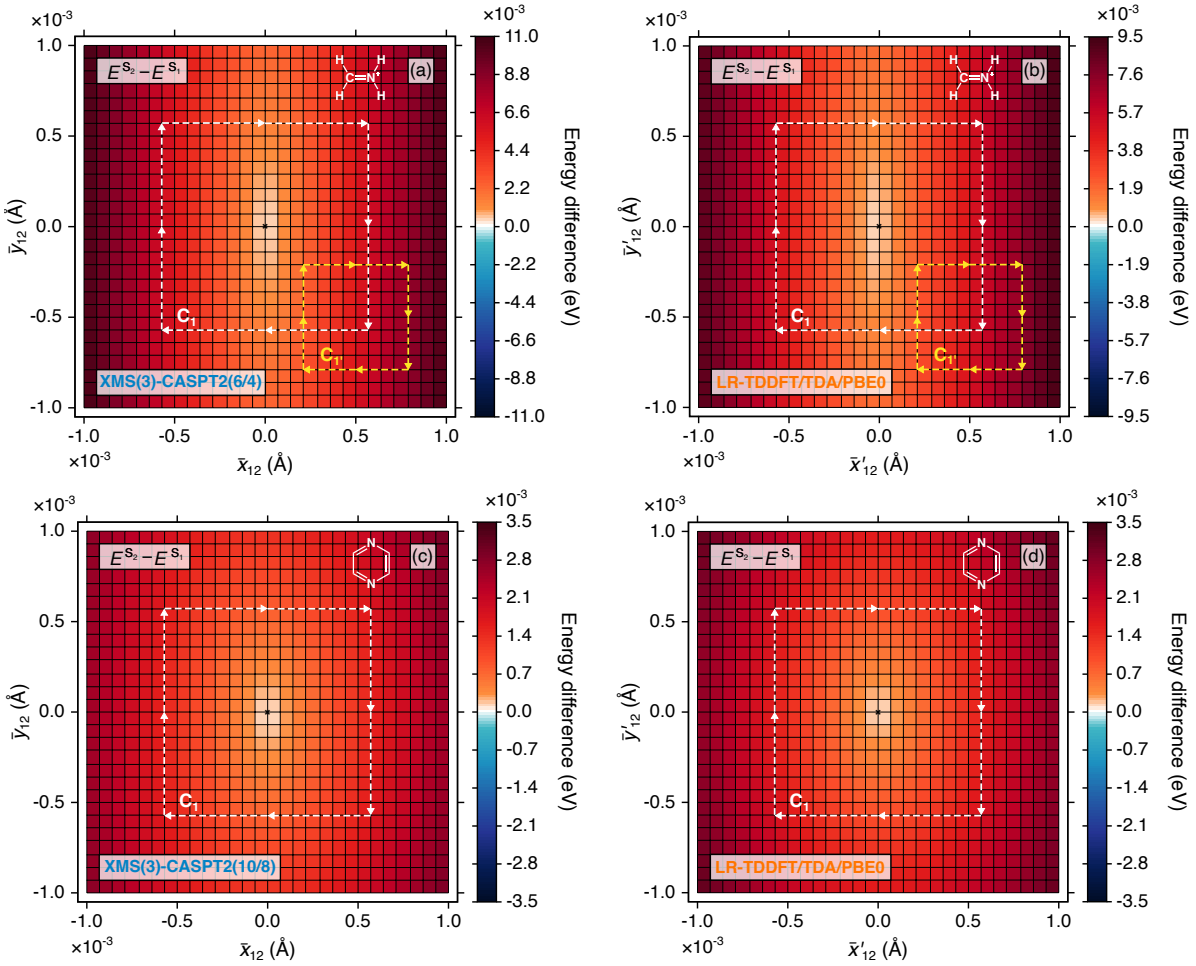

Figure 4.1: 2D colour map of the electronic energy difference between S_1 and S_2 in the vicinity of the S_2/S_1 MECX in **(a)** protonated formaldimine with XMS(3)-CASPT2(6/4)/cc-pVTZ, **(b)** protonated formaldimine with LR-TDDFT/TDA/PBE0/cc-pVDZ, **(c)** pyrazine with XMS(3)-CASPT2(10/8)/cc-pVTZ and **(d)** pyrazine with LR-TDDFT/TDA/PBE0/cc-pVDZ. The dashed arrows indicate the direction of the closed paths, C_1 and $C_{1'}$, along which γ_n in Eq. (4.1) is evaluated–see Table 4.1 for numerical values. The black cross indicates the location of the optimised S_2/S_1 MECX geometry. The Lewis structure of both molecules are given as an inset in each plot.

XMS-CASPT2–a multireference electronic-structure method–has no difficulty in describing CXs involving the ground electronic state.

Predicting the influence of the S_1/S_0 intersection ring in (LR-TD)DFT/TDA/PBE0, however, is less trivial, considering that it comprises an infinite number of degeneracy points, as opposed to a single point of degeneracy. Williams *et al.* [407] showed that the 'defective' CXs between excited electronic states in EOM-CCSD, which show a similar ring-like intersection (although for different reasons[4]), do in fact reproduce the topological phase effect, giving

[4]We note, while it is possible for excitation energies in full LR-TDDFT to erroneously become imaginary

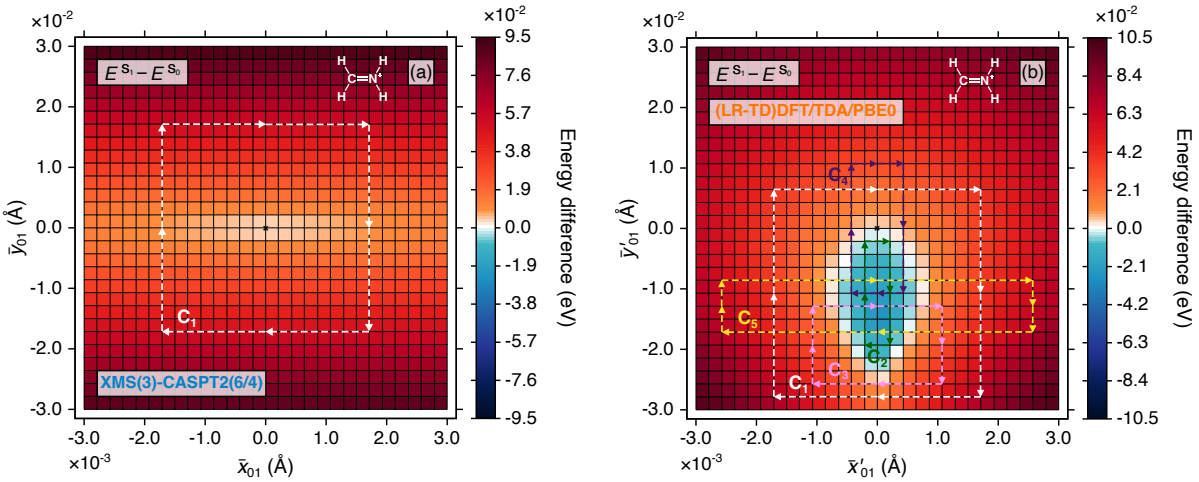

Figure 4.2: 2D colour map of the electronic energy difference between S_0 and S_1 in the vicinity of the S_1/S_0 MECX (or MECP) in protonated formaldimine along an extended branching plane with **(a)** XMS(3)-CASPT2(6/4)/cc-pVTZ and **(b)** (LR-TD)DFT/TDA/PBE0/cc-pVDZ. The dashed arrows indicate the direction of the closed paths, C_1 to C_5, along which γ_n in Eq. (4.1) is evaluated–see Table 4.2 for numerical values. The black cross indicates the location of the optimised S_1/S_0 MECX (or MECP) geometry. The Lewis structure of protonated formaldimine is given as an inset in each plot.

hope for the application of this method in excited-state dynamics simulations, provided the nuclear wave packet never ventures too close to the 'defective' excited-to-excited state CX. We therefore consider whether (LR-TD)DFT/TDA/PBE0 shows a similar positive behaviour for the intersection ring between the ground and first excited electronic states, despite its incorrect dimensionality. Evaluating γ_n for a path enclosing the entire S_1/S_0 intersection ring [C_1 in Fig. 4.2(b)] within the extended branching plane yields a value close to zero (Table 4.2), suggesting that (LR-TD)DFT/TDA/PBE0 fails to reproduce the topological phase.

Table 4.2: Values of γ_n [Eq. (4.1)] along the closed paths C_n (Fig. 4.2) on the branching plane of the S_1/S_0 MECX (or MECP) in protonated formaldimine. Values are reported in units of π.

protonated formaldimine	XMS(3)-CASPT2(6/4)	(LR-TD)DFT/TDA/PBE0
C_1	1.00205	0.00029
C_2	-	0.00620
C_3	-	0.00811
C_4	-	0.00807
C_5	-	0.00066

In order to give a fair judgement of (LR-TD)DFT/TDA/PBE0, however, we ask a follow-up question. Do we obtain a value of γ_n close to π for (LR-TD)DFT/TDA/PBE0, if we instead

at certain nuclear geometries, invoking the TDA (as was done in the present study) forces such excitation energies to be strictly real, but still possibly negative [269, 411, 412]. As such, differences in the behaviour of the (LR-TD)DFT/TDA ground-to-excited state 'defective' CX here, and the EOM-CCSD excited-to-excited state 'defective' CX in Ref. [407] are perhaps not that surprising.

consider a closed path *fully inside* the S_1/S_0 intersection ring (i.e., the region of negative excitation energies)? It could be argued that defining such a path would enclose only a single point of interest related to the tip of one (or both) of the interpenetrating cones (i.e., the supposed geometry of the hypothetical true CX), but would exclude the–to again use the language of Williams *et al*. [407]–'defective' ring of infinite degeneracy points. We therefore looked at a second path, C_2, which is now completely within the intersection ring [Fig. 4.2(b)], yet once again we obtain a value of γ_n close to zero (Table 4.2).

Finally, we also considered three further cases, where only a portion of the intersection ring is enclosed by the path: (i) C_3, which crosses the intersection ring twice along one side of the rectangle; (ii) C_4, which crosses the intersection ring once on one side and once on the opposite side of the rectangle; and (iii) C_5, which crosses the intersection ring four times. In all cases, γ_n is close to zero (Table 4.2).

Our results indicate that even though (LR-TD)DFT/TDA/PBE0 exhibits something reminiscent of two interpenetrating cones (or even an 'approximate' CX [28]) between the ground and first excited electronic states in protonated formaldimine, it does not recover anything resembling the topological phase for any of the closed paths considered.

4.4 Conclusions

The work in this chapter shows that AA LR-TDDFT/TDA/PBE0 is able to accurately reproduce the topological phase accumulated by the adiabatic electronic wavefunction along a path enclosing the S_2/S_1 MECX in protonated formaldimine and pyrazine, despite the use of approximate linear-response (rather than the appropriate quadratic-response) TDDFT $\mathbf{d}_{IJ}(\mathbf{R})$ vectors. The observation provides further evidence that AA LR-TDDFT/TDA offers a reasonable description of CXs between excited electronic states, not only with respect to CX topology and topography, as previously illustrated in Chapter 3, but also with respect to the physics within the immediate vicinity of the degeneracy point. This provides further confidence in the use of AA LR-TDDFT/TDA for excited-state dynamics simulations involving states of predominantly single-excitation character.

For a path enclosing the S_1/S_0 intersection ring exhibited by AA (LR-TD)DFT/TDA/PBE0 in protonated formaldimine, our findings are less fruitful: the topological phase is not reproduced. The same observation is made for a path fully inside the intersection ring and for three paths that cross it. Nonetheless, further investigation is still needed to see whether the lack of the correct topological phase behaviour by the S_1/S_0 intersection ring in AA (LR-TD)DFT/TDA/PBE0 drastically affects the accuracy of nonadiabatic dynamics simulations of protonated formaldimine, especially considering the number of different strategies employed in surface-hopping dynamics simulations to hop between electronic states in the vicinity of CXs. This is the topic of Chapter 5.

CHAPTER 5

On trajectory surface-hopping near ground-to-excited state conical intersections with AA LR-TDDFT

5.1 Introduction

In the previous two chapters, we scrutinised the quality of the PESs in the immediate vicinity of the MECXs (or MECPs), afforded by AA (LR-TD)DFT/TDA and XMS-CASPT2 [and MP2/ADC(2)], from a predominantly static perspective. Consideration of the topological phase in Chapter 4 [344], arguably, brought some dynamical element to the analysis. However, both chapters explicitly highlighted the need to further explore the influence of the AA (LR-TD)DFT/TDA S_1/S_0 intersection ring on the nonadiabatic dynamics of protonated formaldimine. This is the purpose of the present chapter.

Even with the issue of defective ground-to-excited state CXs, AA (LR-TD)DFT/TDA continues to be extensively used in nonadiabatic dynamics simulations [100, 294, 324, 333, 413–418]. Opinions in the literature relating to whether AA (LR-TD)DFT/TDA is at all suitable for following dynamics to the ground electronic state, however, still remain divided. Some argue for optimism [28, 418], at least in achieving semi-quantitative accuracy, whereas others recommend dynamics be halted before such defective regions are encountered [100, 419]. In particular, two recent studies [100, 418] comparing nonadiabatic dynamics run with AA (LR-TD)DFT/TDA to that run with SF-TDDFT reported opposing observations.

The first [418], following the S_1-to-S_0 dynamics in azobenzene, showed that AA (LR-TD)DFT/TDA affords similar quantum yields, S_1 lifetimes and population traces, and hopping and product distributions to SF-TDDFT, despite the former incorrectly exhibiting a dual crossing (i.e., linearly interpenetrating S_1 and S_0 PESs) and not a conical $(F-2)$-dimensional intersection, which is correctly exhibited by the latter. It appears that the average of, for

example, five back-and-forth hops in AA (LR-TD)DFT/TDA, arising from trajectories being temporarily trapped by re-crossings in the defective dual-crossing region, is approximately equivalent[1] to one successful hop near the formally correct CX in SF-TDDFT. The second study [100], in contrast showed for the same molecule as Ref. [191] (see footnote below), that AA (LR-TD)DFT/TDA yields a significantly slower S_1 decay time than SF-TDDFT, due to its linear $(F-1)$-dimensional intersection being too strongly sloped in comparison to the peaked MECX in SF-TDDFT, resulting in much less efficient S_1-to-S_0 population transfer in the former.

Nevertheless, the authors of Ref. [100] still pointed out the main reason for potential optimism in applying AA (LR-TD)DFT/TDA to dynamics between the ground and first-excited states: the reality that most nonadiabatic events seldom occur directly at an MECX (which serve more as mechanistic "signposts" [420]), but rather occur at some other point on the intersection seam, or more likely, away from the intersection seam entirely. This leads one to imagine a situation where a transition from S_1 to S_0 occurs far enough away that the incorrect topology exhibited by AA (LR-TD)DFT/TDA has little consequence to the dynamics. If this is true then the molecular distortions that actually mediate the nonadiabatic transition may differ from those suggested by comparing critical geometries (i.e., FC vs S_J/S_I MECX geometries etc.) alone.

This is indeed the case for the photodynamics of protonated formaldimine, the outcome of which is also strongly dependent on the electronic state the molecule is initially excited to. Previous studies [294, 324, 343, 421–424] have shown that relaxation to the ground state after initial excitation to S_2 occurs via a two step process. First, protonated formaldimine experiences a rapid decay from S_2 to S_1 within 10 fs, mediated by C-N bond elongation whilst the molecule maintains its planarity. Then, it takes only another 30 fs for decay to the ground state to occur, achieved this time through simultaneous (further) C-N elongation and bipyramidalisation. The latter is different to what may be implied by the twisted (and slightly pyramidalised) S_1/S_0 MECX optimised with XMS-CASPT2 (Fig. 3.2 in Chapter 3). In the FC region, the S_2 electronic state exhibits a steep downward gradient along the C-N stretching direction (compared to a barrier along the H-C-N-H torsion direction) [343]. As such, protonated formaldimine initially acquires a large momentum along this coordinate, explaining the importance of C-N elongation not only in the S_2-to-S_1 transition, but also in the S_1-to-S_0 transition (where C-N bond rotation may be expected to dominate). This also leads predominantly to dissociated CH_2^+ and NH_2 photoproducts, with photoproducts characterised by H-migration, H-elimination and H_2-elimination also possible [423], given the excess kinetic energy. The twisted (and slightly pyramidalised) S_1/S_0 MECX optimised

[1]This behaviour is not only restricted to the comparison between AA (LR-TD)DFT/TDA and SF-TDDFT. Other (wavefunction-based) electronic-structure methods, namely CASSCF and state-specific CASPT2, have also been observed to show similar outcomes for the S_1-to-S_0 dynamics of penta-2,4-dieniminium [191], despite their differing abilities to correctly describe ground-to-excited state CXs.

with XMS-CASPT2 is merely the local minimum in the section of the intersection seam characterised by (bi)pyramidalisation [343], with its lack of direct participation in the S_1-to-S_0 transition attributed [343] to the molecule having too much momentum in the C-N stretching direction to get close enough to the MECX before transitioning to S_0 at a higher point on the intersection seam.

There is, however, a noticeable difference in the photodynamics when protonated formaldimine is instead excited to S_1. Now, torsional motion about the C-N bond does indeed dominate the nonadiabatic transition from S_1 to S_0, with the molecule experiencing multiple re-crossings with S_1 until it finally decays to S_0 [421, 425]. An initial delay in the S_1-to-S_0 decay is attributed to the time taken for protonated formaldimine to rotate about the C-N bond from 0° to 90°. Given the lack of excess momenta along the C-N elongation coordinate (in contrast to photodynamics initiated in S_2), only a small portion of photoproducts, if any, are characterised by C-N dissociation. Nevertheless, it should be noted that in both cases (i.e., initial excitation to S_2, and to S_1), previous studies [421, 422] have also found that S_1-to-S_0 decay may occur by a mix of distortions [i.e., combinations of C-N bond elongation, (bi)pyramidalisation and C-N bond torsion], with it being difficult to assign any one specific motion as dominating the transition.

Since the primary focus of this chapter lies in the dynamical effect of the AA (LR-TD)DFT/TDA S_1/S_0 intersection ring, we only consider nonadiabatic dynamics in protonated formaldimine between S_1 and S_0. Therefore, we restrict ourselves to follow two natural distortions along the dynamics: (i) the C-N bond stretch and (ii) the twist about the C-N bond, the latter being the dominant nuclear motion responsible for relaxation to the ground state upon initial promotion to S_1. As evidenced in Fig. 5.1, the natural distortions (see definitions in Section 5.2.2) provide a decent approximation to the analytic branching space vectors [$\bar{\mathbf{x}}_{IJ}(\mathbf{R})/\bar{\mathbf{y}}_{IJ}(\mathbf{R})$ or $\bar{\mathbf{x}}'_{IJ}(\mathbf{R})/\bar{\mathbf{y}}'_{IJ}(\mathbf{R})$] considered in this thesis so far, accurately reproducing the AA (LR-TD)DFT/TDA S_1/S_0 intersection ring [Fig. 5.1(b) vs 5.1(d)], as well as the region in the immediate vicinity of the S_1/S_0 MECX in XMS-CASPT2 [Fig. 5.1(a) vs 5.1(c)]. As such, these two natural distortions may be expected to provide a reasonable window into the behaviour of the nonadiabatic dynamics specifically in the vicinity of the AA (LR-TD)DFT/TDA S_1/S_0 intersection ring. Natural distortions, such as these, allow straightforward interpretation of dynamics in terms of chemically tangible nuclear motion, something that can be difficult to infer from the coupled nuclear motion exhibited by the formal branching space vectors.

An equally compelling question that arises from Fig. 5.1–albeit perhaps not as immediately obvious as the one relating to the effect of deficiencies in AA (LR-TD)DFT/TDA–relates to the idea whether one can possibly determine the "dimension" of a given CX. This is not to be confused with the "dimensionality" of a given CX, which is strictly $F-2$ or two, depending on whether one is referring to the seam or branching space of the CX (assumed to be between two electronic states). Rather, "dimension" refers to the "size" of a given CX, that is, the

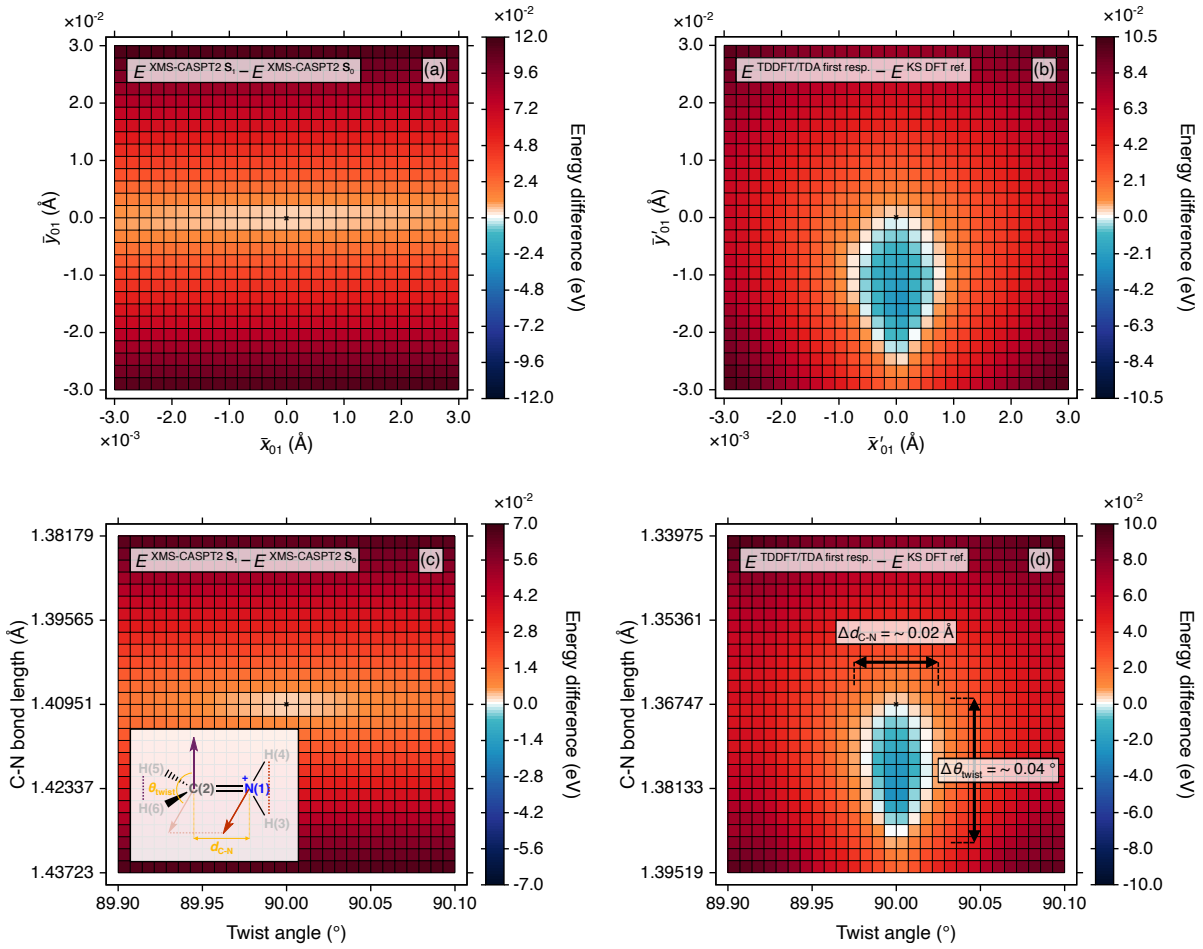

Figure 5.1: 2D colour map of the electronic energy difference between S_0 (reference state) and S_1 (first response state) obtained with **(a)** XMS(3)-CASPT2(8/6)/cc-pVTZ and **(b)** (LR-TD)DFT/TDA/PBE0/cc-pVDZ in the vicinity of the S_1/S_0 MECX (or MECP) in protonated formaldimine along an extended branching plane generated using orthonormalised (and rigidly rotated) branching space vectors. [Note, Fig. 5.1(b) is a direct copy of the energy difference colour map in Fig. 3.5(b).] The energy difference colour maps are replicated in **(c)** and **(d)**, respectively, with the extending branching plane approximated using two natural molecular distortions: stretching along the C-N bond (denoted by the C-N bond distance, $d_{\text{C-N}}$) and twisting about the C-N bond (denoted by the twist angle, θ_{twist}). The black cross indicates the location of the optimised S_1/S_0 MECX (or MECP) geometry. The Lewis structure of (twisted) protonated formaldimine is given as an inset in Fig. 5.1(c), labelled with the definitions of $d_{\text{C-N}}$ and θ_{twist}–see Section 5.2.2.1 for details.

measurable scale of molecular distortions over which the CX persists before the characteristic linearity of the PESs is lifted to higher order. A search of the literature returns very few discussions on the "size" of a CX; the only notable examples that come close to addressing this question are in the work of Coe *et al.* [90] on three-state CXs and the connectivity of intersection seams, and in the work of Littlejohn *et al.* [426] on using Moyal perturbation

theory to calculate nonadiabatic corrections to the Born-Oppenheimer approximation. Both works provide very tentative estimates in atomic units for the length scale characterising the linear region surrounding the intersection seam, either from anecdotal evidence [90], or by considering simplified BO ordering scaling arguments [426]. Needless to say, there is still plenty of room in finding a more tangible answer to the question of what is the "size" of a CX? We attempt to contribute to this in parts of this chapter.

The majority of nonadiabatic dynamics investigations that employ AA (LR-TD)DFT/TDA, including those mentioned earlier, do so within trajectory surface hopping, the workhorse of excited-state dynamics. We do the same in the present chapter, exploring the performance of four different flavours of trajectory surface hopping. Definitions and details of each, as well as a brief summary of other standard nonadiabatic dynamics methods, are provided in Section 5.2.1. The reason for considering all four flavours of trajectory surface hopping is to determine whether any of them can provide a means to reliably use AA (LR-TD)DFT/TDA in dynamics simulations that go all the way to the ground state.

Our work is organised as follows: We first (i) review the theoretical background of each of the four trajectory surface hopping variants under investigation, before (ii) reporting the specific computational details in each case. We then start by (iii) comparing the four trajectory surface hopping approaches at the XMS-CASPT2 level of theory, with a particular focus on the initial S_1-to-S_0 hopping event. Afterwards, we (iv) probe the behaviour of the XMS-CASPT2 dynamics close to the optimised S_1/S_0 MECX, restricting our analysis to only follow the two natural distortions discussed above, and compare this to the equivalent AA (LR-TD)DFT/TDA dynamics. We finish by (v) further scrutinising the AA (LR-TD)DFT/TDA dynamics, along a single exemplar trajectory. This leads to a more general discussion on the use of each trajectory surface hopping variant with AA (LR-TD)DFT/TDA, as well as XMS-CASPT2.

5.2 Methods

5.2.1 A survey of trajectory surface hopping approaches

The background discussion presented in Chapter 2 focussed on the electronic-structure quantities [195, 427] entering Eq. (2.6), namely the electronic PESs and the $\mathbf{d}_{IJ}(\mathbf{R})$ vectors. However, equally important is the approach taken to approximate the nuclear dynamics. A number of methods have been proposed, each associated with varying degrees of approximation, complexity and accuracy [417, 428, 429].

The first family of approaches are the quantum dynamics methods, such as multiconfigurational time-dependent Hartree (MCTDH) [430–432], which treat both the electronic and nuclear degrees of freedom fully quantum mechanically. Such approaches can afford numerically exact dynamics, however, this often comes at the cost of needing to precompute

the underlying PESs, which necessitates a technically involved global fitting procedure, as well as the cost of only being able to consider small molecules, or restricting oneself to only a few nuclear degrees of freedom in larger molecules [433].

The second (and largest) family of methods are the mixed quantum/classical (MQC) approaches, which treat the electronic degrees of freedom quantum mechanically, but the nuclear degrees of freedom fully classically. The nuclei are treated as classical particles governed by Newton's equations of motion, with the nuclear forces determined from the gradient(s) of the electronic PES(s), typically obtained on-the-fly. Notable examples include mean-field Ehrenfest (MFE) [434–436] and trajectory surface hopping (TSH) [436–439]. In MFE dynamics, the evolution of the nuclear wavepacket is approximated by one, or sometimes an ensemble of uncoupled classical trajectories propagated on a time-dependent average of all computed electronic PESs, weighted by the corresponding electronic population (i.e., a mean-field PES), with the outcome of each trajectory solely determined by its initial conditions [417]. Such an approach only provides a reasonable approximation to the true nonadiabatic dynamics if the electronic states involved possess very similar energies and topographical features at each time step, e.g., if the molecule under investigation exhibits a high density of states. If not, then MFE can lead to drastically nonsensical nuclear dynamics due to its mean-field nature. In TSH, the evolution of the nuclear wavepacket is instead approximated by a swarm of uncoupled classical trajectories, each of which evolve, at any given time, on one of the computed electronic PESs, with nonadiabatic transitions (i.e., transfer of nuclear amplitude) being modelled by hops between electronic states, a process which involves the trajectory changing its running state.

The third family of standard nonadiabatic dynamics methods are Gaussian-based approaches, such as ab initio multiple spawning (AIMS) [440–443] and variational multiconfigurational Gaussian (vMCG) [444–446]. These approaches conceptually act as an intermediate between the first two families. Rather than being considered as classical particles (as in MQC methods), nuclei are instead represented by moving multidimensional Gaussian functions [or trajectory basis functions (TBFs)], which themselves evolve classically on the computed electronic PESs based on their centroid position. In AIMS, for example, nonadiabatic transitions are modelled by the transfer of amplitude between one TBF on a given electronic state and another TBF on an electronic state to which the former is coupled. This is achieved in practice thanks to a spawning algorithm that increases the size of the TBF basis, creating a new TBF (i.e., the child) on the coupled electronic state, when the TBF on the running state (i.e., the parent) encounters a region of configurational space characterised by a large $\mathbf{d}_{IJ}(\mathbf{R})$ vector [433]. As such, these spawning events ensure a smooth transfer of nuclear amplitude (in comparison to the abrupt hopping events in TSH). Throughout the remaining dynamics, the parent and child TBFs are coupled to one another and thus can exchange nuclear amplitude as the dynamics progresses, the extent of which is dictated by the corresponding $\mathbf{d}_{IJ}(\mathbf{R})$

vectors [417]. As such, AIMS can naturally account for nuclear quantum effects such as the topological phase, something not explicitly possible in TSH. Similarly, AIMS is derived from first principles (again, unlike TSH), so can converge on the exact quantum dynamics result in the appropriate limit [433]. Nonetheless, despite recent efforts [447–450], the (i) complexity of implementing and analysing AIMS dynamics, the (ii) exponential increase in computational cost with TBF number, and its (iii) arguably greater sensitivity to numerical instabilities arising from poor electronic structure, have all meant that AIMS has yet to experience the same widespread adoption afforded by TSH. Thus, TSH still remains the workhorse of the nonadiabatic dynamics community, the details of which will now be discussed.

In TSH, a classical trajectory A [one of a swarm, sampled typically from a ground-state (thermal) distribution of initial conditions (i.e., nuclear geometries and momenta)] is initially promoted vertically to a given electronic state I, where it can then evolve adiabatically according to BO molecular dynamics. The classical nuclear equations of motion are integrated using conventional algorithms, like the velocity Verlet algorithm [451, 452], with a time step of Δt. The nuclear force experienced by trajectory A is calculated as

$$\mathbf{F}^{A}(t) = -\nabla_{\mathbf{R}} E^{\mathrm{el}}_{*}(\mathbf{R})\Big|_{\mathbf{R}=\mathbf{R}^{A}(t)} , \tag{5.1}$$

where $\nabla_{\mathbf{R}} E^{\mathrm{el}}_{*}(\mathbf{R})$ is the nuclear gradient of the active state, the state on which trajectory A is currently running. The $*$ indicates that the active state can change throughout the dynamics, which only occurs if a certain, in general stochastic, criterion is satisfied. The three variants of TSH discussed in turn below differ in their approach to evaluating the probability of such a transition (or, more specifically, a hop). That is to say, they model regions of strong nonadiabaticity differently. If a hop does successfully take place, then trajectory A evolves on the new electronic state J until it reaches another region of strong nonadiabaticity, where it has the possibility to hop again to a different state.

To preserve total energy during the nuclear dynamics, the kinetic energy is adjusted after each hop to account for the instantaneous difference in nuclear potential energy (i.e., the electronic energy gap). This is done practically by rescaling the nuclear velocities by the potential energy difference in the direction of the $\mathbf{d}_{IJ}(\mathbf{R})$ vector between the two electronic states, to and from which the trajectory hopped [438]. For cases where $\mathbf{d}_{IJ}(\mathbf{R})$ vectors are not formally available (or their calculation viable) for a given electronic structure method, or where $\mathbf{d}_{IJ}(\mathbf{R})$ vectors simply do not enter the working equations of a particular variant of TSH, the nuclear velocities are instead rescaled along the direction of the nuclear linear momenta.

Lastly, it should be noted that large numbers of independent trajectory runs are necessary to converge both the stochastic algorithm (if used) and the initial condition sampling [453]. Nonetheless, it is customary, in practice, to only propagate one trajectory for each initial condition. The main assumption in TSH is that the collective statistical distribution of a swarm

of independent classical trajectories represents the probability density of the true nuclear wavepacket–i.e., the independent trajectory approximation. Needless to say, a large number of trajectories, however, does not guarantee this assumption converges to an exact result; it can still be completely wrong.

5.2.1.1 Fewest-switches surface hopping

Developed by Tully in 1990 [438], the fewest-switches variant of surface hopping (FSSH) is by far the most widely used. In FSSH, each trajectory A is associated with a time-dependent electronic wavefunction, $\tilde{\psi}(\mathbf{r};\mathbf{R}^A(t),t)$, which is typically expanded in a basis of adiabatic electronic states,

$$\tilde{\psi}(\mathbf{r};\mathbf{R}^A(t),t) = \sum_J c_J^A(t)\psi_J(\mathbf{r};\mathbf{R}^A(t))\,, \tag{5.2}$$

where $c_J^A(t)$ are time-dependent (complex) expansion coefficients, which express the importance of each state at time t to the overall electronic wavefunction. Note, we include the explicit time dependence of the nuclear coordinates. Inserting Eq. (5.2) into the electronic TDSE [Eq. (2.65)], left-multiplying by $\psi_I^*(\mathbf{r};\mathbf{R}^A(t))$ and integrating over all electronic coordinates $\mathbf{r}$, affords along trajectory A, a set of coupled equations of motion (one for each electronic state), which govern the time dependence of the expansion coefficients,

$$i\frac{d}{dt}c_I^A(t) = \sum_J c_J^A(t)\left[E_J^{\mathrm{el}}(\mathbf{R}^A(t))\delta_{IJ} - i\sigma_{IJ}(\mathbf{R}^A(t))\right]\,. \tag{5.3}$$

Here, $\sigma_{IJ}(\mathbf{R}^A(t)) = \mathbf{v}^A(t)\cdot\mathbf{d}_{IJ}(\mathbf{R}^A(t))$ is the time-derivative nonadiabatic coupling (TDC) and $\mathbf{v}^A(t) = \frac{d}{dt}\mathbf{R}^A(t)$ is the classical nuclear velocity vector. The electronic equations of motion are typically integrated numerically using the Runge-Kutta [454, 455] or Butcher [456] algorithms. At the start of the dynamics, the value of all electronic coefficients is set to zero, apart from that of the starting state of trajectory A, which is instead set to one. The electronic coefficients are then allowed to propagate on the support of the nuclear dynamics (albeit using a smaller time step, dt). In FSSH, whether trajectory A hops to another state J, or stays in its current state I, is determined via a stochastic (Metropolis-type) algorithm. The FSSH hopping probability, evaluated at each nuclear time step, is given as

$$\mathcal{P}_{I\to J}^{A,\,\mathrm{FSSH}} = \int_t^{t+\Delta t} -\frac{2\Re\left[\Gamma_{IJ}^A(t)\right]}{\Gamma_{II}^A(t)}\,\sigma_{IJ}(\mathbf{R}^A(t))\,dt\,, \tag{5.4}$$

where $\Gamma_{IJ}^A(t) = c_I^{A*}(t)c_J^A(t)$ is an element of the density matrix; the diagonal elements ($I = J$) correspond to adiabatic state populations, whereas the off-diagonal elements ($I \neq J$) correspond to adiabatic state coherences. In Eq. 5.4, we only consider the real part of the adiabatic state coherences (signified by the notation "$\Re[\ldots]$"). At each nuclear time step, a

random number, ζ, is generated from the uniform interval $[0:1]$, to which the FSSH hopping probability is compared. A hop from state I to state J is permitted if the following criterion[2] is satisfied,

$$\sum_{K}^{J-1} \mathcal{P}_{I\to K}^{A,\,\mathrm{FSSH}} < \zeta \leq \sum_{K}^{J} \mathcal{P}_{I\to K}^{A,\,\mathrm{FSSH}} \,. \tag{5.5}$$

Inspecting Eqs (5.4) and (5.5), it is clear that the likelihood of trajectory A successfully hopping at time t depends both on the TDC between the states involved and the corresponding electronic coefficients. A large magnitude in the TDC between states I and J, as well as a reduction in the electronic population of the active state I, implies a much greater chance of trajectory A hopping (i.e., nuclear amplitude being transferred) from electronic state I to J.

In the standard implementation of FSSH, one typically computes the $\mathbf{d}_{IJ}(\mathbf{R})$ vectors, which enter into Eqs (5.3) and (5.4), analytically. Hereafter, we denote this variant of FSSH as FSSH/analytic. However, it was recently shown by Baeck and An [458, 459] that $\mathbf{d}_{IJ}(\mathbf{R})$ vectors between two electronic states can in fact be reasonably approximated simply using the electronic energy difference and its second derivative with respect to the nuclear coordinate, Q [460, 461]. The original formulation of these so-called Baeck-An couplings was restricted to one dimension (hence the scalar Q in the previous sentence, not the vectoral $\mathbf{Q}$) and it assumed a Lorentzian dependence of the $\mathbf{d}_{IJ}(\mathbf{R})$ vectors along this one-dimensional coordinate. By remembering that (i) the full-dimensional $\mathbf{d}_{IJ}(\mathbf{R})$ vector is always projected onto the nuclear velocity vector in FSSH [419] (i.e., it is always recast into the one-dimensional TDC)[3] and (ii) a classical trajectory anyway naturally represents a one-dimensional propagation along a time coordinate [465], it is understandable that the Baeck-An couplings can be suitably applied to multidimensional TSH dynamics. The Baeck-An coupling in FSSH can be generalised as a full-dimensional vector in the direction of the coupling,

$$\mathbf{d}_{IJ}^{\text{Baeck-An}}(\mathbf{R}) = \frac{\mathrm{sgn}(\Delta E_{IJ}^{\mathrm{el}}(\mathbf{R}))}{2} \sqrt{\frac{1}{\Delta E_{IJ}^{\mathrm{el}}(\mathbf{R})} \frac{\partial^2 \Delta E_{IJ}^{\mathrm{el}}(\mathbf{R})}{\partial Q^2}} \overline{\mathbf{Q}} \quad \text{for} \quad \mathbf{R} \approx \mathbf{R}_{\mathrm{c}} \,, \tag{5.6}$$

where sgn() returns a value of $+1$, -1 or 0 depending on whether its argument is positive, negative or zero, respectively; $\overline{Q}$ is the unit vector in the direction of the nonadiabatic coupling; and $\mathbf{R}_c$ is the molecule geometry at which the magnitude of the coupling is maximum [419].

[2]The summations on the left- and right-hand sides of Eq. 5.5 represent cumulative probabilities, which allow the overall uniform interval $[0:1]$ (i.e., the range of possible random numbers) to be discretised into smaller intervals, with a given "smaller" interval being assigned to the hopping to a specific state.[457] The "$<$" on the left-hand side of Eq. 5.5 ensures that each of these "smaller" intervals does not overlap with its neighbours, providing a unique mapping between each discretised random number range and the hopping to a given state. Note, Eq. 5.5 could just as validly been written with two strict inequalities (as opposed to using a strict and non-strict inequality).

[3]It is not uncommon to compute the TDCs directly (compared to calculating the full $\mathbf{d}_{IJ}(\mathbf{R})$ vectors and projecting them onto the nuclear velocities). A popular approximate way of computing TDCs is via the Hammes-Schiffer-Tully approach [439] using wavefunction overlaps [462–464] at successive time steps.

Recasting the electronic energy Hessian as a time derivative via the chain rule and taking the scalar product with the nuclear velocity vector yields the corresponding Baeck-An TDC,

$$\sigma_{IJ}^{\text{Baeck-An}}(t) = \frac{\text{sgn}(\Delta E_{IJ}^{\text{el}}(t))}{2}\sqrt{\frac{1}{\Delta E_{IJ}^{\text{el}}(t)}\frac{d^2\Delta E_{IJ}^{\text{el}}(t)}{dt^2}}, \tag{5.7}$$

where to avoid imaginary values in Eq. (5.7), it is assumed that the TDC is nonzero for positive radicand values, but zero for negative radicand values [419]. This assumption is justified by recognising that near a locally avoided crossing (i.e., a minimum in the energy difference between two adiabatic electronic states), the lower curve tends to be concave and the upper curve convex, so the curvature of the energy gap and thus the radicand in Eq. (5.7) is generally positive [465]. Cases where the radicand is negative are anticipated to occur only away from the region surrounding the CX, so characterised by TDCs which are already close to zero [465]. This argument, however, considers an ideal situation involving stable electronic structure; an interesting question arises whether such an approach for approximating $\mathbf{d}_{IJ}(\mathbf{R})$ vectors is suitable for cases where a given electronic structure method exhibits instabilities, such as negative excitations energies (and thus negative energy gaps). This will be discussed in the context of our results in Section 5.3.3.2 of this chapter.

In practice, the second time-derivative in Eq. (5.7) is calculated numerically. There are several ways of implementing this [419, 465], but the one used in this chapter will be outlined as follows. For the first three nuclear time steps of trajectory A, as well as after any successful hop, the TDC is taken to be zero. At the fourth time step, the second time derivative is calculated by a finite difference procedure using the backward $\mathcal{O}(\Delta t)$ approximation,

$$\frac{d^2\Delta E_{IJ}^{\text{el},A}(t)}{dt^2} \approx \frac{1}{\Delta t^2}\left[2\Delta E_{IJ}^{\text{el},A}(t) - 5\Delta E_{IJ}^{\text{el},A}(t-\Delta t) + 4\Delta E_{IJ}^{\text{el},A}(t-2\Delta t) - \Delta E_{IJ}^{\text{el},A}(t-3\Delta t)\right], \tag{5.8}$$

which requires knowledge of the electronic energy calculated at the three previous time steps, as well as the current.

Overall, using Baeck-An couplings in FSSH, which is often called κTSH [465, 466], but which we denote hereafter as FSSH/Baeck-An, has a number of benefits, namely they can be used in cases where analytic $\mathbf{d}_{IJ}(\mathbf{R})$ vectors are either (i) not (yet) available from a given electronic structure method, or (ii) too computational costly to compute. They also provide (iii) a more feasible route in applying machine learning in nonadiabtic dynamics [466], as predicting energy differences is much less difficult than trying to machine learn the narrow functional form of analytic $\mathbf{d}_{IJ}(\mathbf{R})$ vectors in standard FSSH [419].

Whether one uses analytic or approximate $\mathbf{d}_{IJ}(\mathbf{R})$ vectors, one can not escape the fundamental assumption at the heart of the FSSH approach. FSSH assumes internal consistency between the fractional number of trajectories evolving on a given electronic state I (i.e., the

"classical" population) and the average electronic population of that state (i.e., the "quantum" population) for all times during the dynamics, such that

$$\frac{N_I(t)}{N_{\text{traj}}} \approx \frac{1}{N_{\text{traj}}} \sum_{A=1}^{N_{\text{traj}}} \left| c_I^A(t) \right|^2 . \tag{5.9}$$

The hopping algorithm in FSSH is constructed in such a way that minimises the number of hopping events in an attempt to satisfy Eq. (5.9) [467]. However, in general, there is often a non-negligible (or even significant) difference between the right-hand side and left-hand side of Eq. (5.9), a direct consequence of the intrinsic overcoherence problem in FSSH [468]. By employing classical trajectories and propagating the electronic coefficients of all electronic states on their support, the off-diagonal elements of the density matrix in FSSH are not permitted to vanish, even after a region of strong nonadiabaticity has passed and the two electronic states involved are well separated [417]. In other words, after a hopping event, the electronic population of the non-active state is forced to propagate under the influence (and thus in the direction) of the nuclear force of the active state, despite the gradient of the (non-)active states likely being completely different, something that would be correctly accounted for in the true dynamics (by the natural separability) of the nuclear wavepacket [457]. Over the years, a number of decoherence corrections have been proposed to alleviate this problem [469], the most notable being the energy-based decoherence correction (EDC) of Granucci and Persico [468, 470], inspired by previous work of Truhlar and coworkers [471, 472]. The EDC works to damp the electronic populations of all non-active states, J, by applying an exponential factor after each nuclear time step. For a trajectory A evolving in electronic state I, the electronic coefficients of all states are corrected according to

$$\left| \tilde{c}_J^A(t) \right|^2 = \left| c_J^A(t) \right|^2 \exp\left[\frac{-\Delta t}{\tau_{IJ}} \right] \tag{5.10}$$

$$\left| \tilde{c}_I^A(t) \right|^2 = \left| c_I^A(t) \right|^2 \left[\frac{1 - \sum_{I \neq J} \left| \tilde{c}_J^A(t) \right|^2}{\left| c_I^A(t) \right|^2} \right]^{\frac{1}{2}} , \tag{5.11}$$

where Eq. 5.11 represents the renormalisation of the electronic population of the active state. The decoherence time, τ_{IJ}, can be written down as

$$\tau_{IJ} = \frac{1}{\left| E_I^{\text{el},A} - E_J^{\text{el},A} \right|} \left[1 + \frac{\alpha_{\text{EDC}}}{T_{\text{n}}^A} \right] , \tag{5.12}$$

which shows its inverse dependence on the energy difference between the active (I) and non-active (J) states and on the kinetic energy of trajectory A, T_{n}^A . The empirical parameter, α_{EDC}, is conventionally given a value of 0.1 E_h [471].

5.2.1.2 Landau-Zener surface hopping

A simpler alternative to FSSH based on semiclassical arguments, which has experienced a renaissance in recent years [423, 467, 473–478], is the Landau-Zener surface hopping (LZSH) approach. The original LZ model [479–481] was derived for the crossing of two diabatic electronic states in one dimension, assuming a linear dependence of the diabatic electronic states with nuclear coordinate. First applied in multidimensional TSH by Tully and Preston in the 1970s [437], the LZ transition probability between two diabatic states, I and J, takes the form

$$\mathcal{P}_{J\to I}^{\text{LZSH}} = \exp\left[-\frac{2\pi V_{IJ}^2}{\mathbf{v}\left|\frac{d}{d\mathbf{R}}V_{II}(\mathbf{R}) - \frac{d}{d\mathbf{R}}V_{JJ}(\mathbf{R})\right|}\right], \tag{5.13}$$

where the off-diagonal elements of the diabatic electronic Hamiltonian, V_{IJ} , are considered to be constant and Eq. (5.13) is evaluated only at the crossing point between the two diabatic states. More recently, Belyaev and Lebedev[482] reformulated Eq. (5.13) in terms of adiabatic electronic states, a more appealing option for running TSH. Their adiabatic form of the LZ hopping probability reads as

$$\mathcal{P}_{J\to I}^{A,\,\text{LZSH}} = \exp\left[-\frac{\pi}{2}\sqrt{\frac{\left[\Delta E_{JI}^{\text{el}}(\mathbf{R}^A(t_c))\right]^3}{\frac{d^2}{dt^2}\Delta E_{JI}^{\text{el}}(\mathbf{R}^A(t))\mid_{t=t_c}}}\right], \tag{5.14}$$

and only depends on the electronic energy difference between adiabatic states, I and J (not on the electronic expansion coefficients or $\mathbf{d}_{IJ}(\mathbf{R})$ vectors, as in FSSH). Moreover, the hopping probability in LZSH is not calculated at each nuclear time step, but only at time t_c, the time at which trajectory A reaches a local minimum in the gap (or avoided crossing) between the two adiabatic PESs (i.e., the time at which the corresponding diabatic states cross). This is different to FSSH, where the hopping probability *is* computed at every nuclear time step, allowing a hop to be attempted, in principle, at any (instantaneous) point throughout the dynamics. As such, the FSSH probability is considered a "local" switching probability, whereas that of LZSH is instead considered a "global" switching probability [483, 484]. The reason behind the latter can be explained as follows. In practice, the local minimum in the adiabatic energy gap is obtained numerically via a three-point finite difference procedure [485],

$$\frac{d^2}{dt^2}\Delta E_{IJ}^{\text{el},A}(t) \approx \frac{\Delta E_{IJ}^{\text{el},A}(t-\Delta t) - 2\Delta E_{IJ}^{\text{el},A}(t) + \Delta E_{IJ}^{\text{el},A}(t+\Delta t)}{\Delta t^2} = \frac{2G_{IJ}^{\text{el},A}(t)}{\Delta t^2}, \tag{5.15}$$

which involves computing the second derivative of the energy gap at three consecutive nuclear time steps, therefore requiring the energy gap to be calculated (and monitored) at each nuclear time step. We define $G_{IJ}^{\text{el},A}(t) = \frac{1}{2}[[\Delta E_{IJ}^{\text{el},A}(t-\Delta t) - \Delta E_{IJ}^{\text{el},A}(t)] + [\Delta E_{IJ}^{\text{el},A}(t+\Delta t) - \Delta E_{IJ}^{\text{el},A}(t)]]$

in Eq. (5.15) as the average change in the energy gap between the nuclear time steps around the minimum and thus the resulting LZSH hopping probability is calculated *globally* for these three points [485]. Once a local minimum in the adiabatic energy gap is located, the LZSH probability is calculated according to Eq. (5.14) and compared to a random number uniformly generated from the interval $[0:1]$. If the LZSH probability is larger than the random number, then trajectory A successfully hops to the new state J; if not, trajectory A continues to evolve on its current state I. Note, after a hop occurs, trajectory A must be moved back one nuclear time step in order to recalculate the nuclear force at the energy gap minimum before being allowed to propagate on its new active electronic state.

LZSH offers a straightforward way of interfacing the nuclear dynamics to the electronic structure, given its lack of need for calculating $\mathbf{d}_{IJ}(\mathbf{R})$ vectors, analytic or otherwise. Equally, LZSH does not suffer from the decoherence problem of FSSH [477], as the electronic TDSE is not propagated along each trajectory. Since it can be formulated both with the adiabatic and diabatic representations, LZSH also provides the means to readily simulate intersystem crossing via singlet-triplet transitions [423]. However, like the FSSH/Baeck-An discussed above, LZSH can only formally be applied between two electronic states, rendering its use limited in systems with a high density of states or a strong likelihood of encountering three-state (or higher) intersections.

5.2.1.3 Surface hopping with induced transition

The last variant of TSH to be discussed models regions of strong nonadiabaticity quite differently to that of FSSH and LZSH, in that it employs no stochastic algorithm. Whether a trajectory hops from its running state to another is determined solely by the electronic energy gap between the two adiabatic states dropping below a certain preset threshold. As such, this form of TSH is often referred to as surface hopping with induced transition [486–488] or forced TSH [489, 490]. The former, which we acronymise to SHωIT, is used throughout this chapter, where ω denotes the value of the energy difference threshold. The validity of manually inducing a hop from the upper to lower electronic state when the electronic energy differences reaches a small enough value is rationalised by the fact that, as shown in Eq. (2.43), the $\mathbf{d}_{IJ}(\mathbf{R})$ vector depends inversely on such an energy gap, becoming infinite at a true point of degeneracy. Therefore, it may be assumed that such a crude approach to TSH constitutes a semi-reasonable approximation (albeit arguably naively simple) to a nonadiabatic transition. The application of SHωIT in dynamics is often limited to cases where the employed electronic structure method exhibits defective ground-to-excited state CX, where the corresponding $\mathbf{d}_{IJ}(\mathbf{R})$ vectors are either not available or not deemed reliable. An important question to consider in SHωIT is what value of the energy gap threshold should one take, the answer of which is often chosen based on simple intuition rather than rigorous benchmarking.

5.2.2 Computational details

5.2.2.1 Electronic structure

All electronic structure details relating to XMS-CASPT2, DFT and AA LR-TDDFT calculations performed in this chapter are the same as those reported in Section 3.2.1 of Chapter 3, except for the active space used for XMS-CASPT2. The (6/4) active space employed in the previous two chapters was extended to an (8/6) active space, including a pair of C-N $\sigma\sigma*$ orbitals (Fig. 5.2), in an attempt to reduce total energy conservation problems due to the use of a finite active space [491]. [Note, the two C-H,N-H σ orbitals used in the (6/4) active space, as mentioned in Section 3.3.1 of Chapter 3, are also characterised in the literature as a $\pi'\pi'*$ pair, with π' ($\pi'*$) being orthogonal to the original π ($\pi*$) orbital in the (6/4) active space.]

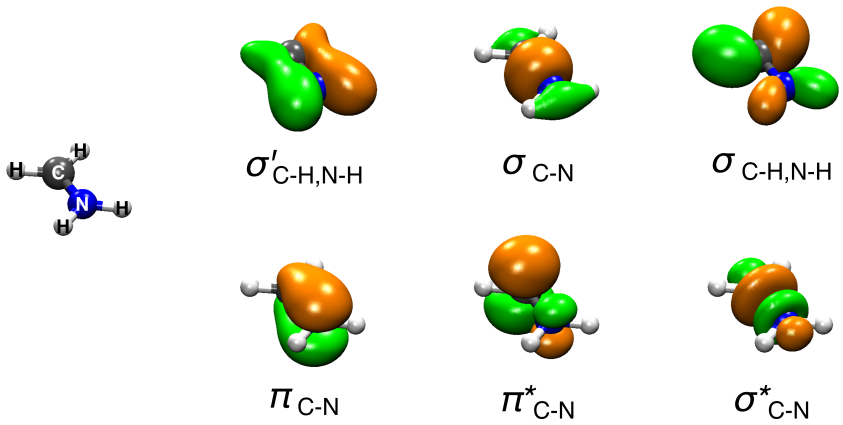

Figure 5.2: New underlying SA-CASSCF natural orbitals employed in the XMS(3)-CASTP2(8/6)/cc-pVTZ calculations for protonated formaldimine. The active space orbitals are presented here for the S_0 minimum geometry of protonated formaldimine plotted using an isovalue of 0.075, with the labelled geometry provided on the left.

5.2.2.2 Plotting the CX branching space (and full potential energy landscape)

All details relating to the optimisation of the S_1/S_0 MECX (or MECP) geometries and the plotting of their corresponding branching spaces along orthonormalised (and rigidly rotated) branching space vectors performed in this chapter are the same as those reported in Sections 3.2.2, 3.2.3, 3.5.1.2 and 3.5.1.3 of Chapter 3. Additional (approximate) branching space plots, as well as full PES landscapes, were also generated by computing the S_0 and S_1 PESs along two natural molecular distortions characterised by (i) the C-N bond distance, defined as

$$d^A_{\text{C-N}}(t) = ||\mathbf{R}^A_{\text{N(1)}}(t) - \mathbf{R}^A_{\text{C(2)}}(t)||\,, \tag{5.16}$$

where $\mathbf{R}_X^A(t)$ is the position of atom X at time t for trajectory A, and by (ii) the twist angle about the C-N bond, defined as

$$\theta_{\text{twist}}^A(t) = \arccos\left[\left(\mathbf{e}_{\text{N(1)-C(2)}}^A(t) \times \mathbf{e}_{\text{H(4)-H(3)}}^A(t)\right) \cdot \left(\mathbf{e}_{\text{C(2)-N(1)}}^A(t) \times \mathbf{e}_{\text{H(6)-H(5)}}^A(t)\right)\right], \tag{5.17}$$

where $\mathbf{e}_{\text{Y-Z}}^A(t) = \frac{\mathbf{R}_Z^A(t) - \mathbf{R}_Y^A(t)}{||\mathbf{R}_Z^A(t) - \mathbf{R}_Y^A(t)||}$ corresponds to a unit vector pointing from atom Y to atom Z at time t and the notation $||\ldots||$ signifies the magnitude of the resulting vector. The inset in Fig. 5.1 gives a graphical representation of $d_{\text{C-N}}^A(t)$ and $\theta_{\text{twist}}^A(t)$, where the explicit time dependence and superscript A have been dropped for brevity. This will continue throughout the rest of the chapter. A 2D grid of 29 $\times$ 29 geometries was generated along a plane spanned by both natural molecule distortions originating from the optimised S_1/S_0 MECX (or MECP) geometry. In each case, the increment used to move along the respective natural molecule distortions away from the corresponding values at the optimised S_1/S_0 MECX (or MECP) geometry was chosen to be the same in XMS-CASPT2 as in (LR-TD)DFT/TDA in order to maximise comparison. At each grid-point geometry, a single XMS-CASPT2 [or (LR-TD)DFT/TDA] calculation was performed, affording the S_0 and S_1 PESs along the two natural molecular distortions. Electronic energies are given relative to the S_0 energy at the S_1/S_0 MECX (or MECP) geometry.

5.2.2.3 Trajectory surface hopping dynamics

XMS-CASPT2. A harmonic Wigner distribution for the ground electronic and vibrational state was employed to randomly sample 200 initial conditions (nuclear geometries and momenta) within the Newton-X 2.4 program package [421, 492, 493]. Protonated formaldimine does not exhibit any low-frequency vibrational modes (i.e., those under 500 cm^{-1}) at the FC geometry [494, 494], suggesting the harmonic approximation for the Wigner distribution is reasonable in this case. The harmonic Wigner distribution was generated on the basis of the MP2/cc-pVTZ S_0 minimum geometry and the corresponding vibrational frequencies; all MP2 calculations were computed using the Turbomole 7.4.1 program package [355, 356]. MP2 typically provides very similar ground-state geometries to XMS-CASPT2, but affords the Hessian of the ground-state electronic energy at a much lower computational cost.

The nonadiabatic dynamics of protonated formaldimine was simulated at the XMS(3)-CASPT2(8/6)/cc-pVTZ level for 100 fs using TSH dynamics with a nuclear time step of 10 a.u. (i.e., $\sim$0.25 fs) and 100 sub-time steps for propagating the electronic quantities. The four versions of TSH were investigated using the ABIN code [495] interfaced with the BAGEL 1.2.0 program package [341]: (i) fewest-switches surface hopping with analytic $\mathbf{d}_{IJ}(\mathbf{R})$ vectors (FSSH/analytic), (ii) FSSH with approximate Baeck-An couplings (FSSH/Baeck-An), (iii) Landau-Zener surface hopping (LZSH) and (iv) surface hopping with induced transition (SHωIT), where ω is the value of the $S_1 - S_0$ energy difference below which a hop is

forced to occur. In each case, the initial conditions were vertically promoted to S_1 under the sudden-excitation approximation with the ensuing dynamics restricted to S_0 and S_1 only. Only one trajectory was propagated for each initial condition. The electronic populations were corrected in the FSSH dynamics by applying the empirical energy-based decoherence scheme of Granucci and Persico [470] using the recommended value of 0.1 a.u. for the decoherence parameter. Equally, $\mathbf{d}_{01}(\mathbf{R})$ vectors in FSSH/analytic and FSSH/Baeck-An were only calculated when the energy difference between S_0 and S_1 dropped below 2.0 eV (e.g., as highlighted below in Fig. 5.13). After a successful hop with FSSH/analytic, the kinetic energy was adjusted by rescaling the nuclear velocities along the direction of the $\mathbf{d}_{IJ}(\mathbf{R})$ vector, however with FSSH/Baeck-An, LZSH and SHωIT, this was instead carried out along the linear momentum direction. The ABIN code includes a check for instabilities in the PESs during LZSH dynamics to prevent artificial hopping due to erroneous abrupt features in the energies. This takes the form of a comparison between central and backward three-point finite difference procedures; if they differ by more than 130% it is taken that this is indicative of electronic energy discontinuities, rather than actually reaching the intersection seam. No such check has been implemented yet for running FSSH/Baeck-An, where PES instabilities are assumed to play similar havoc.

Preliminary exploration of the nonadiabatic dynamics between S_0 and S_1 was performed using FSSH/analytic for the 200 initial conditions without considering any energy windowing. However, to obtain as many trajectories as possible that possess an energy gap less than 0.1 eV at their first S_1-to-S_0 hopping event (i.e., in attempt to encourage the TSH dynamics to pass as close as possible to the S_1/S_0 intersection seam), an additional 5000 initial conditions were sampled from the same harmonic Wigner distribution. A large subset of these possessed an $S_1 - S_0$ energy gap between 7.0 and 8.0 eV (i.e., the energy range that the initial $S_1 - S_0$ energy gap for all trajectories in the first set of 200, which had their first S_1-to-S_0 hopping event occur below 0.1 eV, fell within); out of this subset, 200 extra initial conditions were randomly selected to be used within the subsequent TSH dynamics. Therefore, a total of 400 FSSH/analytic trajectories were run. The total energy was closely monitored in all XMS-CASPT2 TSH trajectories and a total energy conservation criterion was determined, whereby trajectories were discarded if their total energy at a given time step deviated more than $\pm$0.25 eV away from (i) the total energy at the previous time step and (ii) the total energy at the initial time step. This attempted to address the problem of total energy drift and total energy discontinuities, respectively, both of which should not occur in theory, but are often unavoidable in practice, especially when using active-space-based electronic-structure methods. For FSSH/analytic, 238 trajectories fulfilled the total energy conservation criterion. The initial conditions corresponding to these 238 trajectories were subsequently used to perform FSSH/Baeck-An, LZSH and SHωIT (ω = 0.1 eV) dynamics. See Table 5.2 below for a breakdown of the trajectory acceptance statistics. For consistency, we focussed only on

the 107 trajectories shared between all four TSH approaches that fulfilled the total energy conservation criterion above. The initial conditions of these 107 trajectories were then reused to initiate the second variant of the SHωIT approach where ω = 0.2 eV. A further ten trajectories failed to satisfy the total energy conservation criterion, leaving a final number of 97 stable trajectories that were in common between all five TSH approaches, which were then used in the dynamics analysis. Problems with total energy conservation are attributed to using a finite active space; larger active spaces for protonated formaldimine have been reported in the nonadiabatic dynamics literature [i.e., a (12/8) active space] within semi-empirical active-space-based methods [496]. To use such a large active space in XMS-CASPT2 would significantly increase the computational cost and therefore the time taken to run the TSH simulations. The (8/6) active space employed served as a decent compromise for the purposes of this investigation, which is not focussed on the photochemistry of protonated formaldimine *per se*, but rather the comparison of the different TSH methods within the vicinity of its S_1/S_0 MECX.

Table 5.1: Number of trajectories ran and used in the dynamics simulation analysis for each of the TSH approaches at the XMS(3)-CASPT2(8/6)/cc-pVTZ level of theory. Overall, 97 trajectories were shared in common between all TSH approaches, which fulfilled the total energy conservation criterion.

TSH approach	Number of trajectories			
	Total	Discarded	Accepted	Accepted & in common
FSSH/analytic	400	162	238	
FSSH/Baeck-An	238	56	182	
LZSH	238	63	175	97
SHωIT (ω = 0.1 eV)	238	59	179	
SHωIT (ω = 0.2 eV)	107	10	97	

(LR-TD)DFT/TDA. For each flavour of TSH, nine trajectories were simulated at the (LR-TD)DFT/TDA/PBE0/cc-pVDZ level of theory [excluding SHωIT (ω = 0.1 eV)] using the ABIN code interfaced to the GPU-accelerated TeraChem program package [346–352]. The same initial conditions (i.e., MP2/cc-pVTZ nuclear positions and momenta) were used in the (LR-TD)DFT/TDA/PBE0 trajectories as were used in the corresponding XMS-CASPT2 trajectories. All possessed an energy gap below 0.2 eV at their first S_1-to-S_0 hopping event for each flavour of TSH. Analogous to the XMS-CASPT2 TSH dynamics, the (LR-TD)DFT/TDA/PBE0 trajectories were initiated in S_1 and only S_0 and S_1 were considered throughout the 100 fs of dynamics, although ten excited electronic states were computed to encourage correct state ordering. A reduced time step of 1 a.u. (i.e., $\sim$0.025 fs) and an increased DFT grid size were also employed in an attempt to respectively limit total energy conservation issues arising from too large a time step and to improve the stability of the ground-state electronic energy (i.e., to avoid SCF convergence problems and negative excitation energies).

5.2.2.4 Analysis of trajectory surface hopping dynamics simulations

Analysis of the time-dependent electronic state and photoproduct populations was carried out only for the XMS-CASPT2 TSH dynamics. For a given electronic state, the former was calculated as the fraction of trajectories in that state at time t, whereas the latter was calculated as the fraction of trajectories with a twist angle between 0° and 90° (referred to as *cis*) or, the complementary fraction of trajectories with a twist angle between 90° and 180° (referred to as *trans*) at time t.

5.3 Results and discussion

5.3.1 Preliminaries: Full-dimensional analysis of TSH dynamics with XMS-CASPT2

5.3.1.1 Electronic state and photoproduct populations

We start by comparing the electronic state and photoproduct populations of protonated formaldimine for 100 fs of S_1/S_0 dynamics using each TSH approach at the XMS-CASPT2 level of theory (Fig. 5.3). It is important that we first check the behaviour of the four TSH methods using XMS-CASTP2, which we know provides an adequate description of the S_1/S_0 MECX, before applying them to the defective (LR-TD)DFT/TDA/PBE0 intersection ring. Although (adiabatic) electronic state populations are not strictly experimental observables,[4] they are nonetheless still routinely used to compare the accuracy of different electronic structure and/or nuclear dynamics methods. For the time evolution of the photoproduct populations, we follow the value of the twist angle, given its reported importance in the S_1-to-S_0 transition. As discussed in Section 5.2.2.3, we follow 97 trajectories within all four TSH methods, using the same initial conditions of each trajectory across the four TSH approaches in order to ensure consistency.

According to FSSH/analytic [Fig. 5.3(a)], the S_1 population time evolution shows a series of characteristic features. There is an initial delay in the S_1 population decay of 8 fs, in which essentially no hops take place, consistent with the time needed for a rotation of 90° about the C-N bond. This is illustrated by the *trans* photoproduct population equally experiencing an initial decrease only after 8 fs. There is then a fast transfer of population from S_1 to S_0 initiated by the rotation about the C-N bond, before the S_1 population begins to plateau and then rise again to a maximum at 26 fs. The latter is indicative of a significant number of trajectories experiencing re-crossings back to S_1, a consequence of the periodicity in the PESs along the C-N twist coordinate recurrently driving the molecule towards the CX [421]. After 26 fs, the S_1 population steadily decays to S_0, with 50% population transfer achieved after 39 fs and

[4] Not experimentally observable, here, refers to the fact that electronic state populations are dependent on the basis one uses: adiabatic vs diabatic. For a quantity to correspond to a physical observable (i.e., calculated as an expectation value of an operator), it has to be basis-independent (or similarly, gauge-invariant) [30].

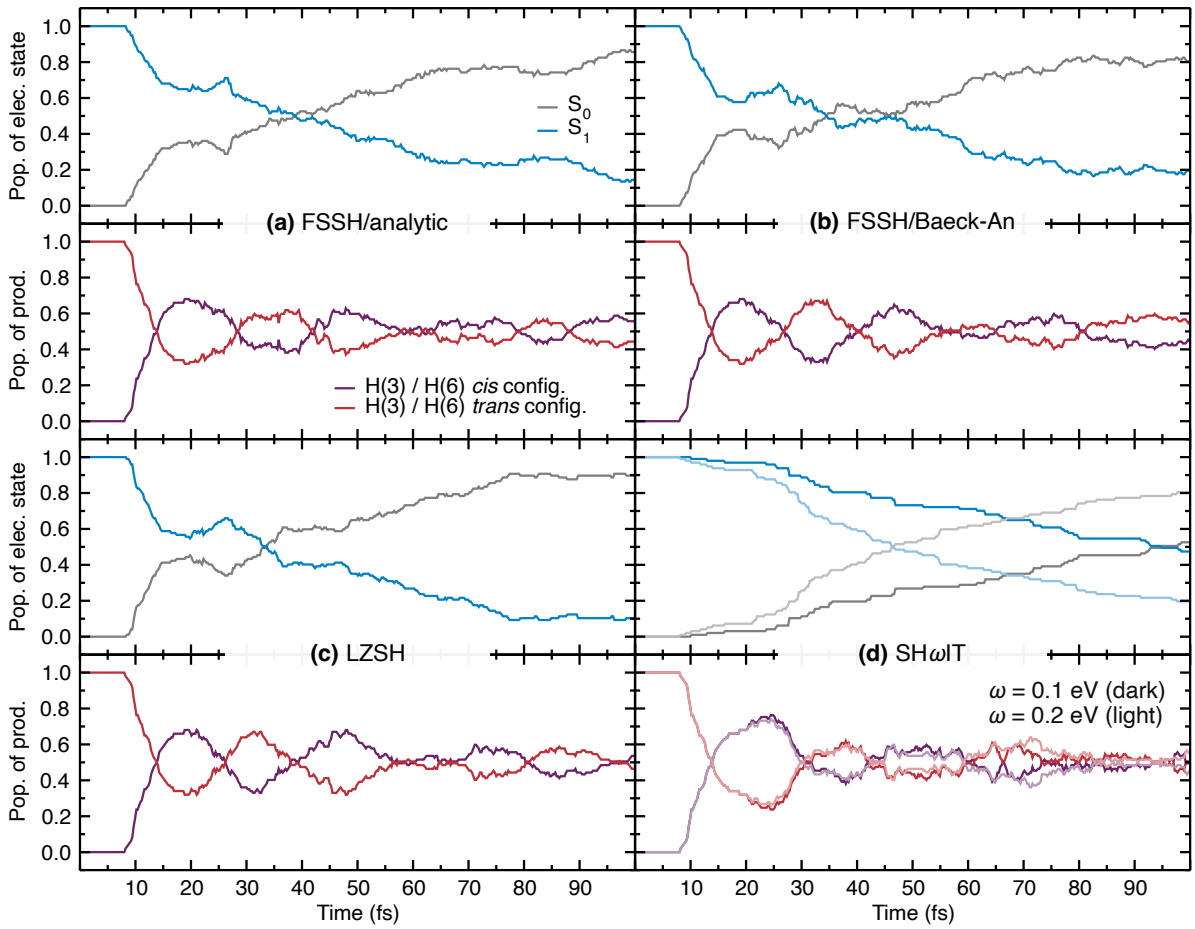

Figure 5.3: Time evolution of the populations of **(upper panel)** the electronic states S_0 (grey) and S_1 (blue) in protonated formaldimine and of **(lower panel)** the molecule adopting a *trans* H(3)/H(6) conformation (red) or a *cis* H(3)/H(6) conformation (purple) for different flavours of TSH dynamics: **(a)** FSSH/analytic, **(b)** FSSH/Baeck-An, **(c)** LZSH and **(d)** SHωIT with ω = 0.1 eV (dark) and ω = 0.2 eV (light). In each case, a swarm of 97 trajectories was considered for 100 fs of dynamics at the XMS(3)-CASPT2(8/6)/cc-pVTZ level of theory.

95% by 100 fs. The time dependence of the electronic state populations is accompanied by the oscillations in the *trans* and *cis* photoproduct populations; rises in the *trans* photoproduct populations coincide with brief rises or plateaus in the S_1 population, implying re-crossings to S_1 with planar molecular conformations.

Overall, FSSH/Baeck-An and LZSH [Fig. 5.3(b) and 5.3(c)] show similar electronic state and photoproduct populations to each other, as well as to FSSH/analytic [423], however there are some differences compared to the latter. Despite exhibiting the same initial delay in decay as FSSH/analytic (*cf.* observations for other rotating molecules by Merritt *et al.* [461]), both FSSH/Baeck-An and LZSH show a slightly faster and greater decrease in the S_1 population after 8 fs. At 20 fs, 42% and 45% population transfer are achieved by FSSH/Baeck-An and LZSH, respectively, in comparison to 36% in FSSH/analytic. Equally, the time taken to reach

50% population transfer is slightly shorter in FSSH/Baeck-An (34 fs) and LZSH (33 fs) than with FSSH/analytic, with FSSH/Baeck-An experiencing an additional occurrence of 50% S_1 population at 45 fs. A more striking difference is that both the FSSH/Baeck-An and LZSH S_1 populations exhibit a distinct levelling off from approximately 77 fs, after which the S_1 population is practically constant, with Baeck-An achieving 81% population transfer by 100 fs, and LZSH 90%. This behaviour at later times is not seen in FSSH/analytic. All of the aforementioned observations likely points toward FSSH/Baeck-An and LZSH slightly overestimating the magnitude of the nonadiabatic coupling between S_0 and S_1, resulting in overestimation of population transfer, as well as increased back-and-forth hopping to S_1; this is consistent with previous studies for other molecules [419, 461, 485, 497].

Table 5.2: Number of trajectories for each of the TSH approaches using XMS(3)-CASPT2(8/6)/cc-pVTZ that do not experience any hops between S_1 and S_0 throughout the 100 fs of dynamics.

TSH approach	Number of trajectories remaining in S_1 throughout the 100 fs of dynamics
FSSH/analytic	3
FSSH/Baeck-An	3
LZSH	1
SHωIT (ω = 0.1 eV)	46
SHωIT (ω = 0.2 eV)	19

Unlike for FSSH/Baeck-An and LZSH, which exhibit semi-quantitative agreement with FSSH/analytic, the time evolution of the electronic populations in SHωIT (ω = 0.1 eV) displays strong qualitative differences to that of FSSH/analytic. SHωIT (ω = 0.1 eV) exhibits an extremely shallow S_1 decay, which manifests in 50% population transfer only being reached after 95 fs, in stark contrast to the behaviour of the other three TSH approaches. Unsurprisingly, no rises in S_1 population are observed during the dynamics, given SHωIT does not allow for back-hopping to the upper state. Increasing the energy gap threshold to ω = 0.2 eV (see Section 5.2.1.3 for details), however, does appear to improve the qualitative agreement between SHωIT and the other TSH methods, with the time taken to reach 50% population transfer reducing to 47 fs [Fig. 5.3(d), light]. When the energy gap threshold is set to ω = 0.1 eV, more trajectories remain in S_1 and do not experience a hop to S_0 within the 100 fs of dynamics (Table 5.2). As such, basing a surface hopping scheme on the energy difference alone (as is done in SHωIT), does not account for possibilities where, despite encountering a region with a moderate separation between the electronic energies (which would preclude hopping in SHωIT with a tight energy threshold), the nonadiabatic coupling between the states is still large enough to afford a transition. This highlights the crudeness of the SHωIT approach, despite its frequent use in the nonadiabatic dynamics community. Moreover, the photoproduct populations in both variants of SHωIT show mediocre agreement to those

of the other TSH approaches. Note, recent work on the S_1/S_0 dynamics of azomethane [427] showed a surprisingly good agreement between FSSH/analytic and SHωIT (ω = 0.1 eV) with XMS-CASPT2 in terms of the duration of different regimes in the S_1 population decay. The contrast between our findings and those of Ref. [427] can be rationalised by the significant likelihood of back-hopping in protonated formaldimine, something not observed in azomethane on the same timescale, and something not captured by SHωIT.

5.3.1.2 Analysis of initial S_1-to-S_0 hopping events

The analysis in Fig. 5.3 broadly compares the different TSH approaches over the entire course of the S_1/S_0 dynamics. Since our interests lie in exploring the behaviour of the different TSH methods in the vicinity of the S_1/S_0 MECX (or the S_1/S_0 intersection seam more generally), it is instructive to focus on one hopping event consistent between all trajectories across the four TSH approaches. An obvious choice would be the first S_1-to-S_0 hopping event. As a result, in Fig. 5.4, we present the distribution of the S_1-S_0 energy gap at the first hopping event across all trajectories for each TSH approach, accompanied (inset) by the distribution of the difference between the S_1 energy at the first hopping event and that at the optimised S_1/S_0 MECX geometry. As such, the former represents how close a trajectory hops to the intersection seam (i.e., whether it hops near a CX), whereas the latter represents how close the trajectory hops to the S_1/S_0 MECX (i.e., the local minimum on the intersection seam). We note that the histograms in Fig. 5.4 do not possess the same number of entries as each other, given that each TSH variant afforded a different number of trajectories that did not experience a hop during the 100 fs of dynamics (Table 5.2).

Interestingly, more FSSH/analytic trajectories initially hop from S_1 to S_0 with an energy gap of 0.3-0.4 eV [Fig. 5.4(a), blue], which is considerably far from the intersection seam, perhaps implying that the intersection seam (or, more specifically, the region of the PES immediately surrounding it) does not play a significant role in the dynamics. Looking at FSSH/Baeck-An [Fig. 5.4(b), blue] and LZSH [Fig. 5.4(c), blue], both give S_1-S_0 energy gap distributions in reasonable agreement with that of FSSH/analytic, despite some subtle differences. Namely, the distribution maximum is shifted higher to 0.4-0.5 eV for FSSH/Baeck-An and shifter lower to 0.2-0.3 eV for LZSH. Equally, a higher (lower) number of LZSH (FSSH/Baeck-An) trajectories have their first S_1-to-S_0 hop at lower energy gaps, closer to the intersection seam than in FSSH/analytic; the opposite is true for higher energy gaps, away from the intersection seam. The behaviour of FSSH/Baeck-An and LZSH is not too surprising. Intrinsically, in the LZSH approach, the trajectory cannot hop until a local minimum in the energy gap has been located and, as such, the trajectory is seemingly forced to be as close to the MECX as possible along its one-dimensional time-coordinate propagation [423]. On the other hand, it has been observed before [419] in other molecules that the Baeck-An expression [Eq. (5.6)] can overestimate the magnitude of the nonadiabatic coupling when the difference

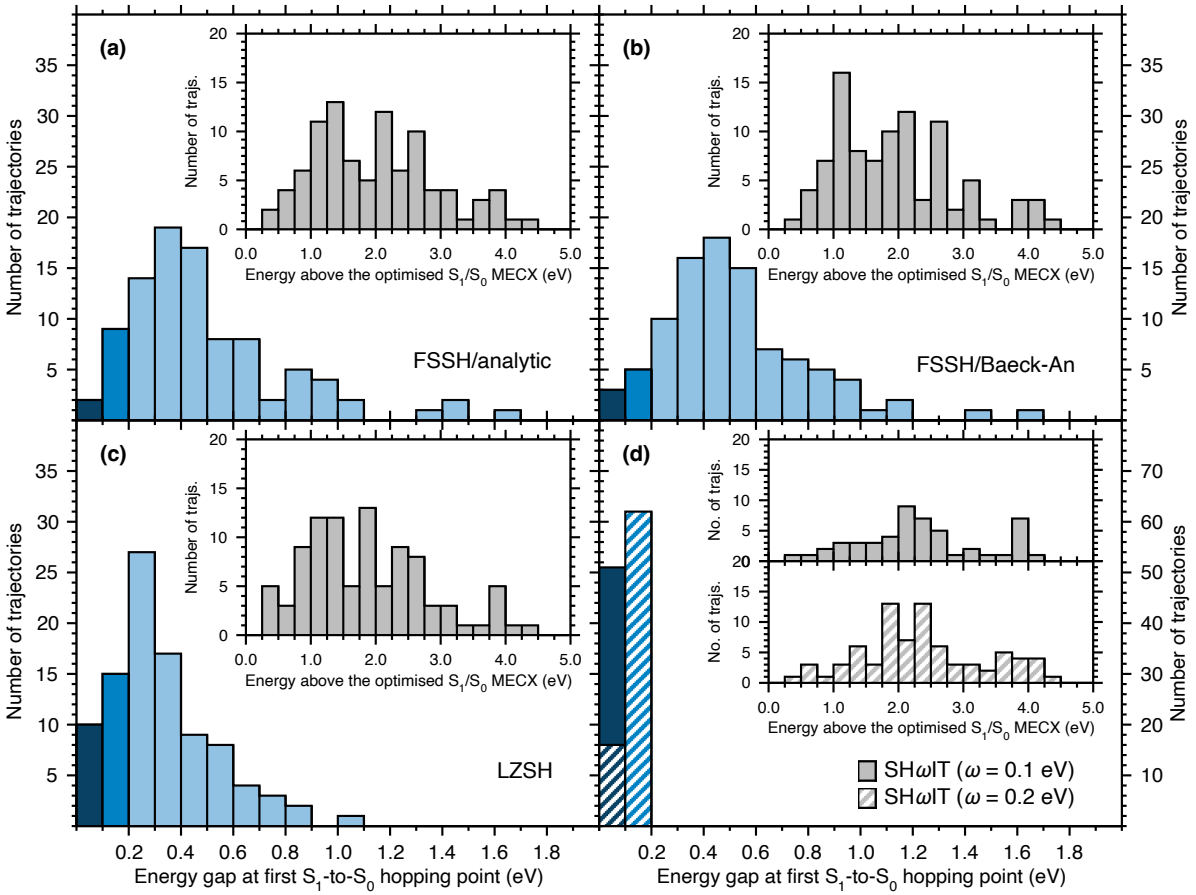

Figure 5.4: Histogram of the $S_1 - S_0$ energy gap at the first S_1-to-S_0 hopping event (blue) in protonated formaldimine for each trajectory considered at the XMS(3)-CASPT2(8/6)/cc-pVTZ level using **(a)** FSSH/analytic (94 trajs.), **(b)** FSSH/Baeck-An (94 trajs.), **(c)** LZSH (96 trajs.) and **(d)** SHωIT with ω = 0.1 eV (51 trajs.) and ω = 0.2 eV (78 trajs.). The $S_1 - S_0$ energy gaps are grouped in intervals of 0.0-0.1 eV (dark blue), 0.1-0.2 eV (mid-blue) and 0.2-2.0 eV (light blue). **Inset:** Histogram of the electronic energy gap between S_1 at the first S_1-to-S_0 hopping geometry of each trajectory and S_1 at the optimised S_1/S_0 MECX geometry (grey). For SHωIT, solid colour indicates ω = 0.1 eV and hashed colour indicates ω = 0.2 eV.

in the electronic energy is large (i.e., when the analytic couplings are expected to be small), resulting in more hops occurring at such energy gaps than expected with FSSH/analytic. This is expected to occur in cases of extreme steepness in the PES topography (the latter being a major dependency of the Baeck-An couplings), as well as due to the Baeck-An expression not depending on the nuclear velocity–a quantity upon which the analytic TDCs do depend and which can cause them to be zero in certain cases, such as at the turning points of bonds [419]. Nevertheless, these extremes are not observed in protonated formaldimine; reiterating again, the overall S_1-S_0 energy gap profiles of FSSH/analytic, FSSH/Baeck-An and LZSH being in sound agreement. This strongly contrasts with SHωIT, where trajectories can only hop with either an initial 0.0-0.1 eV S_1-S_0 energy gap (ω = 0.1 eV), or 0.0-0.2 eV S_1-S_0 energy gap (ω =

0.2 eV), resulting in a distribution [Fig. 5.4(d), blue] completely different to the other three TSH variants. Although this is an obvious result, it is nonetheless interesting to highlight given the routine use of this rudimentary hopping scheme.

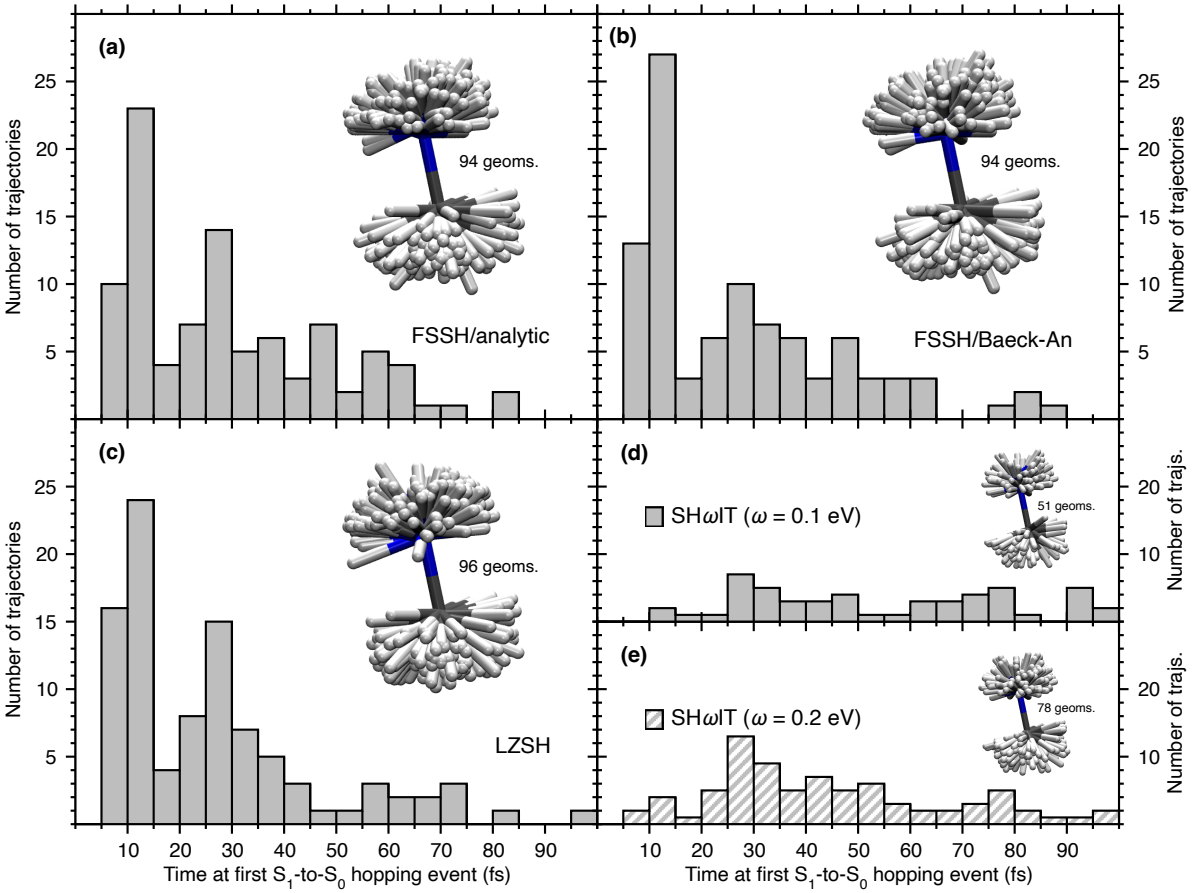

Figure 5.5: Histogram of the times at which the first S_1-to-S_0 hopping event occurs in protonated formaldimine for each trajectory considered at the XMS(3)-CASPT2(8/6)/cc-pVTZ level using **(a)** FSSH/analytic (94 trajs.), **(b)** FSSH/Baeck-An (94 trajs.), **(c)** LZSH (96 trajs.), **(d)** SHωIT with ω = 0.1 eV (51 trajs.) and **(e)** SHωIT with ω = 0.2 eV (78 trajs.). For SHωIT, solid colour indicates ω = 0.1 eV and hashed colour indicates ω = 0.2 eV. **Inset:** Molecular structures of the first S_1-to-S_0 hopping geometries, aligned with respect to the C-N bond.

Considering now the energy at which the trajectories hop above the optimised S_1/S_0 MECX, it is clear that FSSH/analytic, FSSH/Baeck-An and LZSH [Fig. 5.4(a-c), grey] behave similarly, all exhibiting distributions asymmetric about 1.5 eV with the majority of hops occurring quite far away from the S_1/S_0 MECX (i.e., between 1.0-3.0 eV higher in energy). This re-emphasises the practical reality of MECXs not playing as direct a role in the ensuing nuclear dynamics, as suggested by solely comparing key points on the PES. Again, SHωIT gives different energy gap distributions [Fig. 5.4(d), grey] to that of the other three TSH approaches, being flatter and instead symmetric about 2.25 eV, both when ω = 0.1 eV and ω =

0.2 eV, suggesting a possible randomness to the approach.

Lastly, we consider the time at which each trajectory first hops from S_1 to S_0 (Fig. 5.5). FSSH/analytic, FSSH/Baeck-An and LZSH show comparable initial hopping time distributions [Fig. 5.5(a-c)], which are consistent with the full swarm of trajectories being driven towards the intersection seam shortly after photoexcitation, upon which roughly a third experience a hop and transition to S_0 (i.e., large maximum at 10-15 fs). The remaining two thirds continue to evolve on S_1 until a second approach to the intersection seam is attempted, when more trajectories get a chance to hop (i.e., smaller maximum at 25-30 fs). SHωIT (ω = 0.1 eV), on the other hand, exhibits a much flatter distribution with no obvious preferred hopping time [Fig. 5.5(d)]; a small maximum in the SHωIT (ω = 0.2 eV) distribution is observed, however, at 25-30 fs [Fig. 5.5(e)]. Taking the SHωIT initial hopping time distributions together with the other three TSH methods implies that the hops occurring at short time scales must be mediated not by small $S_1 - S_0$ energy gaps (i.e., below 0.2 eV), but rather by sizeable nonadiabatic coupling magnitudes. The insets in Figs 5.5(a-e) show the geometries at the first S_1-to-S_0 hopping events for each TSH method, superimposed along the C-N bond length. Similar geometries are encountered by all four variants of TSH, with most hops occurring when the molecule adopts a twisted [and (bi)pyramidalised] structure, consistent with the section of the intersection seam along which the optimised S_1/S_0 MECX (Chapter 3) was located.

5.3.2 Exploration: Reduced-dimensional analysis of TSH dynamics with (LR-TD)DFT/TDA and XMS-CASPT2

5.3.2.1 TSH dynamics in the vicinity of the XMS-CASPT2 S_1/S_0 MECX

Complementary to the analysis above, it would be interesting to visually compare the trajectories of each of the TSH variants to see if differences in the hopping scheme lead to a different exploration of the PESs. Since we are interested in the influence of the S_1/S_0 MECX (or more specifically, the region of the PESs surrounding it) on the XMS-CASPT2 TSH dynamics, as this is likely the analogous region characterised by the S_1/S_0 intersections ring in (LR-TD)DFT/TDA/PBE0, we consider only those trajectories shared in common between each TSH approach that possess an initial S_1-to-S_0 hopping energy gap within 0.0-0.2 eV (i.e., those in the dark and mid blue bins in Fig. 5.4), not including SHωIT (ω = 0.1 eV). This amounted to nine trajectories in total, which were then projected onto the two natural distortions [Fig. 5.6] discussed in Section 5.2.2.2, namely the C-N bond length, $d_{\text{C-N}}$, and the twist angle, θ_{twist}.

Considering the FSSH/analytic trajectories first [Fig. 5.6(c,d)], it is clear that their behaviour is consistent with what was implied by the time evolution of the electronic state and photoproduct populations. The molecule starts off on S_1 with a roughly non-twisted geometry and a C-N bond length around 1.265 Å [Fig. 5.6(c), red crosses], which is comparable to the

planar optimised XMS-CASPT2 S_0 minimum geometry ($d_{\text{C-N}}$ = 1.279 Å). Twisting about the C-N bond, as well as a slight stretch in the C-N bond quickly results in the molecule being driven straight towards the S_1/S_0 MECX (Fig. 5.6(c), yellow lines), under the influence of the funnel-like topography of the S_1 PES [Fig. 5.6(a)]. Most trajectories pass around (or to the side of) the S_1/S_0 MECX (i.e., approaching tangentially to the $\mathbf{d}_{IJ}(\mathbf{R})$ vector field) before hopping to S_0 (Fig. 5.6(c,d), yellow circles), upon which they explore [Fig. 5.6(d), green lines] either of the two local S_0 minima [Fig. 5.6(b)]. Re-crossings back and forth between S_1 and S_0 are then experienced in some trajectories [Fig. 5.6(c,d), non-yellow circles/triangles], before the end of the 100 fs of dynamics [Fig. 5.6(d), blue crosses]. On first inspection, there appears to be a preference in the FSSH/analytic trajectories for exploring the local minimum at *trans* conformations [i.e., $90^\circ \leq \theta_{\text{twist}} \leq 180^\circ$ in Fig. 5.6(b)], implying perhaps a preference for protonated formaldimine to reform the FC geometry. However, since only 9 trajectories were analysed, such a conclusion may not be statistically valid.

Ignoring this latter point, FSSH/Baeck-An [Fig. 5.6(e,f)] and LZSH [Fig. 5.6(g,h)] show a comparable behaviour to FSSH/analytic. Again, there are some slight differences. Overall, the hopping geometries become more dispersed away from the S_1/S_0 MECX in the following order: LZSH < FSSH/analytic < FSSH/Baeck-An. Both FSSH/analytic and LZSH show hops at twist angles close to that at the S_1/S_0 MECX (i.e., coinciding with the horizontal dashed grey line), with the hops in the former also occurring at a wider range of bond lengths. On the other hand, FSSH/Baeck-An experiences hops at a wider range of twist angles, with a moderate spread in bond lengths also, both of which culminate in a greater dispersion of hopping geometries than in FSSH/analytic and LZSH. This behaviour is consistent with the trend in the distribution of the $S_1 - S_0$ energy gaps at the first hopping event in each of the three methods (Fig. 5.4). The LZSH expression [Eq. (5.14)] encourages trajectories to get closer to the intersection seam in comparison to FSSH/analytic, whereas the Baeck-An expression [Eq. (5.7)] is known to overestimate the nonadiabatic coupling strength, allowing hops to occur at large energy gaps, further away from the intersection seam. Due to the nonadiabatic coupling overestimation, FSSH/Baeck-An also experiences more back-hops to S_1 than the other TSH approaches (i.e., seven coloured triangles in Fig. 5.6(f) vs four and five in Figs 5.6(d) and 5.6(h), respectively). These observations are again in line with previous studies of other molecules [419, 461, 478], and are expected to become more exaggerated the more trajectories are considered beyond the nine here. The SHωIT (ω = 0.2 eV) trajectories [Fig. 5.7(i,j)] explore comparable values of the twist angle and C-N bond length as those in the other TSH methods, despite not experiencing back hops, with the S_1-to-S_0 hopping geometries showing similar agreement.

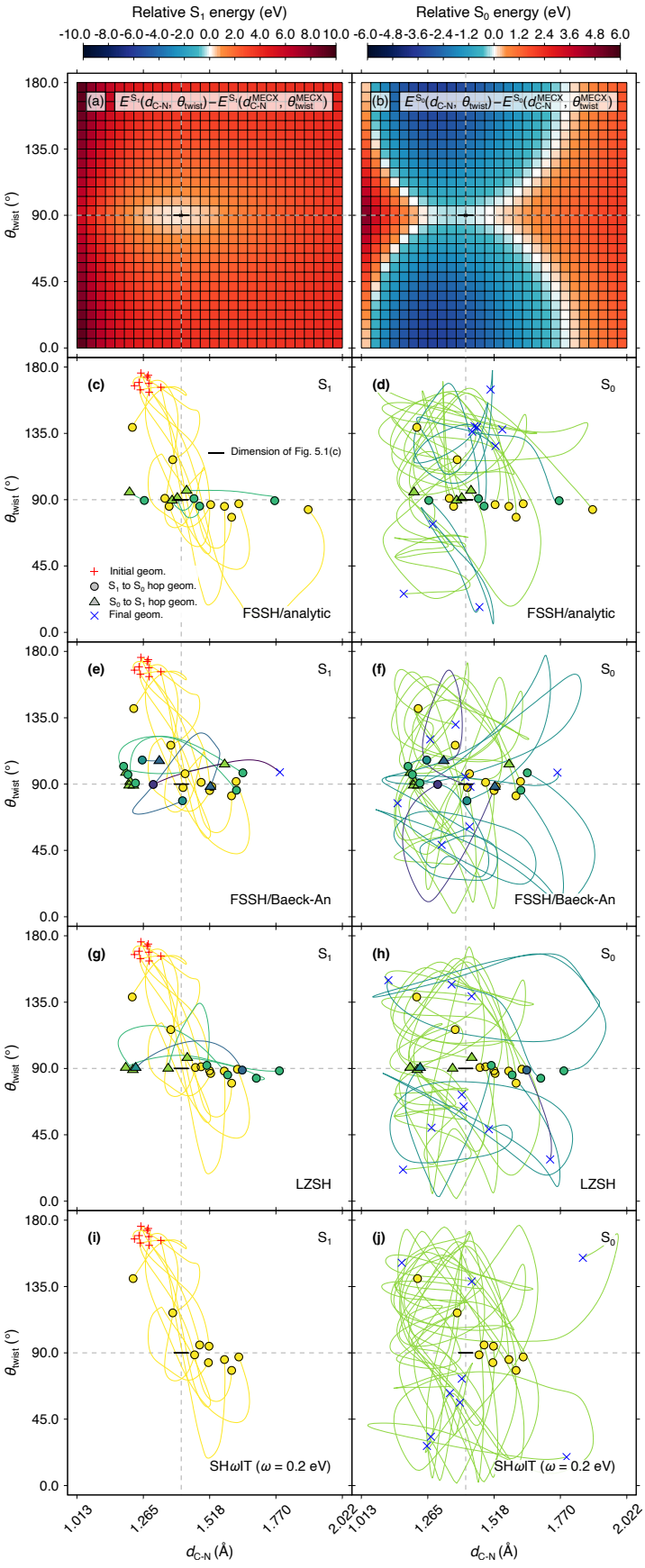

Figure 5.6: Behaviour of the nine TSH trajectories with an energy gap at the first S_1-to-S_0 hopping event below 0.2 eV in protonated formaldimine, which are shared in common between all four flavours of TSH dynamics: **(c, d)** FSSH/analytic, **(e, f)** FSSH/Baeck-An, **(g, h)** LZSH and **(i, j)** SHωIT with ω = 0.2 eV. Projections of the trajectories along two natural molecular distortions–the C-N bond distance, $d_{\text{C-N}}$, and the twist angle, θ_{twist} [as defined in Eq. (5.17)]–are provided at the XMS(3)-CASPT2(8/6)/cc-pVTZ level for 100 fs of dynamics. Initial geometries (red plusses), final geometries (blue crosses), S_1-to-S_0 hopping geometries (coloured circles) and S_0-to-S_1 hopping geometries (coloured triangles) are also given. The line and symbol colour (yellow-green-blue-purple) indicates the time progression of the trajectory with each subsequent hop. 2D colour maps of the S_0 and S_1 electronic energies are provided in **(b)** and **(a)**, respectively, again at the XMS(3)-CASPT2(8/6)/cc-pVTZ level of theory. The black box (appearing as a black line at the point of intersection of the two dashed grey lines) encloses the area spanned by the approximate branching plane used to generate Fig. 5.1(c). The dashed grey lines indicate the values of $d_{\text{C-N}}$ and θ_{twist}, respectively, at the optimised S_1/S_0 MECX geometry. Analysis regarding S_1 is given on the left and that regarding S_0 is given on the right.

Since the trajectories are plotted over the full range of twist angles (i.e., 0.0-180.0°) in Fig. 5.6, it is difficult to grasp how close some trajectories actually get to the S_1/S_0 MECX. This is exemplified by the black box in each plot in Fig. 5.6, which corresponds to the dimension of the energy difference colour map in Fig. 5.1(c), appearing as a black line at the point of intersection of the two dashed grey lines. It would therefore be instructive to replot the nine trajectories along a smaller range of the two natural distortions, closer to the S_1/S_0 MECX. We do this in Fig. 5.7 for twist angles of ~89-91° and C-N bond lengths of ~1.3-1.5 Å on top of an appropriately scaled copy of Fig. 5.1(c). Curiously, in all TSH approaches, no hops occur within the region spanned by Fig. 5.1(c) and virtually no trajectories possess a time step in this region either. Even more notable is the difference in scale between the change in the two natural distortions for one nuclear time step [Fig. 5.7(a)] and that for the region enclosed by Fig. 5.1(c). Most trajectories simply hop over this region, with the average nuclear time step involving a ~1.5° change in the twist angle, yet the region enclosed by Fig. 5.1(c) only spans ~0.04°. If one takes the latter as outlining the approximate "size" of the S_1/S_0 MECX, assuming the two natural distortions are representative approximations to the two branching space vectors, it is clear that the S_1/S_0 MECX is actually much "smaller" than the region explored by the ensuing nuclear dynamics. This strengthens anecdotal evidence that the true role of MECXs (or CXs, more generally) is not for the point of degeneracy to be involved directly in population transfer, but rather for CXs to act in a practical sense as "PES staples" [498], bringing chemically relevant adiabatic states in close enough proximity to one another (and closer than can be achieved by true avoided crossings alone), such that rapid nonadiabatic transitions can occur. It could be tempting to further surmise that if a similar situation occurs in the corresponding (LR-TD)DFT/TDA/PBE0 TSH dynamics, that the defective S_1/S_0 intersection ring (or more aptly, this aesthetically defective "PESs staple") may again not cause too much of a hindrance to the nuclear dynamics.

5.3.2.2 XMS-CASPT2 and (LR-TD)DFT/TDA full PES landscapes

Before inspecting the (LR-TD)DFT/TDA/PBE0 equivalent of Fig. 5.6, it is useful to first examine the S_0 and S_1 PES along these two natural distortions [i.e., 3D versions of the 2D colour maps in Fig. 5.6(a,b)]. The XMS-CASPT2 PESs [Fig. 5.8(a)] show the expected characteristic behaviours for the respective natural distortion extremes: at $\theta_{\text{twist}} = 0.0°$, the PESs are reminiscent of the potential energy curves in a diatomic molecule; at $d_{\text{C-N}} = 1.013$ Å, the sinusoidal periodicity expected for a rotation about a bond is evident. Equally, the S_1 PES exhibits a characteristic funnel-like shape near the point of degeneracy and the S_0 PESs possesses two minima, all of which is already indicated in the 2D colour maps in Fig. 5.6(a,b). The same plot is replicated in Fig. 5.8(b) for (LR-TD)DFT/TDA/PBE0. As mentioned in Section 5.2.2.2, for greatest consistency, the molecule was distorted to the same extent from the MECP geometry in (LR-TD)DFT/TDA/PBE0 as it was from the MECX geometry in

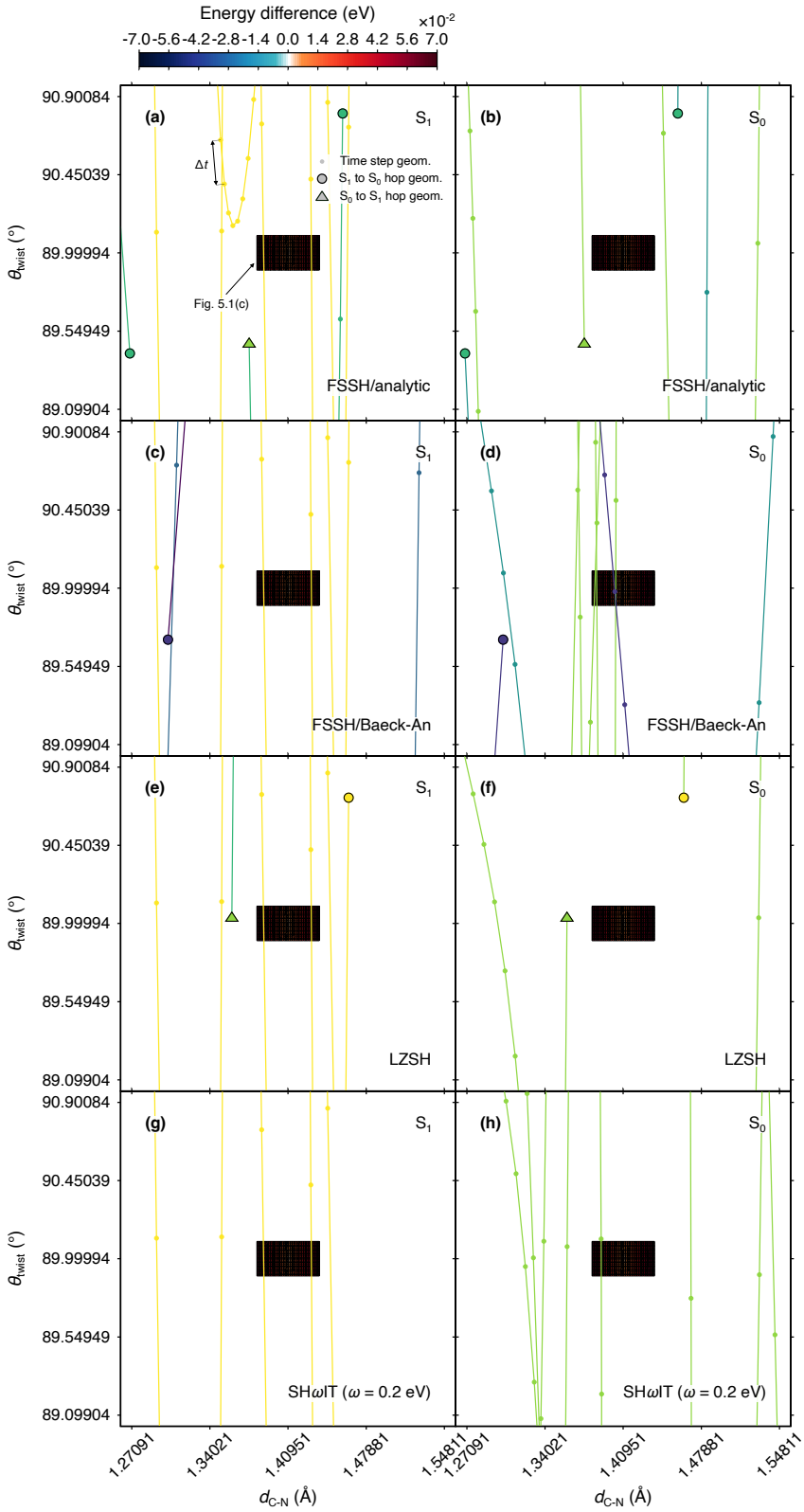

Figure 5.7: Behaviour of the nine TSH trajectories with an energy gap at the first S_1-to-S_0 hopping event below 0.2 eV in protonated formaldimine, which are shared in common between all four flavours of TSH dynamics: **(a, b)** FSSH/analytic, **(c, d)** FSSH/Baeck-An, **(e, f)** LZSH and **(g, h)** SHωIT with ω = 0.2 eV. Same as in Fig. 5.6 for XMS(3)-CASPT2(8/6)/cc-pVTZ, except all plots are now zoomed in (i.e., plotted along smaller variations of $d_{\text{C-N}}$ and θ_{twist}). The 2D colour plot in Fig. 5.1(c) is also included and appropriately scaled. Non-outlined coloured circles indicate each time step geometry; the extent to which $d_{\text{C-N}}$ and θ_{twist} change in an arbitrary nuclear time step, Δt, is explicitly indicated in Fig. 5.7(a) for one of the FSSH/analytic trajectories.

XMS-CASPT2 (i.e., XMS-CASPT2: 2.022 Å − 1.518 Å = 0.504 Å; (LR-TD)DFT/TDA/PBE0: 2.016 Å − 1.512 Å = 0.504 Å). On initial inspection, (LR-TD)DFT/TDA/PBE0 appears to reproduce the behaviour of the PESs in XMS-CASPT2 reasonably well, with S_1 possessing a similar basin-like shape and S_0 exhibiting two minima. Most importantly, at this scale along these two specific natural distortions, the S_0 and S_1 PESs in (LR-TD)DFT/TDA/PBE0 seem to meet at a single point of degeneracy, consistent with observations reported by Tavernelli *et al.* [294]. However, as discussed in Section 3.3.1.3, plotting the PESs along such extreme scans (and thus a more coarse grid of geometries) can falsely give the impression that (LR-TD)DFT/TDA/PBE0 adequately describes the S_1/S_0 degeneracy point. Of course, the results reported in Chapters 3 and 4 highlight the contrary. Nonetheless, at this scale, the S_0 and S_1 PESs are in overall good agreement with those of XMS-CASPT2, with important differences to now be discussed below in Section 5.3.2.3 in the context of the (LR-TD)DFT/TDA/PBE0 TSH trajectories.

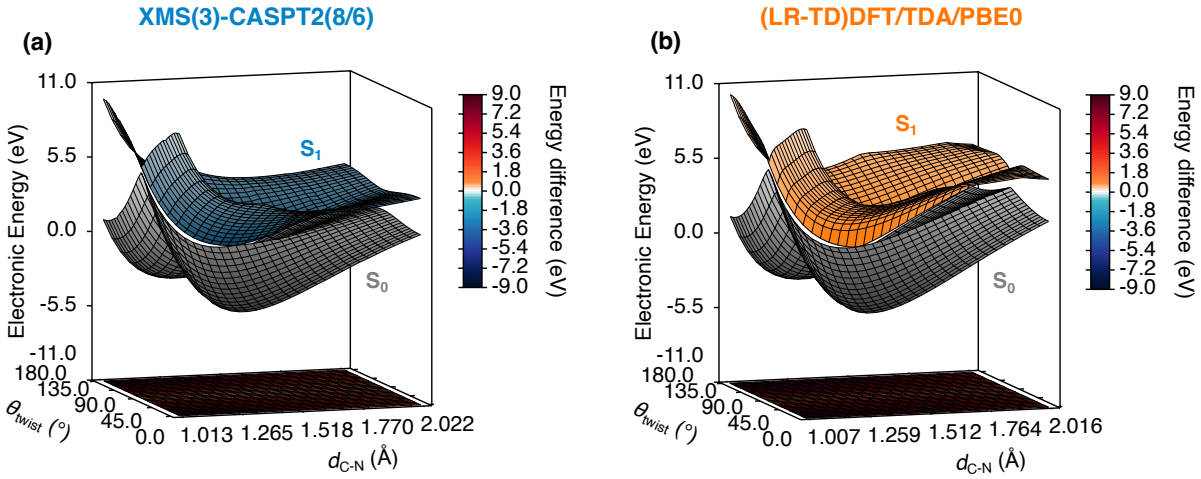

Figure 5.8: Full potential energy landscape characterising the entire 100 fs of nonadiabatic dynamics from S_1 to S_0 along chosen natural molecular distortions in protonated formaldimine. Comparison of the S_0 and S_1 PESs obtained with **(a)** XMS(3)-CASPT2(8/6)/cc-pVTZ (blue/grey) and **(b)** (LR-TD)DFT/TDA/PBE0/cc-pVDZ (orange/grey) plotted along large values of the C-N bond distance, $d_{\text{C-N}}$, and the twist angle, θ_{twist} [as defined in Eq. (5.17)]. In each plot, the MECX (or MECP) geometries were obtained at the same level of theory used to calculate the electronic energies. The base in both plots shows a 2D colour map of the $S_1 - S_0$ energy difference (see colour bar on the right).

5.3.2.3 TSH dynamics in the vicinity of the (LR-TD)DFT/TDA S_1/S_0 MECP

We now consider the (LR-TD)DFT/TDA/PBE0 TSH trajectories. We employ the same nine initial conditions as were used for the nine XMS-CASPT2 TSH trajectories in Fig. 5.6 in order to generate the equivalent figure with (LR-TD)DFT/TDA/PBE0 (Fig. 5.9). (LR-TD)DFT/TDA/PBE0 exhibits a similar behaviour to XMS-CASTP2, with likewise only small

differences between the different TSH approaches. The trajectories head towards the S_1/S_0 MECP, hop to S_0 in its vicinity, then take some time to explore the S_0 minima, with some also experiencing back-hops to S_1. However, there are some key differences. Firstly, the (LR-TD)DFT/TDA/PBE0 trajectories experience oscillations in the C-N bond lengths as they propagate in the direction of the S_1/S_0 MECP, something not experienced by the corresponding XMS-CASPT2 trajectories, which exhibit a much smoother and direct path. When in the ground state, the (LR-TD)DFT/TDA/PBE0 trajectories also do not sample as large a range of C-N bond lengths as those in XMS-CASPT2. This can be rationalised by the S_0 gradient in the vicinity of the minima towards longer C-N bond lengths in (LR-TD)DFT/TDA/PBE0 being more steep than the in XMS-CASPT2, illustrated by comparing the blue region in the S_0 colour map plots in Fig. 5.6(b) and 5.9(b). That of (LR-TD)DFT/TDA/PBE0 spans fewer horizontal grid points than that of XMS-CASPT2, implying that the S_0 PES increases in energy at a faster rate. Moreover, the (LR-TD)DFT/TDA/PBE0 trajectories show fewer re-crossings to S_1 than do the XMS-CASPT2 trajectories. This can be attributed to the steepness of the S_1 PES in the vicinity of the S_1/S_0 MECX, as indicated by the sharp increase the S_1 energy as one moves one grid point away from the degeneracy point along the twist angle in either direction in Fig. 5.1(b) [relative to the XMS-CASPT2 S_1 energy along the same coordinate in Fig. 5.1(a)]. As such, the trajectories find it more difficult to hop back to S_1. A too rapidly varying S_1 PES in the vicinity of the S_1/S_0 MECX is consistent with previous observations in the literature [27], as well as the results presented in Chapter 3 using the analytic branching space vectors.

A further difference between (LR-TD)DFT/TDA/PBE0 and XMS-CASPT2 is the hopping geometries in the former appearing to be much closer to the S_1/S_0 MECP than in the latter. This difference is likely due to the (assumed) significantly underestimated nonadiabatic coupling between S_1 and S_0 in (LR-TD)DFT/TDA/PBE0, resulting in each trajectory having to get closer to the S_1/S_0 MECP in order to hop. By re-plotting Fig. 5.9 and zooming into the region spanned by Fig. 5.1(d), it is clear that (LR-TD)DFT/TDA/PBE0 (Fig. 5.10) has a much higher density of hops (and time steps, more generally) closer to the region spanned by Fig. 5.1(d), with some hops/time steps appearing within this region, but supposedly none with negative excitation energies. Note, we attribute the greater number of time steps near the region enclosed by Fig. 5.1(d) in Fig. 5.10 simply due to the smaller time step used in the (LR-TD)DFT/TDA/PBE0 TSH dynamics (i.e., ~0.025 fs rather than ~0.25 fs in XMS-CASPT2). If one was to consider using the same time step for (LR-TD)DFT/TDA/PBE0 as was used for XMS-CASPT2 [i.e., one ten times larger] and took everything discussed above in isolation, one could falsely assume that the S_1/S_0 intersection ring occurs at such a small scale relative to the nuclear dynamics when projected onto the two natural distortions (i.e., only spanning $\Delta d_{\text{C-N}} = \sim 0.02$ Å; $\Delta\theta_{\text{twist}} = \sim 0.04^\circ$ in Fig. 5.1), that it causes a minimal affect on the dynamics.

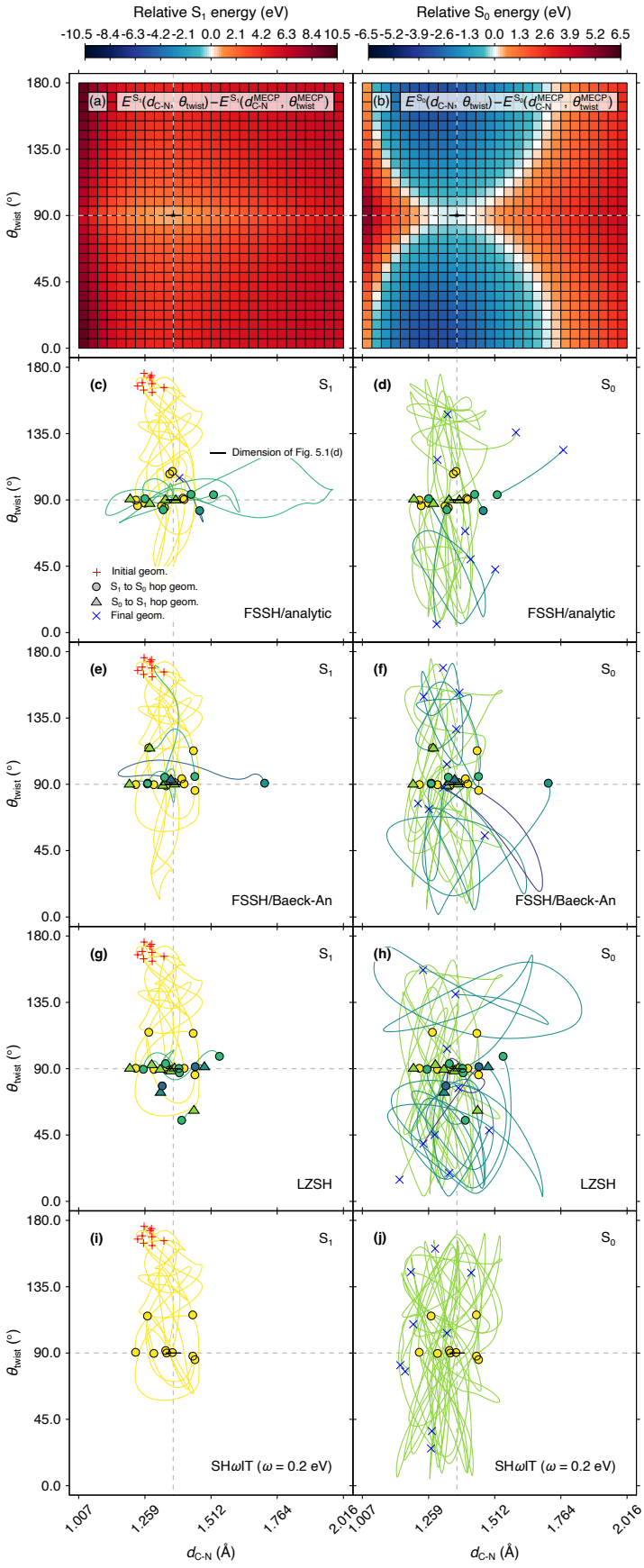

Figure 5.9: Behaviour of the nine TSH trajectories with an energy gap at the first S_1-to-S_0 hopping event below 0.2 eV in protonated formaldimine, which are shared in common between all four flavours of TSH dynamics: **(c, d)** FSSH/analytic, **(e, f)** FSSH/Baeck-An, **(g, h)** LZSH and **(i, j)** SHωIT with ω = 0.2 eV. Projections of the trajectories along two natural molecular distortions–the C-N bond distance, $d_{\text{C-N}}$, and the twist angle, θ_{twist} [as defined in Eq. (5.17)]–are provided at the (LR-TD)DFT/TDA/PBE0/cc-pVDZ level for 100 fs of dynamics. Initial geometries (red plusses), final geometries (blue crosses), S_1-to-S_0 hopping geometries (coloured circles) and S_0-to-S_1 hopping geometries (coloured triangles) are also given. The line and symbol colour (yellow-green-blue-purple) indicates the progression of the trajectory with each subsequent hop. 2D colour maps of the S_0 and S_1 electronic energies are provided in **(b)** and **(a)**, respectively, again at the (LR-TD)DFT/TDA/PBE0/cc-pVDZ level of theory. The black box (appearing as a black line at the point of intersection of the two dashed grey lines) encloses the area spanned by the approximate branching plane used to generate Fig. 5.1(d). The dashed grey lines indicate the values of $d_{\text{C-N}}$ and θ_{twist}, respectively, at the optimised S_1/S_0 MECP geometry. Analysis regarding S_1 is given on the left and that regarding S_0 is given on the right.

However, strict caution should be exercised before making such a conclusion. Each trajectory represents the time evolution of a full-dimensional molecule, so when they are projected onto a reduced number of nuclear degrees of freedom, inevitably some information is lost. Given the intricacies of the problem with the S_1/S_0 intersection ring in (LR-TD)DFT/TDA, it is not surprising that projecting along certain other natural distortions may also reveal similar a S_1/S_0 intersection ring with similar negative excitation energies. Therefore, even though the trajectories in Fig. 5.10 are not expected to encounter a region of negative excitation energy (i.e. inside the intersection ring) by inspecting their projections along $d_{\text{C-N}}$ and θ_{twist}, it may still be the case that they do along other natural distortions. In particular, the way the twist angle is defined [Eq. (5.17)] does not take into account whether the CH_2 or NH_2 moieties are pyramidalised; unlike the more traditional dihedral angle, θ_{twist} offers a true definition of the twist about a bond, uninfluenced by the degree of pyramidalisation at either end of the bond. Equally, the energy difference maps in Fig. 5.1(c) and 5.1(d) are generated by distorting protonated formaldimine along the two chosen nuclear coordinates, whilst keeping all other molecular parameters (i.e., bond lengths, bond angles, dihedrals etc.) fixed at their value at the optimised S_1/S_0 MECP. This is, of course, different to the trajectories, which have all internal coordinates free to vary throughout the dynamics. Nonetheless, it can still be argued that, here, the S_1/S_0 intersection ring–linking back again to the second aim of this chapter–constitutes a "very small" problematic region, and it is conjectured that such an intersection ring remains very small along other relevant natural distortions, like the CH_2 and NH_2 pyramidalisation. The latter are the focus of future investigation.

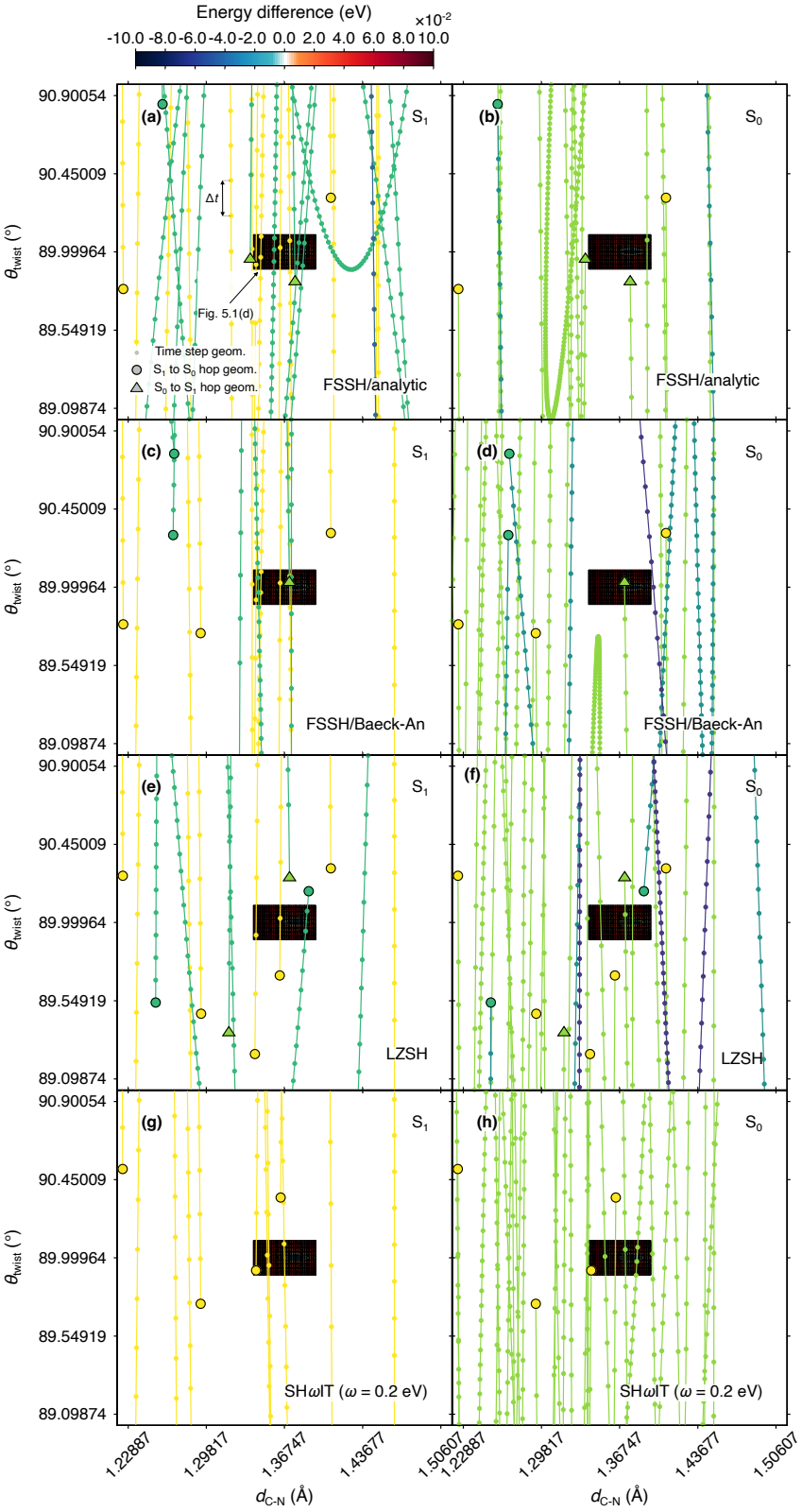

Figure 5.10: Behaviour of the nine TSH trajectories with an energy gap at the first S_1-to-S_0 hopping event below 0.2 eV in protonated formaldimine, which are shared in common between all four flavours of TSH dynamics: **(a, b)** FSSH/analytic, **(c, d)** FSSH/Baeck-An, **(e, f)** LZSH and **(g, h)** SHωIT with ω = 0.2 eV. Same as in Fig. 5.9 for (LR-TD)DFT/TDA/PBE0/cc-pVDZ, except all plots are now zoomed in (i.e., plotted along smaller variations of $d_{\text{C-N}}$ and θ_{twist}). The 2D colour plot in Fig. 5.1(d) is also included and thus appropriately scaled. Non-outlined coloured circles indicate each time step geometry; the extent to a change in the values of $d_{\text{C-N}}$ and θ_{twist} for an arbitrary time step, Δt, is explicitly highlighted in Fig. 5.10(a) for one of the FSSH/analytic trajectories.

5.3.3 Scrutiny: Full-dimensional analysis of a single TSH trajectory with (LR-TD)DFT/TDA and XMS-CASPT2

5.3.3.1 Comparing (LR-TD)DFT/TDA and XMS-CASPT2 in FSSH/analytic

In order to properly scrutinise the affect of the (LR-TD)DFT/TDA S_1/S_0 intersection ring on full-dimensional nuclear dynamics, it is instructive to follow a single exemplar trajectory, one of the nine plotted in Fig. 5.9 and 5.10, and compare it to its XMS-CASPT2 analogue (plotted in Fig. 5.6 and 5.7). We start off by considering only FSSH/analytic. The XMS-CASPT2 trajectory (Fig. 5.11, blue) is characterised by a single successful hop at 22 fs, as indicated by the full and immediate (de)population of (S_1) S_0 at this time [Fig. 5.11(a), blue]. As soon as the trajectory is initiated in S_1, the ground state steadily destabilises [Fig. 5.11(b), blue] until it reaches an energy gap of 0.1 eV with S_1 (i.e., the point at which the trajectory hops), before stabilising again until 30 fs, after which the trajectory maintains an $S_1 - S_0$ energy difference of roughly 5.5 eV for the rest of the dynamics. Note, only every three time steps are depicted by grey circles in Fig. 5.11 (blue) for XMS-CASPT2 [*cf*. only every 21 time steps for (LR-TD)DFT/TDA/PBE0]. The XMS-CASPT2 trajectory propagates with a smoothly varying kinetic energy [Fig. 5.11(c), blue], experiencing a small total energy discontinuity (i.e., ~0.05 eV) at 21 fs [Fig. 5.11(d), blue]. This discontinuity arises due to a similarly small discontinuity in the electronic energy [see Fig. 5.11(b)(i) close-up] and, in the case of FSSH/analytic, does not interfere with the S_1-to-S_0 hopping event. The same is not true for all of the other three TSH approaches (vide infra).

We now consider the analogous (LR-TD)DFT/TDA/PBE0 trajectory [Fig. 5.11, orange] using the same initial conditions. For the first 21 fs (LR-TD)DFT/TDA/PBE0 does a good job at reproducing the S_1 and S_0 states, showing similar oscillations to those in XMS-CASPT2 as the ground state destabilises [Fig. 5.11(b), orange]. This is understandable given the trajectories is far from the S_1/S_0 MECP region. However, after 21 fs, the agreement between (LR-TD)DFT/TDA/PBE0 and XMS-CASPT2 deteriorates, as the trajectory reaches the region surrounding the S_1/S_0 MECP. The (LR-TD)DFT/TDA/PBE0 trajectory is therefore characterised by two failed hops, one at 25 fs (i.e., close to the XMS-CASPT2 hopping time), which is accompanied by a modest reduction (i.e., ~20%) in the S_1 population that is soon regained again, and one slightly later at 34 fs. A successful hop takes place much later in the dynamics at 73 fs. The two failed hops occur at points close to the S_1/S_0 intersection ring, where the S_1 energy exhibits a sharp, cuspidal topography and goes below that of S_1 [Fig. 5.11(b)(ii)]. We provide a 3D representation of the S_0 and S_1 PESs in this region in Fig. 5.12(b), where it is clear that (LR-TD)DFT/TDA/PBE0 affords an S_1 electronic state that varies too rapidly in comparison to that of XMS-CASPT2 [Fig. 5.12(a)], despite the S_0 PESs in both methods showing similar behaviour. Moreover, the two failed hops are accompanied by large jumps in the total energy, both over 0.5 eV, which is considerably larger than the total energy discontinuity

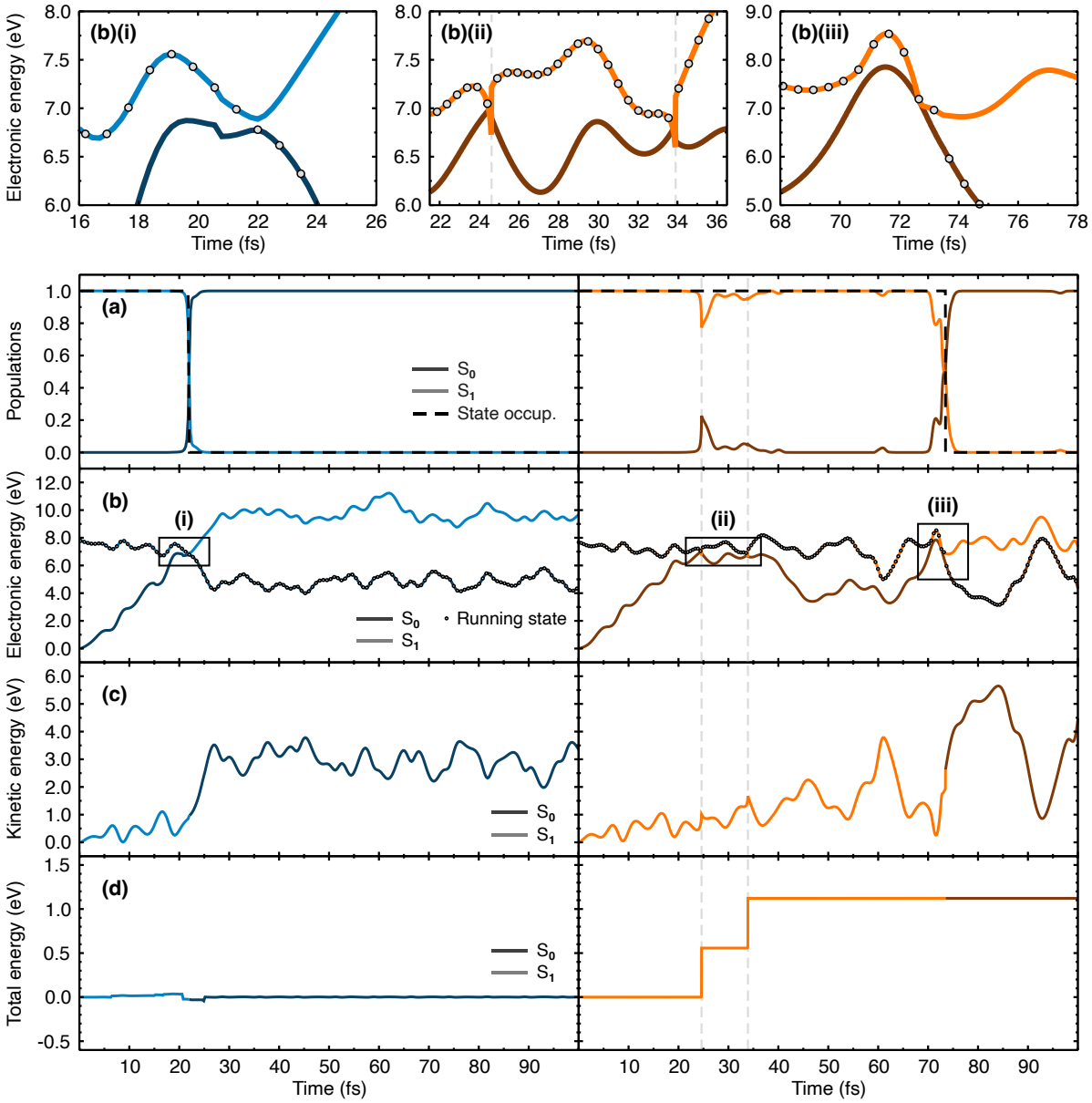

Figure 5.11: Analysis of an exemplar FSSH/analytic trajectory with an energy gap at the first S_1-to-S_0 hopping event below 0.2 eV for protonated formaldimine. Comparison of XMS(3)-CASPT2(8/6)/cc-pVTZ (blue) and (LR-TD)DFT/TDA/PBE0/cc-pVDZ (orange) **(a)** electronic state populations, **(b)** electronic energies, **(c)** kinetic energy and **(d)** total energy for 100 fs of dynamics. The black boxes **(i) to (iii)** in panel (b) outline regions where the S_1 electronic energy (mid colour) comes close to (and even crosses) the S_0 electronic energy (dark colour). The corresponding zoomed-in electronic energy plots are included above the main panels, where the grey circles indicate the running state; an S_1-to-S_0 hop event is portrayed in Figs 5.11(b)(i) and (b)(iii), but not in Fig. 5.11(ii). The vertical dashed grey lines indicate the time at which large discontinuities in the total energy are experienced in the (LR-TD)DFT/TDA/PBE0/cc-pVDZ FSSH/analytic dynamics.

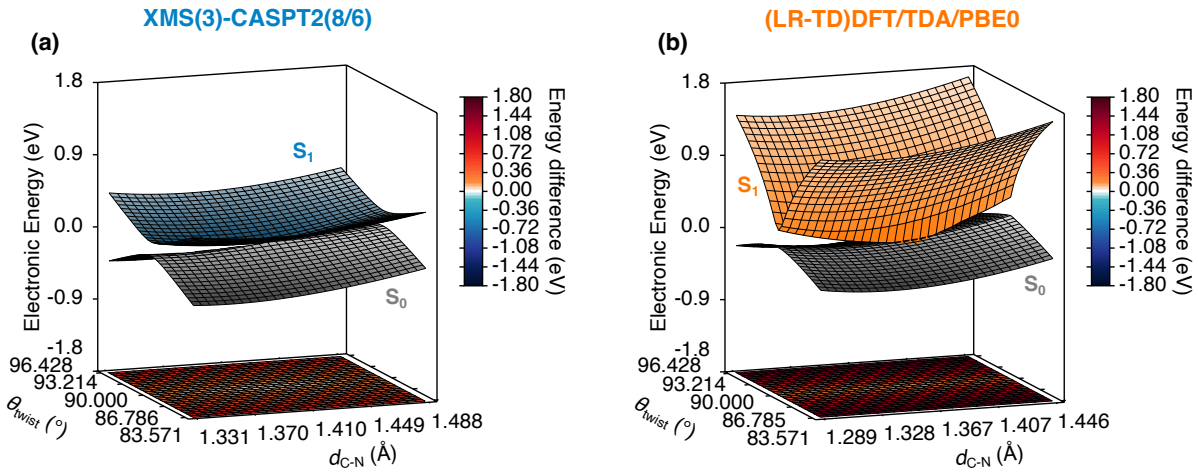

Figure 5.12: Approximate extended branching space of the S_1/S_0 MECX (or MECP) in protonated formaldimine. Comparison of the S_0 and S_1 PESs obtained with **(a)** XMS(3)-CASPT2(8/6)/cc-pVTZ (blue/grey) and **(b)** (LR-TD)DFT/TDA/PBE0/cc-pVDZ (orange/grey) plotted along moderate values of two natural molecular distortions: the C-N bond distance, $d_{\text{C-N}}$, and the twist angle, θ_{twist} [as defined in Eq. (5.17)]. In each plot, the MECX (or MECP) geometries were obtained at the same level of theory used to calculate the electronic energies. The dashed line in the Fig. 5.12(b) indicates the seam where $E_0^{\text{el}}(\mathbf{R}) = E_1^{\text{el}}(\mathbf{R})$. (We note that the rendering of the colours for the PESs does not reflect precisely this intersection.) The base in both plots shows a 2D colour map of the $S_1 - S_0$ energy difference (see colour bar on the right).

experienced by XMS-CASPT2. Such discontinuities can be rationalised by the behaviour in the kinetic energy of the (LR-TD)DFT/TDA/PBE0 trajectory, which at the aforementioned problematic time steps exhibits similarly sharp cusps, physically reminiscent of cases where the nuclei hit a large barrier, resulting in an abrupt change in velocity. On the other hand, the successful hop at 73 fs, which is accompanied by a full population decay to S_0 and no total energy discontinuity, occurs at a time step when the electronic energy gap is small but remains positive [Fig. 5.11(b)(iii)]. The S_1 and S_0 PESs both behaving well around this point, something that is reiterated by the lack of a corresponding cusp in the kinetic energy.

The question still remains why XMS-CASPT2 should successfully hop first time, but (LR-TD)DFT/TDA/PBE0 fails twice before finally hopping successfully. Some insight can be gained by inspecting the magnitude of the TDCs [Fig. 5.13(a)] and $\mathbf{d}_{IJ}(\mathbf{R})$ vectors [Fig. 5.13(b)] along the course of the trajectory for both electronic structure methods. As already mentioned in Section 5.2.2.3, $\mathbf{d}_{IJ}(\mathbf{R})$ vectors (and therefore TDCs) are only computed when the $S_1 - S_0$ energy gap goes below 2.0 eV, which is highlighted in Fig. 5.13 by the grey boxes. Zooming into the large coupling regions in both electronic structure methods, we see a strong contrast between coupling that results in a successful hop and that which does not. The $\mathbf{d}_{IJ}(\mathbf{R})$ vector near the point of hopping in XMS-CASPT2 [Fig. 5.13(b)(i)] has a broad symmetric form with a large magnitude, giving a sizeable area to integrate over. The same is true for the

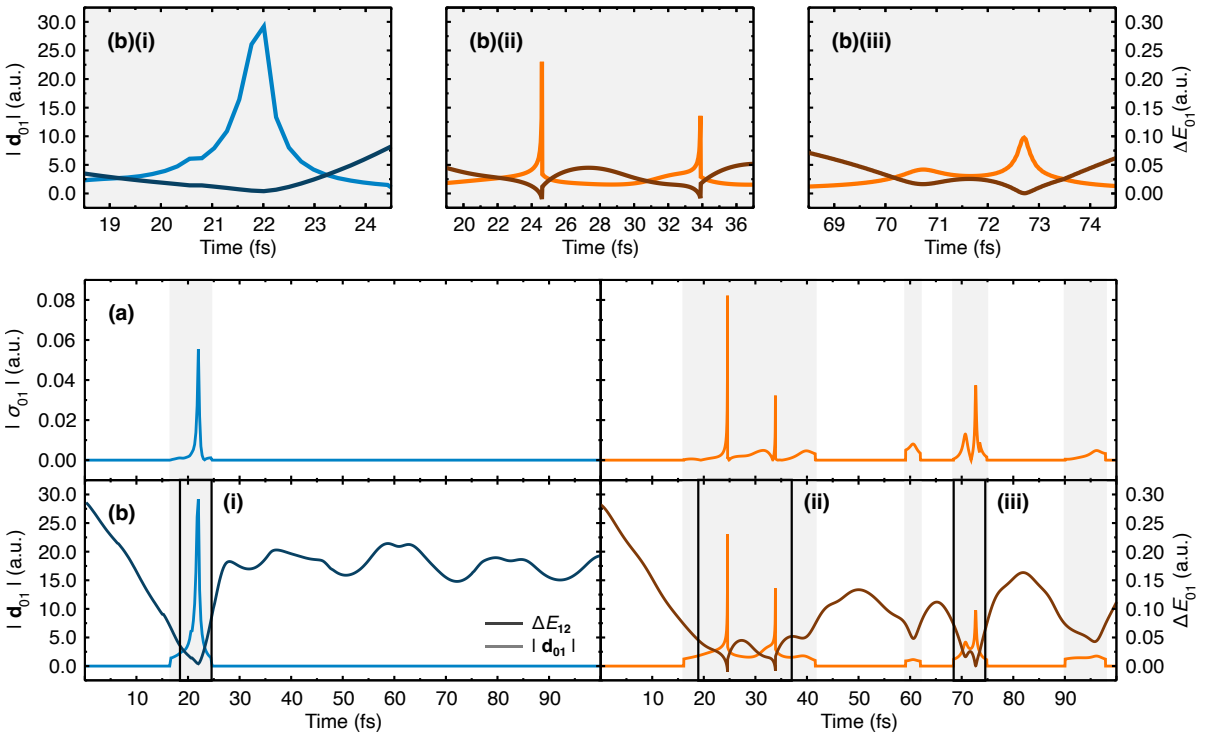

Figure 5.13: Analysis of an exemplar FSSH/analytic trajectory with an energy gap at the first S_1-to-S_0 hopping event below 0.2 eV for protonated formaldimine. Comparison of **(a)** the magnitude of the time-derivative nonadiabatic couplings, $|\sigma_{01}|$ (mid colour); **(b)** the magnitude of the nonadiabatic coupling vectors, $|\mathbf{d}_{01}(\mathbf{R})|$ (mid colour), and the $S_1 - S_0$ electronic energy difference, ΔE_{01} (dark colour), for 100 fs of dynamics using XMS(3)-CASPT2(8/6)/cc-pVTZ (blue) and (LR-TD)DFT/TDA/PBE0/cc-pVDZ (orange). The black boxes **(i) to (iii)** in panel (b) outline the regions where $|\mathbf{d}_{01}(\mathbf{R})|$ takes large values. The corresponding zoomed-in $|\mathbf{d}_{01}(\mathbf{R})|$ plots are included above the main panels; $|\mathbf{d}_{01}(\mathbf{R})|$ appears continuous in Figs 5.13(b)(i) and (b)(iii), but not in Figs 5.13(b)(ii). The grey background indicates time steps for which the $\mathbf{d}_{01}(\mathbf{R})$ vector was calculated–see Section 5.2.2.3 for details.

$\mathbf{d}_{IJ}(\mathbf{R})$ vector at the successful hop in (LR-TD)DFT/TDA/PBE0 [Fig. 5.13(b)(iii)], albeit with a smaller magnitude. However, the $\mathbf{d}_{IJ}(\mathbf{R})$ vectors in (LR-TD)DFT/TDA/PBE0 at the two occurrences of failed hopping [Fig. 5.13(b)(ii)], despite having significant magnitudes (in one case, comparable to that in XMS-CASPT2), are nonetheless strongly asymmetric with almost no integratable area. They also coincide with negative $S_1 - S_0$ energy gaps. This behaviour in the $\mathbf{d}_{IJ}(\mathbf{R})$ vectors across the four hopping events in Fig. 5.13 (successful, as well as failed) is mirrored by the behaviour in the corresponding TDCs [Fig. 5.13(a), orange]. This is an important point, since it is this quantity that directly enters both the FSSH hopping probability [Eq. (5.4)] and the equations of motion for the electronic coefficients [Eq. (5.3)]. If the nuclear time step used is too large relative to the (temporal) width of the TDCs, then the coupling cannot be integrated accurately, affording too small a value for the time integrals that are evaluated when one numerically solves Eqs (5.4) and (5.3), thus resulting in failure to hop

[491]. It is clear that even a time step of ~0.025 fs is not small enough to accurately capture the needle-like nonadiabatic coupling experienced by the (LR-TD)DFT/TDA/PBE0 trajectory at 25 fs and 34 fs; this is again evidenced by S_1 (S_0) attempting to lose (gain) population, but only managing to do so modestly (i.e., ~20%) at these times, before recovering again [Fig. 5.11(a), orange]. We note that such strong, narrow couplings are also reminiscent of trivial unavoided crossings [116, 117].

Despite its small "size" or "dimension", it is evident that the (LR-TD)DFT/TDA/PBE0 S_1/S_0 intersection ring can still cause prominent issues for FSSH/analytic dynamics. Interestingly, however, the above analysis highlights that such issues in (LR-TD)DFT/TDA FSSH/analytic dynamics do not necessarily arise directly from the incorrect topology [i.e., an $(F-1)$-dimensional intersection ring, as opposed to an $(F-2)$-dimensional point of degeneracy] and assumed vanishing $\mathbf{d}_{01}(\mathbf{R})$ vector, but rather the problem largely lies in the significantly distorted topography of the S_1 PES, which leads to abnormally sharp, albeit still sizeable, $\mathbf{d}_{01}(\mathbf{R})$ vectors. Arguably, all of the aforementioned issues arise from the same fundamental problem of (LR-TD)DFT/TDA in the adiabatic approximation (see Section 2.4.2). Nevertheless, given the connection between CX topography and whether a given electronic structure methods adequately includes dynamic electron correlation, it could be questioned whether using a more accurate density functional, one with a more sophisticated incorporation of HF exchange, could lead to a less varying S_1 PES. Although, such a change would not remedy the problem of an incorrect topology, which for the S_1/S_0 intersection ring is debatably not too severe (as outlined in Section 5.3.2), it may still act to reduce the impact of the incorrect topography, typically thought to be the "lesser of the two evils".

5.3.3.2 Comparing non-standard TSH approaches with (LR-TD)DFT/TDA and XMS-CASPT2

We finish this section by briefly discussing the performance of the other TSH approaches–FSSH/Baeck-An, LZSH and SHωIT (ω = 0.2 eV)–coupled with (LR-TD)DFT/TDA/PBE0 and XMS-CASPT2, respectively, for the same exemplar trajectory as above. With XMS-CASPT2, all three non-standard TSH approaches give very similar energy profiles and hopping times to one another [Fig. 5.14(b)-5.14(d), blue], as well as to FSSH/analytic [Fig. 5.11(b), blue], with the trajectory in each case being characterised by a single successful S_1-to-S_0 hopping event. A closer inspection of the hopping region, however, reveals that FSSH/Baeck-An [Fig. 5.14(b)(i)] actually hops as a result of the small discontinuity in the electronic energy at 21 fs, an expected sensitivity in the Baeck-An hopping scheme, but something that FSSH/analytic is not affected by [Fig. 5.11(b)(i)]. Nevertheless, for this specific FSSH/Baeck-An trajectory, the hopping error appears to be of little consequence, since it occurs in a region where the electronic energies already come close together, with the FSSH/Baeck-An hop only occurring 1 fs before that of FSSH/analytic. As such, FSSH/Baeck-An has been saved in this example by

the fortuitously small energy gap. Strikingly, it only takes a relatively small discontinuity to erroneously afford a hop, a point made even more alarming if one considers the same situation happening when instead there is a large energy gap between S_1 and S_0. Such a situation would

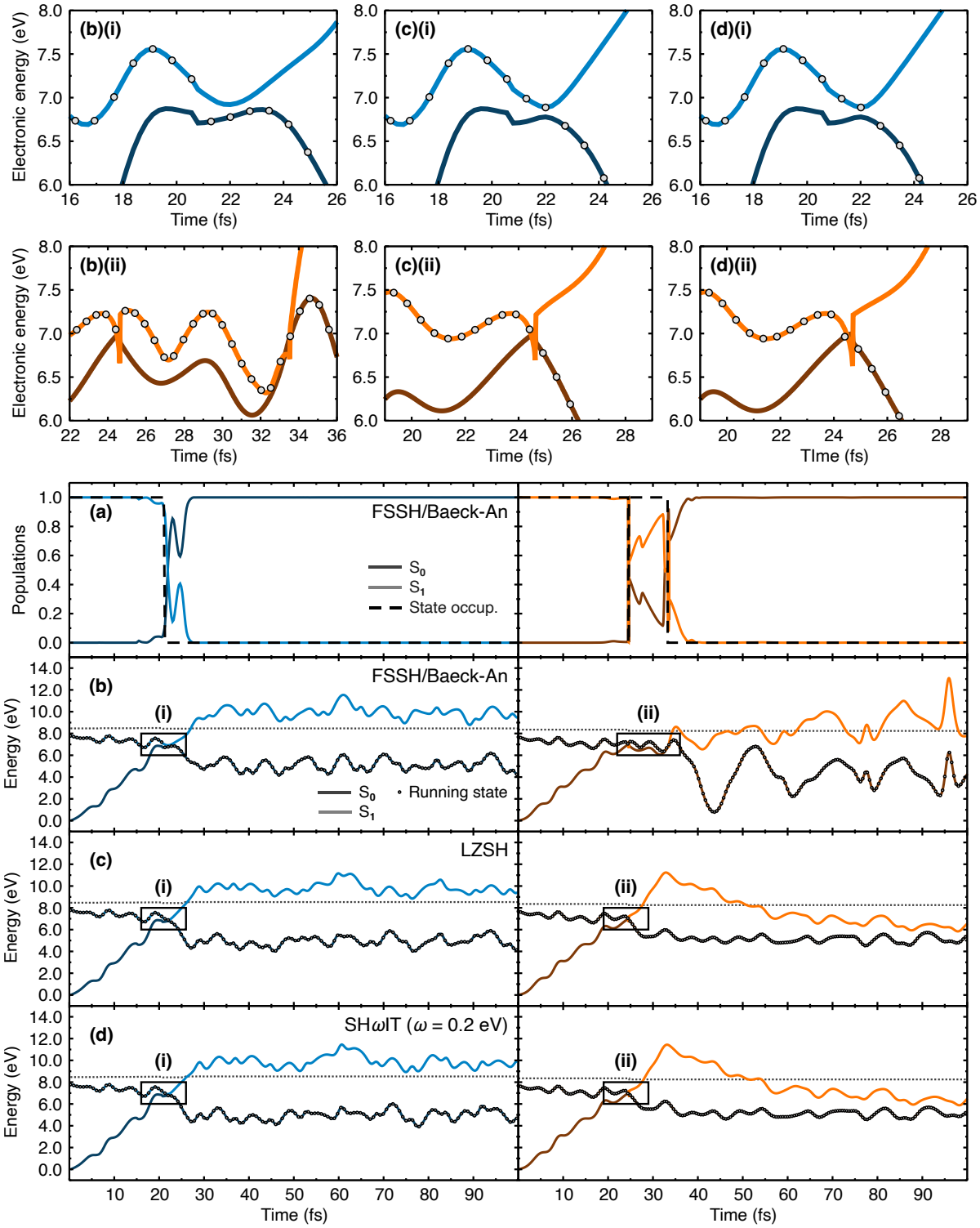

Figure 5.14: (Previous page.) Analysis of exemplar **(a)-(b)** FSSH/Baeck-An, **(c)** LZSH and **(d)** SHωIT (ω = 0.2 eV) trajectories with energy gaps at their respective first S_1-to-S_0 hopping events below 0.2 eV for protonated formaldimine. Comparison of XMS(3)-CASPT2(8/6)/cc-pVTZ (blue) and (LR-TD)DFT/TDA/PBE0/cc-pVDZ (orange) **(a)** FSSH/Baeck-An electronic state populations and **(b)-(d)** electronic energies for 100 fs of dynamics. The horizontal dotted dark grey lines indicate the total energy. The black boxes **(i)** and **(ii)** in panels (b)-(d) outline regions where the S_1 electronic energy (mid colour) comes close to (and even crosses) the S_0 electronic energy (dark colour). The corresponding zoomed-in electronic energy plots are included above the main panels, where the grey circles indicate the running state.

naturally prohibit a hop in FSSH/analytic, but seems likely to result in one in FSSH/Baeck-An, leading to potentially large qualitative differences in electronic state and photoproduct population traces. LZSH is also expected to be susceptible to hopping errors arising from PES discontinuities. The internal check implemented in ABIN (see Section 5.2.2.3 for details), however, safeguards against such possibilities, with LZSH therefore hopping at the same time as FSSH/analytic, unaffected by the energy discontinuity. The check appears to work well globally, evidenced by the previous close agreement between LZSH and FSSH/analytic, both with XMS-CASPT2, in Section 5.3.1. SHωIT (ω = 0.2 eV) also hops at the same time as FSSH/analytic and is similarly unaffected by the PES discontinuity [Fig. 5.14(d)(i)] due the energy gap in its vicinity not becoming lower than 0.2 eV. In a way, SHωIT (ω = 0.2 eV) may be considered less sensitive overall to electronic energy discontinuities than the other two non-standard TSH approaches, given it only depends on zeroth-order electronic quantities (i.e., the energies, themselves), and not on second-order quantities (i.e., the PES curvature).

We now return to the performance of (LR-TD)DFT/TDA/PBE0, with a particular focus on how it fairs in combination with FSSH/Baeck-An. It was noted recently in the literature [419] that in principle, FSSH/Baeck-An could potentially provide a viable protocol beyond using SHωIT for defective ground-to-excited state CXs, that is, performing actual hops, rather than manually switching state when a predefined energy threshold has been met. The study in question [419] applied (LR-TD)DFT/TDA with FSSH/Baeck-An to the S_1/S_0 dynamics of fulvene and thiophene, with a significant number of trajectories either showing no hops at all, or ending prematurely due to singlet-instability issues. In the case of protonated formaldimine, we experienced no such problems; all nine trajectories–admittedly a small number–ran to completion, despite each trajectory experiencing localised points (or time steps) where negative excitation energies were observed. For the purposes of our present study, affording negative excitation energies (i.e., an intrinsic property of the S_1/S_0 intersection ring) was not considered a reason to halt the dynamics, rather the main aim of this thesis has been to probe how such deficiencies in (LR-TD)DFT/TDA arise and how they affect nuclear dynamics.

Interestingly, we see FSSH/Baeck-An hops three times between S_1 and S_0 [Fig. 5.14(a),

orange], twice (i.e, from S_1 to S_0, and back to S_1) in very quick succession around 25 fs, with the third hop (back down to S_0) occurring at 33 fs. Note, the first two hops are not explicitly visible in Fig. 5.14(b)(ii) since not all time steps are plotted for clarity. These FSSH/Baeck-An hopping times are consistent with the times at which (LR-TD)DFT/TDA/PBE0 FSSH/analytic failed to hop (i.e., 25 and 34 fs), which is not too surprising given the similarity in the S_1 and S_0 PESs at this point in the dynamics in both FSSH/Baeck-An [Fig. 5.14(b)(ii)] and FSSH/analytic [Fig. 5.14(b)(ii)]. Comparing the Baeck-An and analytic TDCs together along the course of the dynamics [Fig. 5.15(b)], it is clear why hops are observed with the former, but not with the latter. FSSH/Baeck-An grossly overestimates the coupling strength at the aforementioned time steps, being over 20 times larger than that in FSSH/analytic [see inset in Fig. 5.15(b) for comparison]. Therefore, despite the needle-like form of the TDCs prohibiting hopping in FSSH/analytic due to their extremely narrow width, this is completely outweighed in FSSH/Baeck-An by their sheer magnitude. This is different to comparing the analytic and Baeck-An couplings for XMS-CASPT2 [Fig. 5.15(a)], which are in good overall agreement with one another, showing global maxima at 22 fs.

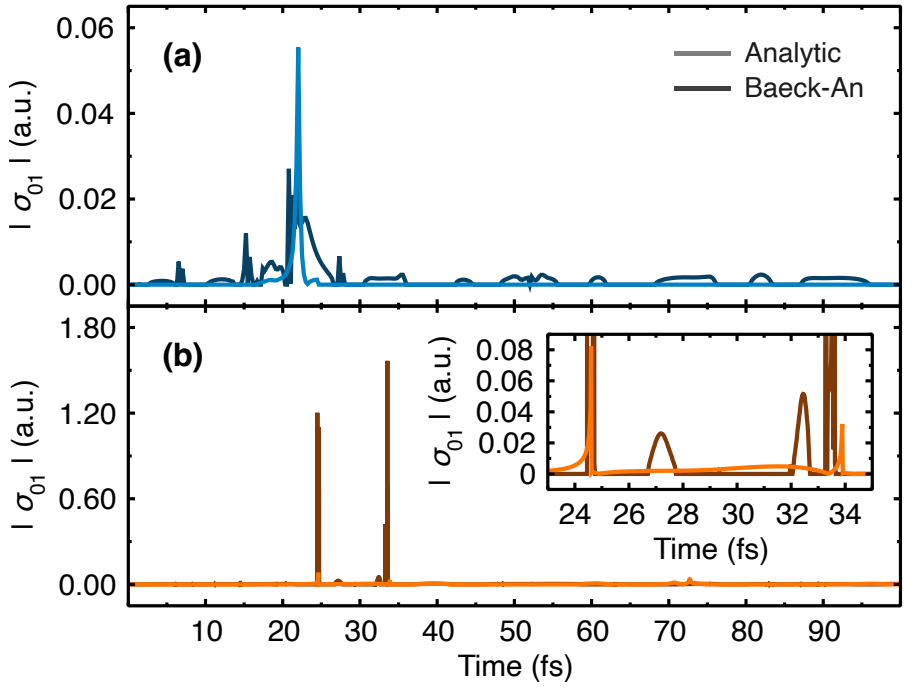

Figure 5.15: Comparison of analytic (mid colour) and Baeck-An (dark colour) TDC magnitudes, $|\sigma_{01}|$, along the 100 fs of FSSH dynamics using **(a)** XMS(3)-CASPT2(8/6)/cc-pVTZ (blue) and **(b)** (LR-TD)DFT/TDA/PBE0/cc-pVDZ (orange). **Inset:** Zoomed in version of the analytic and Baeck-an TDCs with (LR-TD)DFT/TDA/PBE0/cc-pVDZ.

However, one may question how Baeck-An couplings can even be calculated at such time steps, which exhibit negative excitation energies, since the conventional prescription is to return a null coupling if the radicand in Eq. (5.7) is negative. Although the energy difference

is negative at these points, this is accompanied by a strongly negative curvature in the S_1 PES (i.e., the visible cusps), and thus a negative curvature in the energy difference itself. The two negative signs cancel each other, rendering the radicand in the Baeck-An coupling expression [Eq. (5.7)] still positive. If the S_1 PES was more well-behaved, that is, smooth with a positive curvature within the hopping regions, then no Baeck-An couplings would be computed due to the negative radicand in Eq. (5.7). Therefore, it is only as result of inaccuracies in the S_1 PES topography in (LR-TD)DFT/TDA/PBE0 that allow FSSH/Baeck-An to hop in these cases, where the (LR-TD)DFT/TDA/PBE0 exhibits negative excitation energies (i.e., an incorrect topology). This certainly complicates the use of FSSH/Baeck-An with problematic electronic structure, bringing into question its reliability in such instances.

Finally, (LR-TD)DFT/TDA/PBE0 LZSH and SHωIT (ω = 0.2 eV) experience only a single S_1-to-S_0 hop [Fig. 5.14(c) and 5.14(d)] at similar times to that of XMS-CASPT2 (coupled with any of the TSH approaches). Both TSH approaches navigate the defective S_1/S_0 intersection ring in (LR-TD)DFT/TDA/PBE0 relatively well [Fig. 5.14(c)(ii) and 5.14(d)(ii)], but exhibit qualitative differences in their energy profiles after this point when compared to their XMS-CASPT2 equivalents [Fig. 5.14(c)(i) and 5.14(d)(i)]. It is possible for LZSH to hop, despite (LR-TD)DFT/TDA/PBE0 exhibiting negative excitation energies, since the implementation in ABIN uses absolute energy differences in Eq. (5.14). As such, the first time step after the S_1 energy goes below S_0 (i.e., 24.48 fs) corresponds to a local minimum in the absolute energy difference. [Again, we note that this is not explicitly visible in Fig. 5.14(c)(ii).] Interestingly, with (LR-TD)DFT/TDA/PBE0, FSSH/Baeck-An, LZSH and SHωIT (ω = 0.2 eV) trajectories experience markedly smaller total energy discontinuities of ~0.05-0.1 eV compared to those observed for FSSH/analytic (i.e., ~0.5 eV).

5.4 Conclusions

This work has explored the affect of the AA (LR-TD)DFT/TDA/PBE0 S_1/S_0 intersection ring in protonated formaldimine on four variants of TSH dynamics: FSSH/analytic, FSSH/Baeck-An, LZSH and SHωIT. We first tested each of the four variants with XMS-CASPT2 in their full dimensionality, but with a particular focus on the first S_1-to-S_0 hopping event. FSSH/analytic, FSSH/Baeck-An and LZSH show good agreement for electronic state and photoproduct populations, energy gaps and times at hopping, in contrast to SHωIT. FSSH/Baeck-An was shown to slightly overestimate the magnitude of the time-derivative NACs, consistent with earlier studies. A subset of XMS-CASPT2 trajectories, those which possessed an S_1-S_0 energy gap of 0.2 eV and below, were then projected onto two natural distortions, believed to be representative of the two analytic branching space vectors, namely the C-N bond stretch and the twist about the C-N bond. This analysis revealed good agreement between FSSH/analytic, FSSH/Baeck-An and LZSH, with FSSH/Baeck-An showing more dispersed hopping geomet-

ries. The equivalent AA (LR-TD)DFT/TDA/PBE0 TSH trajectories showed similar behaviour, but with slight oscillations along the C-N bond stretching direction when initially in S_1, exploring a smaller range of C-N bond lengths in S_0, and showing fewer backhops. The latter two were rationalised by subtle differences in the AA (LR-TD)DFT/TDA/PBE0 S_1 and S_0 PESs along the two natural distortions compared to those in XMS-CASPT2. Defining an informal, but practical definition for the "size" of the optimised XMS-CASPT2 S_1/S_0 MECX, it was observed that the latter was considerably "smaller" than the region explored by the nuclear dynamics along the two natural distortions, with the same also true for the S_1/S_0 intersection ring in AA (LR-TD)DFT/TDA/PBE0. With this information alone, it could be assumed that the S_1/S_0 intersection ring should not pose a serious problem to the nuclear dynamics, a question that was at the heart of this chapter.

Nonetheless, taking a closer look at an individual exemplar trajectory, it was evident that the S_1/S_0 intersection ring, despite being "small", still can be encountered by trajectories, resulting in large discontinuities in total energy within FSSH/analytic dynamics at points of failed hopping. Such discontinuities, however, were shown to arise not as a direct consequence of the incorrect topology (i.e., a ring of degeneracy, not a point of degeneracy), but as a result of the significantly distorted topography, with the strong cusps in the S_1 PES resulting in erroneously narrow TDCs. FSSH/Baeck-An was observed to remedy the fail hops, but for problematic reasons, namely extreme overestimation of the corresponding TDCs. Admittedly only nine AA (LR-TD)DFT/TDA/PBE0 trajectories were run, with only one being considered in detail. Therefore, an interesting question is whether such striking errors at the individual trajectory level manifest in significant qualitative errors in electronic state and photoproduct populations when more trajectories are considered. Equally, whether increasing the number of AA (LR-TD)DFT/TDA/PBE0 trajectories leads to any that end prematurely before hopping, something that was not experienced here. This is left for future work.

Chapter 6

Conclusions

6.1 Summary

This thesis set out to provide a fair and unbiased assessment of the description of (i) ground-to-excited state and (ii) excited-to-excited state CXs within AA LR-TDDFT, doing so in an internally consistent manner, paying particular attention to the effect of deficiencies in the former. The widespread popularity of AA LR-TDDFT in probing excitations in molecules of moderate size, as well as the mechanistic importance of CXs in nonadiabatic dynamics, both necessitated such an assessment.

After a comprehensive discussion in Chapter 2 on the theoretical background and practical considerations of CXs and LR-TDDFT, Chapter 3 focussed on the description of CXs between excited electronic states by AA LR-TDDFT/TDA. Using the PBE0 exchange-correlation functional, AA LR-TDDFT/TDA afforded a correct topology (i.e., $F-2$) for the S_2/S_1 MECX in protonated formaldimine, despite not using formally appropriate quadratic-response $\mathbf{h}_{IJ}(\mathbf{R})$ vectors to locate the MECX geometry and plot its branching space. A less favourable description, however, was observed for the topography of the S_2/S_1 MECX, as highlighted by differences in the numerical values of recently proposed CX branching space topography parameters calculated for AA LR-TDDFT/TDA/PBE0 in comparison to XMS-CASPT2 or ADC(2). Inspection of the S_2/S_1 MECX in pyrazine further corroborated the ability of AA LR-TDDFT/TDA/PBE0 to give topologically-sound excited-to-excited state CXs. Comparison of different exchange-correlation functionals showed an improvement in the topographical description of the S_2/S_1 MECX in pyrazine, as the overall quality/sophistication of the functional improved. This suggests that it is the quality of the electronic energies afforded by a given electronic-structure method, rather than the quality of the branching space vectors (in

particular, $\mathbf{h}_{IJ}(\mathbf{R})$), that have the greatest impact on the quality of the overall CX branching space. We note, however, that this could (or should) not have been assumed without first explicitly plotting the CX branching space, given the formal requirement of a quadratic-response formalism to calculate excited-to-excited state properties in TDDFT.

Since protonated formaldimine also possesses a characteristic S_1/S_0 MECX, it equally enabled the ground-to-excited problem in AA LR-TDDFT/TDA to be revisited in Chapter 3. Despite showing an incorrect topology (i.e., $F-1$) consistent with previous studies [27, 28, 94, 166, 289–291], AA LR-TDDFT/TDA/PBE0 exhibited an S_1/S_0 intersection ring, as opposed to a strictly linear intersection, as given by both ADC(2) and CIS. Such an intersection ring can be recognised as tying together two supposedly different observations made in the literature before–that of AA LR-TDDFT/TDA, in some cases, giving a linear seam of intersection [27], and other cases, it giving an "approximate" CX, reminiscent of two interpenetrating cones [28]. Both observations can be considered as two sides of the same coin, each emanating from the S_1/S_0 intersection ring; which one is observed depends on the extent to which the molecule is distorted along the S_1/S_0 branching plane from the optimised S_1/S_0 MECP. Of course, further molecules need to be investigated to prove the generality of the S_1/S_0 intersection ring, or at least determine how system-dependent it is. An equally interesting question is whether such a PES feature is also connected to a specific natural distortion (i.e., bond stretch, bond twist, pyramidalisation, etc.) In any case, we note that a number of molecules either have already been discussed to exhibit S_1/S_0 intersection ring-like structures, or have indicated that they may do from plots of their S_1/S_0 MECP branching space. These include oxirane [28, 274], protonated formaldimine [29, 344], benzopyran [499], ethylene [306] and H_3 [27, 297].

In Chapter 4, the topological phase–calculated as the (vector) line integral of the $\mathbf{d}_{IJ}(\mathbf{R})$ vector–was used to confirm whether the use of linear-response, rather than quadratic-response, $\mathbf{h}_{IJ}(\mathbf{R})$ vectors affords the correct physics around the S_2/S_1 MECXs in AA LR-TDDFT/TDA/PBE0 for the same exemplar molecules as Chapter 3. The AA LR-TDDFT/TDA/PBE0 S_1/S_0 intersection ring in protonated formaldimine was equivalently probed to see whether, despite its incorrect topology, it still gives rise to the correct topological phase. The former case (S_2/S_1) was more fruitful than the latter (S_1/S_0). For both molecules, AA LR-TDDFT/TDA/PBE0 correctly returned a value of π for the topological phase for a path enclosing the S_2/S_1 MECX, consistent with XMS-CASPT2. The same was not true, however, for a path enclosing the S_1/S_0 intersection ring, which instead incorrectly returned a value of zero. As the S_1/S_0 intersection ring may be regarded as an infinite number of degeneracy points, it was not immediately clear as to what value the AA LR-TDDFT/TDA/PBE0 topological phase should take in this case. Other paths inside, as well as crossing the ring, equally returned a value of zero. Although the S_1/S_0 intersection ring resembles an "approximate" CX, it does not behave like a true CX, in contrast to similarly defective excited-to-excited state CXs in EOM-CCSD [407].

Lastly, in Chapter 5, we took a pragmatic approach, ignoring the aforementioned failures associated with the AA LR-TDDFT/TDA/PBE0 S_1/S_0 intersection ring in protonated formaldimine and simply applying it to TSH dynamics. Four variants of TSH were compared in the S_1/S_0 dynamics of protonated formaldimine, initially at the XMS-CASPT2 level of theory, with a focus on the first S_1-to-S_0 hopping event. Overall, FSSH/analytic, FSSH/Baeck-An and LZSH showed similar performances to one another, contrasting that of SHωIT; any subtle differences between the former three were rationalised by inherent differences in the hopping schemes. A number of XMS-CASPT2 trajectories were then compared to their AA LR-TDDFT/TDA/PBE0 analogues, projected along two natural distortion in the vicinity of the S_1/S_0 MECX (or MECP). The XMS-CASPT2 and AA LR-TDDFT/TDA/PBE0 TSH trajectories showed similar behaviour to one another across all four variants of TSH, with differences in the nuclear dynamics attributed to differences in the electronic PESs. Considering the "size" of the S_1/S_0 intersection ring along such natural distortions, it appears much "smaller" than the region explored overall by the nuclear dynamics, suggesting naively that the S_1/S_0 intersection ring does not have a large impact on TSH dynamics. Nevertheless, looking at a single AA LR-TDDFT/TDA/PBE0 TSH trajectory in detail along the time coordinate, which naturally considers the full dimensionality of the molecule (as opposed to a reduced number of natural distortions), highlighted that TSH trajectories could still encounter the negative excitation energy region inside the AA LR-TDDFT/TDA/PBE0 S_1/S_0 intersection ring. Large total energy discontinuities were observed at occurrences of failed hops in FSSH/analytic, which were not observed in the other three methods. Failed hopping and total energy discontinuities were both attributed to extremely narrow TDCs, arising from the steeply cusped topography of S_1 in the close vicinity of the S_1/S_0 intersection ring.

6.2 Outlook

Inevitably, several areas of further interest beyond the scope of the this thesis were triggered during its construction. Throughout Chapters 3 and 4, linear-response $\mathbf{h}_{IJ}(\mathbf{R})$ [and $\mathbf{d}_{IJ}(\mathbf{R})$] vectors were used either to construct the MECX (or MECP) branching spaces, or to calculate the corresponding topological phase in AA TDDFT/TDA. As mentioned several times throughout such chapters and in the summary above, linear-response transition properties are only formally appropriate for describing ground-to-excited state CXs, but not excited-to-excited state CXs. A natural extension of the analysis in Chapter 3, would therefore be to employ quadratic-response $\mathbf{h}_{IJ}(\mathbf{R})$ vectors in the generation of the S_2/S_1 MECX branching spaces in protonated formaldimine and pyrazine, in combination with $\mathbf{g}_{IJ}(\mathbf{R})$ vectors and electronic energies obtained using linear-response. Such a study would pave the way to properly answer the question of which affects the quality of the excited-to-excited state CX branching space topography more: the description of dynamic correlation by the choice of

exchange-correlation functional, or the use of a formally appropriate $\mathbf{h}_{IJ}(\mathbf{R})$ vector. Of course, it would be assumed that the topography of excited-to-excited state CXs should improve upon replacing linear-response $\mathbf{h}_{IJ}(\mathbf{R})$ vectors with those from quadratic-response (for a given exchange-correlation functional), however, it cannot be forgotten that such calculations would still remain in the adiabatic approximation. As stressed in Section 3.1, the quadratic density-density response function in the adiabatic approximation exhibits the wrong pole structure [272, 331, 334–337] and thus leads to excited-to-excited state properties diverging erroneously whenever the difference between two excited states (I, J) equals the excitation energy to any other excited state from the ground state (0, K). Most of the discussions in the literature surrounding these divergences highlight their existence along interpolation coordinates between electronic state minima, however, an interesting question would be how do such divergences affect the description of the branching space of an excited-to-excited state CX, if at all? Thinking about the problem loosely, one may question whether divergences in the quadratic-response $\mathbf{h}_{IJ}(\mathbf{R})$ vector could even manifest near an excited-to-excited state CX, since the energy gap between the two excited states involved would be extremely small, so for a divergence in $\mathbf{h}_{IJ}(\mathbf{R})$ to occur in this case, the ground and first-excited start must also be energetically close to one another to allow the two energy differences (I, J and $0, K$) to match. In other words, the molecule would have to possess an excited-to-excited state CX and a ground-to-excited state CX at the same nuclear geometry, or at the very least, at two infinitesimally different nuclear geometries. This bares a striking resemblance to the case near/at a three-state CX, a PES feature that was introduced in Sections 2.2.2.3 and 2.2.3, but was not the focus of this thesis. Assuming such divergences can occur for $I = K$ (or $I \approx K$), then using quadratic-response $\mathbf{h}_{IJ}(\mathbf{R})$ vectors to construct the branching space of e.g., an $S_J/S_K/S_0$ CX may cause significant complications.

An interesting question, more generally, would be what is the description of three-state CXs involving the ground state in AA LR-TDDFT/TDA, that is, not considering possible added complications from quadratic-response excited-to-excited state $\mathbf{h}_{IJ}(\mathbf{R})$ vectors? This thesis would suggest that the coupling between the two excited states involved in such a three-state CX should be adequate, but the coupling of each excited state to the ground state would be defective. Arguably, the five-dimensional branching space (see Section 2.2.2.3) of the e.g., $S_2/S_1/S_0$ three-state CX would be reduced to being three-dimensional, as a result of the $V_{01}(\mathbf{R})$ and $V_{02}(\mathbf{R})$ off-diagonal elements in an analogous version of Eq. (2.40) being trivially zero for all nuclear geometers in AA LR-TDDFT/TDA in this case.

In all AA LR-TDDFT calculations in this thesis, we have employed the TDA. It is widely understood that the TDA is a practical necessity when exploring photochemical paths [28], in order to prevent instability issues arising from imaginary excitation energies, which are possible in full AA LR-TDDFT, but not in AA LR-TDDFT/TDA. The question still remains whether the AA LR-TDDFT/TDA S_1/S_0 intersection ring is retained in full AA LR-TDDFT.

If so, the region inside the intersection ring would be expected to exhibit imaginary, rather than strictly negative, excitation energies. This situation would be reminiscent of defective excited-to-excited state CXs in EOM-CCSD. As discussed in Chapter 4, Williams *et al.* [407] recently showed that such defective excited-to-excited state CXs can correctly return a value of π for the topological phase calculated along a loop enclosing them. Could the same be observed for a possible S_1/S_0 intersection ring in full AA LR-TDDFT?

So far, the discussion in this section has focussed on extensions to the work presented in this thesis, which remain in the adiabatic approximation and the ground-state exchange-correlation functional approximation. Arguably, to get a fuller understanding of exactly "why" AA LR-TDDFT(/TDA) fails to correctly describe ground-to-excited state CXs, one must separate the problem and examine the effect of each approximation in turn. One can either (a) focus on LR-TDDFT and attempt to go beyond the adiabatic approximation (as suggested in Section 2.4.2) by applying recently-proposed [249, 272, 277, 280, 282, 283, 287, 288, 391, 392] frequency-dependent exchange-correlation kernels, or (b) focus on ground-state DFT and determine whether the conventional Kohn-Sham formalism is the root of the problem. The latter is the natural starting point: can formally exact KS-DFT (i.e., using the exact ground-state exchange-correlation functional) correctly describe the lower cone of an S_1/S_0 CX, or at least provide the correct description up to the limit of reaching infinitesimally close to the degeneracy point, without the need to resort to an ensemble DFT [500–505] formalism? The lower cone of a ground-to-excited state CX arguably exhibits two multireference problems, that at the degeneracy point in the CX branching space, and that in the vicinity of the degeneracy point (i.e., along a supposed avoided crossing on the shoulder of the lower surface of the CX). Such an investigation would inevitably consider conical intersections (or degeneracies) at the level of orbital energies, as well as implications–conceptional and practical–of (pure state) non-interacting v-representability [506], something that was touched upon in Section 3.5.1.3. Some discussions of these topics are already present in the literature [28, 94, 232, 274, 291], however, it is the opinion of this author that more can be done to explicitly flag them to a wider audience, across the nonadiabatic dynamics community, as well as the (LR-TD)DFT developer community, more generally. This is exciting work for the near future.

Bibliography

[1] P. Hohenberg and W. Kohn, *Physical Review*, 1964, **136**, B864–B871.

[2] W. Kohn and L. J. Sham, *Physical Review*, 1965, **140**, A1133–A1138.

[3] L. Goerigk, A. Hansen, C. Bauer, S. Ehrlich, A. Najibi and S. Grimme, *Physical Chemistry Chemical Physics*, 2017, **19**, 32184–32215.

[4] W. Kohn, *Reviews of Modern Physics*, 1999, **71**, 1253.

[5] E. Runge and E. K. U. Gross, *Physical Review Letters*, 1984, **52**, 997–1000.

[6] M. E. Casida, *Recent Advances in Computational Chemistry*, World Scientific, 1995, vol. 1, pp. 155–192.

[7] M. Petersilka, U. J. Gossmann and E. K. U. Gross, *Physical Review Letters*, 1996, **76**, 1212–1215.

[8] R. E. Stratmann, G. E. Scuseria and M. J. Frisch, *The Journal of Chemical Physics*, 1998, **109**, 8218–8224.

[9] M. Born and R. Oppenheimer, *Annalen der Physik*, 1927, **389**, 457–484.

[10] R. Car and M. Parrinello, *Physical Review Letters*, 1985, **55**, 2471.

[11] J. Bone, J. Carmona-García, D. Hollas and B. F. E. Curchod, *The Journal of Physical Chemistry A*, 2025, **129**, 9355–9367.

[12] J. Westermayr, M. Gastegger, M. Menger, S. Mai, L. González and P. Marquetand, *Sci*, 2019, **10**, 8100–8107.

[13] J. Westermayr, M. Gastegger and P. Marquetand, *The journal of physical chemistry letters*, 2020, **11**, 3828–3834.

[14] J. O. Richardson, *The Journal of Chemical Physics*, 2023, **158**, 011102.

[15] T. Y. Wang, S. P. Neville and M. S. Schuurman, *The Journal of Physical Chemistry Letters*, 2023, **14**, 7780–7786.

[16] T. Gutleb, R. Barrett, J. Westermayr and C. Ortner, *arXiv preprint arXiv:2407.03731*, 2024.

[17] R. Barrett, C. Ortner and J. Westermayr, *arXiv preprint arXiv:2502.12870*, 2025.

[18] C. Müller, Š. Sršeň, B. Bachmair, R. Crespo-Otero, J. Li, S. Mausenberger, M. Pinheiro Jr, G. Worth, S. A. Lopez and J. Westermayr, *Chemical Science*, 2025, 17542.

[19] J. Whitlow, Z. Jia, Y. Wang, C. Fang, J. Kim and K. R. Brown, *Nature Chemistry*, 2023, **15**, 1509–1514.

[20] C. H. Valahu, V. C. Olaya-Agudelo, R. J. MacDonell, T. Navickas, A. D. Rao, M. J. Millican, J. B. Pérez-Sánchez, J. Yuen-Zhou, M. J. Biercuk, C. Hempel, T. R. Tan and I. Kassal, *Nature Chemistry*, 2023, **15**, 1503–1508.

[21] Y. Wang and D. A. Mazziotti, *Physical Chemistry Chemical Physics*, 2024, **26**, 11491–11497.

[22] S. Zhao, D. Tang, X. Xiao, R. Wang, Q. Sun, Z. Chen, X. Cai, Z. Li, H. Yu and W.-H. Fang, *The Journal of Physical Chemistry Letters*, 2024, **15**, 7244–7253.

[23] E. Koridon, J. Fraxanet, A. Dauphin, L. Visscher, T. E. O'Brien and S. Polla, *Quantum*, 2024, **8**, 1259.

[24] Y. Wang, C. Cianci, I. Avdic, R. Dutta, S. Warren, B. Allen, N. P. Vu, L. F. Santos, V. S. Batista and D. A. Mazziotti, *Journal of Chemical Theory and Computation*, 2025, **21**, 1213–1221.

[25] S. Belaloui, N. E. Belaloui and A. Benslama, *arXiv preprint arXiv:2507.22670*, 2025.

[26] E. Sangiogo-Gil and L. González, *Pure and Applied Chemistry*, 2025, 1–19.

[27] B. G. Levine, C. Ko, J. Quenneville and T. J. Martínez, *Molecular Physics*, 2006, **104**, 1039–1051.

[28] E. Tapavicza, I. Tavernelli, U. Rothlisberger, C. Filippi and M. E. Casida, *The Journal of Chemical Physics*, 2008, **129**, 124108.

[29] J. T. Taylor, D. J. Tozer and B. F. E. Curchod, *The Journal of Chemical Physics*, 2023, **159**, 214115.

[30] A. Prlj, J. T. Taylor, J. Janoš, E. Lognon, D. Hollas, P. Slavíček, F. Agostini and B. F. E. Curchod, 2025, 10.48550/arXiv.2508.05263.

[31] E. Schrödinger, *Physical Review*, 1926, **28**, 1049–1070.

[32] M. Born and K. Huang, *Dynamical theory of crystal lattices*, Clarendon Press ; Oxford University Press, Oxford : New York, 1988.

[33] M. van Horn, T. Cheragwandi and N. H. List, 2025.

[34] F. Agostini and B. F. Curchod, *Foundations of Chemistry*, 2025, 1–21.

[35] N. C. Handy, Y. Yamaguchi and H. F. Schaefer, *The Journal of Chemical Physics*, 1986, **84**, 4481–4484.

[36] J. O. Jensen and D. R. Yarkony, *The Journal of Chemical Physics*, 1988, **89**, 975–982.

[37] M. Baer, *Beyond Born-Oppenheimer: Conical intersections and electronic non-adiabatic coupling terms*, Wiley, Hoboken, N.J, 2006.

[38] D. Yarkony, W. Domcke and H. Köppel, *Conical Intersections: Electronic Structure, Dynamics & Spectroscopy*, World Scientific, 2004.

[39] H. Longuet-Higgins, *Advances in spectroscopy*, 1961, 429–472.

[40] J. P. Malhado, M. J. Bearpark and J. T. Hynes, *Frontiers in chemistry*, 2014, **2**, 97.

[41] W. Zhou, A. Mandal and P. Huo, *The journal of physical chemistry letters*, 2019, **10**, 7062–7070.

[42] R. Maskri and L. Joubert-Doriol, *Philosophical Transactions of the Royal Society A*, 2022, **380**, 20200379.

[43] C. A. Mead and D. G. Truhlar, *The Journal of Chemical Physics*, 1982, **77**, 6090–6098.

[44] D. R. Yarkony, C. Xie, X. Zhu, Y. Wang, C. L. Malbon and H. Guo, *Computational and Theoretical Chemistry*, 2019, **1152**, 41–52.

[45] D. A. McQuarrie and J. D. Simon, *Physical chemistry: a molecular approach*, University science books Sausalito, CA, 1997, vol. 1.

[46] K. Murthy and H. S. Virk, *Defect and Diffusion Forum*, 2014, **347**, 1–34.

[47] H. H. Jaffé and A. L. Miller, *Journal of chemical education*, 1966, **43**, 469.

[48] A. Jablonski, *Nature*, 1933, **131**, 839–840.

[49] S. Mai and L. González, *Angewandte Chemie International Edition*, 2020, **59**, 16832–16846.

[50] A. Manian, Z. Chen, H. Sullivan and S. Russo, 2025, 10.26434/chemrxiv–2025–kp7jf–v2.

[51] S. Mukherjee and M. Barbatti, *Results in Chemistry*, 2022, **4**, 100521.

[52] M. Rivera, L. Stojanovic and R. Crespo-Otero, *The Journal of Physical Chemistry A*, 2021, **125**, 1012–1024.

[53] M. Wenzel and R. Mitric, *The Journal of Chemical Physics*, 2023, **158**, 034105.

[54] E. Fermi, *Nuclear physics: a course given by Enrico Fermi at the University of Chicago*, University of Chicago press, 1950.

[55] J. von Neumann and E. P. Wigner, *Phys. Zschr.*, 1929, 30.

[56] E. Teller, *The Journal of Physical Chemistry*, 1937, **41**, 109–116.

[57] H. E. Zimmerman, *Journal of the American Chemical Society*, 1966, **88**, 1566–1567.

[58] R. B. Woodward and R. Hoffmann, *Journal of the American Chemical Society*, 1965, **87**, 395–397.

[59] R. B. Woodward and R. Hoffmann, *Angewandte Chemie International Edition in English*, 1969, **8**, 781–853.

[60] L. González, D. Escudero and L. Serrano-Andrés, *ChemPhysChem*, 2012, **13**, 28–51.

[61] W. T. A. M. Van der Lugt and L. J. Oosterhoff, *Journal of the American Chemical Society*, 1969, **91**, 6042–6049.

[62] I. Schapiro, F. Melaccio, E. N. Laricheva and M. Olivucci, *Photochemical & Photobiological Sciences*, 2011, **10**, 867.

[63] B. G. Levine and T. J. Martínez, *Annual Review of Physical Chemistry*, 2007, **58**, 613–634.

[64] D. R. Yarkony, *Chemical Reviews*, 2012, **112**, 481–498.

[65] J. Michl, Photochemistry, Berlin, Heidelberg, 1974, pp. 1–59.

[66] J. Michl, *Advanced Series in Physical Chemistry*, WORLD SCIENTIFIC, 2004, vol. 15, pp. i–xvii.

[67] S. Matsika, *Reviews in Computational Chemistry*, John Wiley & Sons, Inc., Hoboken, NJ, USA, 2007, pp. 83–124.

[68] G. J. Atchity, S. S. Xantheas and K. Ruedenberg, *The Journal of Chemical Physics*, 1991, **95**, 1862–1876.

[69] S. S. Xantheas, G. J. Atchity, S. T. Elbert and K. Ruedenberg, *The Journal of Chemical Physics*, 1991, **94**, 8054–8069.

[70] M. Riad Manaa and D. R. Yarkony, *The Journal of Chemical Physics*, 1990, **93**, 4473–4474.

[71] F. Bernardi, S. De, M. Olivucci and M. A. Robb, *Journal of the American Chemical Society*, 1990, **112**, 1737–1744.

[72] F. Bernardi, M. Olivucci and M. A. Robb, *Accounts of Chemical Research*, 1990, **23**, 405–412.

[73] W. Domcke and D. R. Yarkony, *Annual Review of Physical Chemistry*, 2012, **63**, 325–352.

[74] D. G. Truhlar and C. A. Mead, *Physical Review A*, 2003, **68**, 032501.

[75] W. Domcke and D. Yarkony, *Conical intersections: theory, computation and experiment*, World Scientific, 2011, vol. 17.

[76] S. Matsika and P. Krause, *Annual Review of Physical Chemistry*, 2011, **62**, 621–643.

[77] M. S. Schuurman and A. Stolow, *Annual review of physical chemistry*, 2018, **69**, 427–450.

[78] D. Polli, P. Altoè, O. Weingart, K. M. Spillane, C. Manzoni, D. Brida, G. Tomasello, G. Orlandi, P. Kukura, R. A. Mathies, M. Garavelli and G. Cerullo, *Nature*, 2010, **467**, 440–443.

[79] T. J. Martínez, *Nature*, 2010, **467**, 412–413.

[80] X. Zhu and D. R. Yarkony, *Molecular Physics*, 2016, **114**, 1983–2013.

[81] Y. Boeije and M. Olivucci, *Chemical Society Reviews*, 2023, **52**, 2643–2687.

[82] S. Gozem, H. L. Luk, I. Schapiro and M. Olivucci, *Chemical Reviews*, 2017, **117**, 13502–13565.

[83] D. Roca-Sanjuán, A. Francés-Monerris, I. F. Galván, P. Farahani, R. Lindh and Y.-J. Liu, *Photochemistry: Volume 44*, The Royal Society of Chemistry, 2016, vol. 44, pp. 16–60.

[84] L. Blancafort, *ChemPhysChem*, 2014, **15**, 3166–3181.

[85] B. G. Levine, M. P. Esch, B. S. Fales, D. T. Hardwick, W.-T. Peng and Y. Shu, *Annual Review of Physical Chemistry*, 2019, **70**, 21–43.

[86] S. Matsika, *Chemical Reviews*, 2021, **121**, 9407–9449.

[87] D. R. Yarkony, *Advanced Series in Physical Chemistry*, WORLD SCIENTIFIC, 2004, vol. 15, pp. 41–127.

[88] D. R. Yarkony, *The Journal of Physical Chemistry A*, 2001, **105**, 6277–6293.

[89] T. J. Martińez, *Faraday Discuss.*, 2004, **127**, 227–266.

[90] J. D. Coe, M. T. Ong, B. G. Levine and T. J. Martínez, *The Journal of Physical Chemistry A*, 2008, **112**, 12559–12567.

[91] D. Morreale and M. Persico, *The Journal of Physical Chemistry A*, 2024, **128**, 1707–1714.

[92] M. Barbatti, J. Paier and H. Lischka, *The Journal of Chemical Physics*, 2004, **121**, 11614–11624.

[93] D. R. Yarkony, *Accounts of Chemical Research*, 1998, **31**, 511–518.

[94] M. Huix-Rotllant, A. Nikiforov, W. Thiel and M. Filatov, *Topics in Current Chemistry*, 2015, **368**, 445–476.

[95] F. Sicilia, L. Blancafort, M. J. Bearpark and M. A. Robb, *The Journal of Physical Chemistry A*, 2007, **111**, 2182–2192.

[96] D. Tuna, D. Lefrancois, L. Wolański, S. Gozem, I. Schapiro, T. Andruniów, A. Dreuw and M. Olivucci, *Journal of Chemical Theory and Computation*, 2015, **11**, 5758–5781.

[97] M. Persico and G. Granucci, in *Fast Nonadiabatic Dynamics*, Springer International Publishing, Cham, 2018, pp. 141–177.

[98] A. Nikiforov, J. A. Gamez, W. Thiel, M. Huix-Rotllant and M. Filatov, *The Journal of Chemical Physics*, 2014, **141**, 124122.

[99] H. Köuppel, W. Domcke and L. S. Cederbaum, *Advances in chemical physics*, 1984, 59–246.

[100] X. Zhang and J. M. Herbert, *The Journal of Chemical Physics*, 2021, **155**, 124111.

[101] I. Fdez. Galván, M. G. Delcey, T. B. Pedersen, F. Aquilante and R. Lindh, *Journal of Chemical Theory and Computation*, 2016, **12**, 3636–3653.

[102] D. R. Yarkony, *Reviews of Modern Physics*, 1996, **68**, 985–1013.

[103] H. A. Jahn and E. Teller, *Proceedings of the Royal Society of London. Series A-Mathematical and Physical Sciences*, 1937, **161**, 220–235.

[104] R. Renner, *Zeitschrift für Physik*, 1934, **92**, 172–193.

[105] T. J. Lee, D. J. Fox, H. F. Schaefer III and R. M. Pitzer, *The Journal of Chemical Physics*, 1984, **81**, 356–361.

[106] B. J. Chen, E. Pradhan, M. Nooijen and T. Zeng, *ChemPhysChem*, 2024, **25**, e202400130.

[107] A. I. Boothroyd, W. J. Keogh, P. G. Martin and M. R. Peterson, *The Journal of chemical physics*, 1996, **104**, 7139–7152.

[108] M. Dallos, T. Müller, H. Lischka and R. Shepard, *The Journal of Chemical Physics*, 2001, **114**, 746–757.

[109] F. Sicilia, M. J. Bearpark, L. Blancafort and M. A. Robb, *Theoretical Chemistry Accounts*, 2007, **118**, 241–251.

[110] I. D. Petsalakis, G. Theodorakopoulos and J. Wright, *The Journal of Chemical Physics*, 1988, **89**, 6850–6859.

[111] E. F. Kjønstad, R. H. Myhre, T. J. Martínez and H. Koch, *The Journal of Chemical Physics*, 2017, **147**, 164105.

[112] D. R. Yarkony, *The Journal of chemical physics*, 1996, **104**, 7866–7881.

[113] C. A. Farfan and D. B. Turner, *Physical Chemistry Chemical Physics*, 2020, **22**, 20265–20283.

[114] D. R. Yarkony, *The Journal of Chemical Physics*, 2001, **114**, 2601–2613.

[115] I. Fdez. Galván, A. Brakestad and M. Vacher, *Physical Chemistry Chemical Physics*, 2022, **24**, 1638–1653.

[116] G. A. Meek and B. G. Levine, *Chemical Physics*, 2015, **460**, 117–124.

[117] D. Shchepanovska, R. J. Shannon, B. F. Curchod and D. R. Glowacki, *The Journal of Physical Chemistry A*, 2021, **125**, 3473–3488.

[118] S. Gómez, I. F. Galván, R. Lindh and L. González, in *Motivation and Basic Concepts*, John Wiley & Sons, Ltd, 2020, ch. 1, pp. 1–12.

[119] T. Y. Wang, S. P. Neville and M. S. Schuurman, *Journal of Chemical Theory and Computation*, 2025, **21**, 1340–1352.

[120] J. Cuéllar-Zuquin, A. J. Pepino, I. Fdez. Galván, I. Rivalta, F. Aquilante, M. Garavelli, R. Lindh and J. Segarra-Martí, *Journal of Chemical Theory and Computation*, 2023, **19**, 8258–8272.

[121] B. Lasorne, M. J. Bearpark, M. A. Robb and G. A. Worth, *The Journal of Physical Chemistry A*, 2008, **112**, 13017–13027.

[122] D. Asturiol, B. Lasorne, G. A. Worth, M. A. Robb and L. Blancafort, *Physical Chemistry Chemical Physics*, 2010, **12**, 4949–4958.

[123] M. Ben-Nun, F. Molnar, K. Schulten and T. J. Martínez, *Proceedings of the National Academy of Sciences*, 2002, **99**, 1769–1773.

[124] A. M. Virshup, J. Chen and T. J. Martínez, *The Journal of Chemical Physics*, 2012, **137**, 22A519.

[125] J. P. Malhado and J. T. Hynes, *The Journal of Chemical Physics*, 2012, **137**, 22A543.

[126] P. Krause, S. Matsika, M. Kotur and T. Weinacht, *The Journal of Chemical Physics*, 2012, **137**, 22A537.

[127] S. Sen and X. Deupi, *ACS Physical Chemistry Au*, 2024, **4**, 736–749.

[128] J. P. Malhado and J. T. Hynes, *The Journal of Chemical Physics*, 2016, **145**, 194104.

[129] M. van Horn, T. Cheragwandi and N. H. List, 2025.

[130] S. Matsika and D. R. Yarkony, in *Conical Intersections and the Spin-Orbit Interaction*, John Wiley & Sons, Ltd, 2002, pp. 557–581.

[131] N. Matsunaga and S. Koseki, in *Modeling of Spin-Forbidden Reactions*, John Wiley & Sons, Ltd, 2004, ch. 2, pp. 101–152.

[132] B. F. Curchod and A. J. Orr-Ewing, *The Journal of Physical Chemistry A*, 2024, **128**, 6613–6635.

[133] S. Matsika and D. R. Yarkony, *The Journal of Chemical Physics*, 2001, **115**, 2038–2050.

[134] S. Matsika and D. R. Yarkony, *The Journal of Chemical Physics*, 2001, **115**, 5066–5075.

[135] S. Matsika and D. R. Yarkony, *The Journal of Chemical Physics*, 2002, **116**, 2825–2835.

[136] S. Han and D. R. Yarkony, *The Journal of Chemical Physics*, 2003, **118**, 9952–9962.

[137] C. A. Mead, *The Journal of Chemical Physics*, 1979, **70**, 2276–2283.

[138] H. A. Kramers, *Proc. Acad. Amst*, 1930, **33**, 959–972.

[139] D. J. Tannor, in *Introduction to molecular dynamics*, University Science Books, 2007, ch. 9, pp. 185–226.

[140] C. Daggett, K. Yang, C.-X. Liu and L. Muechler, *Chemistry of Materials*, 2024, **36**, 3479–3489.

[141] L. M. Ibele, E. Sangiogo Gil, B. F. E. Curchod and F. Agostini, *The Journal of Physical Chemistry Letters*, 2023, **14**, 11625–11631.

[142] C. A. Mead, *Reviews of Modern Physics*, 1992, **64**, 51–85.

[143] H. C. Longuet-Higgins, *Proceedings of the Royal Society of London. Series A. Mathematical and Physical Sciences*, 1958, **244**, 1–16.

[144] G. Herzberg and H. C. Longuet-Higgins, *Discussions of the Faraday Society*, 1963, **35**, 77.

[145] W. T. Borden, *Pioneers of Quantum Chemistry*, ACS Publications, 2013, pp. 155–195.

[146] C. A. Mead and D. G. Truhlar, *The Journal of Chemical Physics*, 1979, **70**, 2284–2296.

[147] M. V. Berry, *Proceedings of the Royal Society of London. A. Mathematical and Physical Sciences*, 1984, **392**, 45–57.

[148] D. J. Tannor, in *Introduction to molecular dynamics*, University Science Books, 2007, ch. 12, pp. 335–394.

[149] I. G. Ryabinkin, L. Joubert-Doriol and A. F. Izmaylov, *Accounts of chemical research*, 2017, **50**, 1785–1793.

[150] S. P. Keating and C. A. Mead, *The Journal of Chemical Physics*, 1985, **82**, 5102–5117.

[151] M. S. Schuurman and D. R. Yarkony, *The Journal of Chemical Physics*, 2006, **124**, 124109.

[152] M. S. Schuurman and D. R. Yarkony, *The Journal of Physical Chemistry B*, 2006, **110**, 19031–19039.

[153] M. S. Schuurman and D. R. Yarkony, *The Journal of Chemical Physics*, 2006, **124**, 244103.

[154] K. A. Kistler and S. Matsika, *The Journal of Chemical Physics*, 2008, **128**, 215102.

[155] J. D. Coe and T. J. Martínez, *The Journal of Physical Chemistry A*, 2006, **110**, 618–630.

[156] S. Han and D. R. Yarkony, *The Journal of Chemical Physics*, 2003, **119**, 11561–11569.

[157] S. Han and D. R. Yarkony, *The Journal of Chemical Physics*, 2003, **119**, 5058–5068.

[158] B. F. E. Curchod and F. Agostini, *The Journal of Physical Chemistry Letters*, 2017, **8**, 831–837.

[159] A. Abedi, N. T. Maitra and E. K. U. Gross, *Physical Review Letters*, 2010, **105**, 123002.

[160] A. Abedi, N. T. Maitra and E. K. U. Gross, *The Journal of Chemical Physics*, 2012, **137**, 22A530.

[161] F. Agostini and E. K. U. Gross, *Quantum Chemistry and Dynamics of Excited States*, Wiley, 1st edn, 2020, pp. 531–562.

[162] F. Agostini and B. F. E. Curchod, *The European Physical Journal B*, 2018, **91**, 141.

[163] S. K. Min, A. Abedi, K. S. Kim and E. Gross, *Physical Review Letters*, 2014, **113**, 263004.

[164] L. M. Ibele, B. F. E. Curchod and F. Agostini, *The Journal of Physical Chemistry A*, 2022, **126**, 1263–1281.

[165] F. Liu, M. Filatov and T. J. Martínez, *The Journal of Chemical Physics*, 2021, **154**, 104108.

[166] S. Gozem, F. Melaccio, A. Valentini, M. Filatov, M. Huix-Rotllant, N. Ferré, L. M. Frutos, C. Angeli, A. I. Krylov, A. A. Granovsky, R. Lindh and M. Olivucci, *Journal of Chemical Theory and Computation*, 2014, **10**, 3074–3084.

[167] J. W. Park, R. Al-Saadon, M. K. MacLeod, T. Shiozaki and B. Vlaisavljevich, *Chemical Reviews*, 2020, **120**, 5878–5909.

[168] D. R. Hartree and W. Hartree, *Proceedings of the Royal Society of London. Series A-Mathematical and Physical Sciences*, 1935, **149**, 210–231.

[169] C. C. J. Roothaan, *Reviews of Modern Physics*, 1951, **23**, 69.

[170] G. G. Hall, *Proceedings of the Royal Society of London. Series A. Mathematical and Physical Sciences*, 1951, **205**, 541–552.

[171] R. Nesbet, *Proceedings of the Royal Society of London. Series A. Mathematical and Physical Sciences*, 1955, **230**, 312–321.

[172] A. Szabo and N. S. Ostlund, *Modern quantum chemistry: introduction to advanced electronic structure theory*, Dover Publications, Mineola, New York, 1st edn, 1996.

[173] R. Ditchfield, W. J. Hehre and J. A. Pople, *The Journal of Chemical Physics*, 1971, **54**, 724–728.

[174] T. H. Dunning, *The Journal of Chemical Physics*, 1989, **90**, 1007–1023.

[175] A. Hellweg and D. Rappoport, *Physical Chemistry Chemical Physics*, 2015, **17**, 1010–1017.

[176] B. O. Roos, P. R. Taylor and P. E. Sigbahn, *Chemical Physics*, 1980, **48**, 157–173.

[177] T. Helgaker, P. Jørgensen and J. Olsen, in *Short-Range Interactions and Orbital Expansions*, John Wiley & Sons, Ltd, 2000, ch. 7, pp. 256–286.

[178] S. Olsen, *The Journal of Chemical Physics*, 2015, **142**, 044116.

[179] L. N. Tran and E. Neuscamman, *The Journal of Physical Chemistry A*, 2020, **124**, 8273–8279.

[180] S. Ghosh, P. Verma, C. J. Cramer, L. Gagliardi and D. G. Truhlar, *Chemical Reviews*, 2018, **118**, 7249–7292.

[181] R. Neumann, R. H. Nobes and N. C. Handy, *Molecular Physics*, 1996, **87**, 1–36.

[182] D. Casanova and A. I. Krylov, *Physical Chemistry Chemical Physics*, 2020, **22**, 4326–4342.

[183] H.-J. Werner and P. J. Knowles, *The Journal of Chemical Physics*, 1988, **89**, 5803–5814.

[184] K. Andersson, P. Å. Malmqvist, B. O. Roos, A. J. Sadlej and K. Wolinski, *The Journal of Physical Chemistry*, 1990, **94**, 5483–5488.

[185] K. Andersson, P. Å. Malmqvist and B. O. Roos, *The Journal of Chemical Physics*, 1992, **96**, 1218–1226.

[186] J. Finley, P. Å. Malmqvist, B. O. Roos and L. Serrano-Andrés, *Chemical Physics Letters*, 1998, **288**, 299–306.

[187] T. Shiozaki, W. Győrffy, P. Celani and H.-J. Werner, *The Journal of Chemical Physics*, 2011, **135**, 081106.

[188] M. Winslow, W. B. Cross and D. Robinson, *Journal of Chemical Theory and Computation*, 2020, **16**, 3253–3263.

[189] A. D. Mahler and L. M. Thompson, *The Journal of Chemical Physics*, 2021, **154**, 244101.

[190] S. Gozem, M. Huntress, I. Schapiro, R. Lindh, A. A. Granovsky, C. Angeli and M. Olivucci, *Journal of Chemical Theory and Computation*, 2012, **8**, 4069–4080.

[191] S. Gozem, F. Melaccio, R. Lindh, A. I. Krylov, A. A. Granovsky, C. Angeli and M. Olivucci, *Journal of Chemical Theory and Computation*, 2013, **9**, 4495–4506.

[192] S. Sen and I. Schapiro, *Molecular Physics*, 2018, **116**, 2571–2582.

[193] A. Giussani and J. Segarra-Martí, *The Journal of Chemical Physics*, 2024, **161**, 011103.

[194] J. W. Park, *Journal of Chemical Theory and Computation*, 2019, **15**, 3960–3973.

[195] J. Janoš and P. Slavíček, *Journal of Chemical Theory and Computation*, 2023, **19**, 8273–8284.

[196] Y. Nishimoto, S. Battaglia and R. Lindh, *Journal of Chemical Theory and Computation*, 2022, **18**, 4269–4281.

[197] C. Kollmar, K. Sivalingam and F. Neese, *The Journal of Chemical Physics*, 2020, **152**, 214110.

[198] T. Shiozaki, C. Woywod and H.-J. Werner, *Phys. Chem. Chem. Phys.*, 2013, **15**, 262–269.

[199] B. O. Roos and K. Andersson, *Chemical Physics Letters*, 1995, **245**, 215–223.

[200] N. Forsberg and P.-Å. Malmqvist, *Chemical Physics Letters*, 1997, **274**, 196–204.

[201] I. Polyak, L. Hutton, R. Crespo-Otero, M. Barbatti and P. J. Knowles, *Journal of Chemical Theory and Computation*, 2019, **15**, 3929–3940.

[202] M. Heindl and L. González, *Computational and Theoretical Chemistry*, 2019, **1155**, 38–46.

[203] R. Feldmann, M. Mörchen, J. Lang, M. Lesiuk and M. Reiher, *The Journal of Physical Chemistry A*, 2024, **128**, 8615–8627.

[204] T. Helgaker, P. Jørgensen and J. Olsen, in *Multiconfigurational Self-Consistent Field Theory*, John Wiley & Sons, Ltd, 2000, ch. 12, pp. 598–647.

[205] J. Schirmer, *Physical Review A*, 1982, **26**, 2395–2416.

[206] A. B. Trofimov and J. Schirmer, *Journal of Physics B: Atomic, Molecular and Optical Physics*, 1995, **28**, 2299–2324.

[207] A. Dreuw and M. Wormit, *Wiley Interdisciplinary Reviews: Computational Molecular Science*, 2015, **5**, 82–95.

[208] C. Hättig, *Advances in Quantum Chemistry*, Elsevier, 2005, vol. 50, pp. 37–60.

[209] C. Møller and M. S. Plesset, *Physical Review*, 1934, **46**, 618–622.

[210] J. Oddershede, *Advances in quantum chemistry*, Elsevier, 1978, vol. 11, pp. 275–352.

[211] F. Plasser, R. Crespo-Otero, M. Pederzoli, J. Pittner, H. Lischka and M. Barbatti, *Journal of Chemical Theory and Computation*, 2014, **10**, 1395–1405.

[212] E. Marsili, A. Prlj and B. F. Curchod, *Physical Chemistry Chemical Physics*, 2021, **23**, 12945–12949.

[213] B. G. Levine, J. D. Coe and T. J. Martínez, *The Journal of Physical Chemistry B*, 2008, **112**, 405–413.

[214] J. Sanz García, R. Maskri, A. Mitrushchenkov and L. Joubert-Doriol, *Journal of Chemical Theory and Computation*, 2024, **20**, 5643–5654.

[215] M. J. Bearpark, M. A. Robb and H. Bernhard Schlegel, *Chemical Physics Letters*, 1994, **223**, 269–274.

[216] F. Sicilia, L. Blancafort, M. J. Bearpark and M. A. Robb, *Journal of Chemical Theory and Computation*, 2008, **4**, 257–266.

[217] T. W. Keal, A. Koslowski and W. Thiel, *Theoretical Chemistry Accounts*, 2007, **118**, 837–844.

[218] S. Angelico, E. F. Kjønstad and H. Koch, *The Journal of Physical Chemistry Letters*, 2025, **16**, 561–567.

[219] M. R. Manaa and D. R. Yarkony, *The Journal of Chemical Physics*, 1993, **99**, 5251–5256.

[220] C. Ciminelli, G. Granucci and M. Persico, *Chemistry - A European Journal*, 2004, **10**, 2327–2341.

[221] X. Zhang and J. M. Herbert, *The Journal of Chemical Physics*, 2014, **141**, 064104.

[222] S. Maeda, K. Ohno and K. Morokuma, *Journal of Chemical Theory and Computation*, 2010, **6**, 1538–1545.

[223] I. Fdez. Galván and R. Lindh, *Journal of Chemical Theory and Computation*, 2023, **19**, 3418–3427.

[224] E. Vandaele, M. Mališ and S. Luber, *Journal of Chemical Theory and Computation*, 2024, **20**, 856–872.

[225] H. Köppel and B. Schubert, *Molecular Physics*, 2006, **104**, 1069–1079.

[226] J. Witte, M. Goldey, J. B. Neaton and M. Head-Gordon, *Journal of Chemical Theory and Computation*, 2015, **11**, 1481–1492.

[227] C. A. Ullrich and Z.-h. Yang, *Brazilian Journal of Physics*, 2014, **44**, 154–188.

[228] C. J. Cramer, *Essentials of Computational chemistry: theories and models*, Wiley, Chichester, West Sussex, England ; Hoboken, NJ, 2nd edn, 2004.

[229] W. Koch and M. C. Holthausen, *A Chemist's Guide to Density Functional Theory*, Wiley, 1st edn, 2001.

[230] R. G. Parr and W. Yang, *Density-Functional Theory of Atoms and Molecules*, Oxford University Press, 1989.

[231] A. Dreuw and M. Head-Gordon, *Chemical Reviews*, 2005, **105**, 4009–4037.

[232] M. Casida and M. Huix-Rotllant, *Annual Review of Physical Chemistry*, 2012, **63**, 287–323.

[233] K. Burke, J. Werschnik and E. K. U. Gross, *The Journal of Chemical Physics*, 2005, **123**, 062206.

[234] L. Kronik and S. Kümmel, *Physical Chemistry Chemical Physics*, 2020, **22**, 16467–16481.

[235] M. Levy, *On the foundations of density-functional theory.*, 2010.

[236] J. P. Perdew, AIP Conference Proceedings, Antwerp (Belgium), 2001, pp. 1–20.

[237] E. Brémond and C. Adamo, *The Journal of Chemical Physics*, 2011, **135**, 024106.

[238] S. Grimme, *The Journal of Chemical Physics*, 2006, **124**, 034108.

[239] C. Adamo and V. Barone, *The Journal of Chemical Physics*, 1999, **110**, 6158–6170.

[240] A. D. Becke, *The Journal of Chemical Physics*, 1993, **98**, 5648–5652.

[241] J. Sun, A. Ruzsinszky and J. Perdew, *Physical Review Letters*, 2015, **115**, 036402.

[242] T. Van Voorhis and G. E. Scuseria, *The Journal of Chemical Physics*, 1998, **109**, 400–410.

[243] J. P. Perdew, K. Burke and M. Ernzerhof, *Physical Review Letters*, 1996, **77**, 3865–3868.

[244] A. D. Becke, *Physical Review A*, 1988, **38**, 3098–3100.

[245] C. Lee, W. Yang and R. G. Parr, *Physical Review B*, 1988, **37**, 785–789.

[246] S. H. Vosko, L. Wilk and M. Nusair, *Canadian Journal of Physics*, 1980, **58**, 1200–1211.

[247] N. Mardirossian and M. Head-Gordon, *Molecular Physics*, 2017, **115**, 2315–2372.

[248] D. J. Tozer, *Molecular Physics*, 2005, **103**, 145–148.

[249] M. E. Casida and M. Huix-Rotllant, *Topics in Current Chemistry*, 2015, **368**, 1–60.

[250] K. Burke and J. Kozlowski, 2021, 10.48550/arXiv.2108.11534.

[251] P. Elliott, K. Burke and F. Furche, 2007, 10.48550/arXiv.cond–mat/0703590.

[252] N. T. Maitra, *The Journal of Chemical Physics*, 2016, **144**, 220901.

[253] R. van Leeuwen, *Physical Review Letters*, 1998, **80**, 1280–1283.

[254] R. Van Leeuwen, *International Journal of Modern Physics B*, 2001, **15**, 1969–2023.

[255] G. Vignale, *Physical Review A*, 2008, **77**, 062511.

[256] R. van Leeuwen, *Physical Review Letters*, 1999, **82**, 3863–3866.

[257] C. A. Ullrich, *Time-Dependent Density-Functional Theory: Concepts and Applications*, Oxford University Press, 2011.

[258] N. T. Maitra and K. Burke, *Physical Review A*, 2001, **63**, 042501.

[259] N. T. Maitra and K. Burke, *Physical Review A*, 2001, **64**, 039901.

[260] N. T. Maitra, K. Burke and C. Woodward, *Physical Review Letters*, 2002, **89**, 023002.

[261] N. T. Maitra, *Annual Review of Physical Chemistry*, 2022, **73**, 117–140.

[262] A. Castro, H. Appel, M. Oliveira, C. A. Rozzi, X. Andrade, F. Lorenzen, M. A. L. Marques, E. K. U. Gross and A. Rubio, *physica status solidi (b)*, 2006, **243**, 2465–2488.

[263] K. Lopata and N. Govind, *Journal of Chemical Theory and Computation*, 2011, **7**, 1344–1355.

[264] P. Elliott, S. Goldson, C. Canahui and N. T. Maitra, *Chemical Physics*, 2011, **391**, 110–119.

[265] M. Huix-Rotllant, *PhD Thesis*, Université de Grenoble, 2006.

[266] M. E. Casida, *Journal of Molecular Structure: THEOCHEM*, 2009, **914**, 3–18.

[267] M. Isegawa and D. G. Truhlar, *The Journal of Chemical Physics*, 2013, **138**, 134111.

[268] S. Hirata and M. Head-Gordon, *Chemical Physics Letters*, 1999, **302**, 375–382.

[269] F. Cordova, L. J. Doriol, A. Ipatov, M. E. Casida, C. Filippi and A. Vela, *The Journal of Chemical Physics*, 2007, **127**, 164111.

[270] J. M. Herbert, *Theoretical and Computational Photochemistry*, Elsevier, 2023, pp. 69–118.

[271] M. Huix-Rotllant, A. Ipatov, A. Rubio and M. E. Casida, *Chemical Physics*, 2011, **391**, 120–129.

[272] D. B. Dar and N. T. Maitra, *The Journal of Chemical Physics*, 2023, **159**, 211104.

[273] N. T. Maitra, *The Journal of Chemical Physics*, 2006, **125**, 014110.

[274] M. Huix-Rotllant, B. Natarajan, A. Ipatov, C. Muhavini Wawire, T. Deutsch and M. E. Casida, *Physical Chemistry Chemical Physics*, 2010, **12**, 12811.

[275] Y. Horbatenko, S. Lee, M. Filatov and C. H. Choi, *Journal of Chemical Theory and Computation*, 2021, **17**, 975–984.

[276] N. T. Maitra, *Fundamentals of Time-Dependent Density Functional Theory*, Springer Berlin Heidelberg, Berlin, Heidelberg, 2012, vol. 837, pp. 167–184.

[277] P. Romaniello, D. Sangalli, J. A. Berger, F. Sottile, L. G. Molinari, L. Reining and G. Onida, *The Journal of Chemical Physics*, 2009, **130**, 044108.

[278] C.-P. Hsu, S. Hirata and M. Head-Gordon, *The Journal of Physical Chemistry A*, 2001, **105**, 451–458.

[279] F. Plasser, *Journal of Computational Chemistry*, 2025, **46**, e70072.

[280] J. Authier and P.-F. Loos, *The Journal of Chemical Physics*, 2020, **153**, 184105.

[281] M. Huix-Rotllant and M. E. Casida, 2010, 10.48550/arXiv:1008.1478.

[282] M. Thiele and S. Kümmel, *Physical Review Letters*, 2014, **112**, 083001.

[283] N. T. Maitra, F. Zhang, R. J. Cave and K. Burke, *The Journal of Chemical Physics*, 2004, **120**, 5932–5937.

[284] R. J. Cave, F. Zhang, N. T. Maitra and K. Burke, *Chemical Physics Letters*, 2004, **389**, 39–42.

[285] G. Mazur and R. Włodarczyk, *Journal of Computational Chemistry*, 2009, **30**, 811–817.

[286] G. Mazur, M. Makowski, R. Włodarczyk and Y. Aoki, *International Journal of Quantum Chemistry*, 2011, **111**, 819–825.

[287] M. E. Casida, *The Journal of Chemical Physics*, 2005, **122**, 054111.

[288] O. V. Gritsenko and E. Jan Baerends, *Physical Chemistry Chemical Physics*, 2009, **11**, 4640.

[289] M. Huix-Rotllant, M. Filatov, S. Gozem, I. Schapiro, M. Olivucci and N. Ferré, *Journal of Chemical Theory and Computation*, 2013, **9**, 3917–3932.

[290] M. Barbatti and R. Crespo-Otero, *Topics in Current Chemistry*, 2015, **368**, 415–444.

[291] M. E. Casida, B. Natarajan and T. Deutsch, *Fundamentals of Time-Dependent Density Functional Theory*, Springer Berlin Heidelberg, Berlin, Heidelberg, 2012, vol. 837, pp. 279–299.

[292] S. Fantacci, A. Migani and M. Olivucci, *The Journal of Physical Chemistry A*, 2004, **108**, 1208–1213.

[293] J. V. Neumann and E. Wigner, *World Scientific Series in 20th Century Chemistry*, WORLD SCIENTIFIC, 2000, vol. 8, pp. 25–31.

[294] I. Tavernelli, E. Tapavicza and U. Rothlisberger, *Journal of Molecular Structure: THEOCHEM*, 2009, **914**, 22–29.

[295] A. J. Cohen, D. J. Tozer and N. C. Handy, *The Journal of Chemical Physics*, 2007, **126**, 214104.

[296] J. A. Pople, P. M. W. Gill and N. C. Handy, *International Journal of Quantum Chemistry*, 1995, **56**, 303–305.

[297] Y. Yang, L. Shen, D. Zhang and W. Yang, *The Journal of Physical Chemistry Letters*, 2016, **7**, 2407–2411.

[298] B. Kaduk and T. Van Voorhis, *The Journal of Chemical Physics*, 2010, **133**, 061102.

[299] J. M. Herbert and A. Mandal, *Time-dependent density functional theory: Nonadiabatic molecular dynamics*, Jenny Stanford Publishing, 2022, pp. 361–404.

[300] H.-H. Teh and J. E. Subotnik, *The Journal of Physical Chemistry Letters*, 2019, **10**, 3426–3432.

[301] V. Athavale, H.-H. Teh and J. E. Subotnik, *The Journal of Chemical Physics*, 2021, **155**, 154105.

[302] S. L. Li, A. V. Marenich, X. Xu and D. G. Truhlar, *The Journal of Physical Chemistry Letters*, 2014, **5**, 322–328.

[303] L. Xu, V. M. Freixas, F. Aleotti, D. G. Truhlar, S. Tretiak, M. Garavelli, S. Mukamel and N. Govind, *Journal of Chemical Theory and Computation*, 2025, 3600–3611.

[304] Y. Shu, K. A. Parker and D. G. Truhlar, *The Journal of Physical Chemistry Letters*, 2017, **8**, 2107–2112.

[305] Y. Shu, K. A. Parker and D. G. Truhlar, *The Journal of Physical Chemistry A*, 2017, **121**, 9728–9735.

[306] J. M. Herbert, X. Zhang, A. F. Morrison and J. Liu, *Accounts of Chemical Research*, 2016, **49**, 931–941.

[307] S. Lee, M. Filatov, S. Lee and C. H. Choi, *The Journal of Chemical Physics*, 2018, **149**, 104101.

[308] S. Lee, E. E. Kim, H. Nakata, S. Lee and C. H. Choi, *The Journal of Chemical Physics*, 2019, **150**, 184111.

[309] W. Park, K. Komarov, S. Lee and C. H. Choi, *The Journal of Physical Chemistry Letters*, 2023, **14**, 8896–8908.

[310] Y. A. Bernard, Y. Shao and A. I. Krylov, *The Journal of Chemical Physics*, 2012, **136**, 204103.

[311] A. I. Krylov, *Chemical Physics Letters*, 2001, **338**, 375–384.

[312] Y. Shao, M. Head-Gordon and A. I. Krylov, *The Journal of Chemical Physics*, 2003, **118**, 4807–4818.

[313] H. van Aggelen, Y. Yang and W. Yang, *Physical Review A*, 2013, **88**, 030501.

[314] Y. Yang, H. van Aggelen and W. Yang, *The Journal of Chemical Physics*, 2013, **139**, 224105.

[315] Y. Yang, D. Peng, J. Lu and W. Yang, *The Journal of Chemical Physics*, 2014, **141**, 124104.

[316] C. Bannwarth, J. K. Yu, E. G. Hohenstein and T. J. Martínez, *The Journal of Chemical Physics*, 2020, **153**, 024110.

[317] J. K. Yu, C. Bannwarth, E. G. Hohenstein and T. J. Martínez, *Journal of Chemical Theory and Computation*, 2020, **16**, 5499–5511.

[318] N. T. Maitra, *The Journal of Chemical Physics*, 2005, **122**, 234104.

[319] N. T. Maitra and D. G. Tempel, *The Journal of Chemical Physics*, 2006, **125**, 184111.

[320] X. Huang, Z. Pei and W. Liang, *The Journal of Chemical Physics*, 2023, **158**, 044122.

[321] T. A. Niehaus, *The Journal of Chemical Physics*, 2023, **158**, 054103.

[322] V. Chernyak and S. Mukamel, *The Journal of Chemical Physics*, 2000, **112**, 3572–3579.

[323] M. Baer, *Physics Reports*, 2002, **358**, 75–142.

[324] E. Tapavicza, I. Tavernelli and U. Rothlisberger, *Physical Review Letters*, 2007, **98**, 023001.

[325] R. Send and F. Furche, *The Journal of Chemical Physics*, 2010, **132**, 044107.

[326] C. Hu, H. Hirai and O. Sugino, *The Journal of Chemical Physics*, 2007, **127**, 064103.

[327] I. Tavernelli, E. Tapavicza and U. Rothlisberger, *The Journal of Chemical Physics*, 2009, **130**, 124107.

[328] I. Tavernelli, B. F. E. Curchod and U. Rothlisberger, *The Journal of Chemical Physics*, 2009, **131**, 196101.

[329] I. Tavernelli, B. F. E. Curchod, A. Laktionov and U. Rothlisberger, *The Journal of Chemical Physics*, 2010, **133**, 194104.

[330] Z. Li and W. Liu, *The Journal of Chemical Physics*, 2014, **141**, 014110.

[331] Z. Li, B. Suo and W. Liu, *The Journal of Chemical Physics*, 2014, **141**, 244105.

[332] Z. Wang, C. Wu and W. Liu, *Accounts of Chemical Research*, 2021, **54**, 3288–3297.

[333] S. M. Parker, S. Roy and F. Furche, *Physical Chemistry Chemical Physics*, 2019, **21**, 18999–19010.

[334] S. M. Parker, S. Roy and F. Furche, *The Journal of Chemical Physics*, 2016, **145**, 134105.

[335] X. Zhang and J. M. Herbert, *The Journal of Chemical Physics*, 2015, **142**, 064109.

[336] Q. Ou, G. D. Bellchambers, F. Furche and J. E. Subotnik, *The Journal of Chemical Physics*, 2015, **142**, 064114.

[337] D. Dar, S. Roy and N. T. Maitra, *The Journal of Physical Chemistry Letters*, 2023, **14**, 3186–3192.

[338] Q. Ou, E. C. Alguire and J. E. Subotnik, *The Journal of Physical Chemistry B*, 2015, **119**, 7150–7161.

[339] B. Vlaisavljevich and T. Shiozaki, *Journal of Chemical Theory and Computation*, 2016, **12**, 3781–3787.

[340] J. W. Park and T. Shiozaki, *Journal of Chemical Theory and Computation*, 2017, **13**, 2561–2570.

[341] T. Shiozaki, *WIREs Computational Molecular Science*, 2018, **8**, 1–7.

[342] R. Lindh and I. F. Galván, *Quantum Chemistry and Dynamics of Excited States*, Wiley, 1st edn, 2020, pp. 299–353.

[343] M. Barbatti, A. J. A. Aquino and H. Lischka, *Molecular Physics*, 2006, **104**, 1053–1060.

[344] J. T. Taylor, D. J. Tozer and B. F. Curchod, *The Journal of Physical Chemistry A*, 2024, **128**, 5314–5320.

[345] L. Zhang, S. V. Pios, M. Martyka, F. Ge, Y.-F. Hou, Y. Chen, L. Chen, J. Jankowska, M. Barbatti and P. O. Dral, *Journal of Chemical Theory and Computation*, 2024, **20**, 5043–5057.

[346] C. M. Isborn, N. Luehr, I. S. Ufimtsev and T. J. Martínez, *Journal of Chemical Theory and Computation*, 2011, **7**, 1814–1823.

[347] I. S. Ufimtsev and T. J. Martínez, *Journal of Chemical Theory and Computation*, 2008, **4**, 222–231.

[348] I. S. Ufimtsev and T. J. Martínez, *Journal of Chemical Theory and Computation*, 2009, **5**, 2619–2628.

[349] I. S. Ufimtsev and T. J. Martínez, *Journal of Chemical Theory and Computation*, 2009, **5**, 3138–3138.

[350] A. V. Titov, I. S. Ufimtsev, N. Luehr and T. J. Martínez, *Journal of Chemical Theory and Computation*, 2013, **9**, 213–221.

[351] S. Seritan, C. Bannwarth, B. S. Fales, E. G. Hohenstein, S. I. L. Kokkila-Schumacher, N. Luehr, J. W. Snyder, C. Song, A. V. Titov, I. S. Ufimtsev and T. J. Martínez, *The Journal of Chemical Physics*, 2020, **152**, 224110.

[352] S. Seritan, C. Bannwarth, B. S. Fales, E. G. Hohenstein, C. M. Isborn, S. I. L. Kokkila-Schumacher, X. Li, F. Liu, N. Luehr, J. W. Snyder, C. Song, A. V. Titov, I. S. Ufimtsev, L. Wang and T. J. Martínez, *WIREs Computational Molecular Science*, 2021, **11**, 1–16.

[353] M. Ernzerhof and G. E. Scuseria, *The Journal of Chemical Physics*, 1999, **110**, 5029–5036.

[354] C. Hättig, A. Hellweg and A. Köhn, *Physical Chemistry Chemical Physics*, 2006, **8**, 1159.

[355] R. Ahlrichs, M. Bär, M. Häser, H. Horn and C. Kölmel, *Chemical Physics Letters*, 1989, **162**, 165–169.

[356] F. Furche, R. Ahlrichs, C. Hättig, W. Klopper, M. Sierka and F. Weigend, *WIREs Computational Molecular Science*, 2014, **4**, 91–100.

[357] F. Weigend, A. Köhn and C. Hättig, *The Journal of Chemical Physics*, 2002, **116**, 3175–3183.

[358] H. R. Hudock, B. G. Levine, A. L. Thompson, H. Satzger, D. Townsend, N. Gador, S. Ullrich, A. Stolow and T. J. Martínez, *The Journal of Physical Chemistry A*, 2007, **111**, 8500–8508.

[359] D. R. Yarkony, *The Journal of Chemical Physics*, 2000, **112**, 2111–2120.

[360] D. Lefrancois, D. Tuna, T. J. Martínez and A. Dreuw, *Journal of Chemical Theory and Computation*, 2017, **13**, 4436–4441.

[361] V. Bonačić-Koutecký, K. Schöffel and J. Michl, *Theoretica Chimica Acta*, 1987, **72**, 459–474.

[362] V. Bonačić-Koutecký, J. Koutecký and J. Michl, *Angewandte Chemie International Edition in English*, 1987, **26**, 170–189.

[363] P. Du, S. C. Racine and E. R. Davidson, *The Journal of Physical Chemistry*, 1990, **94**, 3944–3951.

[364] S. El-Taher, R. H. Hilal and T. A. Albright, *International Journal of Quantum Chemistry*, 2001, **82**, 242–254.

[365] A. J. A. Aquino, M. Barbatti and H. Lischka, *ChemPhysChem*, 2006, **7**, 2089–2096.

[366] K. Bennett, M. Kowalewski and S. Mukamel, *Journal of Chemical Theory and Computation*, 2016, **12**, 740–752.

[367] M. A. Kochman and B. Durbeej, *The Journal of Physical Chemistry A*, 2019, **123**, 6660–6673.

[368] M. Sapunar, A. Ponzi, S. Chaiwongwattana, M. Mališ, A. Prlj, P. Decleva and N. Došlić, *Physical Chemistry Chemical Physics*, 2015, **17**, 19012–19020.

[369] A. Prlj, B. F. E. Curchod and C. Corminboeuf, *Physical Chemistry Chemical Physics*, 2015, **17**, 14719–14730.

[370] M. A. Kochman and B. Durbeej, *The Journal of Physical Chemistry A*, 2020, **124**, 2193–2206.

[371] F. Siddique, M. Barbatti, Z. Cui, H. Lischka and A. J. A. Aquino, *The Journal of Physical Chemistry A*, 2020, **124**, 3347–3357.

[372] M. Barbatti, *Journal of the American Chemical Society*, 2014, **136**, 10246–10249.

[373] H. Lischka, M. Barbatti, F. Siddique, A. Das and A. J. Aquino, *Chemical Physics*, 2018, **515**, 472–479.

[374] B. Milovanović, J. Novak, M. Etinski, W. Domcke and N. Došlić, *Physical Chemistry Chemical Physics*, 2021, **23**, 2594–2604.

[375] A. Prlj, A. Fabrizio and C. Corminboeuf, *Phys. Chem. Chem. Phys.*, 2016, **18**, 32668–32672.

[376] J. Novak, A. Prlj, N. Basarić, C. Corminboeuf and N. Došlić, *Chemistry - A European Journal*, 2017, **23**, 8244–8251.

[377] M. Dommett and R. Crespo-Otero, *Physical Chemistry Chemical Physics*, 2017, **19**, 2409–2416.

[378] G. Gate, R. Szabla, M. R. Haggmark, J. Šponer, A. L. Sobolewski and M. S. De Vries, *Physical Chemistry Chemical Physics*, 2019, **21**, 13474–13485.

[379] M. A. Kochman, M. Pola and R. J. D. Miller, *The Journal of Physical Chemistry A*, 2016, **120**, 6200–6215.

[380] L. Hutton and B. F. E. Curchod, *ChemPhotoChem*, 2022, **6**, e20220015.

[381] R. Szabla, R. W. Góra and J. Šponer, *Physical Chemistry Chemical Physics*, 2016, **18**, 20208–20218.

[382] C. Woywod, A. Papp, G. J. Halász and A. Vibók, *Theoretical Chemistry Accounts*, 2010, **125**, 521–533.

[383] G. Stock, C. Woywod, W. Domcke, T. Swinney and B. S. Hudson, *The Journal of Chemical Physics*, 1995, **103**, 6851–6860.

[384] M. Sala, S. Guérin and F. Gatti, *Physical Chemistry Chemical Physics*, 2015, **17**, 29518–29530.

[385] C. Woywod, W. Domcke, A. L. Sobolewski and H. Werner, *The Journal of Chemical Physics*, 1994, **100**, 1400–1413.

[386] M. Kanno, Y. Ito, N. Shimakura, S. Koseki, H. Kono and Y. Fujimura, *Physical Chemistry Chemical Physics*, 2015, **17**, 2012–2014.

[387] A. L. Sobolewski, C. Woywod and W. Domcke, *The Journal of Chemical Physics*, 1993, **98**, 5627–5641.

[388] L. Seidner, G. Stock, A. L. Sobolewski and W. Domcke, *The Journal of Chemical Physics*, 1992, **96**, 5298–5309.

[389] A. Köhn and A. Tajti, *The Journal of Chemical Physics*, 2007, **127**, 044105.

[390] S. Thomas, F. Hampe, S. Stopkowicz and J. Gauss, *Molecular Physics*, 2021, **119**, e1968056.

[391] D. Zhang, S. N. Steinmann and W. Yang, *The Journal of Chemical Physics*, 2013, **139**, 154109.

[392] G. Strinati, *La Rivista del Nuovo Cimento*, 1988, **11**, 1–86.

[393] B. K. Carpenter, G. B. Ellison, M. R. Nimlos and A. M. Scheer, *The Journal of Physical Chemistry A*, 2022, **126**, 1429–1447.

[394] F. Rossi, E. F. Kjønstad, S. Angelico and H. Koch, *The Journal of Physical Chemistry Letters*, 2024, **16**, 568–578.

[395] D. V. Cofer-Shabica, V. Athavale and J. E. Subotnik, *The Journal of Chemical Physics*, 2023, **159**, 121101.

[396] P. Pulay and G. Fogarasi, *Chemical Physics Letters*, 2004, **386**, 272–278.

[397] A. Niklasson, P. Steneteg, A. Odell, N. Bock, M. Challacombe, C. Tymczak, E. Holmström, G. Zheng and V. Weber, *The Journal of Chemical Physics*, 2009, **130**, 214109.

[398] A. M. Niklasson, C. Tymczak and M. Challacombe, *Physical Review Letters*, 2006, **97**, 123001.

[399] Y. Aharonov and D. Bohm, *Physical Review*, 1959, **115**, 485.

[400] M. Baer, *Molecular Physics*, 1980, **40**, 1011–1013.

[401] D. R. Yarkony, *The Journal of Physical Chemistry A*, 1997, **101**, 4263–4270.

[402] Y. Wang and D. R. Yarkony, *The Journal of Chemical Physics*, 2021, **155**, 174115.

[403] M. Baer, *Chemical Physics Letters*, 1975, **35**, 112–118.

[404] M. Baer, *Chemical Physics*, 1976, **15**, 49–57.

[405] Q. Ou, S. Fatehi, E. Alguire, Y. Shao and J. E. Subotnik, *The Journal of Chemical Physics*, 2014, **141**, 024114.

[406] Q. Ou, S. Fatehi, E. Alguire, Y. Shao and J. E. Subotnik, *The Journal of Chemical Physics*, 2014, **141**, 069903.

[407] D. M. G. Williams, E. F. Kjønstad and T. J. Martínez, *The Journal of Chemical Physics*, 2023, **158**, 214122.

[408] D. R. Yarkony, *The Journal of Chemical Physics*, 1996, **105**, 10456–10461.

[409] L. Dupuy and N. T. Maitra, *The Journal of Chemical Physics*, 2024, **161**, 134103.

[410] A. V. Akimov, *The journal of physical chemistry letters*, 2018, **9**, 6096–6102.

[411] S. Hirata and M. Head-Gordon, *Chemical Physics Letters*, 1999, **314**, 291–299.

[412] M. J. Peach, M. J. Williamson and D. J. Tozer, *Journal of Chemical Theory and Computation*, 2011, **7**, 3578–3585.

[413] S. Tretiak and S. Mukamel, *Chemical Reviews*, 2002, **102**, 3171–3212.

[414] I. Tavernelli*, U. F. Röhrig and U. Rothlisberger, *Molecular Physics*, 2005, **103**, 963–981.

[415] B. F. E. Curchod, U. Rothlisberger and I. Tavernelli, *ChemPhysChem*, 2013, **14**, 1314–1340.

[416] E. Tapavicza, G. D. Bellchambers, J. C. Vincent and F. Furche, *Physical Chemistry Chemical Physics*, 2013, **15**, 18336–18348.

[417] R. Crespo-Otero and M. Barbatti, *Chemical Reviews*, 2018, **118**, 7026–7068.

[418] L. Yue, Y. Liu and C. Zhu, *Physical Chemistry Chemical Physics*, 2018, **20**, 24123–24139.

[419] M. T. Do Casal, J. M. Toldo, M. Pinheiro Jr and M. Barbatti, *Open Research Europe*, 2022, **1**, 49.

[420] B. F. E. Curchod, A. Sisto and T. J. Martínez, *The Journal of Physical Chemistry A*, 2017, **121**, 265–276.

[421] M. Barbatti, G. Granucci, M. Persico, M. Ruckenbauer, M. Vazdar, M. Eckert-Maksić and H. Lischka, *Journal of Photochemistry and Photobiology A: Chemistry*, 2007, **190**, 228–240.

[422] E. Fabiano, G. Groenhof and W. Thiel, *Chemical Physics*, 2008, **351**, 111–116.

[423] J. Suchan, J. Janoš and P. Slavíček, *Journal of Chemical Theory and Computation*, 2020, **16**, 5809–5820.

[424] D. Hollas, L. Šištík, E. G. Hohenstein, T. J. Martínez and P. Slavíček, *Journal of Chemical Theory and Computation*, 2018, **14**, 339–350.

[425] P. Vindel-Zandbergen, L. M. Ibele, J.-K. Ha, S. K. Min, B. F. Curchod and N. T. Maitra, *Journal of Chemical Theory and Computation*, 2021, **17**, 3852–3862.

[426] R. Littlejohn, J. Rawlinson and J. Subotnik, *The Journal of Chemical Physics*, 2024, **160**, 114103.

[427] T. V. Papineau, D. Jacquemin and M. Vacher, *The Journal of Physical Chemistry Letters*, 2024, **15**, 636–643.

[428] *Quantum chemistry and dynamics of excited states: methods and applications*, ed. L. González and R. Lindh, Wiley, Hoboken, NJ, 2021.

[429] L. L. Cigrang, B. F. Curchod, R. A. Ingle, A. Kelly, J. R. Mannouch, D. Accomasso, A. Alijah, M. Barbatti, W. Chebbi, N. Doslic *et al.*, *The Journal of Physical Chemistry A*, 2025, **129**, 7023–7050.

[430] H.-D. Meyer, U. Manthe and L. S. Cederbaum, *Chemical Physics Letters*, 1990, **165**, 73–78.

[431] M. H. Beck, A. Jäckle, G. A. Worth and H.-D. Meyer, *Physics reports*, 2000, **324**, 1–105.

[432] M. Bonfanti, G. A. Worth and I. Burghardt, in *Multi-Configuration Time-Dependent Hartree Methods: From Quantum to Semiclassical and Quantum-Classical*, John Wiley & Sons, Ltd, 2020, ch. 12, pp. 383–411.

[433] B. F. Curchod and T. J. Martínez, *Chemical Reviews*, 2018, **118**, 3305–3336.

[434] J. Tully and D. Thompson, *DL Thompson, Ed*, 1998, 34.

[435] J. Tully, *Faraday Discussions*, 1998, **110**, 407–419.

[436] J. B. Delos, W. R. Thorson and S. K. Knudson, *Physical Review A*, 1972, **6**, 709.

[437] J. C. Tully and R. K. Preston, *The Journal of Chemical Physics*, 1971, **55**, 562–572.

[438] J. C. Tully, *The Journal of Chemical Physics*, 1990, **93**, 1061–1071.

[439] S. Hammes-Schiffer and J. C. Tully, *The Journal of Chemical Physics*, 1994, **101**, 4657–4667.

[440] T. J. Martínez, M. Ben-Nun and R. D. Levine, *The Journal of Physical Chemistry*, 1996, **100**, 7884–7895.

[441] T. J. Martínez and R. D. Levine, *Journal of the Chemical Society, Faraday Transactions*, 1997, **93**, 941–947.

[442] T. J. Martínez, M. Ben-Nun and R. D. Levine, *The Journal of Physical Chemistry A*, 1997, **101**, 6389–6402.

[443] M. Ben-Nun, J. Quenneville and T. J. Martínez, *The Journal of Physical Chemistry A*, 2000, **104**, 5161–5175.

[444] G. A. Worth, M. A. Robb and I. Burghardt, *Faraday discussions*, 2004, **127**, 307–323.

[445] B. Lasorne, M. J. Bearpark, M. A. Robb and G. A. Worth, *Chemical Physics Letters*, 2006, **432**, 604–609.

[446] G. W. Richings, I. Polyak, K. E. Spinlove, G. A. Worth, I. Burghardt and B. Lasorne, *International Reviews in Physical Chemistry*, 2015, **34**, 269–308.

[447] B. F. Curchod, W. J. Glover and T. J. Martínez, *The Journal of Physical Chemistry A*, 2020, **124**, 6133–6143.

[448] L. M. Ibele, Y. Lassmann, T. J. Martínez and B. F. Curchod, *The Journal of Chemical Physics*, 2021, **154**, 104110.

[449] Y. Lassmann and B. F. Curchod, *The Journal of Chemical Physics*, 2021, **154**, 211106.

[450] Y. Lassmann, D. Hollas and B. F. Curchod, *The Journal of Physical Chemistry Letters*, 2022, **13**, 12011–12018.

[451] L. Verlet, *Physical Review*, 1967, **159**, 98.

[452] W. C. Swope, H. C. Andersen, P. H. Berens and K. R. Wilson, *The Journal of Chemical Physics*, 1982, **76**, 637–649.

[453] L. M. Ibele, A. Nicolson and B. F. Curchod, *Molecular Physics*, 2020, **118**, e1665199.

[454] C. Runge, *Mathematische Annalen*, 1895, **46**, 167–178.

[455] W. Kutta, *Beitrag zur näherungsweisen Integration totaler Differentialgleichungen*, Teubner, 1901.

[456] J. C. Butcher, *Numerical methods for ordinary differential equations*, John Wiley & Sons, 2016.

[457] S. Mai, P. Marquetand and L. González, in *Surface Hopping Molecular Dynamics*, John Wiley & Sons, Ltd, 2020, ch. 16, pp. 499–530.

[458] K. K. Baeck and H. An, *The Journal of Chemical Physics*, 2017, **146**, 064107.

[459] H. An and K. K. Baeck, *Chemical Physics Letters*, 2018, **696**, 100–105.

[460] X. Zhao, I. C. Merritt, R. Lei, Y. Shu, D. Jacquemin, L. Zhang, X. Xu, M. Vacher and D. G. Truhlar, *Journal of Chemical Theory and Computation*, 2023, **19**, 6577–6588.

[461] I. C. Merritt, D. Jacquemin and M. Vacher, *Journal of Chemical Theory and Computation*, 2023, **19**, 1827–1842.

[462] F. Plasser, M. Ruckenbauer, S. Mai, M. Oppel, P. Marquetand and L. González, *Journal of Chemical Theory and Computation*, 2016, **12**, 1207–1219.

[463] I. G. Ryabinkin, J. Nagesh and A. F. Izmaylov, *The journal of Physical Chemistry Letters*, 2015, **6**, 4200–4203.

[464] G. A. Meek and B. G. Levine, *The journal of Physical Chemistry Letters*, 2014, **5**, 2351–2356.

[465] Y. Shu, L. Zhang, X. Chen, S. Sun, Y. Huang and D. G. Truhlar, *Journal of Chemical Theory and Computation*, 2022, **18**, 1320–1328.

[466] Z. Li, F. J. Hernández, C. Salguero, S. A. Lopez, R. Crespo-Otero and J. Li, *Nature Communications*, 2025, **16**, 1194.

[467] W. Xie, M. Sapunar, N. Došlić, M. Sala and W. Domcke, *The Journal of Chemical Physics*, 2019, **150**, 154119.

[468] G. Granucci and M. Persico, *The Journal of Chemical Physics*, 2007, **126**, 134114.

[469] J. E. Subotnik, A. Jain, B. Landry, A. Petit, W. Ouyang and N. Bellonzi, *Annual Review of Physical Chemistry*, 2016, **67**, 387–417.

[470] G. Granucci, M. Persico and A. Zoccante, *The Journal of Chemical Physics*, 2010, **133**, 134111.

[471] C. Zhu, S. Nangia, A. W. Jasper and D. G. Truhlar, *The Journal of Chemical Physics*, 2004, **121**, 7658–7670.

[472] C. Zhu, A. W. Jasper and D. G. Truhlar, *Journal of Chemical Theory and Computation*, 2005, **1**, 527–540.

[473] J. P. Malhado and J. T. Hynes, *Chemical Physics*, 2008, **347**, 39–45.

[474] T. Jíra, J. Janoš and P. Slavíček, *Journal of Chemical Theory and Computation*, 2024, **20**, 10972–10985.

[475] M. Malis and S. Luber, *Journal of Chemical Theory and Computation*, 2020, **16**, 4071–4086.

[476] F. Franco de Carvalho and I. Tavernelli, *The Journal of Chemical Physics*, 2015, **143**, 224105.

[477] W. Xie and W. Domcke, *The Journal of Chemical Physics*, 2017, **147**, 184114.

[478] E. X. Salazar, M. F. Menger and S. Faraji, *Journal of Chemical Theory and Computation*, 2024, **20**, 5796–5806.

[479] L. Landau, *Phys. Z. Sowjetunion*, 1932, **2**, 118.

[480] C. Zener, *Proceedings of the Royal Society of London. Series A, Containing Papers of a Mathematical and Physical Character*, 1932, **137**, 696–702.

[481] E. C. G. Stueckelberg, *Helv. Phys. Acta*, 1932, **5**, 369.

[482] A. K. Belyaev and O. V. Lebedev, *Physical Review A—Atomic, Molecular, and Optical Physics*, 2011, **84**, 014701.

[483] L. Yue, L. Yu, C. Xu, Y. Lei, Y. Liu and C. Zhu, *ChemPhysChem*, 2017, **18**, 1274–1287.

[484] L. Yu, C. Xu, Y. Lei, C. Zhu and Z. Wen, *Physical Chemistry Chemical Physics*, 2014, **16**, 25883–25895.

[485] N. Tokić, T. Piteša, A. Prlj, M. Sapunar and N. Došlić, *Croatica chemica acta*, 2024, **97**, P1–P11.

[486] E. Marsili and B. F. Curchod, *The Journal of Physical Chemistry A*, 2024, **128**, 996–1008.

[487] L. Hutton and B. F. Curchod, *ChemPhotoChem*, 2022, **6**, e202200151.

[488] E. Marsili, A. Prlj and B. F. Curchod, *The Journal of Physical Chemistry A*, 2022, **126**, 5420–5433.

[489] S. M. Parker, S. Roy and F. Furche, *Physical Chemistry Chemical Physics*, 2019, **21**, 18999–19010.

[490] E. R. Miller, S. J. Hoehn, A. Kumar, D. Jiang and S. M. Parker, *The Journal of Chemical Physics*, 2024, **161**, 034105.

[491] S. Mai, P. Marquetand and L. González, in *Surface Hopping Molecular Dynamics*, John Wiley & Sons, Ltd, 2020, ch. 16, pp. 499–530.

[492] M. Barbatti, M. Ruckenbauer, F. Plasser, J. Pittner, G. Granucci, M. Persico and H. Lischka, *Wiley Interdisciplinary Reviews: Computational Molecular Science*, 2014, **4**, 26–33.

[493] M. Barbatti, M. Bondanza, R. Crespo-Otero, B. Demoulin, P. O. Dral, G. Granucci, F. Kossoski, H. Lischka, B. Mennucci, S. Mukherjee *et al.*, *Journal of Chemical Theory and Computation*, 2022, **18**, 6851–6865.

[494] A. Prlj, D. Hollas and B. F. Curchod, *The Journal of Physical Chemistry A*, 2023, **127**, 7400–7409.

[495] D. Hollas, J. Suchan, M. Ončák and P. Slavíček, *PHOTOX/ABIN v1.1*, 2018.

[496] D. Hollas, L. Sistik, E. G. Hohenstein, T. J. Martínez and P. Slavíček, *Journal of Chemical Theory and Computation*, 2018, **14**, 339–350.

[497] R. Souza Mattos, S. Mukherjee and M. Barbatti, *Journal of Chemical Theory and Computation*, 2025, **21**, 2189–2205.

[498] T. J. Marínez, private communication, 2024.

[499] L. J. Doriol, *PhD thesis*, Université Montpellier 2, 2012.

[500] E. H. Lieb, *International Journal of Quantum Chemistry*, 1983, **24**, 243–277.

[501] E. K. U. Gross, L. N. Oliveira and W. Kohn, *Physical Review A*, 1988, **37**, 2805–2808.

[502] E. K. U. Gross, L. N. Oliveira and W. Kohn, *Physical Review A*, 1988, **37**, 2809–2820.

[503] L. N. Oliveira, E. K. U. Gross and W. Kohn, *Physical Review A*, 1988, **37**, 2821–2833.

[504] M. Filatov and S. Shaik, *Chemical Physics Letters*, 1998, **288**, 689–697.

[505] A. Kazaryan, J. Heuver and M. Filatov, *The Journal of Physical Chemistry A*, 2008, **112**, 12980–12988.

[506] E. Trushin, J. Erhard and A. Görling, *Physical Review A*, 2024, **110**, L020802.